UNIVERSITY of LIMERICK

OLLSCOIL LUIMNIGH

Nanotubes Prepared by Electroless Deposition: Investigation of the Nanostructure Formation Mechanism and Characterisation of Physical Properties

David Richardson, B.Sc

Supervisor:

Dr. Fernando M.F. Rhen

Department of Physics and Energy

University of Limerick

This thesis is submitted in partial fulfilment of the requirements for the degree of Doctor of Philosophy

Declaration

Nanotubes Prepared by Electroless Deposition: Investigation of the Nanostructure Formation Mechanism and Characterisation of Physical Properties

Supervisor:

Dr. Fernando M.F. Rhen

This thesis is submitted in partial fulfilment of the requirements for the degree of

Doctor of Philosophy

"It is entirely my own work, and has not been submitted to any other University or higher education institution, or for any academic award in this University. Where use has been made of the work of other people, it has been fully acknowledged and referenced accordindly"

David Richardson

Acknowledgements

I would like to sincerely thank my supervisor Dr. Fernando Rhen for his guidance and advice during the course of my research work. I am also very grateful to the Department of Physics and Energy at the University of Limerick for their continued support throughout my research especially Prof. Noel Buckley, Maria Quinn and Josephine Hogan. I would like to thank the lab technicians in the department, John, John and Eamonn for their continued support and help to all research students. I also wish to thank Dr. Catherine Lenihan for proof reading my thesis.

I would like to thank everybody who has contributed to the work presented in this thesis. I am gratelful to Dr. Fathima Laffir for XPS measurements throughout the course of my research. I also wish to thank Cian McKeown for his TEM imaging skills and Sam Kingston for his help in the lab. I must also thank my sister, Niamh, for her incredible graphical design skills to produce the 3-D schematic diagrams presented in this thesis.

This thesis is dedicated to my parents who have continued to support me throughout my education and my girlfriend, Eva, who has supported me throughout this process. I must also thank all the other post-graduate research students in the Department of Physics and Energy and the MSSI who have continued to make this an enjoyable experience.

This work was supported in part by the Irish Research Council (RS/2011/270) and Science Foundation Ireland (12/IP/1692).

List of Publications and Presentations

Journal Publications

- Richardson, D., Rhen, F.M.F., "Magnetic Properties of Electroless Deposited Ni-Cu-B Nanotube Arrays" *IEEE Trans. Mag.*, 50(11), 2303104 (2014)

- Richardson, D., Rhen, F.M.F., "Investigation of the Electroless Deposition Process of Magnetic Nanostructures" *ECS Trans.*, 64(31), 39 (2015)

- Richardson, D., Rhen, F.M.F., "Magnetic Properties of Co-B Nanostructures Prepared via Electroless Deposition" *Solid. State. Phenom.*, 233-234, 648 (2015)

- Richardson, D., Kingston, S., Rhen, F.M.F., "Synthesis and Characterization of Ni-Fe-B Nanotubes" *IEEE Trans. Mag.*, In Press.

- Richardson, D., Rhen, F.M.F., "Increasing the Magnetisation of Electrolessly Deposited Ni-B Nanotubes" *IEEE Trans. Mag.*, In Press

- Richardson, D., Rhen, F.M.F., "An Investigation of the Electroless Deposition Process and Magnetic Properties of Ni-B Nanostructures" *Mater. Chem. Phys.*, Under Review.

Conference Proceedings

- Richardson, D., Rhen, F.M.F., "Nanostructured Co-B Catalysts for Hydrogen Generation" *Springer. Proc. Energy., 2nd International Congress on Energy Efficiency and Energy Related Materials (ENEFM2014)*, Chapter 60 (2015)

Conference Presentations

- IEEE International Magnetics Conference (INTERMAG) May 11-15, 2015, Beijing, China "Increasing the Magnetisation of Electrolessly Deposited Ni-B Nanotubes" Richardson, D., Rhen, F.M.F., Oral Presentation.

- IEEE International Magnetics Conference (INTERMAG) May 11-15, 2015, Beijing, China "Synthesis and Characterization of Ni-Fe-B Nanotubes" Richardson, D., Kingston, S., Rhen, F.M.F., Oral Presentation.

- 2nd International Congress on Energy Efficiency and Energy Related Materials (ENEFM), Oct 16-19, 2014, Oludeniz, Turkey, "Nanostructured Co-B Catalysts for Hydrogen Generation" Richardson, D., Rhen, F.M.F., Oral Presentation.

- 2nd International Congress on Energy Efficiency and Energy Related Materials (ENEFM), Oct 16-19, 2014, Oludeniz, Turkey, "Nanostructured Catalysts Prepared via Electroless Deposition for Hydrogen Release from $NaBH_4$" Richardson, D., Rhen, F.M.F., Poster Presentation.

- 226th Meeting of the Electrochemical Society (ECS), Oct 5-9, 2014, Cancun, Mexico, "Investigation of the Electroless Deposition Process of Magnetic Nanostructures" Richardson, D., Rhen, F.M.F., Oral Presentation.

- 6th Moscow International Symposium on Magnetism (MISM) June 29- July 3, 2014, Moscow, Russia, "Magnetic Properties of Co-B Nanostructures Prepared via Electroless Deposition" Richardson, D., Rhen, F.M.F., Oral Presentation.

- IEEE International Magnetics Conference (INTERMAG) May 4-8, 2014, Dresden, Germany "Magnetic Properties of Electroless Deposited Ni-Cu-B Nanotube Arrays" Richardson, D., Rhen, F.M.F., Poster Presentation.

Awards

- IRC New Foundations Research Support Grant 2014
- PhD Scholars Bursary, University of Limerick, 2015
- Electrochemical Society Student Travel Grant, ECS Fall Meeting 2014
- IEEE Magnetics Society Student Travel Grant, Intermag 2014

- Microscopy Society of Ireland Student Travel Grant, MSI SMG Joint Symposium 2014

- MSSI Research Day, June 26, 2014, Limerick, Thesis in Three Competition, 1st Place.

- MSSI Research Day, June 27, 2013, Limerick, Thesis in Three Competition, 1st Place.

Abstract

In this research, we investigate electrolessly deposited nanotubes due to their unique associated magnetic and catalytic properties. The main challenge associated with electroless deposition is the formation of a nanotube structure with a uniform wall thickness. In this study, we investigate the electroless deposition process of nanotubes within a polycarbonate membrane. By identifying the conditions required to ensure a kinetically controlled deposition process, we achieve the formation of continuous nanotubes with a uniform wall thickness.

Electrolessly deposited alloys containing Ni, Fe and Co are magnetic and have many potential applications in future technologies. In this work, we investigate the magnetic properties of a series of alloys including Ni-B, Ni-Fe-B, Co-B and Ni-Cu-B nanotube structures. We establish the relationships between the magnetic properties of the nanostructure and their structure and compositional parameters. We also characterise the magnetic reversal mechanisms associated with the nanotube structure, which depend on the alloy used. We achieve a maximum specific magnetisation of 84.3 J T^{-1} kg^{-1} and a minimum coercivity of 0.003 T.

Alloyed deposits containing B can be used to catalyse hydrogen release from an alkaline $NaBH_4$ solution. In this study, a variety of nanostructured alloys, including Ni-B, Co-B, NiCu-B, NiFe-B and NiCo-B and CoNiFe-B are investigated as catalysts for hydrogen generation. We show that nanostructured catalysts have larger hydrogen generation than metallic films with a maximum hydrogen generation rate of 10,800 ml min^{-1} g^{-1}.

Table of Contents

List of Figures

Chapter 2

Chapter 3

Chapter 4

Chapter 5

Chapter 6

List of Tables

Chapter 2

Chapter 3

Chapter 5

Chapter 6

Chapter 1 – Introduction

Since carbon nanotubes were first fabricated in 1991, nanotubes of various dimensions and compositions have been synthesised for a wide range of applications. Metallic nanotubes have become the focus of much attention due to their unique magnetic and electrical properties which differ from that of the bulk material. The catalytic properties of nanostructures are also of interest due to their large surface area. In general, metallic nanotubes are usually deposited via one of three processes: electroless deposition, electrochemical deposition or chemical vapour deposition. Each process has unique advantages and disadvantages. A literature review of nanotube formation and their associated physical properties is presented in Chapter 2.

Electroless deposition has acquired much interest as it is a simple and cheap method of nanostructure preparation. Nowadays, nanostructures with a wide variety of potential applications in areas such as magnetism, electronic devices, hydrogen catalysis and biotechnology are deposited via electroless deposition. Electroless deposition requires a reducing agent, which acts as an electron donor during the deposition process. However, the use of a reducing agent results in the co-deposition of the electron donor with the metal. In this research, we use dimethylamineborane (DMAB) as a reducing agent, which results in the co-deposition of boron along with the metal deposited. A detailed explanation of the electroless deposition chemistry and the characterisation methods used to determine the physical properties of the nanostructures is given in Chapter 3.

The electroless deposition of nanotubes requires a template structure onto which the alloy can adhere and grow. The most common template structures used are porous

polycarbonate (PPC) membranes and anodic aluminum oxide (AAO) membranes. However, a detailed investigation of the electroless deposition process within a template structure and a characterisation of the associated physical properties of the deposits is lacking. Due to the deposition process involved, there are many challenges associated with the electroless deposition of nanotubes. Previously, it has been found that the deposition rate on the membrane surface is larger than within the nanotube pores, resulting in the formation of end-closed nanotubes. We propose that this is due to a diffusion limited deposition process occuring within the membrane pores. Therefore, to achieve the formation of continuous nanotubes with a uniform wall thickness a kinetically controlled reaction is required. By achieving a kinetically controlled reaction, deposition throughout the template would occur at the same rate, both on the membrane surface and within the nanotube pores. We propose that this would lead to the formation of continuous nanotubes with a uniform wall thickness.

In Chapter 4, we investigate the electroless deposition process in detail using a polycarbonate membrane as a template structure to analyse the stages of electroless deposition and nanotube formation. The pores of the membrane, in which the nanotubes form, are 400 nm in diameter and 20 μm in length. An electroless Ni-B deposition process is used as an examplar to conduct a detailed investigation of the reaction kinetics within the membrane pores. The kinetics of the reaction are controlled by varying the bath temperature, pH and reactant concentrations. We provide evidence to show that if deposition within the membrane pores is kinetically controlled, continuous uniform nanotubes are formed. We show that if deposition within the nanotube is diffusion limited, incomplete and non-uniform end-closed nanotubes are formed. Through the investigation of electroless Ni-B deposition, we present a simplified method to determine the type of deposition that is occurring

within the nanotube structure. By ensuring that electroless deposition is kinetically controlled throughout the nanotube structure, the preparation of continuous Ni-B nanotubes with uniform wall thickness is achieved.

Magnetic nanotubes with a range of compositions, including Ni-P, Co-P, CoFe-B and CoNiFe-B, have been prepared previously using an electroless deposition method. Magnetic nanostructures are of great interest as their magnetic properties differ from that of the bulk material. They are being explored for potential use in emerging areas of energy, power-technologies and bio-magnetics. Due to the diversity of potential applications, a large amount of research is being conducted to find new nanostructures with suitable magnetic and electrical properties. Nanotubes are of particular interest as their magnetic properties can be controlled through the variation of both the composition and the structure. In Chapter 5, we present an investigation of the magnetic properties of electrolessly deposited nanotubes of varying compositions. From this study, we aim to establish methods of controlling the magnetic properties of the nanotubes.

We have deposited a variety of magnetic nanotube structures of varying compositions including Ni-B, Co-B, Ni-Fe-B and Ni-Cu-B via an electroless deposition method. Due to the presence of B from the electroless deposition process, the specific magnetisation of the electroless deposit is lower than that of the bulk magnetic element. In this work, methods to increase the specific magnetisation of the electrolessly deposited nanotubes are investigated. We investigate the magnetic properties of the electrolessly deposited nanostructures, such as coercivitiy, remanence and saturation magnetisation, as functions of composition, crystallinity and structure. Through the variation of these properties, we show that the magnetic properties of the nanostructures can be controlled. Control over the magnetic

properties provides endless opportunities to tailor the magnetic properties of electrolessly deposited nanotubes to suit a range of potential applications.

Electrolessly deposited transition metal-boron alloys can also be used as catalysts for the generation of hydrogen from an alkaline $NaBH_4$ solution. The viability of hydrogen technology as a future alternative to non-renewable energy sources requires low cost fuel cells, safe and cheap storage media and efficient methods of hydrogen generation. Our research is focussed on increasing the efficiency of the hydrogen generation process by using the electrolessly deposited nanostructures that we have prepared. Although noble metals have been shown to have large catalytic activities, due to their cost, alternative cheap non-noble transition metal catalysts are the focus of research in the area. Previously nanostructured B alloy catalysts such as nanoparticles and porous films have been shown to have large hydrogen generation rates. Due to the increased catalytic surface area of that electrolessly deposited nanotubes that we have prepared, we inferred that a large catalytic activity can be achieved.

In Chapter 6, we investigate the hydrogen generation rates of the nanostructured catalysts as a function of composition and structure. Through variations in the electroless deposition time, the wall thickness and internal diameter are varied and the associated effect on the hydrogen generation rate is investigated. The effect of temperature of the alkaline $NaBH_4$ is investigated along with the $NaBH_4$ concentration. The recyclability of the electrolessly deposited nanostructured catalysts and their potential for use in future technologies is also examined. We show that nanostructures have relatively large hydrogen genertaion rates, though further advances are required to achieve a viable technology.

There are 3 main research objectives associated with this research. The first research objective is to understand and control the electroless deposition process so that the formation of continuous nanotubes with a uniform wall thickness can be achieved. The second objective is to characterise and control the magentic properties of electrolessly deposited nanotubes with unique compositions, so that the properties can be tailored to suit a range of potential applications. Finally, we characterise the catalytic properties of the nanotubes with the objective of achieving a large hydrogen generation rate from an alkaline $NaBH_4$ solution using electrolessly deposited nanostructures. Each of these are unique studies with many potential applications for future technologies.

Chapter 2 – Literature Review

2.1 **Introduction**

In this chapter the literature concerning relevant areas of this research is reviewed including the electroless deposition process, the composition and crystal structure of the deposit, the magnetic properties of the nanotubes and the use of electrolessly deposited media in hydrogen generation applications.

The review begins by examining the electroless deposition process and how this process is used to prepare metallic alloy nanotubes. The composition and crystal structure of electrolessly deposited materials are investigated, because they affect the properties of the deposit. Electrochemical deposition is an alternative method with which nanotubes can be fabricated and a comparison between the two processes is presented.

Electrolessly deposited nanotubes have wide ranging potential for magnetic applications, including magnetic recording media, power technologies, electronic components and bio-technology [1-4]. Therefore, the current research on the magnetic properties and the magnetic reversal mechanisms associated with a nanotube structure are examined. If the associated magnetic properties of the nanotubes can be fully understood it will be possible to tailor the nanotubes to suit a range of potential applications.

Electrolessly deposited metallic alloys also have catalytic properties and are currently researched as catalysts for the release of hydrogen from sodium borohydride. The use of transition metal catalysts in hydrogen generation is investigated, along with their

hydrogen generation rates and potential for use in future technologies. The findings of the literature review will form the basis of the research carried out in this thesis.

2.2 Electroless Deposition

2.2.1 Discovery

In 1946, A. Brenner and G.E. Riddell [5] accidently stumbled across the electroless deposition method when they observed an unusual chemical reaction occurring in an electrochemical Ni plating bath. They noticed that, for certain plating reactions, current efficiencies of 130 % were obtained. They determined that this efficiency was only possible if electroless deposition of Ni was occurring at the anode. They then developed a method of depositing Ni on a steel or Ni surface without the application of an external current which they termed "electroless plating".

In its simplest terms, electroless deposition can be considered as the sum of two chemical reactions occurring within a deposition bath. The first is the oxidation of a reducing agent to liberate electrons, while the second is the reduction of the metal ion to pure metal with these electrons as shown in Eqns. 2.1 and 2.2. For the oxidation-reduction reaction to occur, the potential of Eqn. 2.1 must be lower than the potential of Eqn. 2.2.

$$Red_{agent} \rightarrow Ox + e^{-} \quad (2.1)$$

$$Metal^{+2} + 2e^{-} \rightarrow Metal^{0} \quad (2.2)$$

The prediction made in 1946 was that electroless deposition would not replace electrodeposition, but would instead be useful for specialist applications. To this day the prediction has proved true, with electroless deposition being used for unique

applications such as the deposition of nanostructures [6-8] and components of electronic circuit boards [9-13].

2.2.2 Metals

Electroless deposition allows for the deposition of a wide variety of metals including Ni [14,15], Co [16,17], Fe [18,19], Cu [20,21], Au [22,23], Ag [24,25], Pt [22] and Pd [22,26]. The metals are usually dissolved in the deposition bath in the form of sulphates [6,18,19] or chlorides [14,15,22]. In these compounds the metal exists as an ion with a charge of +2 which is reduced during the electroless deposition process. It is also possible to deposit a number of metals at the same time to form alloys such as Ni-Co [27,28], Co-Ni-Fe [6,29-31], Ni- Fe [32,33] and Co-Fe [32,33]. The electrode potentials for Ni, Co and Fe, which are magnetic metals that can be deposited, are shown in Eqns. 2.3 - 2.5 [29].

$$Ni^{+2} + 2e^{-} = Ni \qquad E^{0} = -250\ mV \tag{2.3}$$

$$Co^{+2} + 2e^{-} = Co \qquad E^{0} = -280\ mV \tag{2.4}$$

$$Fe^{+2} + 2e^{-} = Fe \qquad E^{0} = -440\ mV \tag{2.5}$$

2.2.3 Reducing Agents

Reducing agents are needed for the electroless deposition process because they act as electron donors for the reduction of metal ions. Presently, the most common reducing agents for electroless deposition of metals are sodium hypophosphite [28,34,35] and dimethylamine borane (DMAB) [6,29,36]. The deposit is not pure metal but rather an alloy which contains either phosphorous or boron depending on the reducing agent used.

2.2.4 Catalysts

Electroless deposition will only occur on a catalytic surface. If the deposited metal is also catalytic, the reaction will continue unaided in an auto-catalytic manner [37]. Pd is the most common catalyst for the activation of substrates [6,29,35,38]. For an autocatalytic reaction to occur, the deposited metal such as Ni, Co or Au must have catalytic properties. It has been observed that for both a DMAB and hypophosphite reducing agent, Ni and Co can autocatalyse the reaction [39]. However, other transition metals such as Fe and Cu offer smaller catalytic potentials and are usually co-deposited with another metal which has autocatalytic properties.

2.3 Electroless Deposition Mechanism

In 1966, Judge et al. [40] were the first group to recognise that the electroless growth occurred as a hemispherical deposit. Deposited Co-P films were allowed to decay into cobalt oxide which would affect the remanent magnetisation. They knew that the fraction of cobalt oxidised was given by Eqn. 2.6,

$$\frac{\Delta X}{X_0} = \frac{\Delta M_r}{M_{r0}} \tag{2.6}$$

where X = weight of unoxidised cobalt per unit area and M_r = remanent moment. Although a linear dependence would be expected for the oxidation of a thin film, the authors found an $M_{r0}^{2/3}$ fit dependence. Because the surface area scales with a 2/3 dependence, this indicates that the surface consists of electroless hemispherical deposits.

In 1968, J. P. Marton and M. Schlesinger [41] were the first to describe the electroless process in detail. They found that the deposition on activated dielectric substrates was

selective and that initial deposition occurred at catalytic Pd sites, forming electrolessly deposited islands at each nucleation point. As deposition continued, the islands grew in size and coalesced to form a continuous film. Ni-P islands from this study are shown in Fig. 2.1(a). Some islands have already coalesced to form a continuous film. However, if electroless deposition occurred on a Ni substrate, the deposits formed were continuous and no islands were observed as Ni acts as a catalyst for the reaction as shown in Fig. 2.1(b).

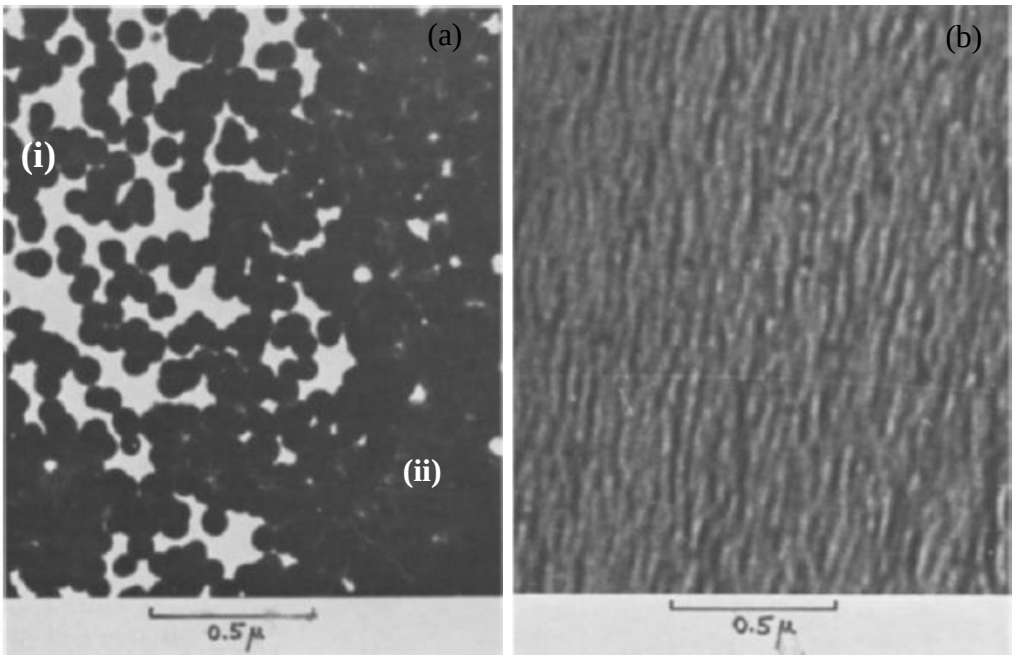

Figure 2.1: (a) TEM image of a Ni-P deposit on an activated substrate. Two distinct regions of growth are visible **(i)** Ni-P islands nucleating at catalytic Pd sites and **(ii)** Ni-P islands coalescing to form a continuous film **(b)** A continuous Ni-P film electrolessly deposited on a Ni substrate with no activation step [41].

It was found that the island diameter growth was constant with respect to deposition time and that the Ni-P islands maintained their circular shape until coalescence occurred. This indicates that the island growth is isotropic and that the islands are hemispheres located base down on the substrate, confirming the finding of Judge et al. [40]. Similar results were observed by R. Sard [42] with the preparation of electrolessly deposited Cu films.

Using an in situ scanning tunnelling microscopy (STM) technique, Homma et al. [43] investigated the electroless deposition process of Ni-P on a graphite substrate. With the in situ STM technique, the electroless deposition mechanism could be investigated during the deposition process. At the initial nucleation stage, Ni-P particles were observed to form at catalytic Pd sites. Once they reach a diameter of 20 – 30 nm, they coalesce to form larger particles as shown in Fig. 2.2(a). As deposition continues, a film is formed on the surface. As shown in Fig. 2.2(b), the film is uneven and consists of grains with diameters of 20 – 30 nm, indicating that the particle diameters do not increase after coalescence occurs.

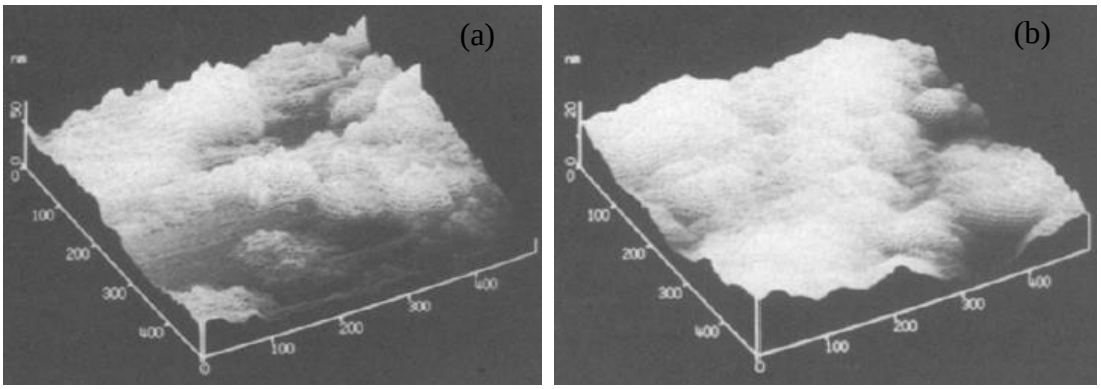

Figure 2.2: STM images of (a) Initial growth of Ni-P on an activated substrate (b) A continuous Ni-P film formed after coalescence of Ni-P islands [43].

In 1993, with more modern TEM imaging, Severin et al. [44] were able to observe Ni-P particles with diameters as small as 2 nm nucleating on the surface after only 6 seconds of deposition. A TEM micrograph taken at the earliest possible stage of growth is shown in Fig. 2.3, indicating that initial deposition occurs on catalytic sites as small as 2 nm in diameter. Once all Pd particles are covered, the reaction becomes autocatalytic and films with thicknesses of up to 40 μm can be deposited [45].

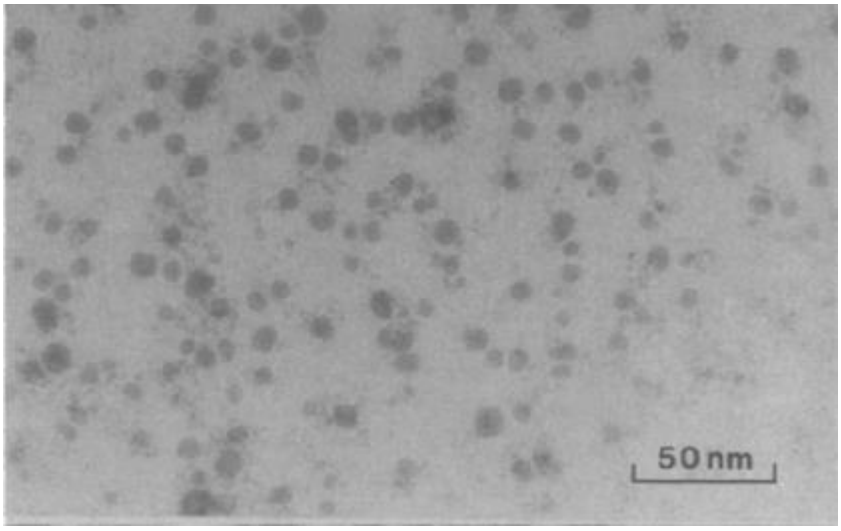

Figure 2.3: Initial Ni-P deposition at catalytic Pd sites with particles less than 2 nm in diameter visible [44].

2.4 Effect of Deposition Bath Parameters

2.4.1 Bath Concentration

The deposition rate and composition of an electrolessly deposited alloy is dependent on the chemicals used in the deposition bath. Increases in concentration of the ion source and reducing agent show a corresponding increase in the deposition rate, while an increased complexing agent concentration results in a decrease in the deposition rate [46]. It has been shown previously that changes in concentration of the reducing agents, either DMAB [47], or hypophosphite [48], result in small changes in B and P concentration. In the case of DMAB, an increase in concentration from 0.025 M to 0.1 M within the deposition bath resulted in alloy compositions of $Ni_{81}B_{19}$ and $Ni_{77}B_{23}$ respectively [47]. In the same study, Co-B compositions range from $Co_{93}B_7$ to $Co_{88}B_{12}$ from DMAB concentrations of 0.025 M and 0.1 M. The catalytic activity for the oxidation of DMAB is much smaller in the Co-B system than for Ni-B. As a result, the boron content of Co-B alloys were significantly smaller than those of Ni-B alloys with the same deposition bath composition [47]. It was also recorded that changes in the concentration of stabilising agents, resulted in minor changes in the

composition of the deposited alloy [39,47]. For example, as shown in Fig. 2.4, a change in sodium citrate concentration from 0.05 M to 0.4 M resulted in an increased B content from 2 wt. % to 3.5 wt. %. However, while using sodium tartrate or sodium malonate as the complexing agent, no change in B content was recorded as complexing agent concentration was varied [47].

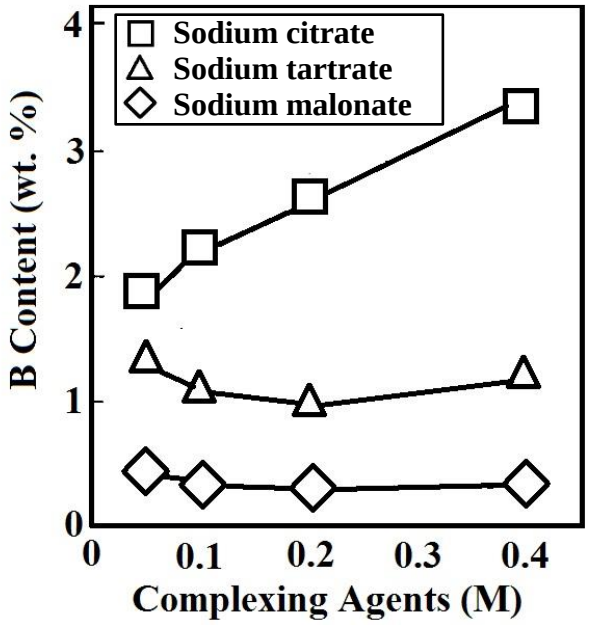

Figure 2.4: Graph of B content on Co-B films as a function of complexing agent concentration for sodium citrate, sodium tartrate and sodium malonate [47].

2.4.2 Bath Temperature

As bath temperature increases, there is a corresponding increase in the electroless deposition rate [49,50]. W.T. Evans and M. Schlesinger [51] found that, although the electroless deposition rate was strongly related to the bath temperature, the composition of the Ni-B deposit was independent of bath temperature. In contrast, using a deposition bath with $NiCl_2$ as the active source of Ni ions and $NaBH_4$ as the reducing agent, Anik et al. found that boron content is affected by bath temperature [14]. A bath temperature of 80 °C resulted in the formation of $Ni_{74}B_{26}$, while a bath temperature of 95 °C forms an alloy of $Ni_{69}B_{31}$. Small changes in the composition

with respect to temperature using DMAB as the reducing agent were also recorded [52]. The kinetics of the chemical reactions involved depends on the type of deposition bath used and therefore different deposition baths may or may not have temperature dependence on the alloy composition.

2.4.3 Bath pH

It has been shown previously that an increasing pH results in an increased deposition rate [53]. It has also been shown that the B and P content is strongly dependant on the pH of the deposition bath and an increase in pH corresponds to a decrease in the B or P content [14,51,54-56]. As shown in Fig. 2.5, Evans and Schlesinger [51] found that electroless Ni deposition with DMAB as the reducing agent resulted in a deposit with a composition of $Ni_{65}B_{35}$ at pH 6. An increase to pH 9 formed $Ni_{91}B_9$. Similar results were found for sodium hypophosphate with a $Ni_{79}P_{21}$ alloy formed at pH 6, whereas an alloy of $Ni_{91}P_9$ was deposited at a pH of 9 [55].

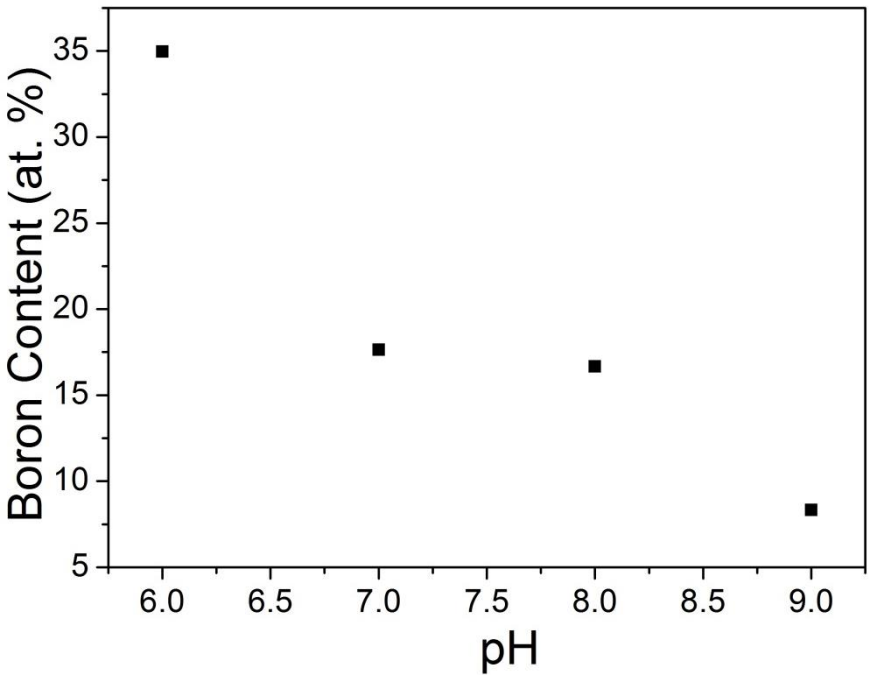

Figure 2.5: Boron content in an electrolessly deposited Ni-B film as a function of deposition bath pH. Data from Evans and Schlesinger [51].

The grain size and crystallinity of the film are also affected by changes in pH and composition. It was found that as the pH increases, the size of the deposited islands and grains also increase [51,54]. Matsubara et al. [55], provided a model to describe the increase in grain size and non-uniformity with an increasing bath pH, as shown in Fig 2.6(a). Initially, deposition will occur randomly at catalytic Pd sites and is independent of pH. Sites at which deposition occurs rely on Ni to auto-catalyse the reaction further. At a pH of 9 there is a large Ni content. These Ni-P islands expand at a fast rate and cover active Pd particles at which catalytic deposition has not occurred, as shown in Fig 2.6(b). However, at low pH, the islands grow slowly and all active Pd particles have time to catalyse the deposition reaction. The island size distribution of the deposited Ni-P films with thickness of 70 nm is shown for deposition baths of pH 9 and pH 6 in Fig 2.6(c,d). Films deposited at pH 6 have a relatively uniform grain size of between 10 and 20 nm, whereas at pH 9 there is a large variation in grain size between 30 – 80 nm (Fig. 2.6(g,h)). Therefore, the authors concluded that a low pH is required to obtain uniform thin films.

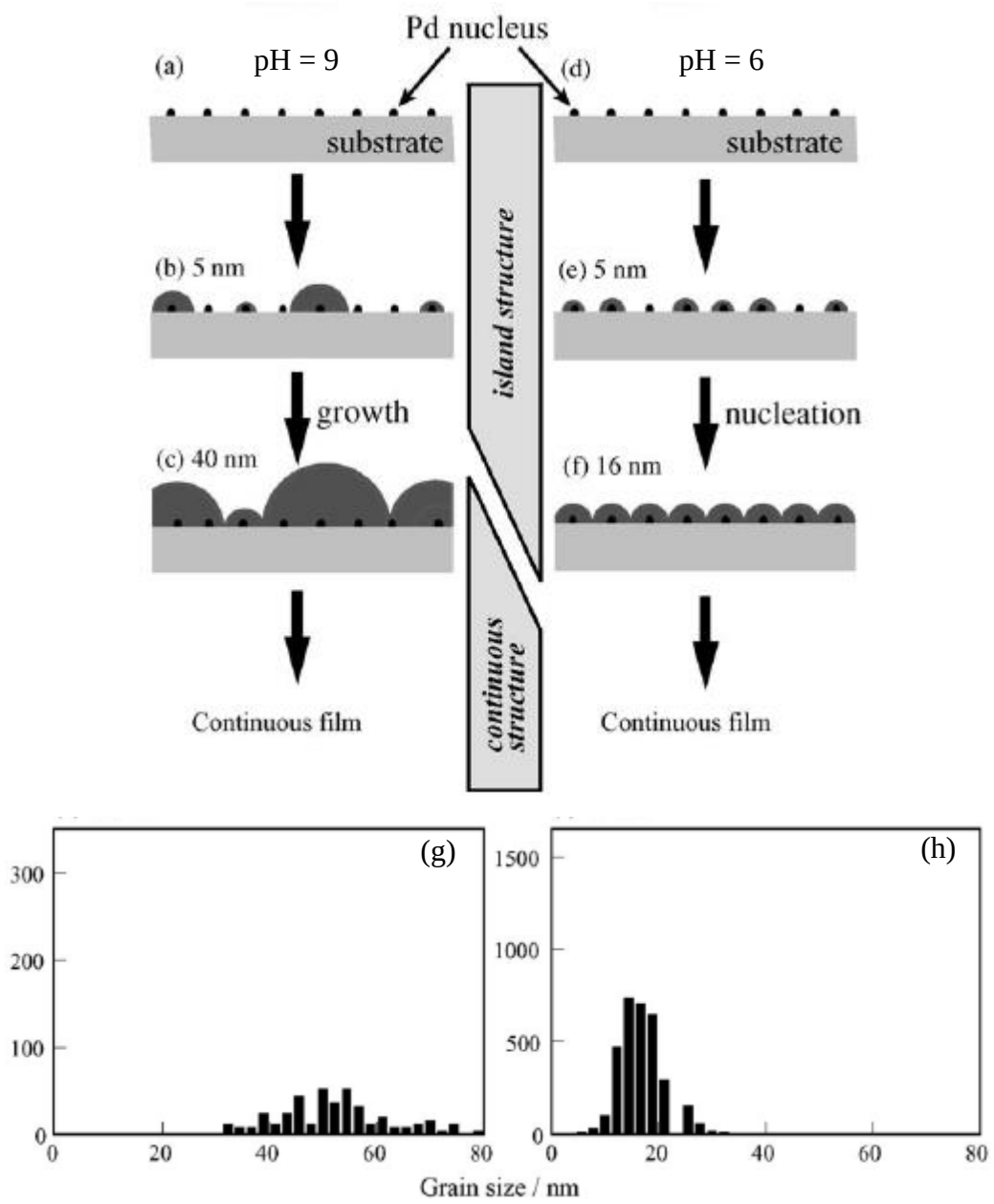

Figure 2.6: Electroless deposition growth process of Ni-P for **(a,b,c)** fast deposition rate with a bath pH 9 and **(d,e,f)** low deposition rate at pH 6. Distribution of Ni-P grain sizes for **(g)** pH 9 and **(h)** pH 6 [55].

2.4.4 Crystallinity

The crystallinity of the deposit is a function of boron or phosphorous content and hence a function of the bath pH. Diffraction patterns of Ni-B are shown in Fig. 2.7(a,b). The diffraction pattern at pH 6 indicates an almost completely amorphous structure. However, the diffraction pattern recorded at pH 8 is characteristic of face centered cubic (FCC) Ni. Boron is acting as an inhibitor to the

formation of a crystal structure and as pH increases, boron content decreases, resulting in an increased crystallinity [51]. It was also found that, post annealing at 500 ºC, a large amount of boron diffused to the surface, resulting in the formation of an FCC Ni crystal structure for all pH values irrespective of B content, as shown in Figure 2.7(c,d).

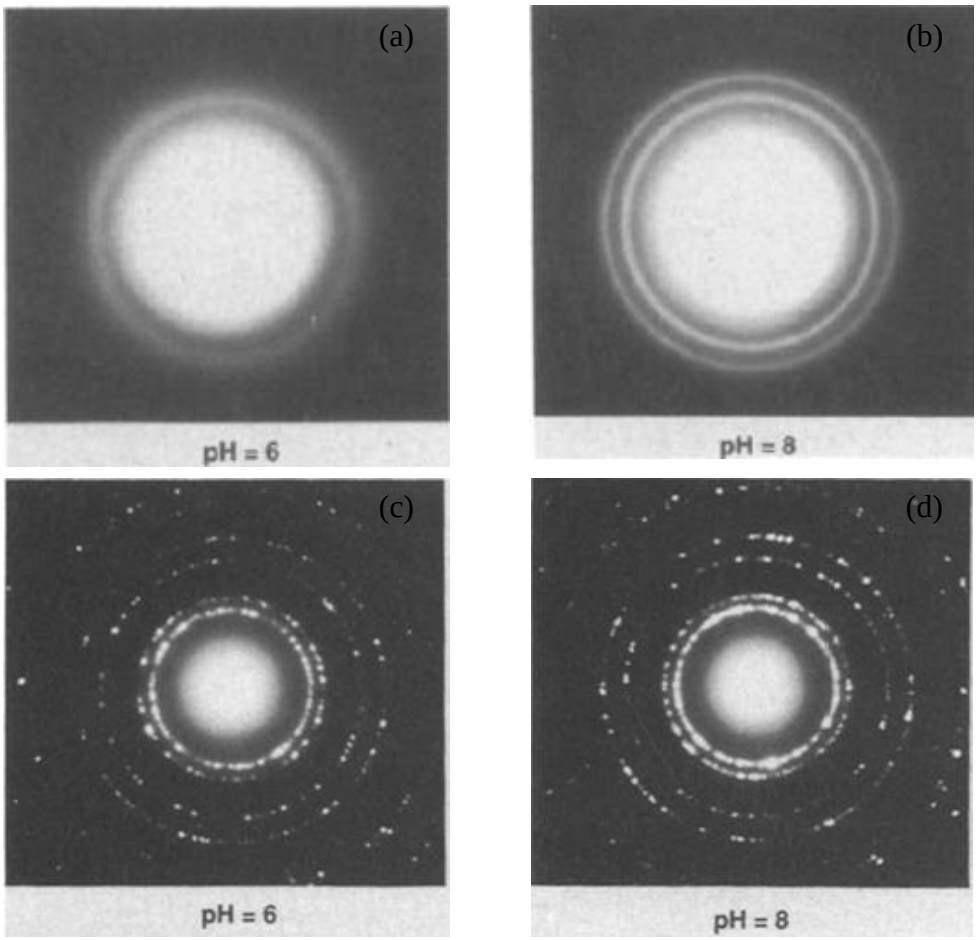

Figure 2.7: Electron diffraction patterns of (a) as deposited $Ni_{65}B_{35}$ deposited at pH 6 and (b) $Ni_{92}B_8$ deposited at pH 8. (c,d) Electron diffraction patterns of Ni-B post annealing at 500 °C deposited at pH 6 and 8 respectively [51].

X-ray diffraction (XRD) analysis of electrolessly deposited Ni-B films indicates that they comprise of more than an FCC phase [14,39,52,57-59] as the crystallinity and phases present depend on the B composition [54]. Studies of Ni-B have noted the existence of a mainly amorphous structure post deposition [60]. However, post annealing, crystallisation of the film occurs and two phases are formed, namely, Ni

FCC and nickel borides in the form of Ni_3B, as shown in Fig. 2.8 [14,39,52,59,61]. However, these results differ to those published previously [51], where it was claimed that B diffuses to the surface and the crystal structure is purely FCC, though an XRD analysis of the deposit was lacking in this study. A Ni_2B phase has also been recorded for high annealing temperatures above 400 °C [14,39,58,59]. Similar results have been recorded for a Co-B alloy [62] with an amorphous phase present post deposition, while annealing results in the formation of a stable Co_3B phase.

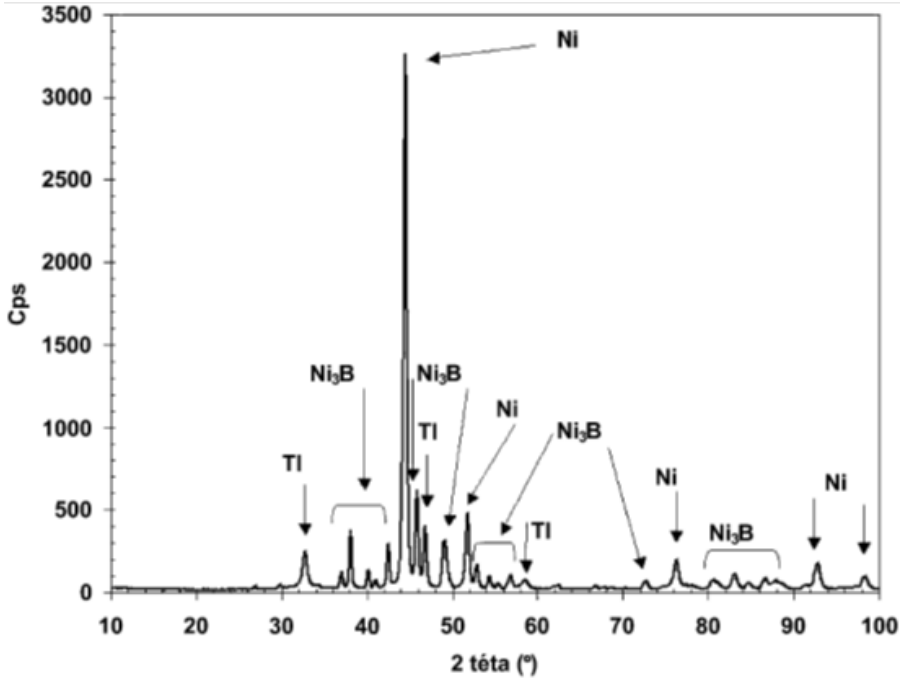

Figure 2.8: XRD pattern of an electrolessly deposited Ni-B film post heat treatment at 400 °C for 1 hour [39].

Tsai and Chao [63] investigated the crystallinity of elctrolessly deposited Ni-P. Fig. 2.9 shows a high resolution transmission electron microscope (HRTEM) image of a $Ni_{90}P_{10}$ film, indicating that the deposit possesses a nanocrystalline structure with nanocrystals approximately 4-8 nm in size. The d spacing of the crystals was found to be 2.03 Å, which corresponds to a FCC (1 1 1) Ni crystal structure. This indicates that the crystalline regions are composed of pure Ni. They propose that the P atoms have zero solubility within the Ni lattice. Instead, during the deposition process, the P

atoms gather around the FCC Ni crystals and as the P content increases the size of the nanocrystals decrease, but the deposit does not become amorphous. Tsai and Chao [63] state that conventional techniques such as X-ray and electron diffraction are limited in distinguishing between amorphous and nano-crystalline phases and that HRTEM imaging is required to provide direct evidence of the crystal structure.

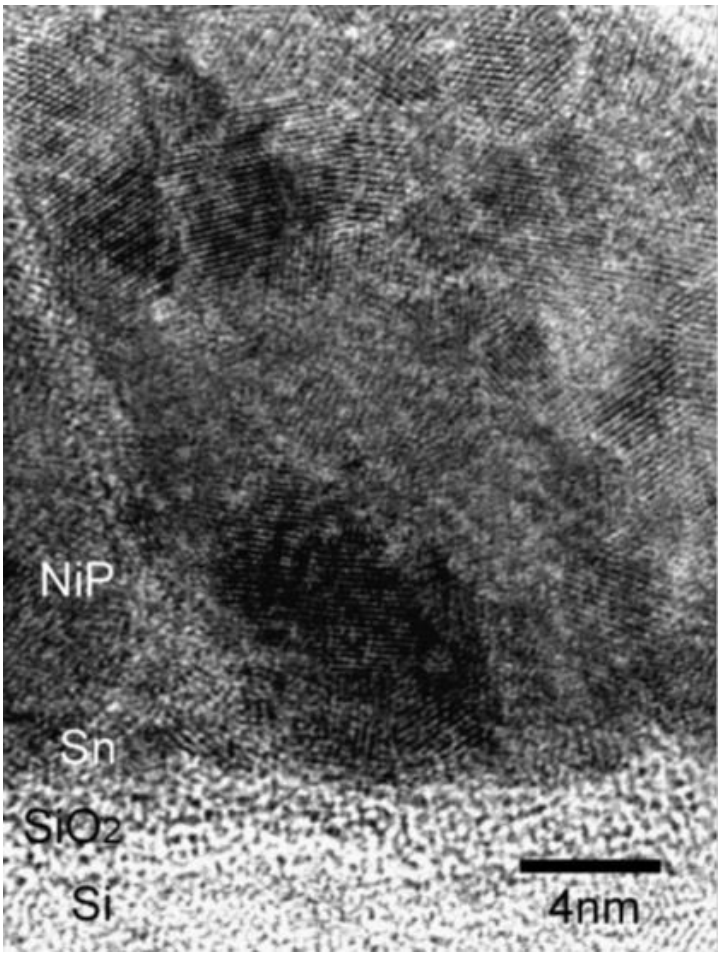

Figure 2.9: HRTEM image of electrolessly deposited Ni-P on a Si substrate [63].

2.5 Nanostructures

2.5.1 Template Synthesis

The growth of nanotubes, nanowires and various other nanostructures within a template structure is a major research focus in modern nanotechnology [64,65]. The preparation of the nanostructures within a template can be achieved by a variety of methods. The most common are electroless deposition [6,29] and electrodeposition [66,67]. Others include chemical vapour deposition [68-70] and atomic layer deposition [71,72]. The main use of template synthesis is the formation of ordered arrays of nanotubes and nanowires with varying lengths and diameters. Template based synthesis is a simple, cheap and reliable process which can easily be scaled up into mass production. The size, shape, diameter, length and densities of the nanostructures are all controlled by the size and shape of the template. The two most common template structures that are used are radiation track etched porous polycarbonate membranes [73] and anodic aluminum oxide (AAO) [74] membranes.

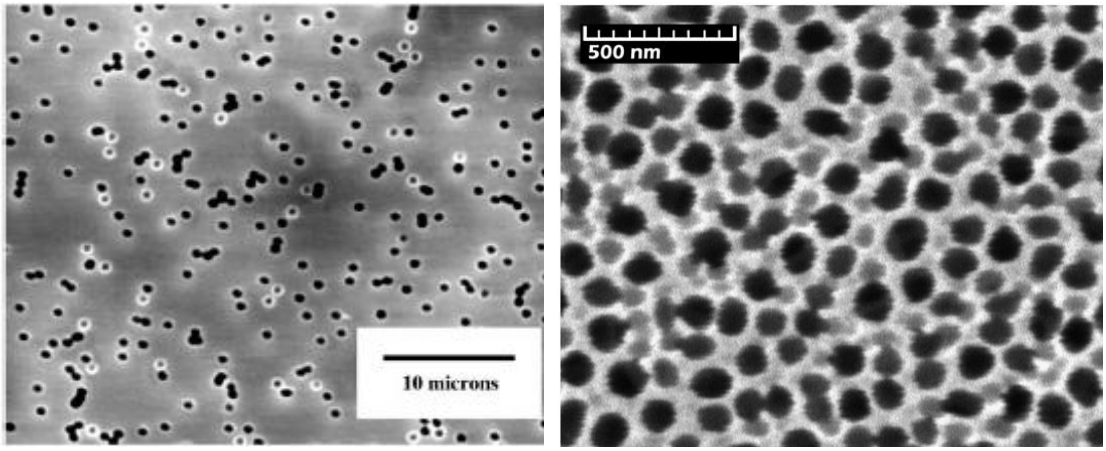

Figure 2.10: SEM images of **(a)** Polycarbonate membrane and **(b)** Aluminum Oxide membrane used as template structures for nanotube and nanowire synthesis [29,75].

2.5.2 Electroless Nanotube

The electroless deposition process of a nanotube array within a template structure is shown in Fig. 2.11. Initially, the walls of the membrane are sensitised, followed by activation with a catalyst as shown in Fig. 2.11(b). The activated template is then placed in an electroless deposition bath to deposit the metallic alloy. The first nanotubes deposited via this method were Au nanotubes on a polycarbonate membrane [76]. Since then, a large amount of work has been carried out on the electroless deposition process of a wide variety of metallic nanotubes. Compositions including Ni-P [34,35,38,77], Co-P [78,79], Fe-Co-B [80] and Co-Ni-Fe-B [6,29] have all been prepared previously. However, the electroless deposition process is still not fully understood or controlled and there is a major discrepancy in the literature between the formation of end-closed nanotubes capped at both ends and the formation of continuous wires.

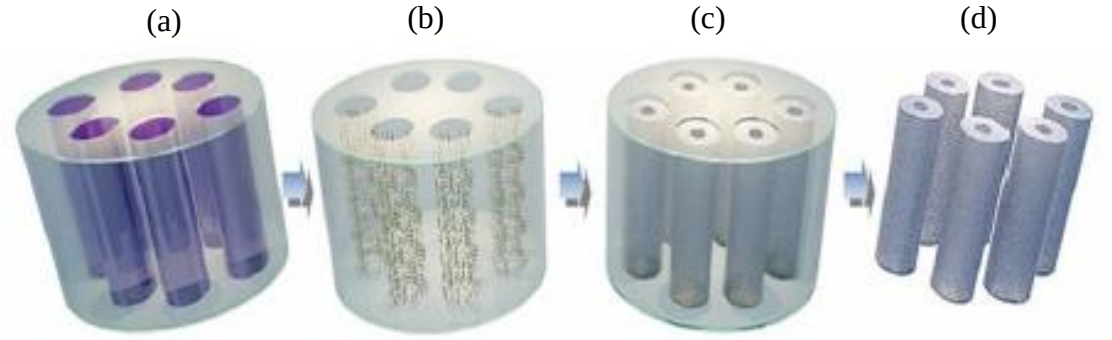

Figure 2.11: Schematic illustration of the procedure to synthesize nanotubes within a porous membrane following steps (a) sensitisation (b) activation (c) nanotube growth and (d) template removal [81].

Lin et al. [35] deposited Ni-P within an AAO membrane using electroless deposition. The nanotubes had a length of 10 μm and a diameter of 250 nm giving an aspect ratio of 40. They have shown that the deposition process is the same as that described previously for electroless deposited films in section 2.3. Initial deposition occurs at

each catalytic Pd nuclei to form Ni-P islands along the membrane walls, as shown in Fig. 2.12. Continuous nanotubes are not formed until the particles coalesce.

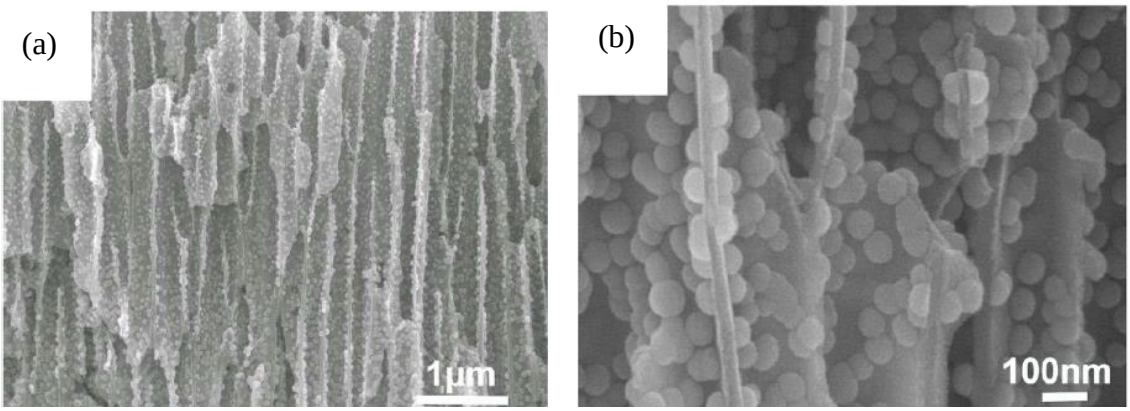

Figure 2.12: SEM images of initial Ni-P electroless deposition within an AAO membrane with Ni-P islands visible after 2 minutes of deposition for (a) low magnification and (b) high magnification [35].

Initially, once conformal electroless deposition is achieved, a reduction in transparency of the membrane is observed, as shown in Fig. 2.13(b). A reduction in transparency with a dull deposit occurs because nano-metallic particles typically appear black. However, excessive deposition occurs and the pores become blocked as a continuous film is formed on the surface on the membrane. This is characterised by a shiny deposit observable on the membrane surface, as shown in Fig. 2.13(c). In this paper, no explanation is given for the closing of the membrane pores, although the authors suggest that the nanotubes may be incomplete and have varying wall thicknesses [35].

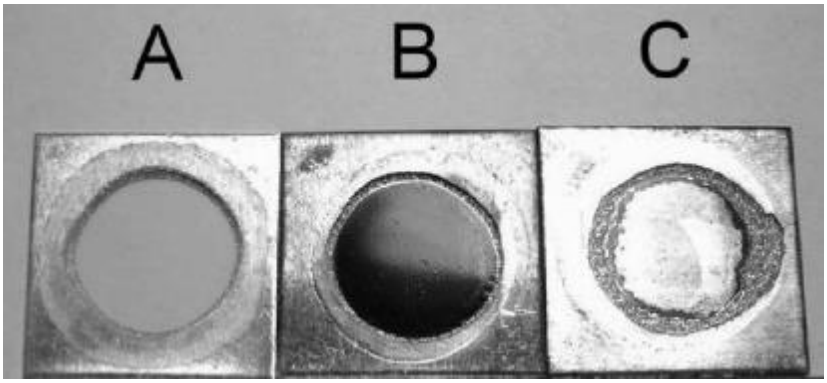

Figure 2.13: Images of (a) Original AAO template structure (b) AAO membrane after the deposition of Ni-P nanostructures and (c) AAO membrane with a continuous film deposited on the surface [35].

In the same year, Enculescu et al. [38] were also preparing Ni-P nanotubes via electroless deposition within a polycarbonate membrane and provided a theory explaining the results found by Lin et al. [35]. They noted that the process of deposition inside the pores is determined by two parameters: the reaction rate and the diffusion rate. As diffusion of the reactants is limited inside the pores, they found that deposition occurs at a slower rate inside the pores than on the external surfaces of the membrane. Therefore, a high reaction rate can cause the closing of the pores at the surface. This prevents diffusion of reactants inside the nanotube pores and leads to incomplete nanotube growth. By decreasing the temperature they were able to achieve more complete tubes, as shown in Fig. 2.14. However, deposition does not take place uniformly throughout the sample. As electrolyte diffusion is limited within the nanotube pores, a maximum aspect ratio between 50 and 70 was achieved by Enculescu et al. [38].

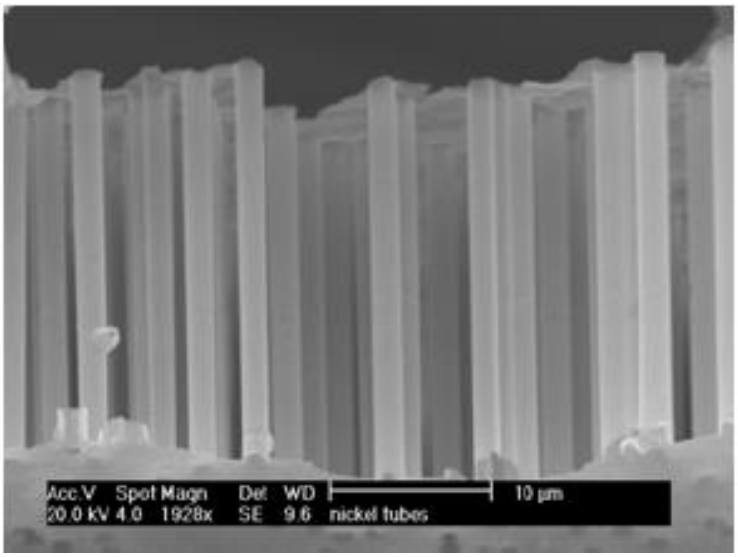

Figure 2.14: SEM image of continuous Ni-P nanotubes with an aspect ratio of 50 electrolessly deposited within a polycarbonate membrane [38].

Li et al. [2.78] and Wang et al. [78,82] indicate that some of the problems encountered during the electroless deposition process are due to deposition occurring on the membrane surface. While depositing Cu-P [82] and Co-P [78] they noticed that a

large amount of metal was deposited on the membrane surface and very little metal was deposited within the nanotube structure. In order to prevent the membrane surface becoming activated, it was polished after the activation step as shown in Fig. 2.15.

Therefore, deposition only takes place within the nanotube pores and not on the surface of the membrane. For low deposition times, nanotubes were formed, while it was claimed that prolonged deposition times resulted in increased wall thicknesses and the formation of nanowires.

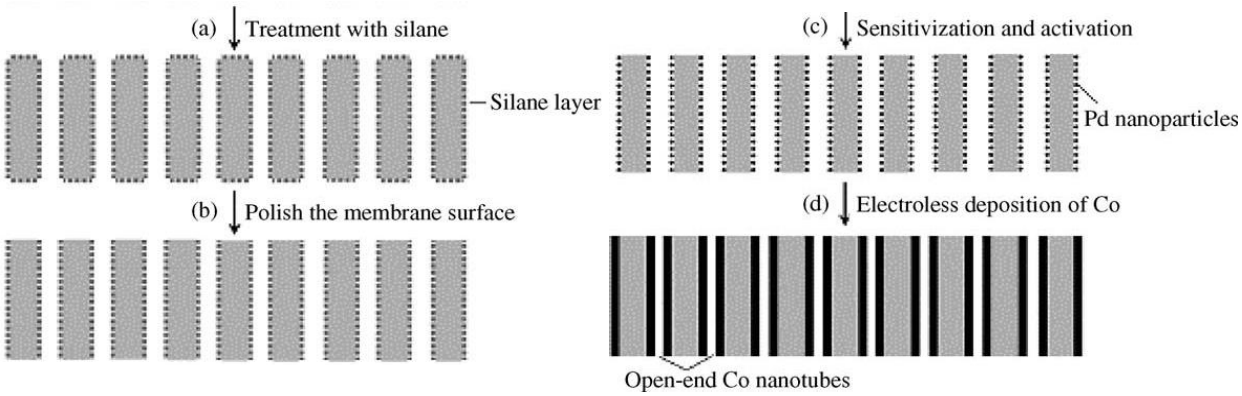

Figure 2.15: Schematic digram for the synthesis of nanotube arrays by electroless deposition while preventing deposition on a membrane surface. (a) Step 1 - Membrane is modified with silane. (b) Step 2 - Membrane is polished to remove silane from the surface. (c) Step 3 - Membrane is activated with Pd nanoparticles along the pore walls only. (d) Step 4 - Deposition occurs along the pore walls to form nanotubes [82].

However, a similar method of nanotube deposition was investigated by Azizi et al. [29]. In this paper, Co-Ni-Fe-B nanotubes were deposited within an AAO membrane with a pore diameter of 110 nm. The lengths of the nanotubes are not given. The surfaces of the membrane were lightly sanded post activation to remove any catalytic particles from the AAO surface. Even though the deposition was carried out at room temperature and the membrane surface was polished, end-closed nanotubes with wall thickness of 15 nm were formed. While the SEM image obtained by Azizi et al. [29] in Fig. 2.16(a) could represent the formation of continuous nanowires, TEM imaging of the structure proves that end-closed nanotubes are deposited. This indicates that the structures obtained by Li et al. [2.78] and

Wang et al. [78,82] may have been end-closed nanotubes and not nanowires, as TEM imaging needs to be carried out to confirm the formation of nanowires. In the studies by Li et al. [2.78] and Wang et al. [78,82] only SEM images, similar to the image in Fig. 2.16(a) were obtained and could have resulted in the misidentification of nanowires instead of nanotubes.

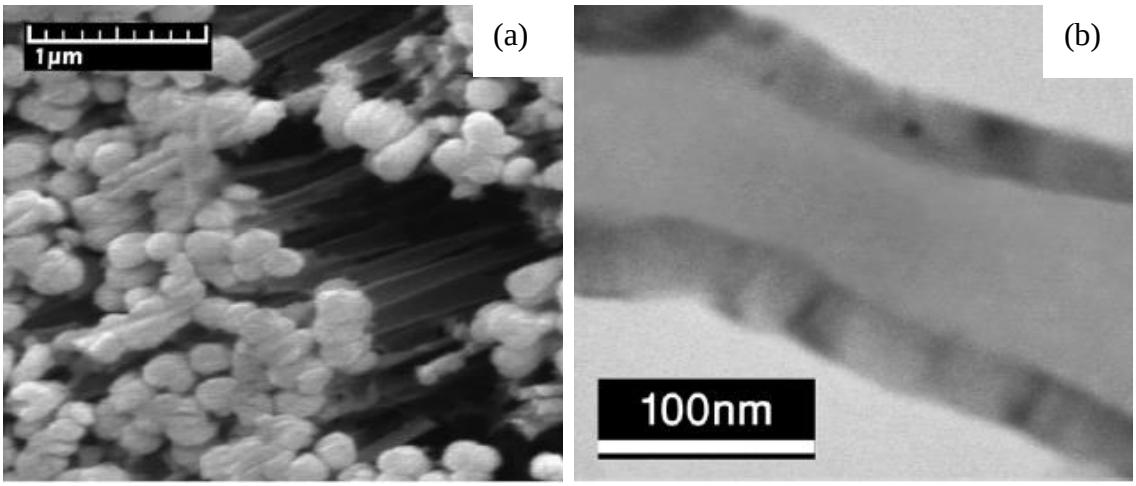

Figure 2.16: (a) SEM image of end-closed CoNiFe-B nanotubes and (b) TEM image of CoNiFe-B end-closed nanotube indicating a wall thickness of 15 nm [29].

The stages involved in the formation of end-closed nanotubes are shown in Fig. 2.17. Azizi et al. [29] claims that the deposition rate within the nanotube structure is low due to localised changes in pH during the deposition process. However, as the pH outside the nanotube pores is more stable, the deposition rate near the film surface is higher than within the nanotube pores. This leads to accumulation an of CoNiFe-B particles at the nanotube ends forming end-closed nanotubes.

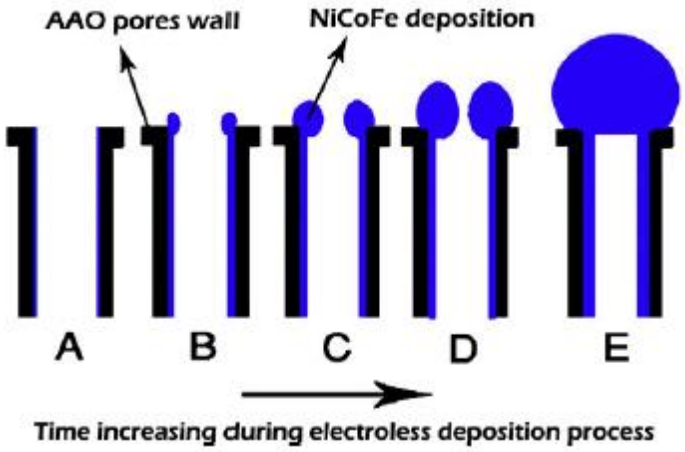

Figure 2.17: Schematic diagram representing the stages of end-closed nanotube formation during the electroless deposition process [29].

Although these investigations have had difficulty obtaining continuous nanotubes before they become end-closed [29,35,38,78,82], Ren et al. [34] claim to have successfully synthesised both Ni-P nanotubes and Ni-P nanowires with an aspect ratio of 800 via electroless deposition. However, the SEM, Fig. 2.18(a), and TEM, Fig. 2.18(b), images show less than 1 µm of the total length of the nanostructure and conclusive evidence of the formation of a continuous nanostructure 60 µm in length is not shown.

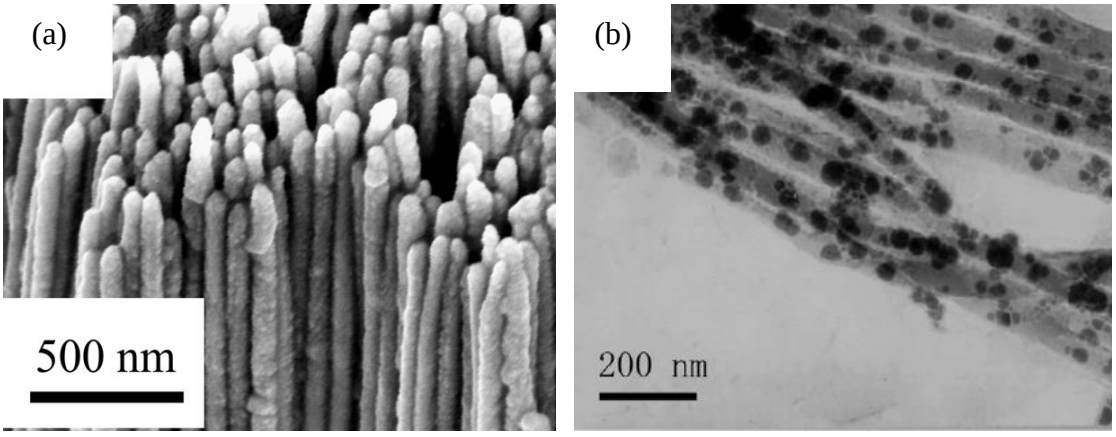

Figure 2.18: (a) SEM and (b) TEM images of what are believed to be Ni-P nanowires deposited via electroless deposition [34].

The SEM image of the nanowires shown in Fig. 2.18 (a) could represent end-closed nanotubes similar to that of Azizi et al. [29] in Fig. 2.16. The TEM shown in

Fig. 2.18 (b) also indicates that each structure contains many nanoparticles and they are not continuous Ni-P nanowires.

However, even today, it is still unclear as to the exact mechanism that occurs and whether nanotubes or nanowires are formed. In 2014, Muench et al. [83] prepared a rhombohedral template on a mica substrate and claim that both nanotubes and nanowires can be formed via electroless deposition. They state that Ag nanotubes could not be formed in templates with a pore diameter of 220 nm and only nanowires were formed. However, with large pore diameters greater than 450 nm, nanotubes could be formed. The SEM images of the deposited nanowire and nanotube are shown in Fig 2.19 (a) and (b) respectively and no experimental proof of the formation of nanowires is given. Again, the nanowires look very similar to that of the end-closed nanotubes prepared by Azizi et al. [29]. Therefore, it is essential that a complete analysis of the deposition process is carried out, so that the process can be fully understood.

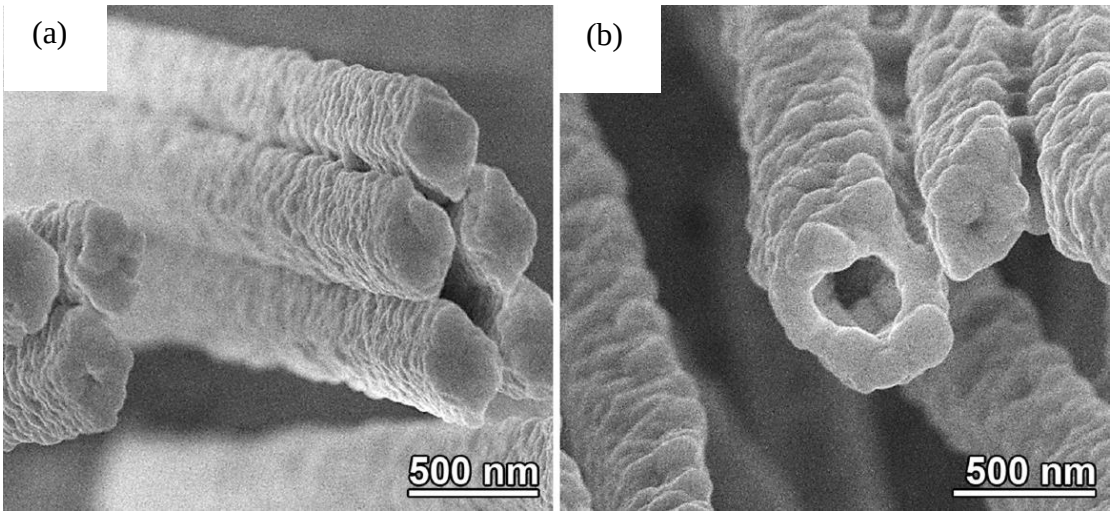

Figure 2.19: SEM images of Au rhombohedral (a) nanowires and (b) nanotubes deposited via electroless deposition [83].

2.5.3 Non-Membrane Template Synthesis

Other nanostructures such as carbon nanotubes (CNT), discovered by Iijima et al. [84] in 1991 have also been used as a template structure for the electroless deposition of metals [85-87]. CNTs are used as they have a strong linear structure and can easily be dispersed within solution. As the metal is deposited on the external walls of the CNTs, the external diameter of the CNT is equal to the internal diameter of the deposited metallic nanotubes. Utilizing this method, nanotubes with an internal diameter as small as 3 nm can be prepared, as shown in Fig. 2.20. Other structures which have been used as templates include carbon nanofibers [88,89] and SiO_2 nanotubes [90].

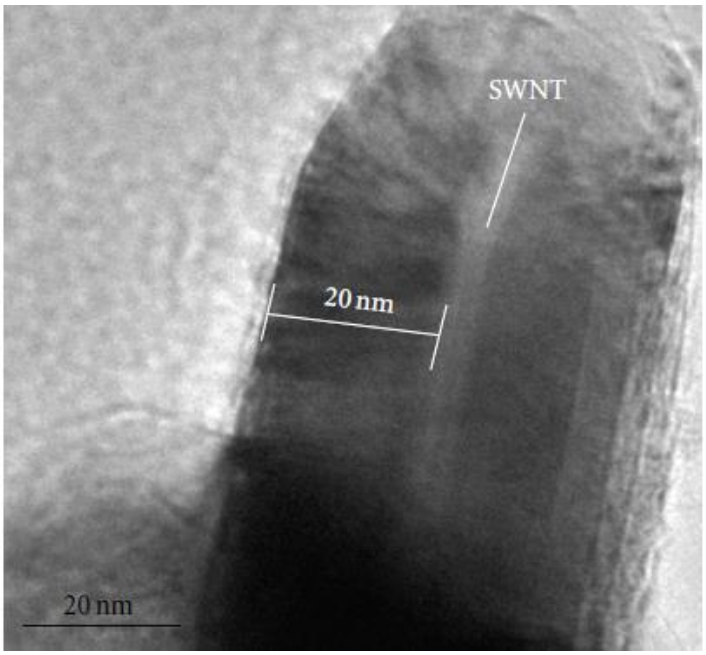

Figure 2.20: TEM image of a single-walled CNT acting as a template structure for the electroless deposition of a Ni-P nanotube [85].

2.5.4 Summary

After a review of the relevant literature, it is clear that there is currently a lack of understanding of the electroless deposition process within a template structure. The literature remains unclear as to whether the deposition process results in the formation of end-closed nanotubes or nanowires. Therefore, in this thesis we will investigate the

electroless deposition within a template structure with the aim of achieving a method for the formation of nanotubes with a uniform wall thickness.

2.6 Electrochemical Deposition

2.6.1 Overview

Electrodeposition is one of the most common methods of metal deposition onto a substrate [91]. Using a template structure such as a PC or AAO membrane, the formation of metallic nanostructures is possible. Given that the membranes are insulating materials, a pre-metal layer must be deposited on the membrane surface to act as a cathode for the electrochemical reaction. This is usually achieved via sputter deposition [92]. As shown in Fig 2.21, nanowires will be formed if the nanotube pore is completely covered with sputtered metal. For the end-closed structure, initial deposition occurs on the electroplated metal at the base of the membrane pores and grows following a bottom up mechanism forming nanowires. However, if the pores are end-opened after sputtering, deposition occurs preferentially along the membrane wall due to particles sputtered on the wall surface to form nanotubes. Once a continuous metal deposit is formed, the tubes grow thicker and become nanowires. In a study by Fu et al. [93], nanotubes with a maximum length of 2 μm could be obtained, while nanowires could be grown to the full length of the membrane.

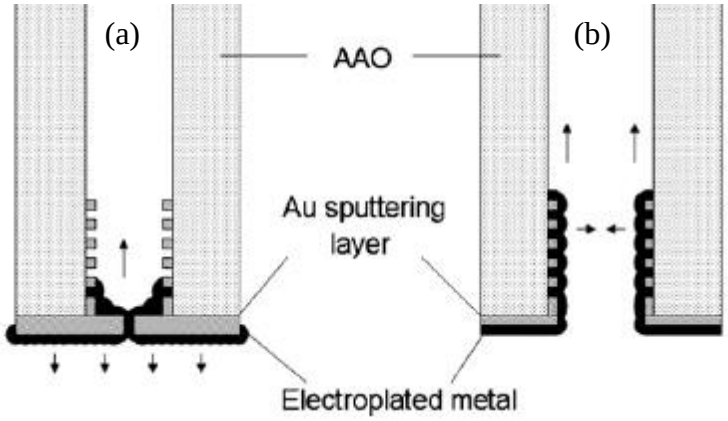

Figure 2.21: Schematic illustration of electroplating process in a template structure for (a) blocked pores to form continuous nanowires and (b) unblocked pores to form nanotubes [93].

A similar method has been used to deposit a variety of metallic nanowires including Ni [94-97], Co [98,99] and Fe [100,101]. Some of the challenges with this method were outlined by Jin et al. [94]. As the nanostructure is blocked from one end, bubbles are trapped within the membrane once submerged in an electrolyte preventing the formation of nanowires. Small amounts of impurities can lead to different deposition rates within membrane pores. If this occurs, some nanowires will grow more rapidly than others. Once these are fully grown, they cause lateral growth on the membrane surface, thus closing the pores of unfilled nanowires.

In order to deposit continuous nanotubes without the formation of nanowires, preferential deposition along the pore wall of the template is required. In 1991, the same year as carbon nanotubes were first synthesised [84], Brumlik and Martin [102,103] prepared gold nanotubes via electrochemical deposition. By treating the membrane with a silane prior to deposition, metallic deposition was achieved along the pore walls to form nanotubes. This acted as a molecular anchor to bind electrochemically deposited Au to the walls of the template membrane.

Li et al. [104] proposed that there is an adsorption energy associated with the walls of an AAO membrane. They suggest that Ni ions will be adsorbed onto the membrane

walls and nanotubes will be formed if the adsorption energy is larger than the applied electric field. If the electric field and the adsorption energy are similar, nanotubes and nanowires will exist simultaneously as shown in Fig. 2.22. By controlling the applied potential, it is possible to produce either nanotubes or nanowires. It is likely that this mechanism explains the formation of 40 μm Ni, Co and Fe nanotubes achieved by Han et al. [66] using an AAO membrane which they attributed to sputtered gold particles. As sputtered gold particles will only deposit on the first few microns of the pore wall, it is unlikely that the gold particles can cause the preferential growth of 40 μm nanotubes along the pore walls.

Tourillon et al. [105] achieved the fabrication of Co and Fe nanotubes within a polycarbonate membrane using electrochemical deposition. They proposed that the metal 2^{+} ions complexed with the carbonate functional groups on the membrane wall allowing for the preferential growth of nanotubes. Sharif et al. [67] were also using polycarbonate membranes for the deposition of Ni, Co and Fe nanotubes. Although they attributed the preferential growth along the membrane walls to sputtered gold particles, it is also possible that it is due to the complexing of metal ions with the carbonate functional groups on the membrane wall.

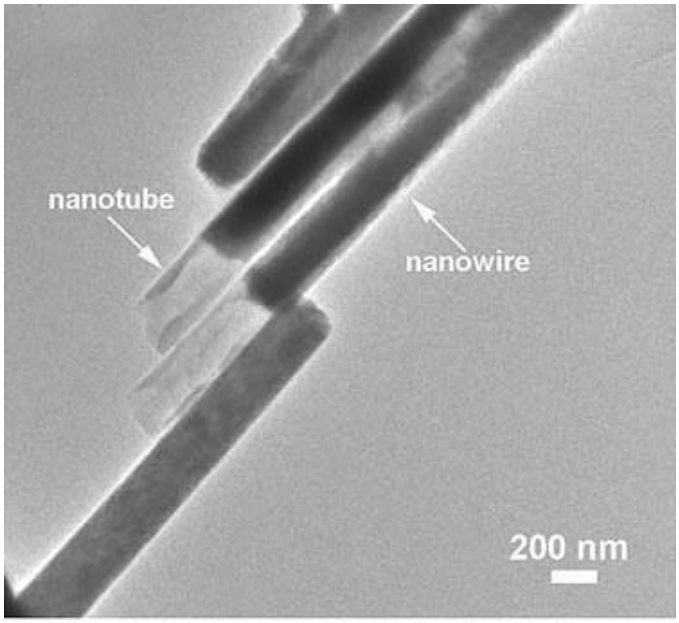

Figure 2.22: TEM image of the simultaneous existence of Ni nanotubes and nanowires during the electrochemical deposition process [104].

However, the addition of chemicals prior to or during deposition is the best method to ensure preferential metal deposition along the pore walls. Membrane pre-treatment is a method in which a chemical, usually a silane, which has a strong affinity for the metal being deposited, is attached to the pore walls [103,106,107]. Although silanes promote deposition along the pore walls, the applied potential must be kept small. This prevents the formation of nanowires. Another method of membrane pre-treatment is the electroless deposition of metallic nanoparticles within the nanotube pores. This enables preferential deposition along the membrane wall [108]. Tao et al. [109] added pluronic P123 to the electrochemical bath because it promoted Ni deposition along the pore walls. Images of the resultant nanotubes for each of these methods are shown in Fig. 2.23(a,b,c) and indicate that membrane pre-treatment promotes preferential deposition along the membrane walls. This results in the formation of continuous nanotubes up to 20 μm in length [107] and are superior to other electrodeposition methods, without a pre-treatment step.

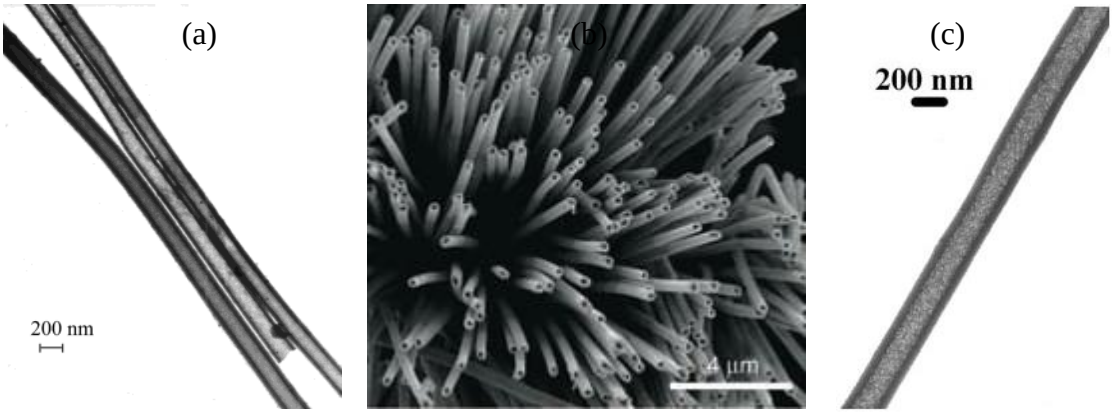

Figure 2.23: TEM and SEM images of continuous Ni nanotubes deposited via electrochemical deposition post membrane pre-treatment with (a) silane [107] (b) metallic particles [108] and (c) pluronic P123 [109].

2.6.2 Composition and Structure

Unlike electroless deposition, electrochemical deposition of a single element is possible without the formation of an alloy. Instead a pure metal with no impurities present can be deposited [106]. The electrochemcial deposition of Ni results in the formation of an FCC structure, as indicated by XRD analysis of both nanotubes [1,107,109], Fig. 2.24(a), and nanowires [94-97], Fig. 2.24(b). The peak intensities of each study differs, thus indicating that the electrochemical deposition process or nanotube dimensions may have a bearing on the crystallographic orientation.

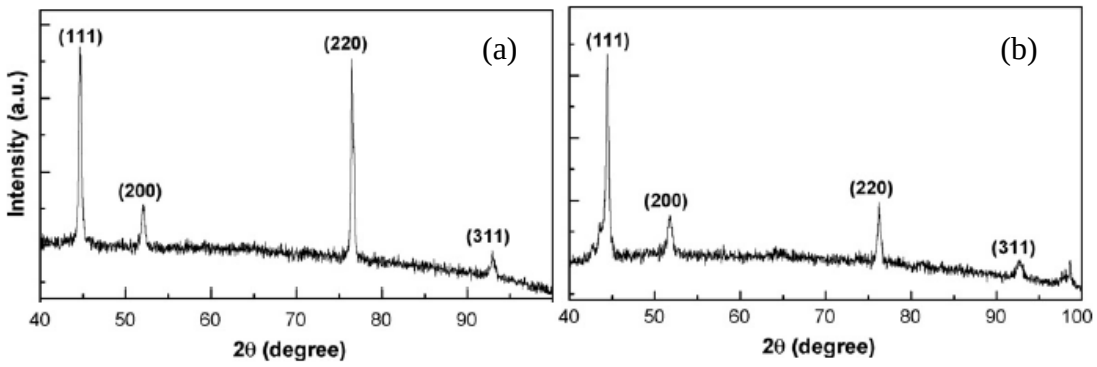

Figure 2.24: XRD patterns of (a) Ni nanowire and (b) Ni nanotube arrays deposited via electrochemical deposition [1].

Electron diffraction patterns of the Ni nanotubes indicate a polycrystalline structure of FCC Ni. However, electron diffraction patterns of Co and Fe, shown in Fig. 2.25 (a) and (b) respectively, indicate that Co is made up of a mixture of an FCC and

hexagonal close packed (HCP) structure while Fe nanotubes consist of FCC and body centred cubic (BCC) crystal structures [105]. High resolution TEM imaging [104] indicates that the deposited metal has many different crystallographic orientations. This confirms the observations recorded for the XRD and electron diffraction images.

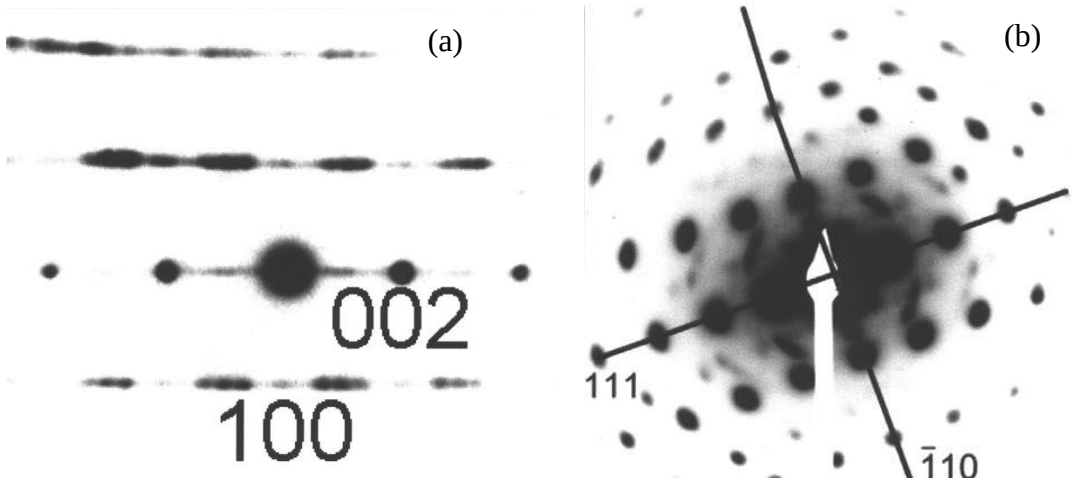

Figure 2.25: Electron diffraction patterns of (a) Co nanotubes and (b) Fe nanotubes deposited via electrochemical deposition [105].

2.7 Comparison between Electroless and Electrochemical Deposition

Electroless deposition usually results in the formation of an amorphous alloy comprising of the deposited metal and either boron or phosphate [110]. On the other hand, electrochemical deposition results in a pure metal with no impurities [106]. The deposit is polycrystalline and a diffraction pattern can be observed [1].

Both electroless and electrochemical techniques can be used to fabricate nanostructures within a template [101,111]. Electroless deposition forms nanotubes within the membrane pore and a thin film is also deposited on both sides of the membrane [78]. Electrochemical deposition results in the formation of nanotubes or

nanowires connected by a film at the base, unless deposition is allowed to continue past the point at which the pores are completely filled [93].

Electroless deposition guarantees the formation of nanotubes because initial deposition occurs along the membrane wall [35]. However, electrochemical deposition often occurs via a bottom up method, forming nanowires. In this case, extra modifications to the deposition process have to be made in order to achieve a nanotube structure [106]. For nanowire formation, electrochemical deposition is the best method as it guarantees the formation of a continuous nanowire. It is possible that, with electroless deposition, end-closed nanotubes will be formed and not nanowires [29]. For nanotubes with small diameters, the maximum aspect ratio achievable with electroless deposition is limited [38] and in this case electrochemical deposition may also be the best option. However, as discussed previously, the coexistence of nanotubes and nanowires may occur [104]. Although both methods can be used to synthesise metallic nanotubes we will investigate the electroless deposition process as we feel this is the best method to form nanotubes with a uniform wall thickness and large aspect ratio.

2.8 Magnetic Properties

2.8.1 Effect of Boron or Phosphorous

The saturation magnetisation of electrolessly deposited films is dependent on the B [54,112,113] or P contents [114,115]. An increase in B or P content has a corresponding decrease in magnetisation. For electrolessly deposited Ni, it has been shown that the introduction of B or P into the nickel matrix enlarges the interatomic distance of Ni atoms. This results in a decrease of the exchange force, thus reducing

the specific magnetisation [116]. Fig. 2.26 displays an increasing specific magnetisation of Ni-B films as the B content decreases.

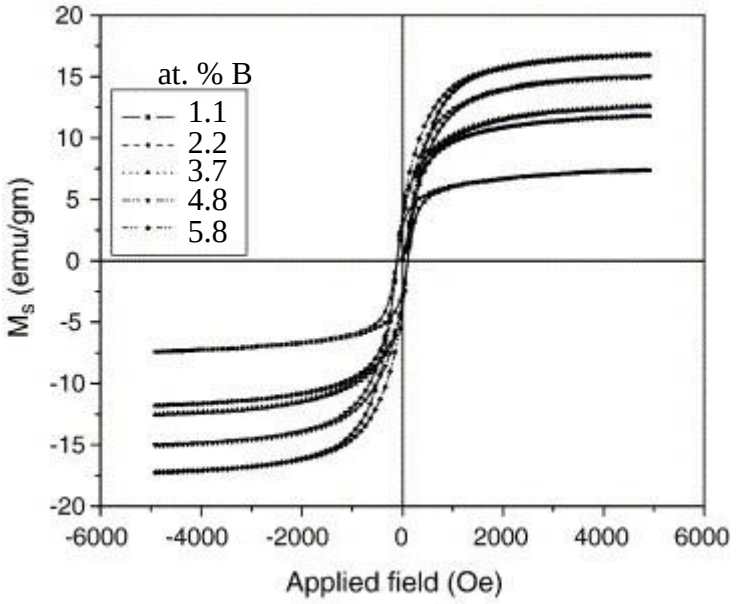

Figure 2.26: Hysterises loops for electrolessly deposited Ni-B films with boron contents ranging from 1.1 at. % to 5.8 at. % [54].

It has been shown that annealing results in an increased magnetic moment due to formation of a crystal structure comprising of both a Ni phase and a Ni_3P phase [54,114]. The coercivity of electrolessly deposited magnetic films is also dependent on B or P content [117-120]. However, unlike specific magnetisation, the dependence of coercivity on B or P varies for different alloys, as shown in Fig. 2.27. For Fe-Co-B [113,119] there was a slight increase in coercivity up to a B content of 4 at. % followed by a decrease up to a content of 16 at. % as show in Fig 2.27(a). Above a B content of 16 at. %, an increase in the coercivity was recorded. A B composition between 4 – 16 at. % corresponds to an amorphous structure. This results in soft magnetic properties. Similarly, the coercivity of Fe-Zr-B decreases with increasing B content as an increased B content results in an amorphous structure [120]. However, for $Fe_{60}Al_{40}$-B [118], as B content increases, the coercivity increases. This is due to the formation of a hard Fe_2B phase with an increasing boron content.

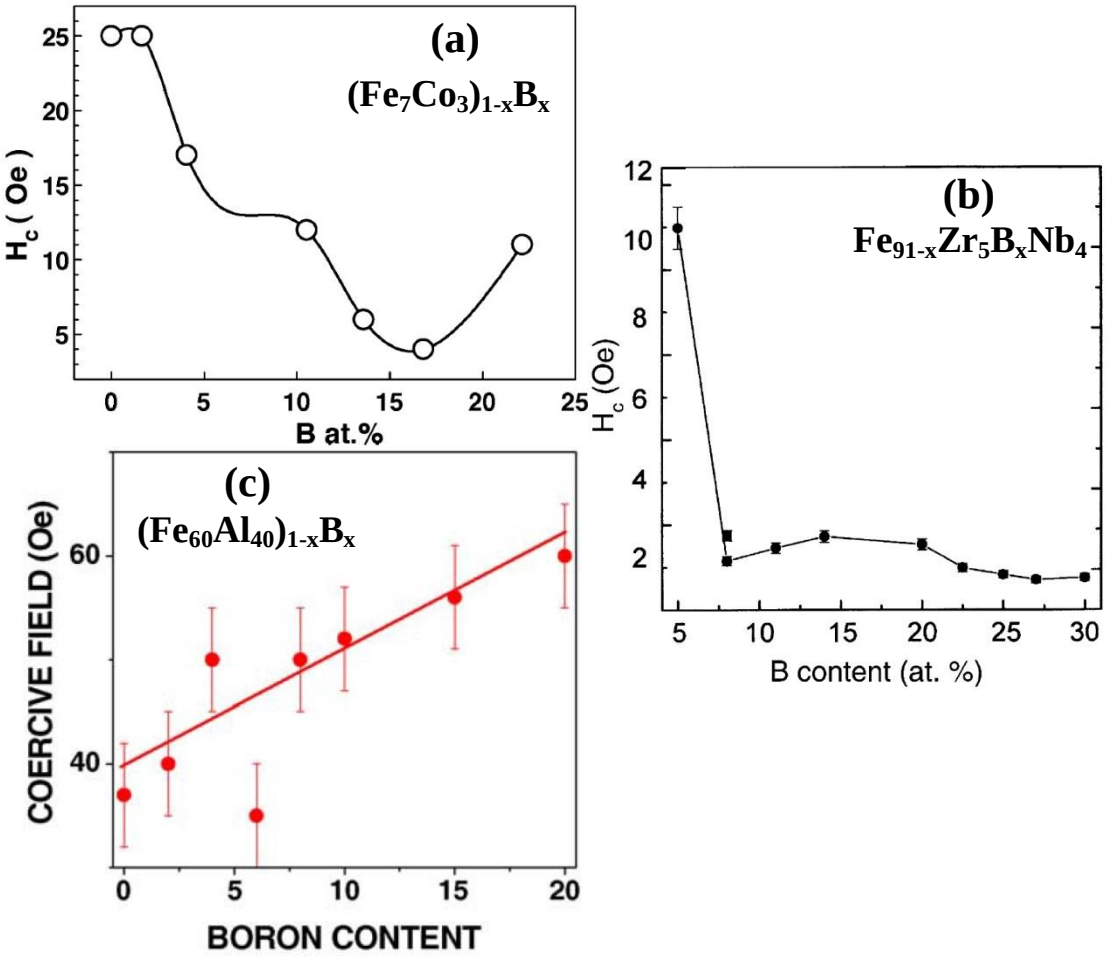

Figure 2.27: Effect of B content on the coercivity of **(a)** $(Fe_7Co_3)_{1-x}B_x$ [113] **(b)** $Fe_{91-x}Zr_5B_xNb_4$ [120] and **(c)** $(Fe_{60}Al_{40})_{1-x}B_x$ [118].

2.9 Magnetic Nanostructures

The ferromagnetic properties of materials with dimensions in the nanometer range differ significantly from their bulk properties [121]. Ferromagnetic nanowires and nanotubes exhibit unique and tunable magnetic properties due to their shape anisotropy [122]. These magnetic nanostructures have many practical applications in modern nanotechnology and in recent years have become a focus for many researchers. Magnetic nanotubes have potential applications in areas such as magnetic recording media [123-127], electronic devices [128-130] and biotechnology, specifically targeted drug delivery [131-135]. The magnetic properties of nanostructures have been investigated with particular emphasis on three areas:

(1) magnetisation reversal processes within the arrays, (2) factors that determine the effective easy axis of the structures and (3) magnetic interaction between the individual nanotubes and wires [127].

Nanowires possess two geometrical properties, radius and length, that can be independently adjusted to alter the magnetic properties. Although less studied than nanowires, nanotubes allow for the variation of a third degree of freedom, the wall thickness. Consequently, nanotubes have the potential to be used in a much wider variety of applications, because nanotubes exhibit magnetic properties that could not be obtained in nanowires [72]. To benefit from this, a detailed understanding of the magnetisation processes occurring in such structures is of great importance.

2.9.1 Magnetic Reversal Process

For ideal magnetic nanotubes with a small number of defects, there are three possible reversal mechanisms, as shown in Fig. 2.28. The first is coherent rotation (left image) in which all magnetic moments rotate simultaneously and no domain wall exists during the magnetic switching process. The coherent reversal mechanism can only occur within very short nanotubes where the length of the tube is of the same order as the wall thickness [136].

In longer tubes, instead of a coherent rotation, a domain boundary appears at one extremity of the tubes and propagates along the tube length, reversing the magnetisation from one saturated state to the other. This can occur via one of two possible mechanisms, vortex wall reversal and transverse wall reversal. These reversal mechanisms are similar but the organization of the magnetic moments within the domain boundary differs. In the vortex wall reversal (central image), also known as the curling reversal mode, magnetic moments rotate progressively via propagation of

a vortex domain wall. In the transverse wall reversal mechanism (right hand image), magnetic moments rotate progressively via propagation of a transverse domain wall. In vortex mode, the magnetic moments remain within the wall of the magnetic material, whereas in transverse mode a net magnetisation component appears in the *x*, *y* plane. Therefore, a vortex reversal mode is more favourable for thin tubes and a transverse reversal mode dominates in thicker tubes in which the importance of surface effects is lower [72]. As it is the energy associated with the tube wall which determines the reversal mode, the height of the tube has no effect on the reversal process [136].

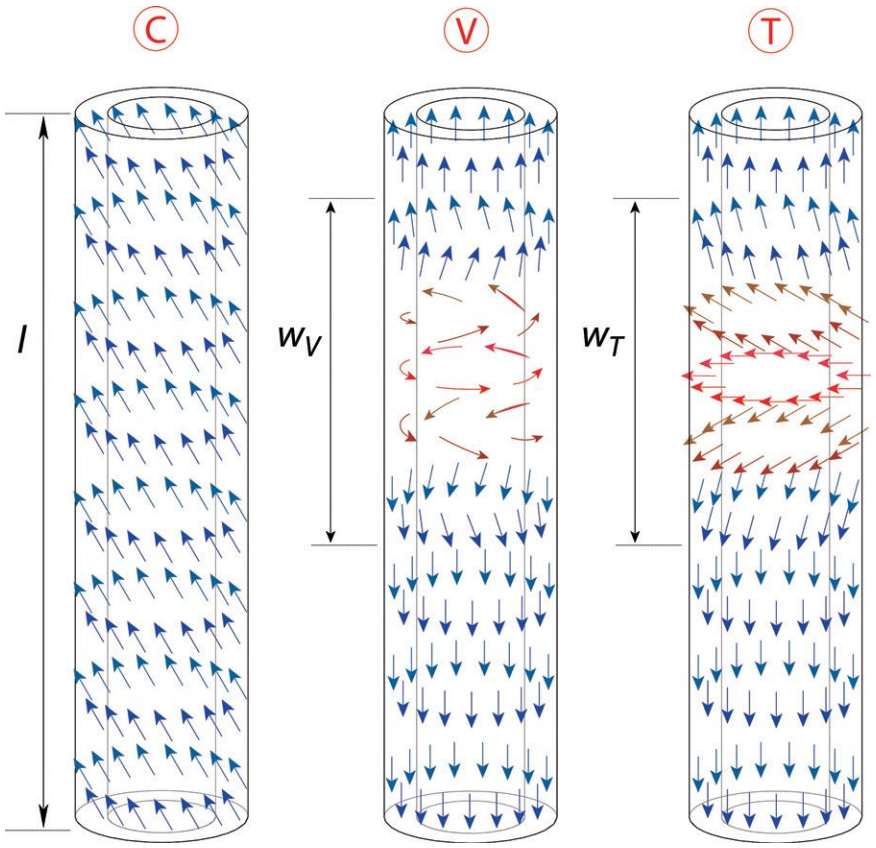

Figure 2.28: Schematic diagrams of possible magnetic reversal modes for magnetic nanotubes showing coherent rotation labelled C, vortex reversal mode also known as curling labelled V and transverse reversal labelled *T*. W_V and W_T correspond to the domain wall width of the reversal modes [71].

2.9.2 Reversal Mechanism Modelling

The magnetic switching of ferromagnetic nanotubes as a function of their geometry have been investigated by Landeros et al. [136] using numerical simulations and analytical calculations. They have investigated the vortex mode and transverse mode reversal mechanisms of nanotubes with very small outer radii of only 15 nm. Using numerical simulations, they have calculated the *x*, *y* and *z* components of magnetisation as a function of the position along the tube axis and time for a wide range of wall thicknesses. Their data is presented in terms of $\beta = a/R$, where a = internal tube radius and R = external tube radius. Therefore, $\beta = 0$ corresponds to a nanowire and $\beta = 1$ corresponds to a nanotube with very small wall thickness. For a vortex reversal mechanism, the magnetisation components in the *x* and *y* directions, m_x and m_y should average to zero. However, for a transverse reversal mechanism, one or both of the magnetisation components should be non-zero.

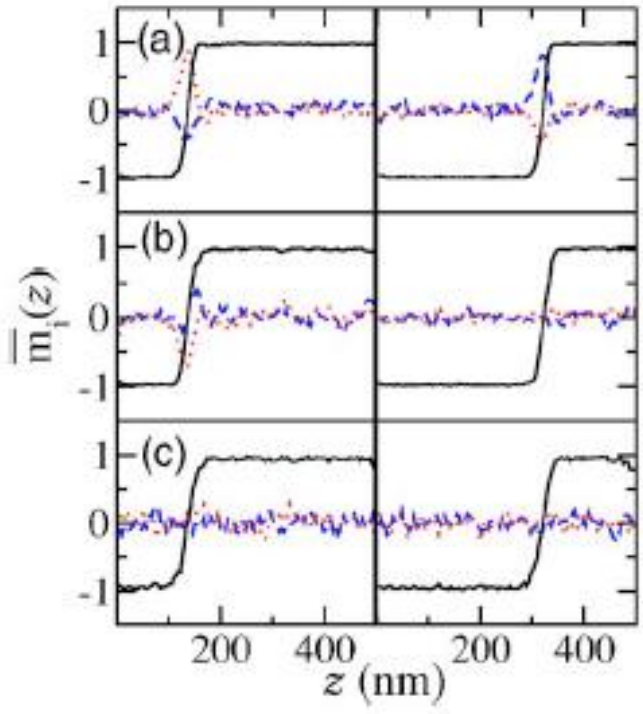

Figure 2.29: Snapshots of the reversal of tubes defined by (a) $\beta = 0.17$, (b) $\beta = 0.33$ and (c) $\beta = 0.5$ at two different stages of the process. The x-axis represents the position along the tube and the y-axis gives the average magnetisation in the *x* direction M_X (red line), *y* direction M_Y (blue line) and z direction M_Z (black line) [136].

The results of their simulations in Fig. 2.29 show the *x*, *y* and *z* magnetisation components when the domain wall propagates along the tube axis for three different β values. For β = 0.17, Fig. 2.29(a), there is a clear transverse reversal mode with magnetisation components present in both the *x* and *y* direction. For β = 0.33, Fig. 2.29(b), there is a change in the type of reversal mode present with respect to time. Initially, a transverse reversal mode is present but when the domain wall propagates along the tube, the reversal mechanism switches to a curling type mechanism as m_x and m_y average to zero. In Fig. 2.29(c) the tube wall has become thin when β = 0.5 and only a curling reversal mode is present. From these results, it was concluded that a transverse mode was always present when $\beta < 0.33$ and a vortex mode was present when $\beta > 0.5$. However, for $0.33 < \beta < 0.5$ both the vortex and transverse modes are possible.

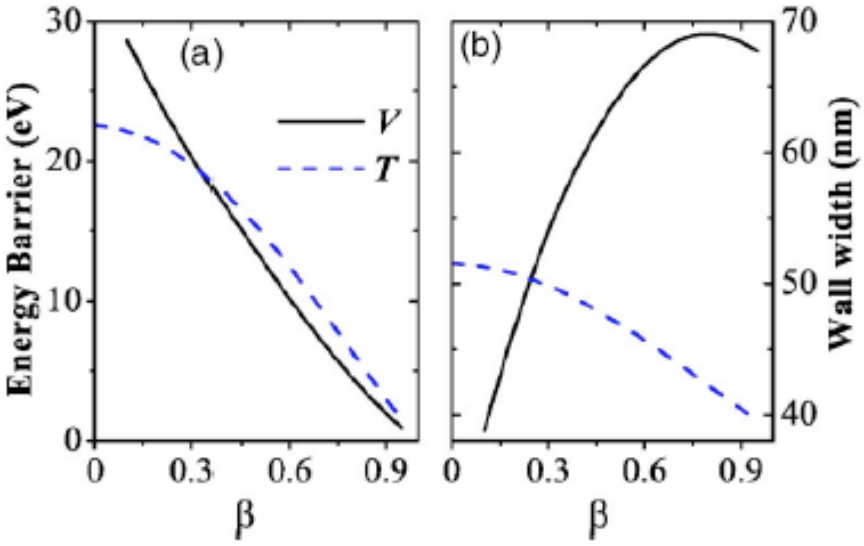

Figure 2.30: (a) Energy barrier associated with the vortex (solid black line) and transverse (blue dashed line) reversal mechanisms for different values of β and **(b)** Magnetic domain wall widths for the vortex W_V (black line) and transverse W_T (blue dashed line) reversal mechanisms [136].

The analytical calculations of energy barrier and domain wall width for both vortex and transverse modes are shown in Fig. 2.30(a) and (b). It was found that the crossing point of the energy barriers corresponds to a change of reversal mechanism from

transverse to vortex when β = 0.33. The domain wall widths, W_v and W_T in Fig. 2.30(b), are calculated to range from 30 to 70 nm. Therefore, for very short tubes $H \approx W$, it is not possible to accommodate a transverse or vortex domain wall, resulting in a coherent mode of reversal.

This work was further investigated by Bachmann et al. [137] using experimental data from Fe_3O_4 nanotubes with an outer diameter of 50 nm. They recorded a maximum coercivity for a wall thickness of 13 nm, which corresponds to a β value of 0.48. The recorded data is shown in Fig. 2.31. Numerical calculations of the expected coercivity for the vortex mode of the nanotubes were calculated using an adapted Stoner-Wolfarth model [138] and corresponds to the curve labelled (*V*) in Fig 2.31. The curve labelled (*T*) corresponds to a model for the transverse reversal mode provided by Chang et al. [139]. The vortex and transverse curves cross at d_w = 13 nm, indicating that a change from a vortex to a transverse reversal mode occurred at β = 0.48, matching the experimental data. The calculated coercivity values are much larger than those experimentally observed. This is due to dipolar coupling of the magnetic nanotubes. Allowing for this in the calculations [140], a closer match to the experimental data can be obtained represented by the lowest curve in Fig 2.31. However, deviations from the theoretical curve are still present especially for small wall thicknesses. These are attributed to structural imperfections in the tube [140].

From these results, it can be seen that the coercivity and reversal mechanism of magnetic nanotubes can be controlled by altering the associated geometry. The possibility of fabricating nanotubes with modulations in diameter and wall thickness is also discussed [137]. These nanotubes would consist of segments reversing their magnetisation via different modes and accordingly at different fields. This has many potential uses in modern technologies especially in the area of magnetic data storage.

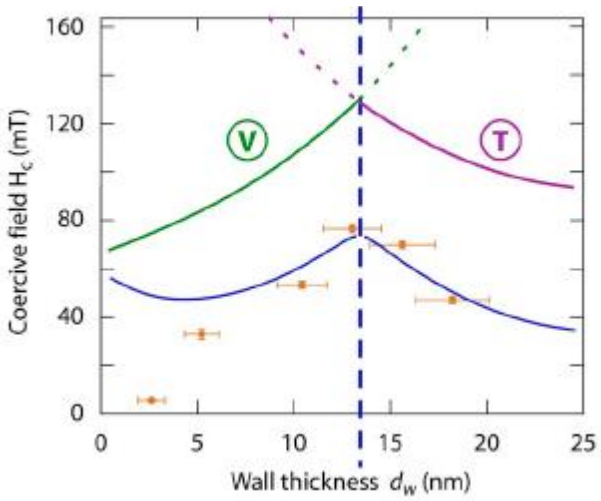

Figure 2.31: Wall thickness dependence of the coercive field for Fe_3O_4 nanotube tube arrays with 50 nm outer diameter. Data points correspond to experimental data, while curves labelled *V* and *T* are calculated values for isolated tubes in vortex and transverse modes, respectively. Curve through the experimental data points, represents calculated values of tubes taking into account dipolar coupling [137].

2.9.3 Critical Radius

It has been claimed that through numerical and theoretical simulations, there exists a critical outer radius at which the magnetic reversal mechanism changes from transverse to vortex [136,140,141]. For small external radii, the reversal mechanism is expected to be a transverse reversal mechanism, while for large external radii a vortex reversal mechanism will occur. The critical radius also depends on the wall thickness of the nanotubes and so is a function of β. The calculated critical radii for Co, Ni and Fe are shown in Fig 2.32(a). The curves can be considered as a phase diagram which separates the transverse mode (bottom left) from the vortex reversal mode (top right) [136]. From these results it is claimed that, irrespective of the wall thickness, once the external radius is large, greater than 25 nm, a vortex reversal mode should occur. The critical radius is also dependant on the direction of the applied magnetic field [141], Fig 2.32(b) and will be discussed in the next section.

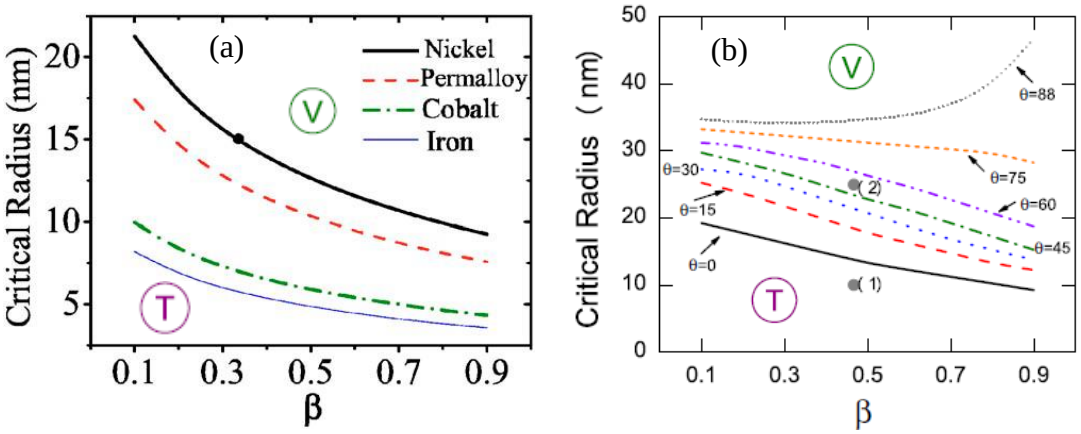

Figure 2.32: Critical radius of magnetic nanotubes vs. β for **(a)** a range of different metals and **(b)** different angles of applied magnetic field for Ni nanotubes, where 0 ° indicates a magnetic field applied parallel to the tube axis. Both graphs can be considered as phase diagrams for a change from a transverse to vortex reversal mechanism [136,141].

2.9.4 Magnetic Anisotropy

The magnetic reversal process has an effect on the magnetic anisotropy of the nanotube structures. Albrecht et al. [71] have discussed the coercivity of magnetic nanotubes with respect to the direction of the applied magnetic field for both vortex and transverse reversal modes. They found a clear relationship between the coercivity and angle of applied magnetic field. For a vortex reversal mechanism, a minimum coercivity is recorded when the magnetic field is applied parallel to the nanotube axis as shown in Fig. 2.33. However, for a transverse reversal mode, the minimum coercivity is recorded with the field applied perpendicular to the nanotube axis. The absolute values of the coercivities shown in Fig. 2.33 depend on external radius, wall thickness and composition as well as the spacing between adjacent tubes.

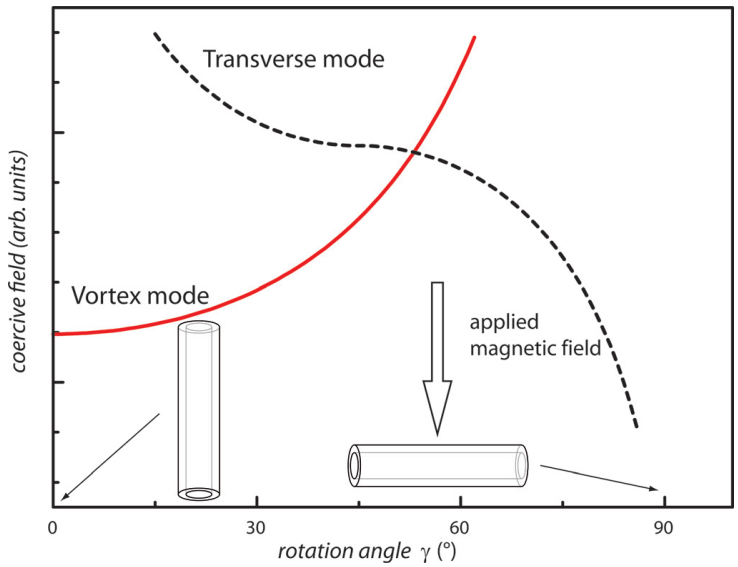

Figure 2.33: Modelled coercivity values for vortex and transverse reversal mechanisms as a function of direction of applied magnetic field where where 0 ° indicates a magnetic field applied parallel to the tube axis [71].

The nanotubes will reverse their magnetisation by whichever mode opens an energetically accessible route first, that is, the mode which offers the lowest coercivity [71]. By examining the shape of a graph of coercivity vs. angle of applied field, it is possible to determine the type of reversal mechanism that is occurring. When nanotubes switch their reversal mode from a vortex to a transverse reversal mode, an M-shaped graph of coercivity vs. angle of applied field is recorded. If the reversal mechanism is purely vortex, a U-shaped graph with a minimum coercivity parallel to the nanotube axis will be recorded.

An M-shaped graph is shown in Fig. 2.34 [71], indicating the nanotube reversal mechanism changes from vortex to transverse. The maximum coercivity is recorded at the angle at which the reversal mode changes corresponding to the crossing of a phase line in Fig. 2.32(b). The angle at which a change occurs depends on the external radius and wall thickness as well as the composition of the nanotubes. Numerical simulations of Ni nanotubes provided by Allende et al. [141] provide similar results. They found that for a small external radius of 10 nm, only transverse reversal is

observed. However, as the external radius is increased to 25 nm, the M-shaped curve is observed as the reversal mechanism changes from vortex to transverse modes.

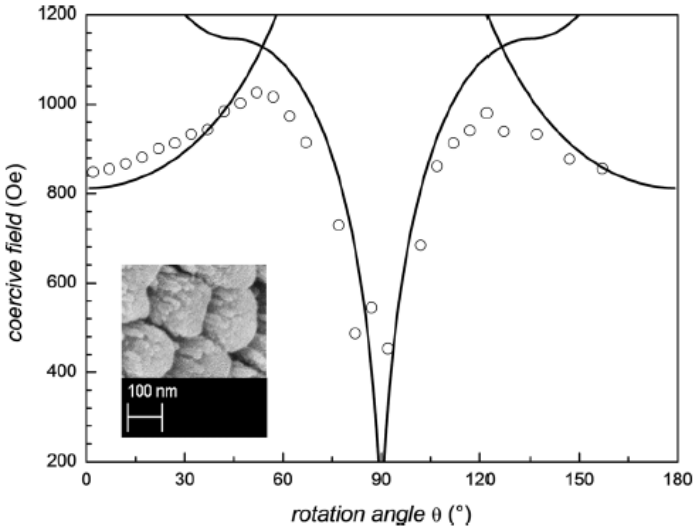

Figure 2.34: Coercivity as a function of direction of applied field of Fe_3O_4 nanotubes with an external radius = 70 nm and wall thickness = 10 nm. Solid lines represent numerical simulations of coercivity values of vortex and transverse modes indicating that the reversal mechanism changes at an angle of approx. 50 ° [71].

2.9.5 Experimental Data

Experimental data from synthesised magnetic nanotubes of varying compositions, external radii and wall thickness have been investigated with respect to the simulations presented above. Sharif et al. [67] prepared Co, Ni and Fe nanotubes via electrochemical deposition with an outer diameter of 600 nm and wall thicknesses of 50 nm and 150 nm, corresponding to β values of 0.83 and 0.5 respectively. These nanotubes have similar dimensions to the nanotubes which are deposited in this study via electroless deposition. For nanotubes with $\beta = 0.83$, an M-shaped graph of coercivity vs. angle of applied field is obtained for all nanotube compositions as shown in Fig. 2.35(a). The angle at which the reversal mechanism switches for both Co and Fe is approximately 20º, while the switch occurs at 40º for Ni nanotubes. The outer diameter of the nanotubes far exceeds any critical radius discussed previously in section 2.9.3 in which a vortex reversal mechanism would be expected [136]. The

models in sections 2.9.2 and 2.9.3 only presented the magnetic properties of nanotubes with small external radii and so may not be applicable to nanotubes with much larger outer radii.

As a side note, Sharif et al. [67] claim that the reversal mechanism changes from coherent rotation to a vortex (curling) reversal mechanism, and not transverse to vortex. This reference to coherent rotation, also stated in other publications [66,122,142], actually refers to a transverse reversal mechanism. This discrepancy is due to the fact that there was a lack of understanding of the reversal mechanisms prior to the recent investigations of nanotube magnetism [136,137,141].

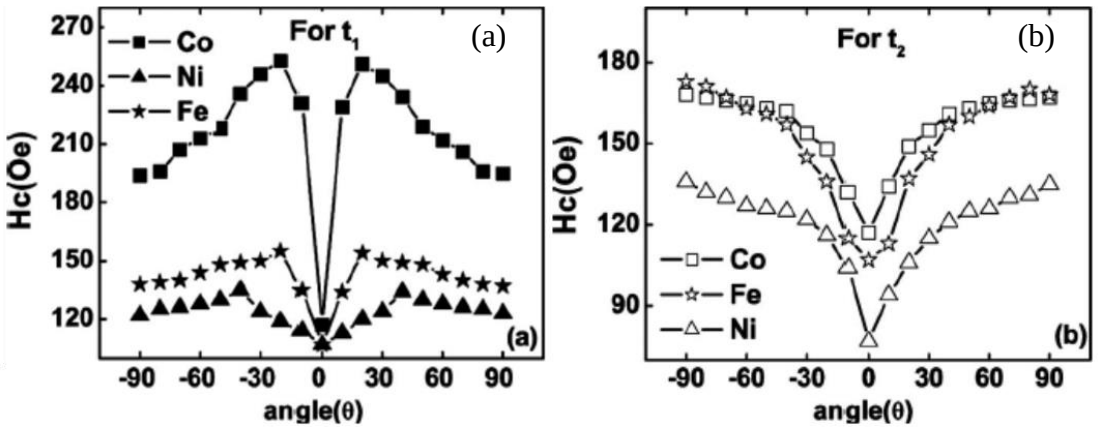

Figure 2.35: Coercivity as a function of direction of applied magnetic field for nanotubes with external radius of 300 nm and β values of (a) 0.83 displaying an M-shaped curve indicating a transition from vortex to transverse reversal modes and (b) 0.5 showing a U-shaped graph indicating a vortex reversal mode for all angles [67].

For β = 0.5, a vortex reversal mode was observed for all composition and angles resulting in a U-shaped graph of coercivity vs. angle of applied field as shown in Fig. 2.35(b). This result is expected due to the large external radius for which a vortex reversal mechanism is favourable. Ahmad et al. [142] investigated Co nanotubes with length of 10 µm and external radius of 100 nm. Again, a vortex reversal mechanism was observed with coercivity values of 245 Oe and 235 Oe recorded perpendicular and parallel to the nanotube axis. This indicates that there may be very little anisotropy associated with a vortex reversal mode while there is a large anisotropy

present if the reversal mode changes from vortex to transverse. Li et al. [143] recorded similar results for Co nanotubes with an external radius of 60 nm with coercivities of approximately 200 Oe, measured perpendicular and parallel to the nanotube axis. This indicates the presence of a vortex reversal mechanism. The smooth reversal process observed for these nanotubes is consistent with the fact that the magnetisation wraps around the tube in a vortex type reversal mechanism.

2.9.6 Easy – Hard Axis

It has been reported in the literature that magnetic nanotubes can display isotropic behaviour [77,108,144], an easy axis parallel the nanotube axis [1,144] or an easy axis perpendicular to the nanotube axis [109,145]. In general the easy and hard axis of magnetic nanotubes is dependent on the external radius of the nanotubes.

Ni nanotubes [1] along with Co and Ni [144] nanotubes with external radii of less than 30 nm, display an easy axis parallel to the nanotube axis. For these nanotubes, the remanent magnetisation for the applied field parallel to the tube axis is larger than that for the perpendicular direction. This indicates that the easy axis of magnetisation is orientated along the nanotube axis. Because these nanotubes have a small external radius, a transverse reversal mechanism occurs, resulting in an easy axis parallel to the tube axis as shown in Fig. 2.36.

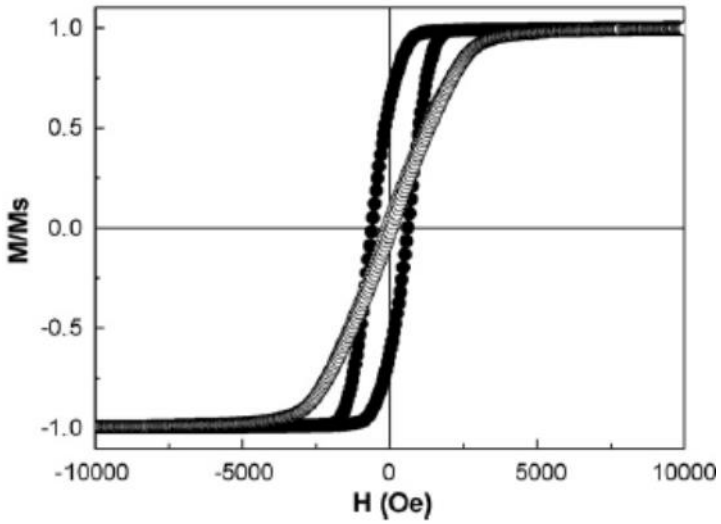

Figure 2.36: Magnetic hysterises loop of Ni nanotubes with an external radius of 22.5 nm. The wall thickness is not given. Black dots correspond to a magnetic field applied parallel to the nanotube axis and the white circles correspond to a perpendicular magnetic field. [1].

However, nanotubes with small external radii have proved difficult to fabricate and so the vast majority of nanotubes reported in the literature reverse via a vortex mechanism or a mixture of vortex and transverse reversal. In these cases, the nanotubes either display an isotropic behaviour or an easy axis perpendicular to the nanotube axis. The reason why an easy axis is preferred over isotropic behaviour still remains unclear. As mentioned previously in a study by Sharif et al. [67], both a vortex only and a mixture of vortex and transverse reversal modes could be obtained for Co, Ni and Fe nanotubes by varying the wall thickness. However, in both cases an easy axis was observed perpendicular to the nanotube axis indicating that the reversal mechanism does not distinguish between an easy axis and isotropic behaviour. Studying Ni nanotubes of outer radius 100 nm and $\beta = 0.5$, Tao et al. [109] found that the nanotubes displayed a clear anisotropy with an easy axis present perpendicular to the nanotube axis as shown in Fig 2.37. This is similar to results found in other investigations [145].

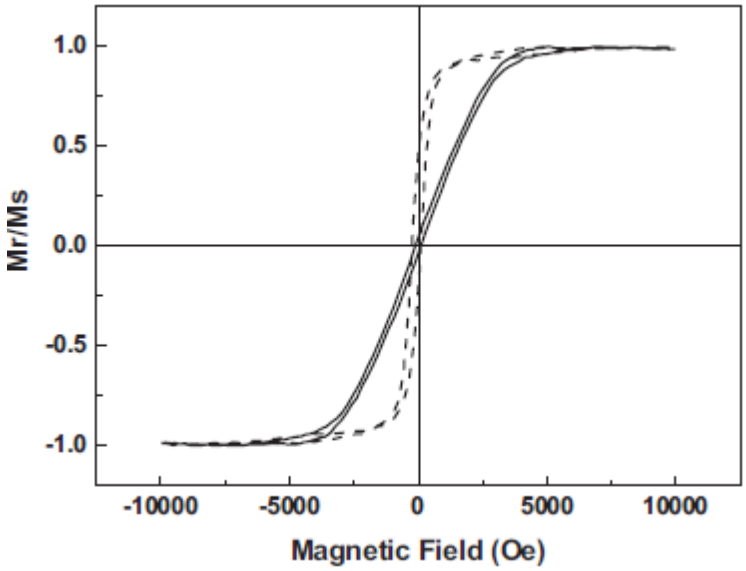

Figure 2.37: Magnetic hysterises loop of Ni nanotubes with an external radius of 125 nm and wall thickness of 50 nm. The solid line corresponds to a magnetic field applied parallel to the nanotube axis and dashed line corresponds to a perpendicular magnetic field [109].

The magnetic properties of a wide range of ferromagnetic nanotubes with external radius > 200 nm for varying lengths and compositions are presented in Table. 2.1, for a magnetic field applied parallel and perpendicular to the nanotube axis. As the intrinsic properties of different alloys are distinct, variations in the coercivities (H_C) and remanent squareness (SQ) are observed. The remanent squareness (remanent magnetisation divided by saturation magnetisation) of all nanotubes is largest when measured perpendicular to the nanotube axis. This indicates that the easy axis is perpendicular to the tube axis irrespective of the composition of the nanotubes.

Composition	**L (μm)**	Hc_{par} **(Oe)**	Hc_{perp} **(Oe)**	SQ_{par}	SQ_{perp}	**Template**
Fe	6	145	149	0.05	0.22	PC
Co	6	158	197	0.11	0.37	PC
Ni	6	80	127	0.06	0.31	PC
Fe	40	364	163	0.09	0.35	AAO
Co	40	115	75	0.03	0.05	AAO
Ni	40	111	102	0.16	0.24	AAO

$Ni_{64}Fe_{36}$	15	84	68	0.03	0.26	AAO
$Co_{90}Pt_{10}$	12	125	177	0.06	0.09	AAO
$Co_{80}Fe_{17}B_3$	10	353	108	0.04	0.4	AAO
$Co_{75}Cr_{13}Pt_{12}$	10	251	135	0.03	0.13	AAO

Table 2.1: Table showing properties of magnetic nanotubes for a range of compositions with outer an external radius > 200 nm [66].

Isotropic behaviour has also been observed for nanotubes of varying composition and sizes including Ni [108] Ni and Co [144] and FePt [146]. All the nanotubes mentioned here have relatively large outer radii > 80 nm and there were almost no differences recorded between the hysteresis curves measured perpendicular and parallel to the nanotube axis. This indicates an isotropic behaviour for the nanotubes. A range of magnetic properties have been reported for nanotubes, indicating that the magnetic properties are possibly affected by many parameters, including size, shape and composition, though no definitive theory has been established. However, all these reports are for nanotubes formed via electrochemical deposition. In this study, we will investigate the magnetic properties of electrolessly deposited nanotubes.

2.9.7 Electrolessly Deposited Nanotubes

Although a wide range of metallic nanotubes have been deposited via electroless deposition, to date there has been a lack of investigation of their associated magnetic properties. Investigations of electrolessly deposited Ni-P nanotubes by Ren et al. [34] and Hai-Peng et al. [77] indicate the magnetic properties of the nanotubes are dependant on the size of the nanotube radius. A large anisotropy was recorded for nanotubes with an external diameter of 35 nm and wall thickness of 10 nm. A maximum coercivity of 84 mT (840 Oe) was recorded parallel to the nanotube axis and 18 mT (180 Oe) was recorded perpendicular to the nanotube axis [34]. These

results indicate that a transverse reversal mechanism is present and there is a large anisotropy associated with the nanotubes.

However, a vortex reversal mechanism was recorded for Ni-P nanotubes with an external radius of 100 nm and wall thickness of 40 nm [77]. A maximum coercivity of 39.6 mT (396 Oe) was recorded perpendicular to the nanotube axis. A relatively small anisotropy was recorded with 30.3 mT (303 Oe) recorded parallel to the nanotube axis [77]. For a CoFe-B nanotube array with an external radius of 100 nm, a maximum coercivity of 60 mT (600 Oe) was recorded perpendicular to the nanotube axis with a minimum coercivity of 50 mT (500 Oe) recorded parallel to the nanotube axis [80], indicating the presence of a vortex reversal mechanism.

The reason for the difference in the results between the studies is unclear, though it may be due to the porosity of the membranes used. For the Ni-P nanotubes with 35 nm external radius, an interatomic spacing of 100 nm and a deposition time of 1 hour was used [34]. Therefore, it is possible that the anisotropy present was due to the presence of a Ni-P film on the membrane surface. For the 100 nm nanotubes, a deposition time of 30 minutes was used, while a porosity of 30 % was recorded for the AAO membrane [77]. On the other hand, for the CoFe-B nanotubes a deposition time of only 20 seconds with a minimal atomic spacing was used. Therefore, the isotropic behaviour observed may be due to the lack of a magnetic film on the film surface [80]. It is also possible that the nanotube wall is extremely thin after such a short deposition time. From these results, it is clear that currently there is a lack of understanding of the magnetic properties of electrolessly deposited nanotubes and a lack of compositions investigated. Therefore, in this thesis, we will investigate the magnetic properties of electrolessly deposited nanotubes, with a range of unique compositions, with the aim of controlling the associated magnetic properties.

2.10 Hydrogen Generation

2.10.1 Viability

The viability of hydrogen technology as a future alternative to non-renewable energy sources requires low cost fuel cells, safe and cheap storage media and efficient methods of hydrogen generation. The heat of combustion of hydrogen is 3 times larger than that of hydrocarbons, 142 MJ Kg^{-1} compared to 47 MJ Kg^{-1} [147]. Hydrogen fuel cells have an overall energy efficiency of 50 – 60 %, compared with that of combustion engines of less than 25 % [148] and the by-product of hydrogen combustion is water, thus making it an environmentally friendly energy source. Therefore, it is clear that hydrogen has potential to replace currently used fossil fuels and become a viable energy source in the future.

2.10.2 Sodium Borohydride ($NaBH_4$)

Hydrogen storage is currently an important area of research especially for portable applications. Metal hydrides are one possible storage mechanism due to the relatively large amount of stored hydrogen, the stability in a basic solution and the fact that hydrogen release from these hydrides is relatively simple. One such metal hydride that has received a large amount of attention is sodium borohydride ($NaBH_4$). Sodium borohydride decomposes readily in the presence of water to release hydrogen. However, a basic $NaBH_4$ solution is stable and hydrogen is only released in the presence of a suitable catalyst according to the reaction,

$$NaBH_4 + 2H_2O \xrightarrow{catalyst} NaBO_2 + 4H_2 \qquad (2.7)$$

Currently, the main barrier to the use of $NaBH_4$ as an alternative for hydrogen storage is the gravimetric and volumetric storage densities of hydrogen [148]. The

Department of Energy (DOE) in the USA have set hydrogen storage targets of 5.5 wt. % H_2 by the year 2015, with an ultimate target of 7.5 wt. %. $NaBH_4$ has storage density of 10.6 wt. % of hydrogen, which is above the required target of 7.5 wt. %. However, with the additional weight of water required, the catalyst used and the cell required for hydrogen release, this is reduced to below the required limit. While work is continuing on the development of higher storage capacities of $NaBH_4$, work on potential catalysts that can be used is also ongoing.

2.10.3 Noble Metals

A large range of catalysts have been investigated to release hydrogen from an alkaline $NaBH_4$ solution. Brown and Brown [149] were the first to investigate hydrogen release from $NaBH_4$ using noble metals as catalysts. In their work, they investigated many metals including Ru, Rh, Pd, Os, Ir and Pt. They found that Pt and Rh displayed the largest hydrogen generation activities. Since then, most of the research attention has focussed on 3 metals, Pt [150-152], Ru [153-156] and Rh [157,158], which have been shown to produce hydrogen at a large rate as shown in Table. 2.2.

Author	**Catalyst / Substrate**	**Activity (ml H_2 / min / g)**	**Temperature (°C)**	**Ref**
Amendola et.al	Ru/IRA-400	3,770	25	[153]
Ozkar et al.	Ru Nanoclusters	96,800	25	[154]
Liang et al.	Ru/Graphite	32,300	30	[156]
Liu et al.	$Ru/LiCoO_2$	270,000	25	[159]
Bai et al.	Pt/C	175,570	25	[151]
Ersoz et al.	$Pt/LiCoO_2$	83,600	20	[160]

Kojima et al.	$Pt/LiCoO_2$	206,500	22	[150]
Wu et al.	Pt/C	115,450	-	[161]
Larichev et al.	Rh/TiO_2	21,000	23	[158]
Simagina et al.	Rh/TiO_2	360,000	40	[157]

Table 2.2: Hydrogen generation activities for a range of noble metal catalysts loaded on a supporting substrate.

The earliest catalyst with a large hydrogen generation was developed by Kojima et al. [150] in 2002. They was found that 1 g of Pt catalyst could produce up to 200 L of H_2 in 1 minute. Pt loaded on a carbon substrate has also been shown to have good catalytic properties [151,161]. Using an Ru catalyst, Liu et al. [159] achieved a hydrogen generation rate of 300,000 ml min^{-1} g^{-1}. The largest hydrogen generation rate achieved with a noble metal catalyst was Rh on a TiO_2 substrate, with a hydrogen generation rate of 360,000 ml min^{-1} g^{-1}. However, this was carried out at a temperature of 40 ºC which is higher than the temperature of 25-30 ºC used in most other studies. Using a similar catalyst at 23 ºC, Larichev et al. [158] achieved an activity of only 21,000 ml min^{-1} g^{-1}, indicating that temperature has a large influence on the hydrogen generation rate. Although these catalysts have very high hydrogen generation rates, due to their high cost they are not suitable for large scale catalysis in future technologies.

2.10.4 Transition Metal Catalysts

Due to the high cost involved with noble metal catalysts, alternative cheap catalysts are currently the focus of research in the area. One such alternative is transition metal catalysts, which were first described by Schlesinger et al. [162] in 1962. They found that Co was the most active transition metal followed by Ni, with Fe, Cu and Mn all

showing very small activities. The addition of B or P has been shown to greatly enhance the catalytic properties of the metal [163].

In recent years, a wide variety of catalysts have been investigated including Co-B [164-170], which is the most promising due to its large activity, Co-P [16,171,172], Ni-B [168,173,174], Co-Ni-B [27,175] and Co-Fe-B [176]. Some of these methods involve the use of powders or nanoparticles [27,167,168,175]. Ni foam has also been widely used as a substrate due to its high porosity and low density [33,165,166,176]. Other substrates include Cu [16,171], TiO_2, $Al2O_3$ and CeO_2 [169] and multi-walled carbon nanotubes [170]. The vast majority of these catalysts are deposited via electroless deposition with hydrogen generation rates of the best catalysts shown in Table 2.3.

Author	Catalyst / Substrate	Activity (ml H_2 / min / g)	Temperature (°C)	Ref
Patel et al.	Co-Cr-B Powder	3,400	25	[177]
Metin et al.	Ni Nanoclusters	4,250	25	[178]
Patel et al.	Co-P-B / Glass	4,300	25	[179]
Patel et al.	Co-B / Glass	5,000	25	[180]
Huang et al.	Co-B / MWCNT	5,100	30	[170]
Rakap et al.	Co Nanoparticles	6,100	25	[181]
Lee et al.	Co-B / Ni-Foam	7,200	20	[182]
Krishnan et al.	Co-B Nanoparticles	8,500	25	[166]
Dai et al.	Co-B / Ni-Foam	11,000	30	[165]
Dai et al.	Co-W-B / Ni-Foam	15,000	30	[183]

Liang et al.	Fe-Co-B / Ni-Foam	22,000	30	[33]
Muir et al.	Co-B / Ni-Foam	24,400	30	[17]
Liu et al.	Co-B Nanoparticles	26,000	30	[184]

Table 2.3: Hydrogen generation activities for a range of transition metal catalysts loaded on a supporting substrate or in nanostructured form.

As can be seen from Table 2.3, Co-B alloys have the largest hydrogen generation rates, which are comparable to those of noble metals. It is important to note that the most active catalysts consist of Co-B deposited in nanostructured form, either as Co-B nanoparticles, on a porous Ni-foam substrate or on a multi-walled carbon nanotube (MWCNT). The large hydrogen generation rates are due to the large catalytic surface area of the nanostructures. Although Co-B nanoparticles have the largest recorded hydrogen generation rates, their potential for future applications is limited as they are difficult to remove from solution and be recycled. Therefore, nanostructured materials, with recycling potential such as a Ni foam substrate will be important in finding suitable catalysts for future use.

2.11 Hydrogen Generation Rate Parameters

2.11.1 Temperature

Catalysts used for hydrogen generation from $NaBH_4$ have an associated activation energy. Therefore, as temperature of the bath increases, there is a corresponding increase in the hydrogen generation rate. The relationship between the hydrogen production rate, r, the activation energy, E, and the temperature, T, is given by the Arrhenius equation [185],

$$r = k_0 e^{-\frac{E}{RT}} \quad (2.8)$$

$$\ln(r) = \ln(k_0) - \frac{E}{RT} \quad (2.9)$$

An Arrhenius plot of ln (r) vs. $1/T$ obtained using Eqn. 2.9 is shown in Fig. 2.38. Activation energies of Co-B deposited on Ni foam were found to be 73.2 kJ mol^{-1} [17] and 33 kJ mol^{-1} [165], of Co-B nanoparticles, 43 kJ mol^{-1} [167] and Co-B deposited on carbon nanotubes, 40 kJ mol^{-1} [170].

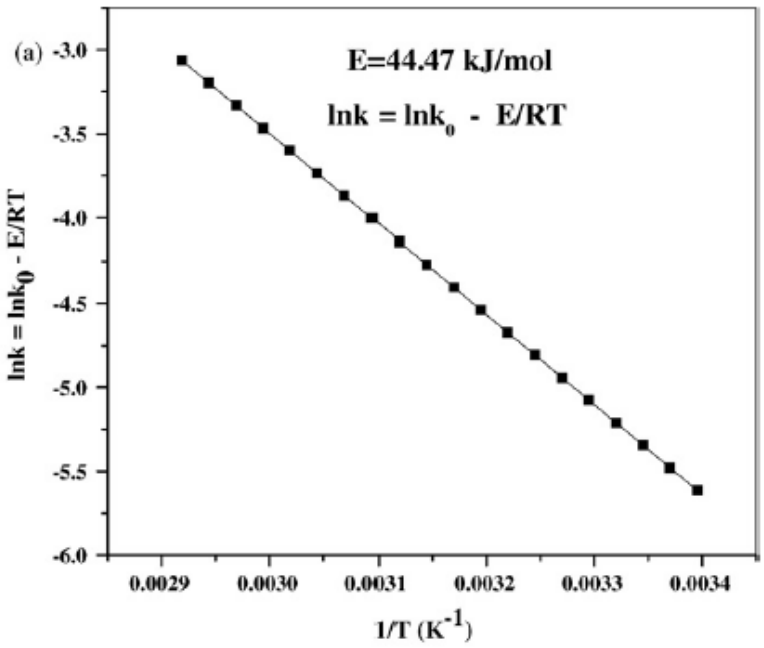

Figure 2.38: Arrhenius plot of Co-B loaded on Ni foam displaying a linear relationship between the natural log of the hydrogen generation rate and $1/T$ [166].

2.11.2 $NaBH_4$ Concentration

Although there is a general agreement in the scientific community that increasing temperature results in an increased hydrogen generation rate, there is no such agreement with $NaBH_4$ concentration. In the literature, the $NaBH_4$ concentration of the hydrogen generation bath is commonly referenced to as wt. %. Maximum hydrogen generation rates for various catalysts have been recorded for concentrations ranging from 1 wt. % to 20 wt. % as shown in Table 2.4. Catalysts deposited onto Ni

foam have maximum hydrogen generation rates at the largest $NaBH_4$ concentrations, although no explanation is given in the literature.

Author	Catalyst / Substrate	$NaBH_4$ Concentration	Ref
Wu et al.	Ni-B Powder	0.25 wt. %	[174]
Wu et al.	Co-B Nanoparticles	1 wt. %	[167]
Liu et al.	Ni-B Powder	1 wt. %	[186]
Jeong et al.	Co-B Powder	5 wt. %	[164]
Ye et al.	Co / Al_2O_3	5 wt. %	[187]
Liang et al.	Co-B / Ni Foam	10 wt. %	[176]
Muir et al.	Co-B / Ni Foam	15 wt. %	[17]
Liang et al.	Fe-Co-B / Ni-Foam	20 wt. %	[33]

Table 2.4: $NaBH_4$ concentrations at which maximum hydrogen generation rates are achieved for a range of transition metal catalysts.

Many theories have been presented to explain the phenomenon of high $NaBH_4$ concentration causing low hydrogen generation rates. Firstly, as shown in Eqn. 2.7, two water molecules are required to react with $NaBH_4$ at the catalyst surface to release H_2. The adsorption of water onto the catalytic surface may be limited by an increase in $NaBH_4$ concentration resulting in a decrease in catalytic activity [176]. Ye et al. [187] attribute the decrease to an increase in solution viscosity, though this may relate to the same point. Colloids such as $NaBO_2$ are known to form during hydrogen generation and adhere to the catalyst reducing the associated activity. It is also possible that as $NaBH_4$ concentration increases, there is an increase in the number of colloids formed. This decreases the catalytic activity resulting in a reduced hydrogen generation rate [176]. The kinetics of sodium borohydride hydrolysis on

Ni-B have been described recently by Wu et al. [174]. In this study the reaction rate is given by Eqn. 2.10, where k_1, K_{BH4} and K_{OH} are reaction constants.

$$r = k_1[NaBH_4][NaOH] = \frac{k_1 K_{BH_4}[BH_4^-]K_{OH}[OH^-]}{\left(1 + K_{BH_4}[BH_4^-] + K_{OH}[OH^-]\right)^2} \quad (2.10)$$

Therefore, when the sodium borohydride concentration is large the equation is reduced to,

$$K_{BH_4}[BH_4^-] \gg 1 + K_{OH}[OH^-]$$

$$r = \frac{k_1 K_{OH}[OH^-]}{K_{BH_4}[BH_4^-]} \quad (2.11)$$

This indicates that the reaction rate is inversely proportional to the sodium borohydride concentration and a small hydrogen generation rate is observed. However, for very low $NaBH_4$ concentrations the equation can be written as,

$$K_{BH_4}[BH_4^-] \ll 1 + K_{OH}[OH^-]$$

$$r = \frac{k_1 K_{BH_4}[BH_4^-]}{K_{OH}[OH^-]} \quad (2.12)$$

At low $NaBH_4$ concentrations, an increase in the reaction rate with respect to $NaBH_4$ concentration is observed. As shown in Fig. 2.39, Wu et al. [174] achieved a maximum hydrogen generation rate at a $NaBH_4$ concentration of approximately 0.25 M L^{-1}. An increase in deposition rate with respect to $NaBH_4$ concentration was observed below 0.25 M L^{-1}, while a decrease was observed above 0.25 M L^{-1}.

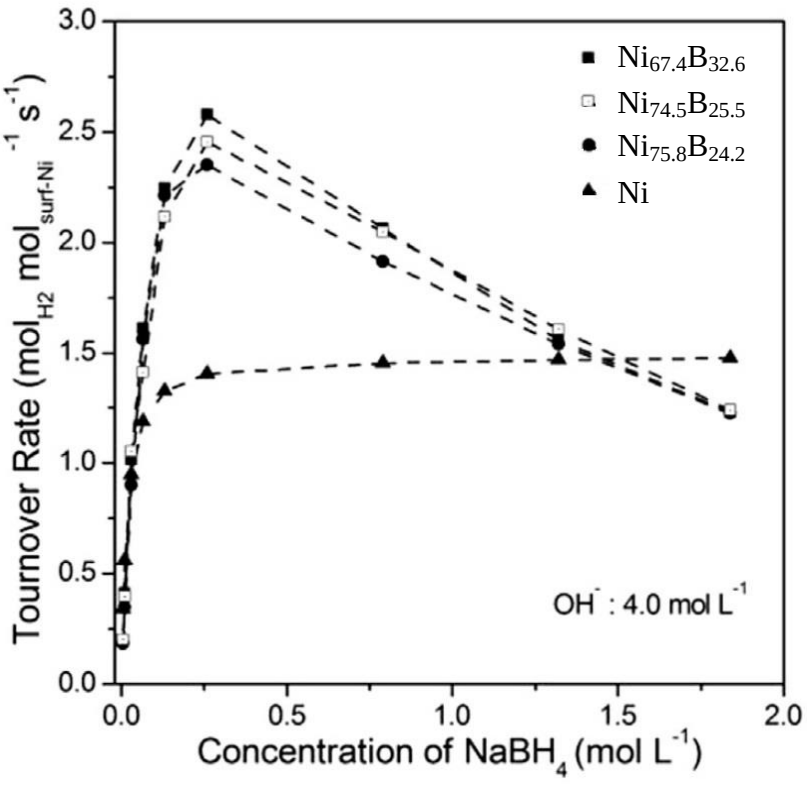

Figure 2.39: Hydrogen generation of Ni-B catalysts as a function of $NaBH_4$ concentration [174].

2.11.3 Recyclability

Despite the large amount of investigation into transition metal catalysts, only a few researchers have conducted tests to determine their long-term cyclic stability. This is a critical issue for practical hydrogen storage applications and must therefore be considered in addition to the basic catalytic properties of the metals. After only 6 cycles, Rakap et al. [181] and Liang et al. [33] observed a 50 % drop in catalytic activity for Co nanoclusters and Co-Fe-B on Ni foam respectively. The drop in catalytic activity is likely due to the formation of an oxide on the metal surface during hydrogen generation [117]. Dai et al. [183] found a more promising result using Co-W-B on Ni foam with a 10 % decrease in activity after 6 cycles. It is possible that Co-W-B retained its activity better than Co-Fe-B as tungsten unlike iron does not oxidise easily.

2.11.4 Potential

Muir et al. [17], who achieved one of the largest hydrogen generation rates of 24,400 ml min^{-1} g^{-1} in 2014, have discussed the power capabilities of their Co-B catalyst. Their hydrogen generation rate is equivalent to 1 mol H_2 min^{-1} g^{-1}, which is capable of producing 3.2 kA. With a fuel cell voltage of 0.7 V, this equates to 2.2 kW per gram of catalyst. To power a 100 kW engine, they would require 45 g of catalyst which equates to 700 cm^2 of surface area. This indicates that there is a potential for use of Co-B catalysts in future technologies though larger generation rates are still desirable. The hydrogen storage capacity they achieved was only 3.2 wt. %, approximately half the 5.5 wt. % target set by the DOE for 2015. This technology is still below the DOE targets and short-term progress is needed for this technology to be considered viable in the future.

2.12 Conclusion

After analysing the current literature, it is clear that the formation of nanotubes via an electroless deposition process is not fully understood. There is an inconsistency between the formation of end-closed nanotubes and continuous nanowires. In this study a detailed investigation of the electroless deposition will be carried out to determine the deposition mechanisms involved within a template structure. Here, we investigate the conditions required to form continuous nanotubes with uniform wall thicknesses. To achieve this, the parameters of the deposition bath will be varied and the effect on the resultant nanostructure will be investigated. This study aims to determine the deposition mechanism within the nanostructure so that the electroless deposition process can be controlled.

Previously, although there have been studies on the magnetic properties of nanotubes and the reversal mechanisms involved, investigations of the magnetic properties of electrolessly deposited nanotubes have been limited. Here, the magnetic properties of a variety of alloyed nanotubes will be investigated. The effect of size, shape, composition and crystallinity on the magnetic properties of the nanotubes will all be examined.

Electrolessly deposited metallic alloys can also act as catalysts for hydrogen generation from sodium borohydride. As nanotubes have a large catalytic surface area, this study aims to investigate the catalytic properties of electrolessly deposited nanotubes. It is proposed that catalysis of hydrogen release from sodium borohydride will occur at a large rate due to the large surface area associated with the electrolessly deposited nanotubes.

2.13 **References**

[1] X. W. Wang, Z. H. Yuan, S. Q. Sun, Y. Q. Duan and L. J. Bie, *Materials Chemistry and Physics*, **112**, 329 (2008).

[2] S. Xue, C. Cao, D. Wang and H. Zhu, *Nanotechnology*, **16**, 1495 (2005).

[3] I. Betancourt, G. Hrkac and T. Schrefl, *Journal of Applied Physics*, **104**, 023915 (2008).

[4] C. A. Haberzettl, *Nanotechnology*, **13**, R9 (2002).

[5] A. Brenner and G. E. Riddell, *Journal of Research of the National Bureau of Standards*, **37**, 31 (1946).

[6] J. F. Rohan, D. P. Casey, B. M. Ahern, F. M. F. Rhen, S. Roy, D. Fleming and S. E. Lawrence, *Electrochemistry Communications*, **10**, 1419 (2008).

[7] J. Sudagar, J. Lian and W. Sha, *Journal of Alloys and Compounds*, **571**, 183 (2013).

[8] T. Zhai, X. Lu, G. Cui, G. Wu, J. Qu and Y. Tong, *Journal of Materials Chemistry C*, **1**, 5149 (2013).

[9] C. H. Ting and M. Paunovic, *Journal of The Electrochemical Society*, **136**, 456 (1989).

[10] Y. Shacham-Diamand, V. Dubin and M. Angyal, *Thin Solid Films*, **262**, 93 (1995).

[11] P. J. McNally, J. Kanatharana, B. H. W. Toh, D. W. McNeill, A. N. Danilewsky, T. Tuomi, L. Knuuttila, J. Riikonen, J. Toivonen and R. Simon, *Journal of Applied Physics*, **96**, 7596 (2004).

[12] T. R. Hendricks and I. Lee, *Thin Solid Films*, **515**, 2347 (2006).

[13] Y. Shacham-Diamand, T. Osaka, Y. Okinaka, A. Sugiyama and V. Dubin, *Microelectronic Engineering*, **132**, 35 (2015).
[14] M. Anik, E. Körpe and E. Şen, *Surface and Coatings Technology*, **202**, 1718 (2008).
[15] B. Oraon, G. Majumdar and B. Ghosh, *Materials & Design*, **29**, 1412 (2008).
[16] X. Zhang, J. Zhao, F. Cheng, J. Liang, Z. Tao and J. Chen, *International Journal of Hydrogen Energy*, **35**, 8363 (2010).
[17] S. S. Muir, Z. Chen, B. J. Wood, L. Wang, G. Q. Lu and X. Yao, *International Journal of Hydrogen Energy*, **39**, 414 (2014).
[18] M. A. Dinderman, W. J. Dressick, C. N. Kostelansky, R. R. Price, S. B. Qadri and P. E. Schoen, *Chemistry of Materials*, **18**, 4361 (2006).
[19] G. F. Huang, W. Q. Huang, L. L. Wang, Y. Meng, Z. Xie and B. S. Zou, *Electrochimica Acta*, **51**, 4471 (2006).
[20] G. H. Yang, E. T. Kang, K. G. Neoh, Y. Zhang and K. L. Tan, *Colloid and Polymer Science*, **279**, 745 (2001).
[21] R. L. Jackson, *Journal of The Electrochemical Society*, **137**, 95 (1990).
[22] L. A. Porter, H. C. Choi, A. E. Ribbe and J. M. Buriak, *Nano Letters*, **2**, 1067 (2002).
[23] M. A. Raj and S. A. John, *RSC Advances*, **5**, 4964 (2015).
[24] A. K. Kalkan and S. J. Fonash, *The Journal of Physical Chemistry B*, **109**, 20779 (2005).
[25] D. A. Brevnov, T. S. Olson, G. P. López and P. Atanassov, *The Journal of Physical Chemistry B*, **108**, 17531 (2004).
[26] M. Ranjbar, N. Tahmasebi Garavand, S. M. Mahdavi and A. Iraji zad, *Solar Energy Materials and Solar Cells*, **94**, 201 (2010).
[27] R. Fernandes, N. Patel, A. Miotello and M. Filippi, *Journal of Molecular Catalysis A*, **298**, 1 (2009).
[28] M. Rakap, E. E. Kalu and S. Özkar, *International Journal of Hydrogen Energy*, **36**, 254 (2011).
[29] A. Azizi, M. Mohammadi and S. K. Sadrnezhaad, *Materials Letters*, **65**, 289 (2011).
[30] W. L. Liu, S. H. Hsieh, H. C. Yan and W. J. Chen, *Applied Surface Science*, **258**, 1806 (2011).
[31] J. F. Rohan, B. M. Ahern, K. Reynolds, S. Crowley, D. A. Healy, F. M. F. Rhen and S. Roy, *Electrochimica Acta*, **54**, 1851 (2009).
[32] L. Yu, S. K. Kang, O. Jinka, M. Mason, S. A. Cordes and L. T. Romankiw, in *Electronic Components and Technology Conference (ECTC), 2014 IEEE 64th*, p. 1782 (2014).
[33] Y. Liang, P. Wang and H. B. Dai, *Journal of Alloys and Compounds*, **491**, 359 (2010).
[34] X. Ren, C. H. Jiang, X. M. Huang and D. D. Li, *Physica E*, **41**, 349 (2009).
[35] S. C. Lin, C. H. Lai and P. W. Wu, *Electrochemical and Solid-State Letters*, **11**, D1 (2008).
[36] J. F. Rohan, B. M. Ahern and L. C. Nagle, *ECS Transactions*, **1**, 1 (2006).
[37] H. H. Hsu, C. W. Teng, S. J. Lin and J. W. Yeh, *Journal of The Electrochemical Society*, **149**, C143 (2002).
[38] I. Enculescu, M. Sima, M. Enculescu, E. Matei, M. E. Toimil Molares and T. H. Cornelius, *Optoelectronics and Advanced Materials-Rapid Communications*, **2**, 133 (2008).
[39] F. Delaunois, J. P. Petitjean, P. Lienard and M. Jacob-Duliere, *Surface and Coatings Technology*, **124**, 201 (2000).
[40] J. S. Judge, J. R. Morrison and D. E. Speliotis, *Journal of The Electrochemical Society*, **113**, 547 (1966).
[41] J. P. Marton and M. Schlesinger, *Journal of The Electrochemical Society*, **115**, 16 (1968).
[42] R. Sard, *Journal of The Electrochemical Society*, **117**, 864 (1970).

[43] T. Homma, T. Yamazaki and T. Osaka, *Journal of The Electrochemical Society*, **139**, 732 (1992).
[44] J. W. Severin, R. Hokke, H. Van der Wel and G. de With, *Journal of the Electrochemical Society*, **140**, 682 (1993).
[45] T. H. Hentschel, D. Isheim, R. Kirchheim, F. Müller and H. Kreye, *Acta materialia*, **48**, 933 (2000).
[46] H. Ashassi-Sorkhabi, H. Dolati, N. Parvini-Ahmadi and J. Manzoori, *Applied Surface Science*, **185**, 155 (2002).
[47] T. Saito, E. Sato, M. Matsuoka and C. Iwakura, *Journal of Applied Electrochemistry*, **28**, 559 (1998).
[48] K. H. Hur, J. H. Jeong and D. N. Lee, *Journal of Materials Science*, **25**, 2573 (1990).
[49] K. M. Gorbunova, M. V. Ivanov and V. P. Moiseev, *Journal of The Electrochemical Society*, **120**, 613 (1973).
[50] N. Dadvand, G. Jarjoura and G. J. Kipouros, *Journal of Materials Science: Materials in Electronics*, **19**, 51 (2008).
[51] W. T. Evans and M. Schlesinger, *Journal of the Electrochemical Society*, **141**, 78 (1994).
[52] Z. Abdel Hamid, H. B. Hassan and A. M. Attyia, *Surface and coatings technology*, **205**, 2348 (2010).
[53] Y. Liu and Q. Zhao, *Applied Surface Science*, **228**, 57 (2004).
[54] I. Baskaran, R. Sakthi Kumar, T. S. N. Sankara Narayanan and A. Stephen, *Surface and Coatings Technology*, **200**, 6888 (2006).
[55] H. Matsubara, T. Yonekawa, Y. Ishino, N. Saito, H. Nishiyama and Y. Inoue, *Electrochimica Acta*, **52**, 402 (2006).
[56] A. H. Graham, R. W. Lindsay and H. J. Read, *Journal of the Electrochemical Society*, **112**, 401 (1965).
[57] M. H. Staia, E. S. Puchi, G. Castro, F. O. Ramirez and D. B. Lewis, *Thin Solid Films*, **355**, 472 (1999).
[58] C. T. Dervos, J. Novakovic and P. Vassiliou, *Materials Letters*, **58**, 619 (2004).
[59] T. S. N. Sankara Narayanan and S. K. Seshadri, *Journal of Alloys and Compounds*, **365**, 197 (2004).
[60] K. H. Krishnan, S. John, K. N. Srinivasan, J. Praveen, M. Ganesan and P. M. Kavimani, *Metallurgical and Materials Transactions A*, **37**, 1917 (2006).
[61] K. H. Lee, D. Chang and S. C. Kwon, *Electrochimica Acta*, **50**, 4538 (2005).
[62] S. U. Jeong, E. A. Cho, S. W. Nam, I. H. Oh, U. H. Jung and S. H. Kim, *International Journal of Hydrogen Energy*, **32**, 1749 (2007).
[63] T. K. Tsai and C. G. Chao, *Applied Surface Science*, **233**, 180 (2004).
[64] J. Martín, J. Maiz, J. Sacristan and C. Mijangos, *Polymer*, **53**, 1149 (2012).
[65] J. L. Perry, C. R. Martin and J. D. Stewart, *Chemistry-A European Journal*, **17**, 6296 (2011).
[66] X. F. Han, S. Shamaila, R. Sharif, J. Y. Chen, H. R. Liu and D. P. Liu, *Advanced Materials*, **21**, 4619 (2009).
[67] R. Sharif, S. Shamaila, M. Ma, L. D. Yao, R. C. Yu, X. F. Han and M. Khaleeq-ur-Rahman, *Applied Physics Letters*, **92**, 032505 (2008).
[68] J. Joo, B. H. Kim, D. H. Park, H. S. Kim, D. S. Seo, J. H. Shim, S. J. Lee, K. S. Ryu, K. Kim, J. I. Jin, T. J. Lee and C. J. Lee, *Synthetic Metals*, **153**, 313 (2005).
[69] J. H. He, C. S. Lao, L. J. Chen, D. Davidovic and Z. L. Wang, *Journal of the American Chemical Society*, **127**, 16376 (2005).
[70] C. Shi, G. Wang, N. Zhao, X. Du and J. Li, *Chemical Physics Letters*, **454**, 75 (2008).
[71] O. Albrecht, R. Zierold, S. Allende, J. Escrig, C. Patzig, B. Rauschenbach, K. Nielsch and D. Görlitz, *Journal of Applied Physics*, **109**, 093910 (2011).

[72] J. Bachmann, J. Jing, M. Knez, S. Barth, H. Shen, S. Mathur, U. Gösele and K. Nielsch, *Journal of the American Chemical Society*, **129**, 9554 (2007).
[73] R. L. Fleisher, P. B. Price and R. M. Walker, "*Nuclear Tracks in Solids: Principles and Applications*", University of California Press (1975).
[74] R. C. Furneaux, W. R. Rigby and A. P. Davidson, *Letters to Nature*, **337**, 147 (1989).
[75] A. G. Leyva, P. Stoliar, M. Rosenbusch, V. Lorenzo, P. Levy, C. Albonetti, M. Cavallini, F. Biscarini, H. E. Troiani, J. Curiale and R. D. Sanchez, *Journal of Solid State Chemistry*, **177**, 3949 (2004).
[76] V. P. Menon and C. R. Martin, *Analytical Chemistry*, **67**, 1920 (1995).
[77] L. Hai-Peng, H. Man-Gui, C. Li and D. Long-Jiang, *Chinese Physics B*, **20**, 060701 (2011).
[78] W. Wang, N. Li, X. Li, W. Geng and S. Qiu, *Materials Research Bulletin*, **41**, 1417 (2006).
[79] X. Y. Yuan, G. S. Wu, T. Xie, Y. Lin and L. D. Zhang, *Nanotechnology*, **15**, 59 (2004).
[80] Z. Liu, W. L. Li and W. D. Fei, *Modern Physics Letters B*, **27**, 1341006 (2013).
[81] M. Huang, Y. Zhang, F. Li, L. Zhang, R. S. Ruoff, Z. Wen and Q. Liu, *Scientific reports*, **4** (2014).
[82] N. Li, X. Li, X. Yin, W. Wang and S. Qiu, *Solid State Communications*, **132**, 841 (2004).
[83] F. Muench, U. Kunz, H. F. Wardenga, H.-J. Kleebe and W. Ensinger, *Langmuir : the ACS journal of surfaces and colloids*, **30**, 10878 (2014).
[84] S. Iijima, *nature*, **354**, 56 (1991).
[85] W. Li, H. Jin, Y. Hao, T. Chen, J. Dai and Q. Wang, *Journal of Nanomaterials*, **2011**, 348958 (2011).
[86] Q. Li, S. Fan, W. Han, C. Sun and W. Liang, *Japanese Journal of Applied Physics: Part 2 Letters*, **36**, L501 (1997).
[87] J. H. Byeon and J. Hwang, *Surface and Coatings Technology*, **203**, 357 (2008).
[88] S. Arai, M. Endo, S. Hashizume and Y. Shimojima, *Electrochemistry Communications*, **6**, 1029 (2004).
[89] G. Xie, Z. Wang, G. Li, Y. Shi, Z. Cui and Z. Zhang, *Materials Letters*, **61**, 2641 (2007).
[90] S. L. Cheng and W. C. Hsiao, *Electrochemical and Solid-State Letters*, **10**, D142 (2007).
[91] I. Gurrappa and L. Binder, *Science and Technology of Advanced Materials*, **9**, 043001 (2008).
[92] T. M. Whitney, P. C. Searson, J. S. Jiang and C. L. Chien, *Science*, **261**, 1316 (1993).
[93] J. Fu, S. Cherevko and C. H. Chung, *Electrochemistry Communications*, **10**, 514 (2008).
[94] C. G. Jin, W. F. Liu, C. Jia, X. Q. Xiang, W. L. Cai, L. Z. Yao and X. G. Li, *Journal of Crystal Growth*, **258**, 337 (2003).
[95] F. Tian, J. Zhu and D. Wei, *The Journal of Physical Chemistry C*, **111**, 12669 (2007).
[96] M. M. A. Imran, *Journal of Alloys and Compounds*, **455**, 17 (2008).
[97] J. B. Shi, Y. C. Chen, C. W. Lee, Y. T. Lin, C. Wu and C. J. Chen, *Materials Letters*, **62**, 15 (2008).
[98] M. A. Kashi, A. Ramazani and A. Khayyatian, *Journal of Physics D*, **39**, 4130 (2006).
[99] J. Rivas, A. Kazadi Mukenga Bantu, G. Zaragoza, M. C. Blanco and M. A. López-Quintela, *Journal of Magnetism and Magnetic Materials*, **249**, 220 (2002).
[100] J. Azevedo, C. T. Sousa, A. Mendes and J. P. Araújo, *Journal of Nanoscience and Nanotechnology*, **12**, 9112 (2012).
[101] X. F. Qin, C. H. Deng, Y. Liu, X. J. Meng, J. Q. Zhang, F. Wang and X. H. Xu, *IEEE Transactions on Magnetics*, **48**, 3136 (2012).
[102] C. R. Martin, *Advanced Materials*, **3**, 457 (1991).

[103] C. J. Brumlik and C. R. Martin, *Journal of the American Chemical Society*, **113**, 3174 (1991).
[104] X. Li, Y. Wang, G. Song, Z. Peng, Y. Yu, X. She and J. Li, *Nanoscale research letters*, **4**, 1015 (2009).
[105] G. Tourillon, L. Pontonnier, J. P. Levy and V. Langlais, *Electrochemical and Solid-State Letters*, **3**, 20 (2000).
[106] S. Xue, C. Cao and H. Zhu, *Journal of Materials Science*, **41**, 5598 (2006).
[107] J. Bao, C. Tie, Z. Xu, Q. Zhou, D. Shen and Q. Ma, *Advanced Materials*, **13**, 1631 (2001).
[108] W. Lee, R. Scholz, K. Nielsch and U. Gösele, *Angewandte Chemie*, **117**, 6204 (2005).
[109] F. Tao, M. Guan, Y. Jiang, J. Zhu, Z. Xu and Z. Xue, *Advanced Materials*, **18**, 2161 (2006).
[110] G. O. Mallory and J. B. Hajdu, "*Chapter 1 - The Fundamental Aspects of Electroless Nickel Plating*", in *Electroless Plating: Fundamentals and Applications*, William Andrew (1990).
[111] C. C. Lo, C. C. Huang, C. M. Liu, C. Chen, C. Y. Kuo, H. J. Lin and Y. C. Tseng, *Journal of Magnetism and Magnetic Materials*, **323**, 1950 (2011).
[112] S. Nakagawa and K. I. Hirata, *Journal of Magnetics*, **18**, 155 (2013).
[113] I. Kim, J. Kim, K. H. Kim and M. Yamaguchi, *IEEE Transactions on Magnetics*, **40**, 2706 (2004).
[114] T. Osaka, M. Usuda, I. Koiwa and H. Sawai, *Japanese Journal of Applied Physics*, **27**, 1885 (1988).
[115] A. Bai and C. C. Hu, *Materials Chemistry and Physics*, **79**, 49 (2003).
[116] B. D. Cullity and C. D. Graham, "*Introduction to Magnetic Materials*", John Wiley & Sons (2011).
[117] J. H. Kim, K. T. Kim, Y. M. Kang, H. S. Kim, M. S. Song, Y. J. Lee, P. S. Lee and J. Y. Lee, *Journal of Alloys and Compounds*, **379**, 222 (2004).
[118] M. M. Rico, J. M. Greneche and G. A. Pérez Alcázar, *Journal of Alloys and Compounds*, **398**, 26 (2005).
[119] C. L. Platt, M. K. Minor and T. J. Klemmer, *IEEE Transactions on Magnetics*, **37**, 2302 (2001).
[120] B. Yao, L. Si, H. Tan, Y. Zhang and Y. Li, *Journal of Non-Crystalline Solids*, **332**, 43 (2003).
[121] J. Hu, T. W. Odom and C. M. Lieber, *Accounts of Chemical Research*, **32**, 435 (1999).
[122] J. Escrig, M. Daub, P. Landeros, K. Nielsch and D. Altbir, *Nanotechnology*, **18**, 445706 (2007).
[123] M. Sharma, B. K. Kuanr, V. Veerakumar, A. Basu and Z. J. Celinski, *IEEE Transactions on Magnetics*, **50**, 280104 (2014).
[124] J. W. Lau and J. M. Shaw, *Journal of Physics D: Applied Physics*, **44**, 303001 (2011).
[125] K. Pitzschel, J. Bachmann, J. M. Montero-Moreno, J. Escrig, D. Görlitz and K. Nielsch, *Nanotechnology*, **23**, 495718 (2012).
[126] M. P. Proenca, J. Ventura, C. T. Sousa, M. Vazquez and J. P. Araujo, *Journal of Physics: Condensed matter*, **26**, 116004 (2014).
[127] R. Skomski, *Journal of Physics: Condensed Matter*, **15**, R841 (2003).
[128] M. T. Bohr, *IEEE Transactions on Nanotechnology*, **1**, 56 (2002).
[129] P. J. Burke, *Solid-State Electronics*, **48**, 1981 (2004).
[130] A. J. C. Baur and Y. Mayer, "*Coil-based electronic & electrical components (such as coils, transformers, filters and motors) based on nanotechnology*", U.S. Patent, 0163414, Nov. (2002).
[131] S. J. Son, J. Reichel, B. He, M. Schuchman and S. B. Lee, *Journal of the American Chemical Society*, **127**, 7316 (2005).

[132] Z. G. Yue, W. Wei, Z. X. You, Q. Z. Yang, H. Yue, Z. G. Su and G. H. Ma, *Advanced Functional Materials*, **21**, 3446 (2011).
[133] N. K. Shrestha, J. M. Macak, F. Schmidt-Stein, R. Hahn, C. T. Mierke, B. Fabry and P. Schmuki, *Angewandte Chemie International Edition*, **48**, 969 (2009).
[134] M. Eisenstein, *Nature Methods*, **2**, 484 (2005).
[135] H. Hillebrenner, F. Buyukserin, J. D. Stewart and C. R. Martin, *Nanomedicine*, **1**, 39 (2006).
[136] P. Landeros, S. Allende, J. Escrig, E. Salcedo, D. Altbir and E. E. Vogel, *Applied Physics Letters*, **90**, 102501 (2007).
[137] J. Bachmann, J. Escrig, K. Pitzschel, J. M. Montero Moreno, J. Jing, D. Görlitz, D. Altbir and K. Nielsch, *Journal of Applied Physics*, **105**, 07B521 (2009).
[138] E. C. Stoner and E. P. Wohlfarth, *IEEE Transactions on Magnetics*, **27**, 3475 (1991).
[139] C. R. Chang, C. M. Lee and J. S. Yang, *Physical Review B*, **50**, 6461 (1994).
[140] J. Escrig, J. Bachmann, J. Jing, M. Daub, D. Altbir and K. Nielsch, *Physical Review B*, **77**, 214421 (2008).
[141] S. Allende, J. Escrig, D. Altbir, E. Salcedo and M. Bahiana, *The European Physical Journal B*, **66**, 37 (2008).
[142] N. Ahmad, J. Y. Chen, J. Iqbal, W. X. Wang, W. P. Zhou and X. F. Han, *Journal of Applied Physics*, **109**, 07A331 (2011).
[143] D. Li, R. S. Thompson, G. Bergmann and J. G. Lu, *Advanced Materials*, **20**, 4575 (2008).
[144] M. Daub, M. Knez, U. Goesele and K. Nielsch, *Journal of Applied Physics*, **101**, 09J111 (2007).
[145] K. Nielsch, F. J. Castano, C. A. Ross and R. Krishnan, *Journal of Applied Physics*, **98**, 034318 (2005).
[146] Y. Sui, R. Skomski, K. D. Sorge and D. J. Sellmyer, *Applied Physics Letters*, **84**, 1525 (2004).
[147] L. Schlapbach and A. Züttel, *Nature*, **414**, 353 (2001).
[148] S. S. Muir and X. Yao, *International Journal of Hydrogen Energy*, **36**, 5983 (2011).
[149] H. C. Brown and C. A. Brown, *Journal of the American Chemical Society*, **84**, 1494 (1962).
[150] Y. Kojima, K. I. Suzuki, K. Fukumoto, M. Sasaki, T. Yamamoto, Y. Kawai and H. Hayashi, *International Journal of Hydrogen Energy*, **27**, 1029 (2002).
[151] Y. Bai, C. Wu, F. Wu and B. Yi, *Materials Letters*, **60**, 2236 (2006).
[152] D. Xu, H. Zhang and W. Ye, *Catalysis Communications*, **8**, 1767 (2007).
[153] S. C. Amendola, S. L. Sharp-Goldman, M. Saleem Janjua, M. T. Kelly, P. J. Petillo and M. Binder, *Journal of Power Sources*, **85**, 186 (2000).
[154] S. Özkar and M. Zahmakıran, *Journal of Alloys and Compounds*, **404–406**, 728 (2005).
[155] C. L. Hsueh, C. Y. Chen, J. R. Ku, S. F. Tsai, Y. Y. Hsu, F. Tsau and M. S. Jeng, *Journal of Power Sources*, **177**, 485 (2008).
[156] Y. Liang, H. B. Dai, L. P. Ma, P. Wang and H. M. Cheng, *International Journal of Hydrogen Energy*, **35**, 3023 (2010).
[157] V. I. Simagina, P. A. Storozhenko, O. V. Netskina, O. V. Komova, G. V. Odegova, T. Y. Samoilenko and A. G. Gentsler, *Kinetics and Catalysis*, **48**, 168 (2007).
[158] Y. V. Larichev, O. V. Netskina, O. V. Komova and V. I. Simagina, *International Journal of Hydrogen Energy*, **35**, 6501 (2010).
[159] C. H. Liu, B. H. Chen, C. L. Hsueh, J. R. Ku, M. S. Jeng and F. Tsau, *International Journal of Hydrogen Energy*, **34**, 2153 (2009).
[160] Y. Ersoz, R. Yildirim and A. N. Akin, *Chemical Engineering Journal*, **134**, 282 (2007).
[161] C. Wu, H. Zhang and B. Yi, *Catalysis Today*, **93–95**, 477 (2004).

[162] H. I. Schlesinger, H. C. Brown, A. E. Finholt, J. R. Gilbreath, H. R. Hoekstra and E. K. Hyde, *Journal of the American Chemical Society*, **75**, 215 (1953).
[163] A. Levy, J. B. Brown and C. J. Lyons, *Industrial & Engineering Chemistry*, **52**, 211 (1960).
[164] S. U. Jeong, R. K. Kim, E. A. Cho, H. J. Kim, S. W. Nam, I. H. Oh, S. A. Hong and S. H. Kim, *Journal of Power Sources*, **144**, 129 (2005).
[165] H. B. Dai, Y. Liang, P. Wang and H. M. Cheng, *Journal of Power Sources*, **177**, 17 (2008).
[166] P. Krishnan, S. G. Advani and A. K. Prasad, *Applied Catalysis B*, **86**, 137 (2009).
[167] Z. Wu and S. Ge, *Catalysis Communications*, **13**, 40 (2011).
[168] A. A. Vernekar, S. T. Bugde and S. Tilve, *International Journal of Hydrogen Energy*, **37**, 327 (2012).
[169] Y. C. Lu, M. S. Chen and Y. W. Chen, *International Journal of Hydrogen Energy*, **37**, 4254 (2012).
[170] Y. Huang, Y. Wang, R. Zhao, P. K. Shen and Z. Wei, *International Journal of Hydrogen Energy*, **33**, 7110 (2008).
[171] K. S. Eom, K. W. Cho and H. S. Kwon, *Journal of Power Sources*, **180**, 484 (2008).
[172] T. H. Oh and S. Kwon, *International Journal of Hydrogen Energy*, **37**, 15925 (2012).
[173] Y. Chen and H. Kim, *Fuel Processing Technology*, **89**, 966 (2008).
[174] Z. Wu, X. Mao, Q. Zi, R. Zhang, T. Dou and A. C. K. Yip, *Journal of Power Sources*, **268**, 596 (2014).
[175] J. C. Ingersoll, N. Mani, J. C. Thenmozhiyal and A. Muthaiah, *Journal of Power Sources*, **173**, 450 (2007).
[176] J. Liang, Y. Li, Y. Huang, J. Yang, H. Tang, Z. Wei and P. K. Shen, *International Journal of Hydrogen Energy*, **33**, 4048 (2008).
[177] N. Patel, R. Fernandes and A. Miotello, *Journal of Catalysis*, **271**, 315 (2010).
[178] Ö. Metin and S. Özkar, *Journal of Molecular Catalysis A*, **295**, 39 (2008).
[179] N. Patel, R. Fernandes, N. Bazzanella and A. Miotello, *Thin Solid Films*, **518**, 4779 (2010).
[180] N. Patel, R. Fernandes, G. Guella, A. Kale, A. Miotello, B. Patton and C. Zanchetta, *The Journal of Physical Chemistry C*, **112**, 6968 (2008).
[181] M. Rakap and S. Özkar, *Applied Catalysis B*, **91**, 21 (2009).
[182] J. Lee, K. Y. Kong, C. R. Jung, E. Cho, S. P. Yoon, J. Han, T. G. Lee and S. W. Nam, *Catalysis Today*, **120**, 305 (2007).
[183] H. B. Dai, Y. Liang, P. Wang, X. D. Yao, T. Rufford, M. Lu and H. M. Cheng, *International Journal of Hydrogen Energy*, **33**, 4405 (2008).
[184] B. H. Liu and Q. Li, *International Journal of Hydrogen Energy*, **33**, 7385 (2008).
[185] K. J. Laidler, *Journal of Chemical Education*, **61**, 494 (1984).
[186] B. H. Liu, Z. P. Li and S. Suda, *Journal of Alloys and Compounds*, **415**, 288 (2006).
[187] W. Ye, H. Zhang, D. Xu, L. Ma and B. Yi, *Journal of Power Sources*, **164**, 544 (2007).

Chapter 3 – Experimental

3.1 Introduction

There are 3 main research objectives associated with this research. The first aim is to understand and control the electroless deposition process so that the formation of continuous nanotubes with a uniform wall thickness can be achieved. The second aim of the study is to characterise and control the magentic properties of electrolessly deposited nanotubes with unique compositions, so that the properties can be tailored to suit a range of potential applications. Finally, we characterise the catalytic properties of the nanotubes with the aim of achieving a large hydrogen generation rate from an alkaline $NaBH_4$ solution using electrolessly deposited nanostructures. To achieve each of these research objectives a range of experiments must be undertaken.

Our first research objective requires a controllable electroless deposition process within a template structure. To achieve this, we investigate the chemistry of the electroless deposition process. In this chapter, the chemistry of the deposition process and role of the chemicals involved are discussed in detail. The deposition baths and experiments used to control the electroless deposition rates are also discussed.

Characterisation of the electrolessly deposited nanostructures is required to achieve all three research objectives. Each of the characterisation techniques are described individually in this chapter. The nanostructure of the deposited alloys is imaged using a scanning electron microscope (SEM) and a transmission electron microscope (TEM). The composition of the deposit is determined using energy dispersive X-ray spectroscopy (EDS) and X-ray photon spectroscopy (XPS). The crystal structure is investigated using X-ray diffraction (XRD). To achieve our second research objective,

the magnetic properties of the deposited nanostructure are investigated as functions of nanostructure, composition and crystal structure. This is done using a vibrating sample magnetometer (VSM).

Our third research objective requires the investigation of the catalytic activity of electrolessly deposited alloys as a function of composition and nanostructure. In this chapter, the hydrogen generation bath, the chemicals used and the experimental technique used for hydrogen generation are presented.

3.2 Template Synthesis

The growth of nanotubes, nanowires and various other nanostructures within a template structure is a major research focus in modern nanotechnology [1]. Template based synthesis is a simple, cheap and reliable process which is currently used to deposit nanotubes via both electrochemical [2,3] and electroless [4-6] deposition. The size, shape, diameter, length and densities of the nanostructures are all controlled by the size and shape of the template. The template structures used must meet the requirements of the deposition method to be used. For electrochemical deposition a non-conductive template is needed. This is also true to a certain degree for electroless deposition, to prevent electron transfer through the substrate. The template must be chemically stable in the deposition solution and the solution must be able to wet the template for deposition to occur [7]. It is important that the deposited nanostructures can be removed from the template structure, so that they can be isolated for further use and imaging. For almost all electrochemical and electroless deposition baths, polycarbonate and AAO membranes are suitable template structures and are the most commonly used.

3.2.1 Polycarbonate Membrane

PC membranes are synthesised by bombarding a polycarbonate sheet, typically 6 to 20 μm in thickness, with nuclear fission fragments to create damage tracks and then by chemically etching these tracks into pores [8]. The fabricated pores can have a uniform size and diameters ranging from 10 nm to 1 μm. The pores are randomly distributed throughout the membrane surface and often overlap. Pore densities can be as high as 10^{13} pores m^{-2} [9]. An image of a typical porous polycarbonate membrane with pore diameters of 400 nm is shown in Fig 3.1. These membranes have been used by many groups to electrolessly [5,6,10] and electrochemically [2,3,11,12] deposit nanotubes.

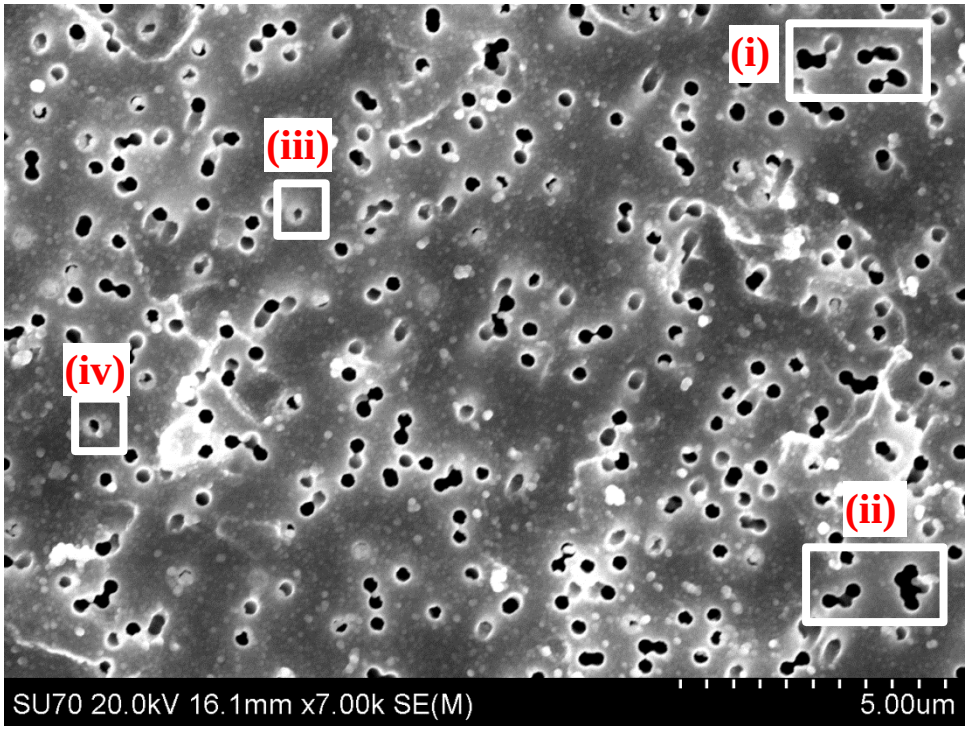

Figure 3.1: SEM image of a tracked etched polycarbonate membrane that we used as a template structure for electroless nanotube deposition with a pore diameter of 400 nm.

As shown in Fig. 3.1 (i-iv), there are many defects associated with the polycarbonate membrane. Due to the fabrication process, the pores are randomly distributed throughout the membrane. Pores can overlap to form defects where the pore wall is

shared between a number of pores, which are labelled (i) and (ii) in Fig. 3.1. The chemical etching process does not always occur perfectly perpendicular to the membrane surface. For this reason, some pores can grow into each other within the template structure. Some pores are incomplete and do not fully grow through the full length of the template structure. Also, while there are variations in the exact pore diameter, some pores do not grow to the expected diameter of 400 nm labelled (iii) and (iv) in Fig. 3.1.

3.2.2 Anodic Aluminum Oxide (AAO) Membrane

AAO membranes are fabricated by the anodic oxidation of an aluminum sheet in solutions of sulfuric, oxalic or phosphoric acids [13]. The oxide cells self-organize into hexagonal close packed arrangement, forming a honeycomb-like structure as shown in Fig 3.2. The pores of the AAO membrane are parallel, uniform and uniformly distributed across the surface. The pore diameter and density of the pores can be tuned across a wide range of sizes by properly choosing the anodization conditions. Commonly, pore diameters range from 10 nm to 1 μm and pore density ranges between 10^{12}–10^{14} pores m^{-2} [14].

AAO membranes are commonly used for the electroless deposition of nanotubes [4,15-17], although the AAO membrane must be treated with a silane prior to electroless deposition to increase the number of binding sites for electrolessly deposited particles. The AAO membranes have also been used for the electrochemical deposition of both nanotubes [18-21] and nanowires [22-25].

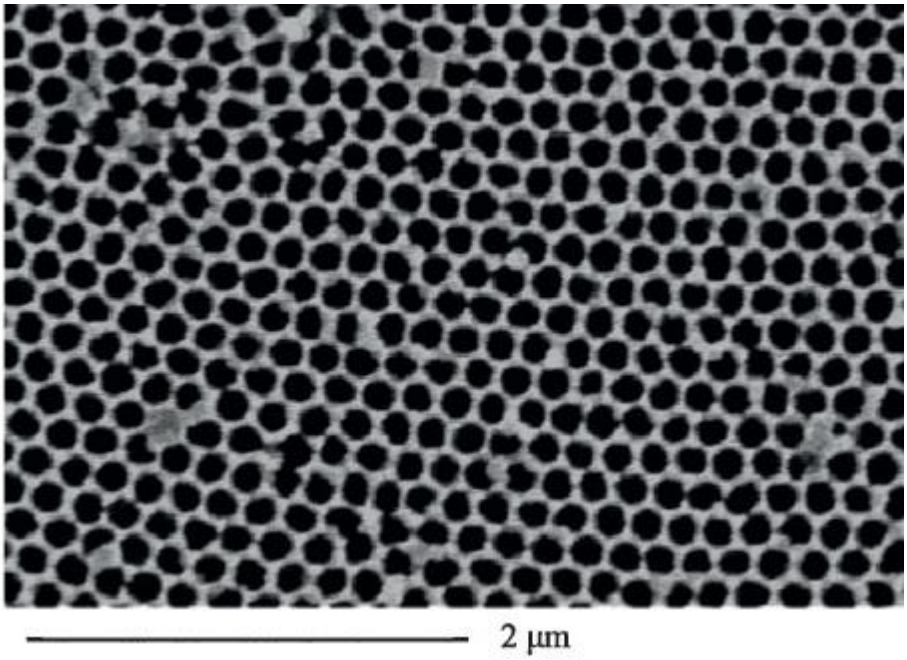

Figure 3.2: Anodic Aluminum Oxide (AAO) membrane with a pore diameter of 200 nm [2].

3.2.3 Comparison

There are advantages and disadvantages associated with both polycarbonate and AAO membranes, which are outlined in Table. 3.1.

Polycarbonate	Aluminum Oxide (AAO)
Pore diameter 10 nm - 1 μm	Pore diameter 10 nm - 1 μm
Pore density 10^{11} - 10^{13} m^{-2}	Pore density 10^{12} - 10^{14} m^{-2}
Flexible	Brittle
Easy to handle	Careful handling required
No pre-modifcation required	Silane pre-treatment required [17]
Randomly distributed pores	Uniformly distributed pores
Large number of defects	Reduced number of defects
Melting point 240 °C	Melting point 2080 °C
Dissolves in alkaline solution	Dissolves in alkaline solution

Table 3.1: Comparison of polycarbonate and AAO template structures which can be used for electroless deposition.

As there are many advantages and disadvantages associated with each membrane, both are commonly used for nanostructure fabrication research.

3.2.4 Experimental Template Structure

For this study, the templates used were Whatmann® cyclopore track etched polycarbonate membranes. These were bought direct from the company and an SEM image of a membrane that was used is shown in Fig. 3.1. The membranes were circular in shape and had a diameter of 0.025 m and a thickness of 20 μm. The track etched pores had an external diameter of 400 nm and the manufacturer gave a nominal pore density of 1.64×10^{12} pores m^{-2}. The surface area of the polycarbonate membrane is 4.9×10^{-4} m^2 and so contains approximately 8.05×10^8 pores within the polycarbonate membrane. In total, the polycarbonate membrane surface area consists of approximately 20 % pores and 80 % membrane surface.

Each pore has a diameter of 400 nm and a length of 20 μm. This corresponds to a volume of 2.51×10^{-18} m^3 and a surface area of 2.51×10^{-11} m^2 for each nanotube pore within which electroless deposition will take place. Prior to electroless deposition the membrane must be activated with a catalyst as discussed in section 3.4. An image of the membrane prior to and post electroless deposition is shown in Fig. 3.3.

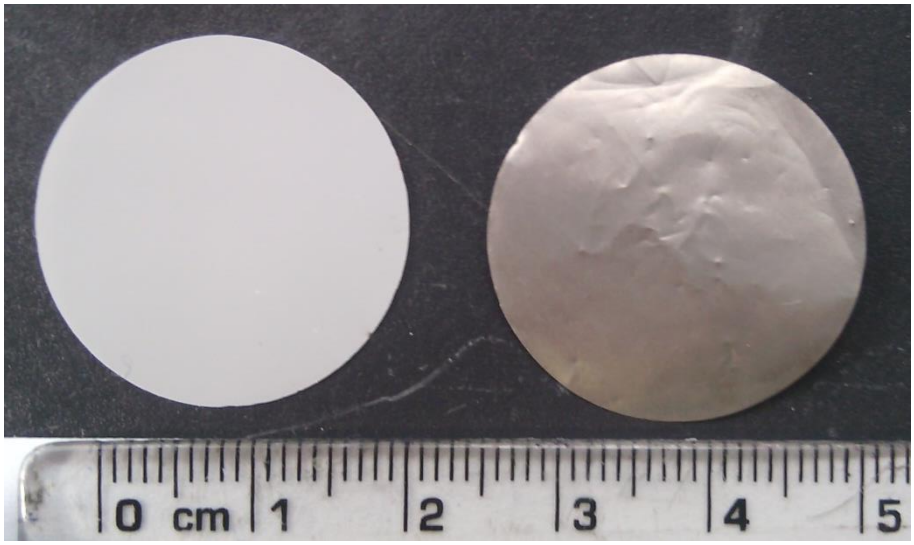

Figure 3.3: Image of polycarbonate membrane that we used for nanotube deposition **(a)** as received and **(b)** after electroless deposition (sample shown is electrolessly deposited Co-B alloy).

To obtain the total mass of the deposited metal, the mass of the membrane must be recorded prior to and post deposition. To measure the mass, a Sartorius microbalance was used. A frequency distribution of 300 polycarbonate membranes that were used in our experiments is shown in Fig. 3.4. Of the 300 polycarbonate membranes measured, the mass of the membranes ranged from 7.95 mg to 8.85 mg. The average mass of a polycarbonate membrane was found to be 8.43 mg with a standard deviation of 0.195 mg. As the mass of each individual membrane is different, the mass needs to be recorded prior to each electroless deposition. From this, accurate measurements of the mass of the electrolessly deposited alloy can be obtained. In certain cases, the membranes were placed in the electroless deposition bath simultaneously. In these cases, the membranes were grouped together by mass to ensure the associated error was minimised to below 0.1 mg.

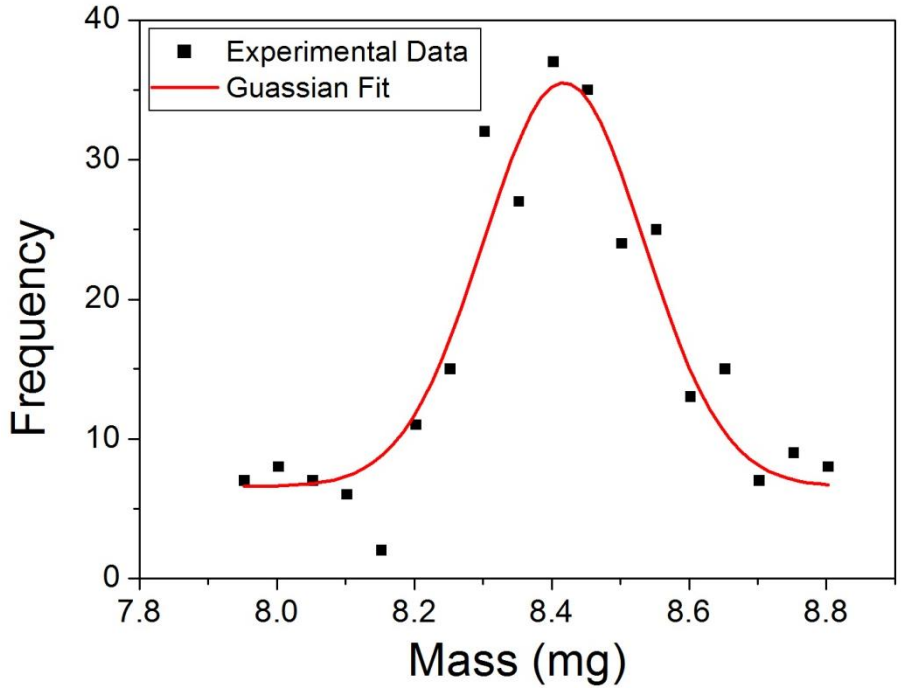

Figure 3.4: Frequency distribution of mass for 300 Whatmann cyclopore track etched polycarbonate membranes 0.025 m in diameter that we used in this study as templates for the electroless deposition of metallic alloy nanotubes.

3.3 Chemicals

All chemicals used in this study were purchased from Sigma-Aldrich. The purity of the chemicals supplied was provided in Sigma-Aldrich documentation, as shown in Table 3.2.

Grade	Definition
% purity	Chemistry products defined by their assay value as a percent purity.
ACS reagent	Meets or exceeds American Chemical Society (ACS) specifications.
FCC	Chemicals that meet the latest testing specifications of the United Food Chemicals Codex (FCC) For R&D and testing purposes only.
ReagentPlus®, Reagent grade	≥95% for general laboratory use.

Table 3.2: Sigma-Aldrich chemical grading system.

We had to carry out a wide range of the experiments to achieve each of our research objectives. To carry out these experiments a variety of chemicals were required. The electroless deposition process used to fabricate the nanostructured alloys required a sensitising agent, an activating agent, an active ion source, a reducing agent and a complexing agent. The catalytic activity of the deposited nanostructures was investigated as a function of hydrogen release from a transition metal borohydride. Each of the chemicals used in these experiments and their associated properties are shown in Table. 3.3.

Chemical	**Formula**	**Grade**	**Molecular Mass g mol^{-1}**	**Function**
Tin (II) Chloride	$SnCl_2$	ACS Reagent 98 %	189.62	Sensitising Agent
Hydrochloric Acid	HCl	35 %	36.46	Sensitising Solution
Palladium (II) Chloride	$PdCl_2$	ACS Reagent 99 %	177.31	Activating Agent
Nickel (II) Sulfate Hexahydrate	$NiSO_4.6H_20$	ACS Reagent 99 %	262.84	Active Ion Source
Cobalt (II) Sulfate Heptahydrate	$CoSO_4.7H_20$	Purity ≥ 95 %	281.10	Active Ion Source
Iron (II) Sulfate Heptahydrate	$FeSO_4.7H_20$	ACS Reagent 99 %	278.01	Active Ion Source
Copper (II) Sulfate Pentahydrate	$CuSO_4.5H_20$	ACS Reagent 98 %	249.68	Active Ion Source
Dimethylamine Borane (DMAB)	$C_2H_{10}BN$	ACS Reagent 97 %	58.92	Reducing Agent
Lactic Acid	$C_3H_6O_3$	FCC 85 %	90.08	Complexing Agent
Ammonium Citrate Dibasic	$C_6H_{14}N_2O_7$	ACS Reagent 98 %	226.19	Complexing Agent
Sodium Hydroxide	NaOH	ACS Reagent 98 %	40.00	Control pH
Potassium Hydroxide	KOH	ACS Reagent > 85 %	56.11	Control pH
Sodium Borohydride	$NaBH_4$	ACS Reagent 98 %	37.83	Hydrogen Storage

Table 3.3: Chemicals used as the source of metal ions for the electroless deposition process.

3.4 Bergstrom Method

Electroless deposition requires the presence of an active catalyst, in order for a chemical reaction to occur between a metal ion and a reducing agent. A relatively widespread method of substrate activation is the deposition of a Pd catalyst via a two-step activation process known as the Bergstrom method, first described by E.A. Bergstrom in 1955 [26]. This method involves the initial sensitisation of the substrate by immersion in a sensitisation bath containing $SnCl_2$ to deposit Sn^{+2} ions on the surface. The substrate is then activated by immersion in an activation bath containing $PdCl_2$. This results in the replacement of the Sn^{+2} ions with Pd^0 which acts as a catalyst for the electroless deposition of metals. The Bergstrom method has become the most common experimental method to activate a substrate with a Pd catalyst and has been used on a range of substrates to deposit thin films [27-29] and nanostructures [5,16,30,31].

3.4.1 Sensitisation

Tin chloride ($SnCl_2$) is used in our experiments as a sensitising agent, keeping in line with the Bergstrom method. The sensitisation solution that we used contained 0.013 M $SnCl_2$ in a 0.24 M HCl solution. A sensitisation solution comprising of $SnCl_2$ and HCl is not stable and a colloid of Sn^{+2} and Sn^{+4} ions forms [32]. These colloids are required as part of the membrane activation process. The colloid ions which form in the sensitisation solution can exist in the form of hydroxyl complexes or chlorine-complexed. The hydroxyl mechanism for an Sn^{+2} ion is shown in Eqn. 3.1.

$$Sn^{+2} + H_2O \rightarrow Sn(OH)^{+1} + H^{+} \qquad (3.1)$$

A single divalent Sn^{+2} ion can hydrolyse more than one molecule of water and usually exists in the form of $Sn_2(OH)_2{}^{+2}$ or $Sn_3(OH)_4{}^{+2}$. Sn^{+2} can also remain in the form of

$SnCl_y^{(2-y)}$, depending on the concentration of the HCl used in the sensitising bath. These forms include $SnCl^{+1}$, $SnCl_2$, $SnCl_3^{-1}$ and $SnCl_4^{-2}$. As the HCl concentration increases, the amount of chlorine-complexed Sn^{+2} increases while the fraction of hydroxyl complex decreases [33].

While in solution or during sample preparation, the Sn^{+2} ions can oxidise into tetravalent Sn^{+4} ions. In this case, the Sn can exist in the hydroxyl form of $Sn(OH)_4$ or in the chlorine-complexed form of $SnCl_6^{-2}$. In a freshly prepared solution of $SnCl_2$ and HCl, it has been shown that approximately 5% of the Sn ions will exist in the form of Sn^{+4} [33]. However, oxidation of Sn^{+2} to Sn^{+4} occurs in solution when exposed to air. Only Sn^{+2} and not the Sn^{+4} ions are involved in the activation reaction with Pd. If a stock solution was prepared it would need to be stored in an oxygen free environment to prevent the oxidation of Sn^{+2} to Sn^{+4}. Therefore, a fresh sensitisation solution was made prior to substrate activation.

The polycarbonate membrane was immersed in the sensitising solution at 40 ºC for 10 minutes to deposit the Sn^{+2} colloids on the membrane walls and membrane surface. During the sensitisation process the membranes sink in the $SnCl_2$ + HCl solution. Therefore, the membranes are placed at an angle with the walls of the beaker to ensure that the solution wets the entire membrane. The total surface coverage is dependent on the sensitisation time with longer times resulting in denser Sn coverage [27].

When a substrate is placed in the sensitisation bath the adsorption of Sn^{+2} ions can be described by Eqn. 3.2 where S^* represents the polycarbonate membrane utilized in this case as the substrate, *aq* represents an aqueous state of the Sn^{+2} ions and *ad* represents an adsorbed state.

$$S^* + Sn^{+2}(aq) \rightarrow S^*.Sn^{+2}(ad) \quad (3.2)$$

The Sn^{+2} ions that are adsorbed onto the membrane surface will also oxidise when exposed to air. Therefore, the sensitised polycarbonate membranes were transferred directly from the sensitisation bath to the activation bath to ensure maximum Sn^{+2} coverage for the reduction of Pd ions during the activation process.

3.4.2 Activation

In this study, a palladium chloride ($PdCl_2$) solution was used to deposit a Pd catalyst on the membrane surface for the electroless deposition process. The activation solution used contained 1.4 x 10^{-3} M $PdCl_2$. The activation process was carried out for 10 minutes at 65 ºC.

Activation of the substrate occurs through the galvanic replacement of the adsorbed Sn^{+2} with Pd^0 via the reaction given in Eqn. 3.3 [34],

$$S^*.Sn^{+2}(ad) + Pd^{+2}(aq) + \rightarrow S^*.Pd^0(ad) + Sn^{+4}(aq) \quad (3.3)$$

When the Pd^{+2} comes in contact with the Sn^{+2} colloid on the polycarbonate membrane a redox reaction occurs, with the oxidation of Sn^{+2} ions and the reduction of Pd^{+2} ions. Pd deposition occurs at active Sn^{+2} sites. This results in a deposit, comprising of small clusters of Pd particles. The Pd particles will act as catalytic sites for the electroless deposition process. Pd coverage is only dependant on the Sn coverage and once all of the available Sn^{+2} sites have reacted with Pd^{+2}, the Pd coverage becomes independent of deposition time and Pd^{+2} concentration. Again, similar to the sensitisation process, the membranes are placed at an angle to the walls of the beaker during the activation process.

There exists a critical Pd coverage below which no electroless deposition will occur. The exact Pd particle density required to catalyse the electroless deposition reaction depends on the metal that is being deposited. For Ni the reported minimum Pd coverage required to catalyse electroless deposition is 5 x 10^{17} m^{-2} [35,36]. The Pd coverage also depends on the hydrophobicity of the substrate. The number of activation sites is large for hydrophilic surfaces but this is reduced for hydrophobic surfaces [37]. As the polycarbonate membrane is considered to be hydrophilic with a large contact angle, the Pd coverage is large and the minimum surface required can easily be achieved.

The exact Pd coverage that is achieved via our sensitisation method is not known as we have not carried out quantitative research via Rutherford backscattering tests to determine the concentration of the Pd deposit. However, similar activation methods have been used previously and have been capable of catalysing the required electroless deposition reaction [5]. After the activation step, the membranes were placed in an oven at 85 ºC and allowed to dry for 15 minutes.

3.5 Electroless Deposition

3.5.1 Introduction

For electroless deposition two chemicals are required. The first is a metal salt which will provide the active metal cations for electroless deposition. The second is a reducing agent which will provide the electrons to reduce the cations. The general equations for the electroless deposition reaction are shown in Eqns. 3.4 and 3.5,

$$Red_{agent} \rightarrow Ox + e^{-} \quad (3.4)$$

$$Metal^{+2} + 2e^{-} \rightarrow Metal^{0} \quad (3.5)$$

In general for a controlled electroless deposition reaction, for which deposition only occurs on the activated substrate, at least two more chemicals are required. The first is a complexing agent which will complex with the free metal ions, limiting the reaction rate and preventing precipitation of the deposition bath. The second is a catalyst at which the redox reaction can occur. In order for continuous deposition to be achieved, the deposited metal must also act as a catalyst. In this case, the reaction is termed an autocatalytic reaction and will continue until the electroless deposition bath is depleted of its components or reaches an unsuitable pH or temperature.

3.5.2 Role of Catalyst

To fully understand the role of the catalyst in the redox reaction, the fundamentals of the electrochemical reaction must be understood. In solution Eqns. 3.4 and 3.5 occur in both the forward and reverse directions. Therefore, the reaction in Eqn. 3.5 should be written correctly as,

$$Metal^{+2} + 2e^{-} \leftrightharpoons Metal^{0} \quad (3.6)$$

The current-overpotential curves for the forward and reverse reactions are shown in Fig. 3.5. The solid curve represents the forward reduction reaction in which the metal ion gains electrons and is reduced to an uncharged metal. The dashed curve represents the reverse oxidation reaction in which the metal atom gains electrons and is oxidised back into ion form. The Butler-Volmer equation gives the current of the oxidation and reduction reactions as a function of the applied potential. These are shown in Eqn. 3.7 and Eqn. 3.8 respectively,

$$i_{ox} = i_0 e^{\frac{\beta F \eta}{RT}} \tag{3.7}$$

$$i_{red} = i_0 e^{-\frac{(1-\beta) F \eta}{RT}} \tag{3.8}$$

where, i_{ox} = oxidation current, i_{red} = reduction current, i_0 = exchange current, β = symmetry factor, F = Faraday constant, η = activation overpotential which is defined as $(E - E_{eq})$, E = electrode potential, E_{eq} = equilibrium potential, R = Ideal gas constant and T = temperature. The net current i is given by $i_{ox} - i_{red}$. The potential at which the net current is zero is termed the reduction potential or equilibrium potential of the metal, U_{Metal}.

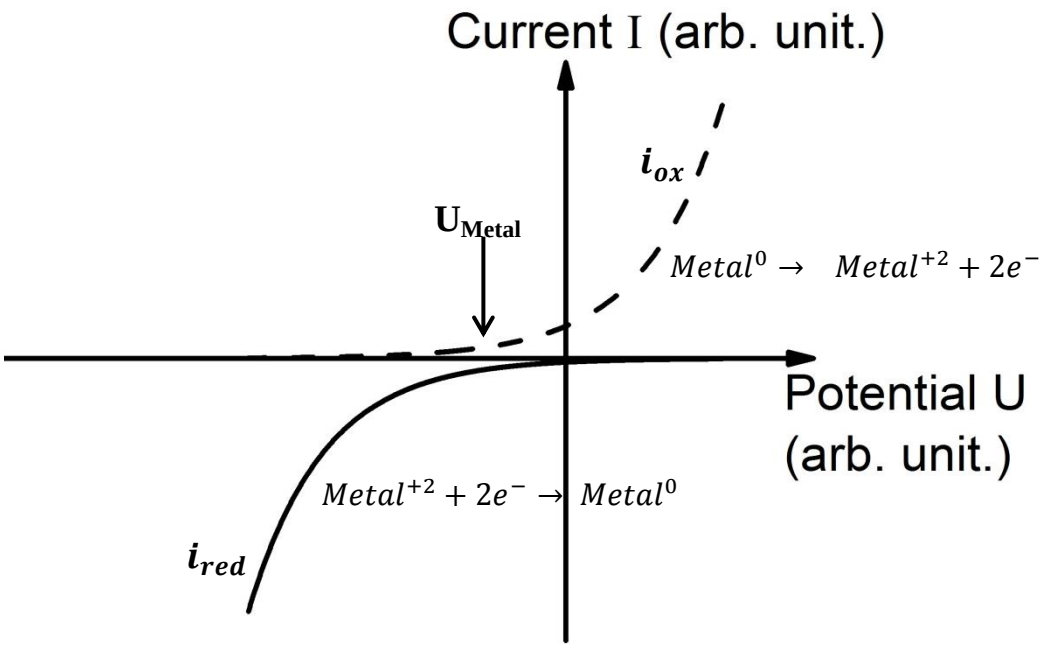

Figure 3.5: The current overpotential curves for the reduction of a metal ion in the forward and reverse directions, given by Eqn. 3.6. Image adapted from [38].

A similar curve can be formed for the oxidation of the reducing agent. The reversible reaction that occurs within solution is given by Eqn. 3.9.

$$Red_{agent} \leftrightharpoons Ox + e^- \tag{3.9}$$

Fig. 3.6 shows the current overpotential curves for the oxidation of the reducing agent (solid blue line) and the reversible reduction of the oxidised product (dashed blue

line). Similarly, for this reaction, a reduction potential is established at the point at which the net current is 0. The reduction of metal ions and the oxidation of the reducing agent are occurring simultaneously within the deposition bath. Provided the equilibrium potential of the reducing agent is lower than the equilibrium potential of the metal, electron transfer from the reducing agent to the metal ion can occur. As shown in Fig. 3.6, a mixed potential, U_{Mix}, between the reduction reaction and the oxidation reaction is formed between the equilibrium potentials of the reducing agent, U_{Red}, and of the metal, U_{Metal}. At U_{Mix} the oxidation current, $I_{Ox,}$ equals the reduction current, I_{Red}. However, without the presence of a catalyst, $I_{Ox,}$ and I_{Red} are very low and the electroless deposition rate is negligible.

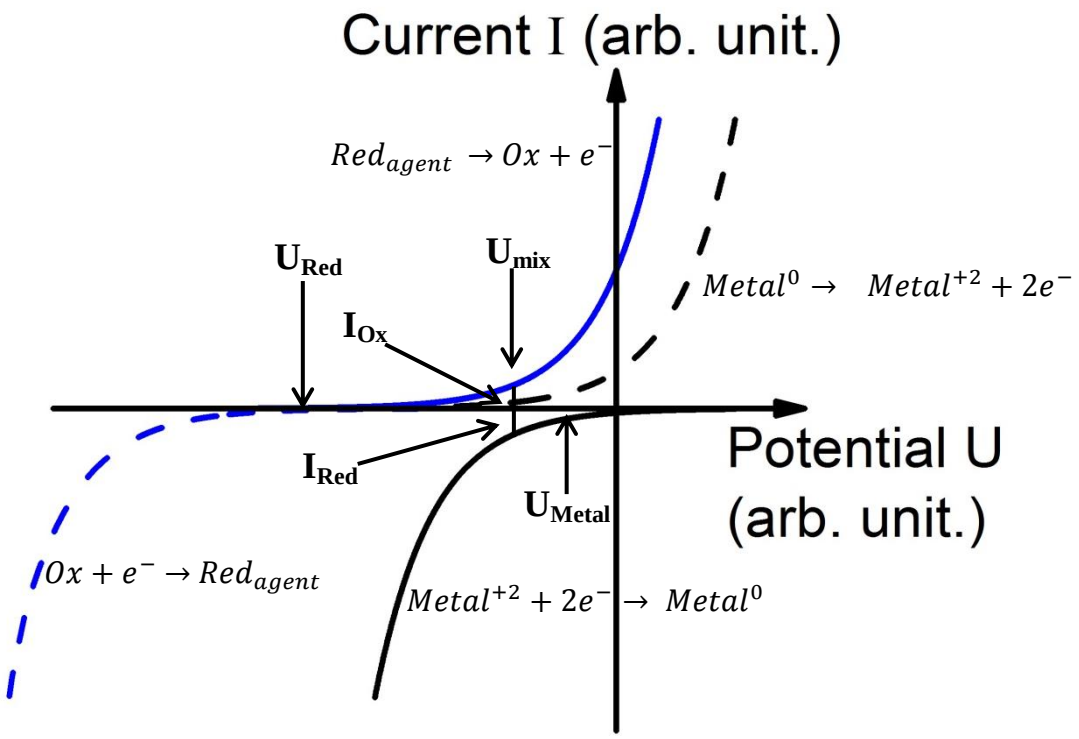

Figure 3.6: The current overpotential curves for the oxidation of the reducing agent and the reduction of the metal ions, resulting in the formation of a mixed potential. Image adapted from [38].

Therefore, a catalyst is required to increase the mixed potential. When a suitable catalyst is present, the kinetics of the reaction are altered. The catalyst acts as an electron bridge for the transfer of electrons to take place between the reducing agent

and the metal. Therefore, in the presence of a catalyst the rate at which the reducing agent is oxidised increases as a function of potential, as shown by the red curve in Fig. 3.7 [39]. The blue curve gives the current-overpotential for the reducing agent without the presence of a catalyst, shown previously in Fig. 3.6. The equilibrium potential of the reducing agent remains the same irrespective of the presence of a catalyst. However, due to an increased oxidation current, I_{Ox}^{Cat}, a new mixed potential, U_{Mix}^{Cat}, for the electroless deposition redox reaction is formed at a more negative value, as shown in Fig. 3.7. At this new mixed potential, the equilibrium current is larger than that obtained previously without a catalyst present. Therefore, the rate at which metal ions are reduced is increased, thus resulting in an increased deposition rate. By using a catalyst, the deposition rate is no longer negligible and a controllable electroless deposition process can be achieved.

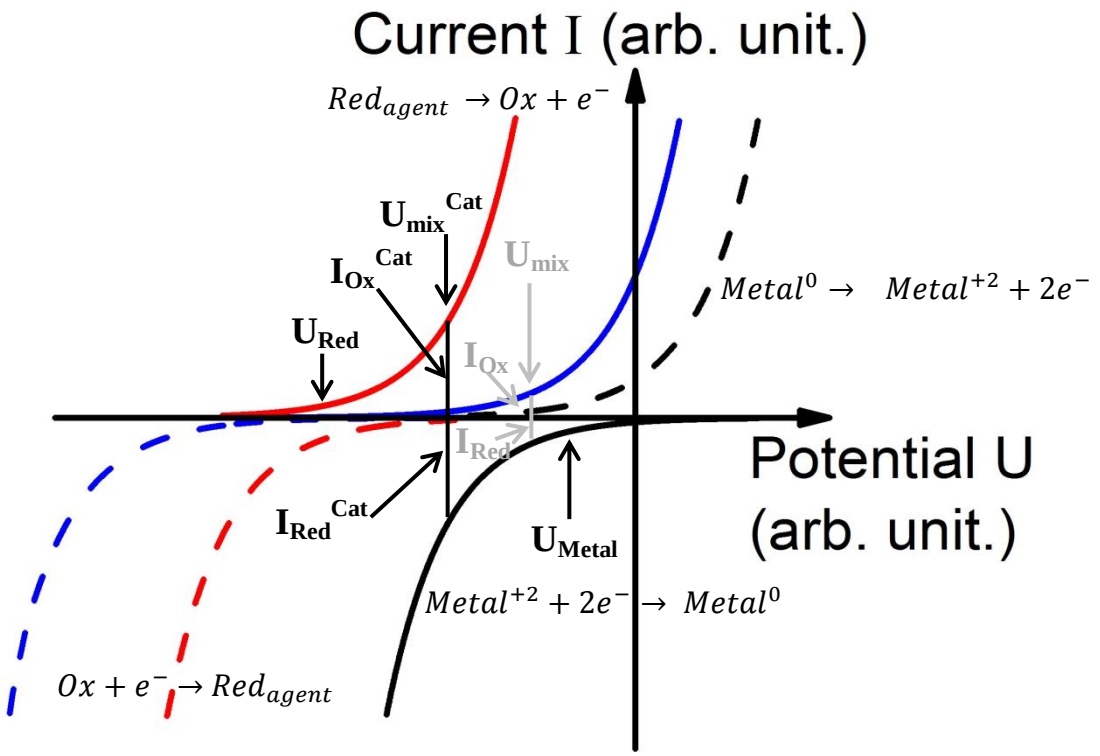

Figure 3.7: The current overpotential curves for the oxidation of the reducing agent and the reduction of the metal ions in the presence of a catalyst. Image adapted from [39].

In this study Pd is used as a catalyst for the electroless deposition of Ni^{+2}, Co^{+2}, Fe^{+2} and Cu^{+2} ions. Other potential catalysts include Pt, Au and Ag. As Ni and Co are also catalysts for the reaction, an autocatalytic sustainable deposition process will occur when Ni or Co are electrolessly deposited.

3.5.3 Active Ion Source

In this study the metals deposited via electroless deposition are Ni, Co, Fe and Cu. The metal salts used are sulphates in which the metals exist as ions with a positive charge of +2. There is an ionic bond between the metal ion and the sulphate ion and the metal is complexed with water molecules to form hydrates, as shown in Fig. 3.8 for $NiSO_4.6H_2O$ [40]. The bonds between the metal ions and the water molecules are dipolar interactions. Ni^{+2} is said to have 6 co-ordination sites at which dipolar bonds with water molecules can be formed, resulting in a hexahydrate compound. Cobalt and iron complex with 7 water molecules forming a heptahydrate while copper can bond with 5 water molecules to form a pentahydrate.

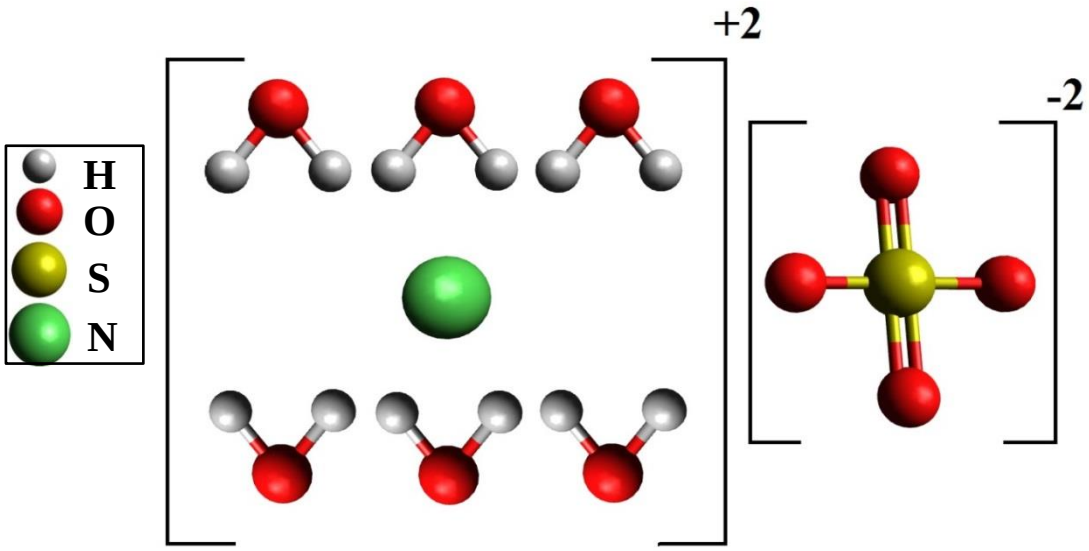

Figure 3.8: Schematic diagram of nickel (II) sulfate hexahydrate. Image adapted from [40].

When dissolved in solution, the colour of the electrolyte is dependent on the metal ions that are present. Fig. 3.9 shows the electroless deposition solutions for each of the metal ions in Table 3.3, with colours of green, pink, yellow and blue observed for Ni, Co, Fe and Cu respectively. According to crystal field theory, this phenomenon is due to the splitting of the energy levels in the *d* orbitals of the metals when complexed with water molecules [41]. Therefore, only transition metals with unfilled d-orbitals give colour to a solution. For example, a copper sulphate solution is blue, as shown in Fig. 3.9(d). For a copper hydrate molecule, the energy gap between the split energy levels of the d orbital corresponds to the wavelength of red light, approximately 1.9 eV. Therefore, when white light is passed through the copper sulphate solution, red light is absorbed and electrons are promoted from the lower d energy level to the higher energy level. The mixture of the remaining wavelengths gives a cyan colour (light blue) [42].

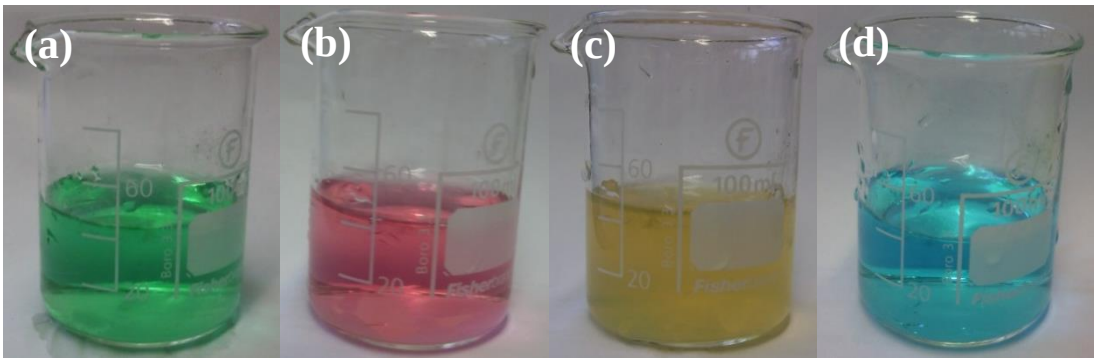

Figure 3.9: Metal ion electrolytes that we have used for electroless deposition containing (a) $NiSO_4$ - Green (b) $CoSO_4$ - Pink (c) $FeSO_4$ - Yellow (d) $CuSO_4$ – Cyan.

3.5.4 Complexing Agent

The role of a complexing agent is to form a complex with the Ni^{+2} ion, reducing the number of free metal ions. This allows for a controllable electroless deposition reaction to take place. In this study two complexing agents are used, diammonium citrate dibasic and lactic acid. A diammonium citrate molecule is shown in Fig. 3.10.

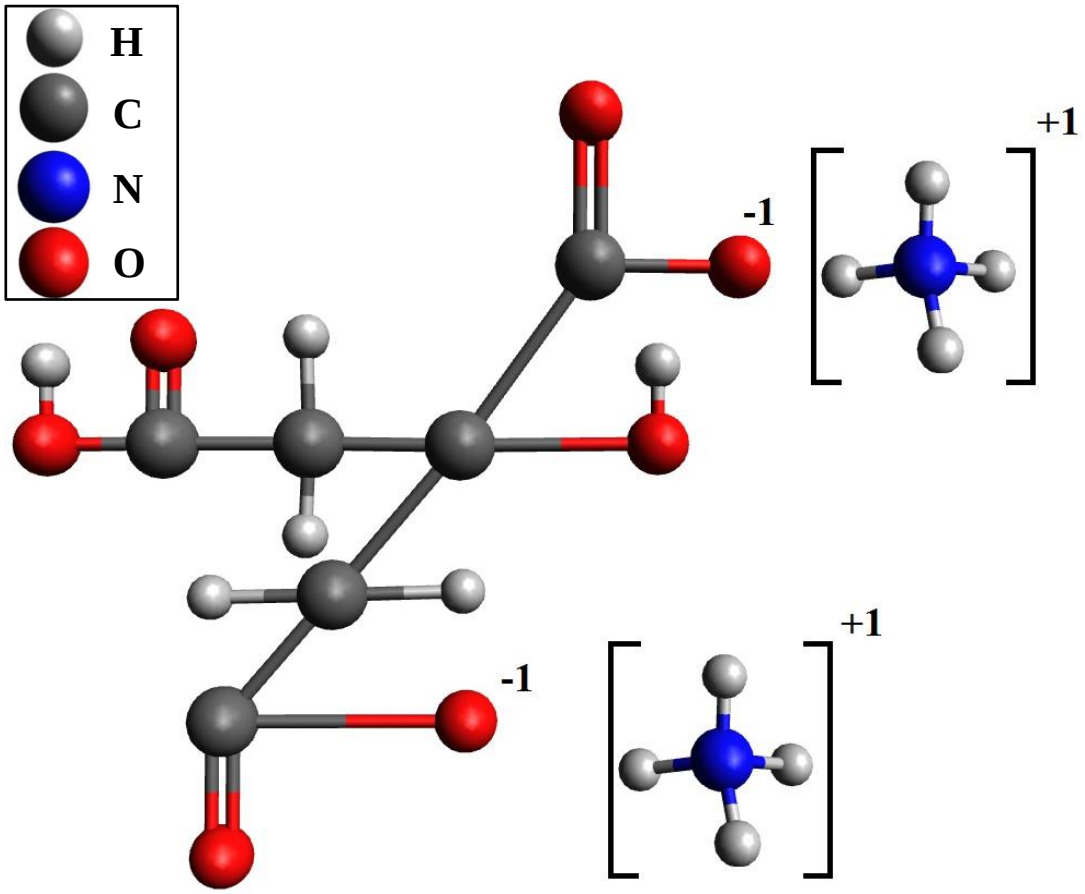

Figure 3.10: Schematic diagram of the structure of a diammonium citrate molecule. Image adapted from [43].

When metal +2 ions in solution come in contact with a citrate molecule, a complex is formed, as shown for Ni in Fig. 3.11. The Ni ion has six co-ordination sites which are occupied by water molecules, forming a hexahydrate complex [44]. However, a citrate molecule can co-ordinate with the metal ion at three of the co-ordination sites to form a complex. In this process, 3 H_2O molecules are displaced from the hexahydrate complex, while 3 of the Ni coordination sites remain bonded to H_2O molecules. Once in complexed form with the citrate molecule, the metal ions are no longer free to react with the reducing agent for electroless deposition to occur [44].

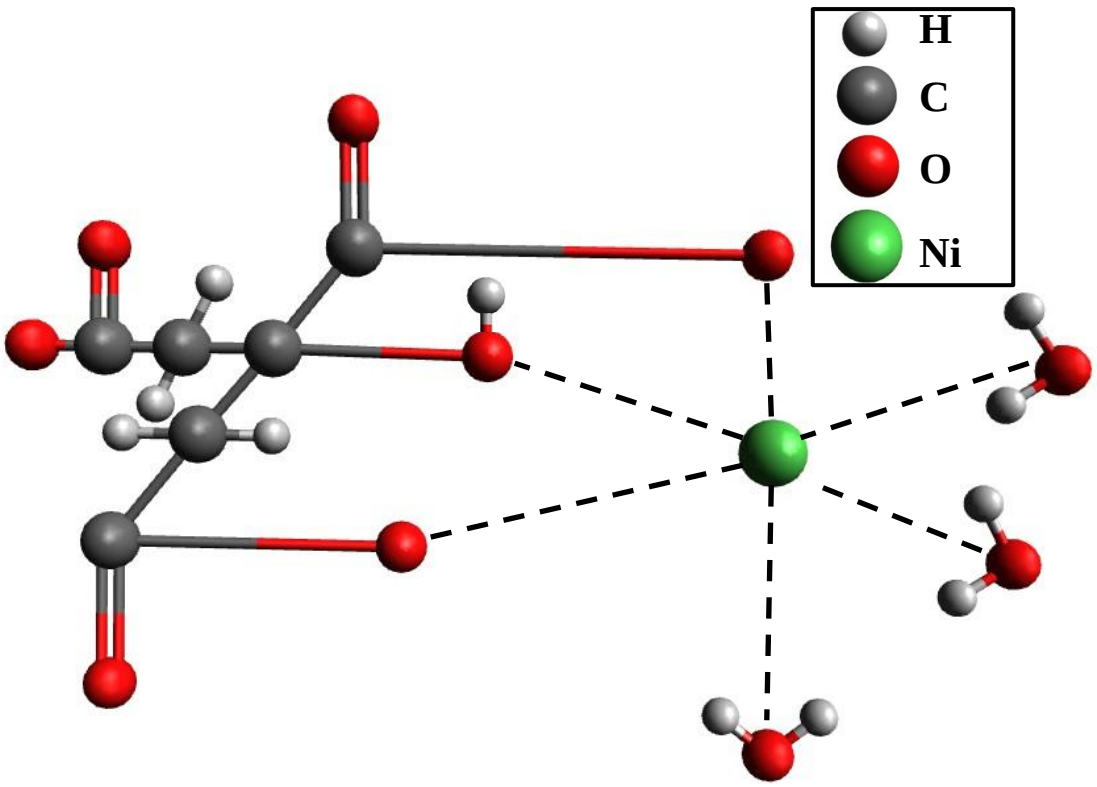

Figure 3.11: Schematic diagram of the complex formed between a Ni ion and a citrate molecule. Image adapted from [44].

A state of dynamic chemical equilibrium is achieved when the forward and reverse chemical reactions occur at the same rate and no changes in concentrations are observed with respect to time. When in solution, the nickel complex dissociates to form an equilibrium amount of free metal ions as shown in Eqn. 3.10, where the citrate ion is represented by the letter *L* and the metal by the letter *M*. By controlling the citrate concentration, the free nickel ion concentration can be regulated.

$$ML \quad \rightleftharpoons \quad M^{+2} + L \tag{3.10}$$

The equilibrium constant of concentration, K_c, gives the ratio of products to reactants for a reaction that is at dynamic equilibrium and for Eqn. 3.10 can be defined as,

$$K_c = \frac{[M^{+2}][L]}{[ML]} \tag{3.11}$$

An increase in citrate concentration on the right hand side of the equation will result in a corresponding decrease of M^{+2} ions on the right hand side and an increased *ML* concentration. Thus by controlling the citrate concentration within solution, the number of free metal ions can be controlled.

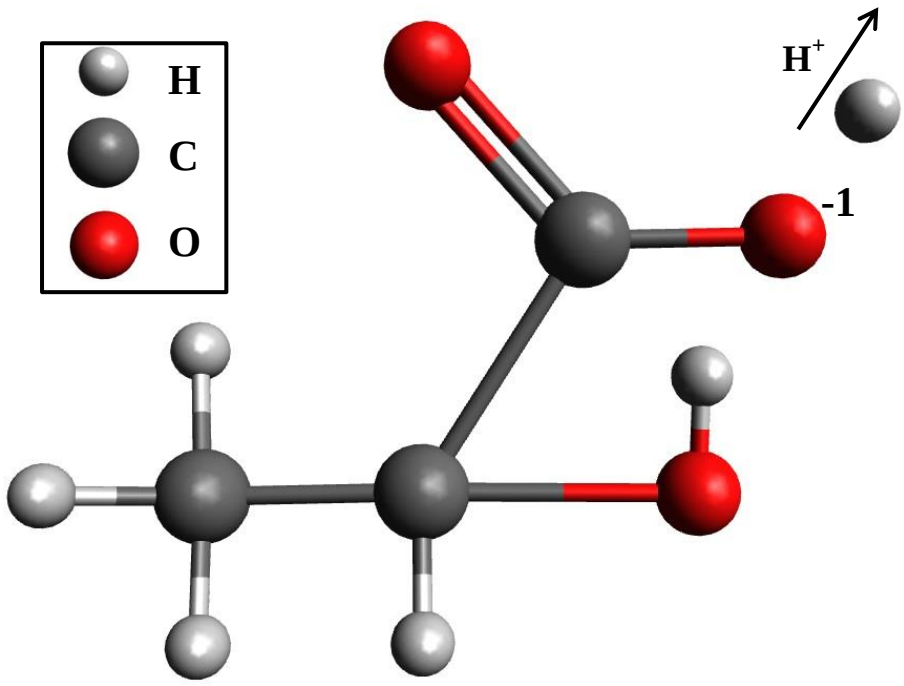

Figure 3.12: Schematic diagram of the structure of a lactic acid molecule that becomes negatively charged in solution with the loss of a H^+ proton. Image adapted from [44].

A similar mechanism is involved for the complexing of the metal ion with the lactic acid molecules. Similar to the citrate molecule, lactic acid has two single bonds with oxygen molecules which can complex with the metal ion. When in solution a lactic molecule loses a proton and one of the oxygen atoms becomes negatively charged as shown in Fig. 3.12.

One lactic acid molecule can complex with two activation sites of the metal ion [44]. Therefore, more than one lactic acid molecule may complex with the metal as shown in Fig. 3.13. The processes associated with the lactic acid complex are similar to those of diammonium citrate and can be treated as the same mechanisms.

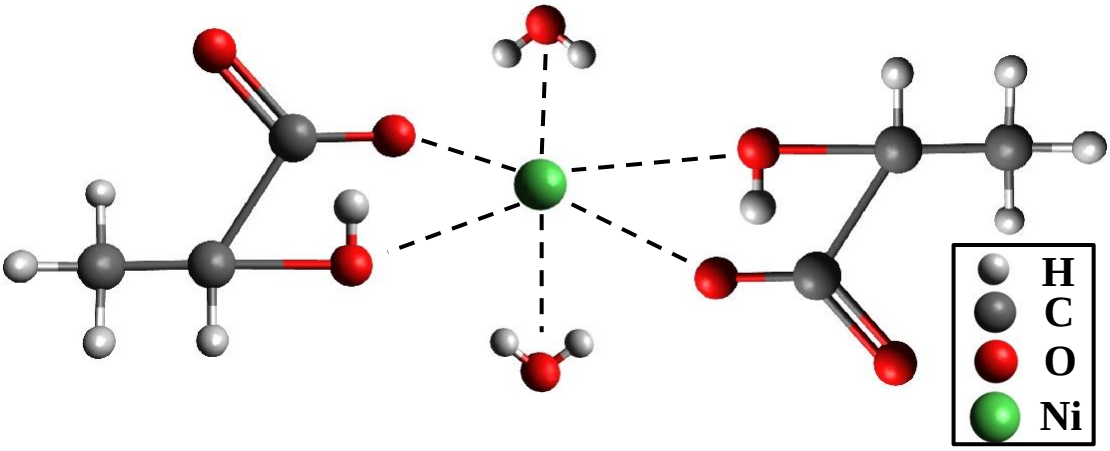

Figure 3.13: Schematic diagram of the complex formed between a Ni ion and two lactic molecules. Image adapted from [44].

The use of complexing agents controls the amount of free metal ions in solution. This controls the deposition reaction and prevents the precipitation of metal salts within the solution. Through the use of diammoniun citrate and lactic acid, we can control the electroless deposition reaction.

3.5.5 Reducing Agent

Reducing agents are required for the electroless deposition process to occur as they act as electron donors in the reaction. Presently, the most common reducing agents for electroless deposition of metals are sodium hypophosphite [16,45] and dimethylamine borane [46,47]. Other reducing agents include sodium borohydride [48,49] and hydrazine [50,51]. With any of these reducing agents, the deposit is not pure metal but contains either phosphorous, boron or nitrogen depending on which reducing agent is used. The four reducing agents shown in Fig. 3.14 have a similar structure with two or more active hydrogen atoms present to facilitate electron transfer. The redox reaction in Eqns. 3.4 and 3.5 occurs due to the dehydrogenation of the reducing agent. As a result, hydrogen gas is released as a by-product in the electroless deposition process. Experimental observations indicate that the reduction reactions are considerably more

complicated than the simple stoichiometric equations and each reducing agent has its own unique reduction process [52].

Dimethylamine borane (DMAB) $(CH_3)_2NHBH_3$	Sodium hypophosphite NaH_2PO_2
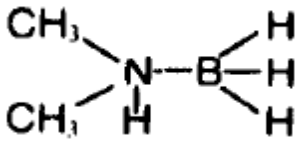	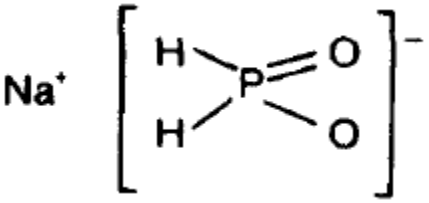
Sodium borohydride $NaBH_4$	Hydrazine N_2H_4
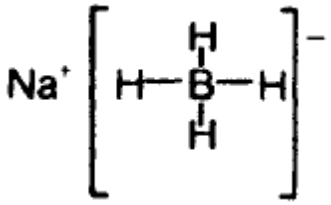	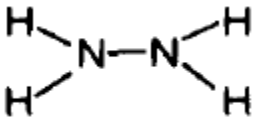

Figure 3.14: Table of reducing agents which can be used in the electroless deposition process [44].

In this study dimethylamine borane (DMAB) is used as the reducing agent. A schematic diagram of a DMAB molecule is shown in Fig. 3.15.

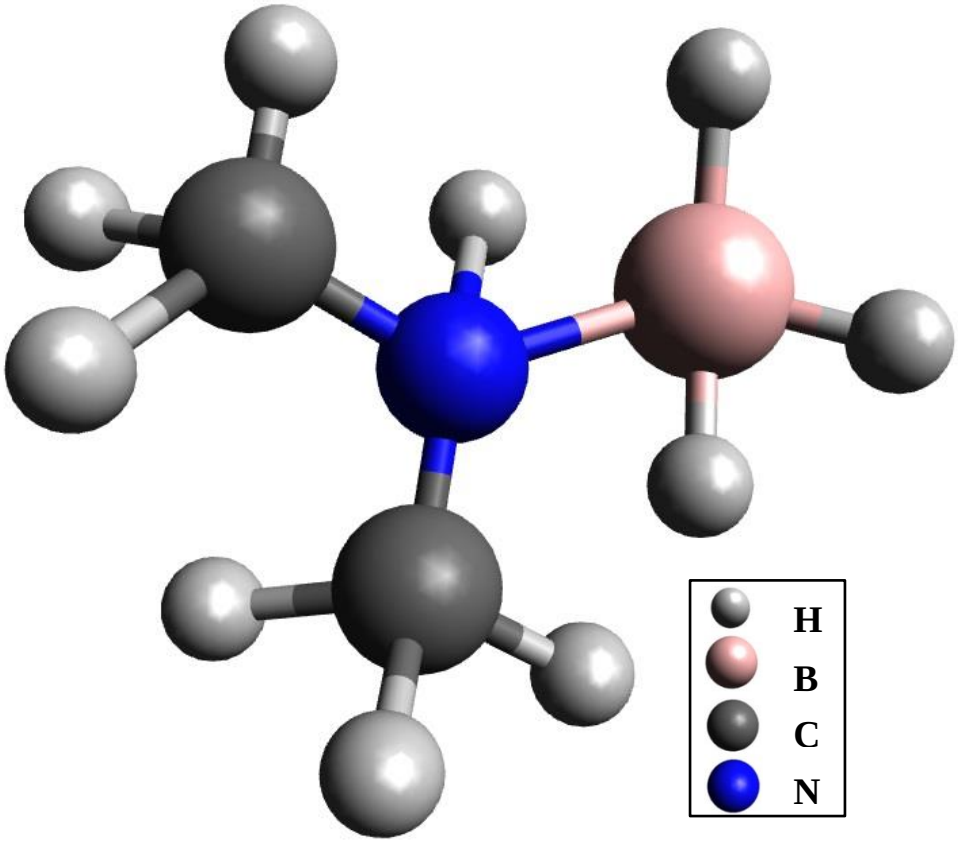

Figure 3.15: Schematic diagram of DMAB which is used to reduce metal ions. Image adapted from [44].

DMAB is a compound which comprises of a coordinate covalent bond between a dimethyamine $(CH_3)_2NH$ molecule and a borane BH_3 molecule. The N atom provides both the electrons for the covalent bond and this is termed a coordinate covalent bond. The N possesses a positive charge while the B atom which acts as the electron acceptor possesses a negative charge. DMAB has three hydrogen atoms bound to the boron atom which can donate electrons for the reduction of the metal +2 ions. The negative charge associated with the BH_3 molecule allows it to provide electrons for the reduction of metal ions. DMAB has an operational pH range of 6-12 [53]. Below a pH of 6, the metal ions are not reduced and no electroless deposition occurs. Above a pH of 12, the deposition bath is unstable and metal precipitates into solution, as will be discussed in section 3.7. The use of DMAB as the reducing agent results in the

co-deposition of boron and the metal, forming a boron alloy. The boron content of the deposit depends on the pH of the electrolyte during electroless deposition.

3.6 Electroless Deposition Chemistry

For DMAB, the electroless deposition process can occur via one of two chemcial reactions [44]. The first is a simple redox reaction between the metal ion and the DMAB molecule at the catalytic site. The second is the formation of a metal hydroxide molecule which is involved in the deposition process. It is likely that both reactions occur simultaneously depending on concentrations of free metal ions and metal hydroxide molecules. In this section, the chemical process will be discussed in terms of a Ni reduction reaction, though a similar process can be applied to any of the metal ions that are deposited in this study.

Theoretically, due to the three active hydrogen atoms in the borane molecule, it should be possible to reduce 3 Ni ions with one DMAB molecule, given by Eqn. 3.12 [44]. Ni can also be co-deposited with B via the process given by Eqn. 3.13 [44]. In these processes, free Ni^{+2} ions are reduced by DMAB resulting in the deposition of Ni and B.

$$3Ni^{+2} + (CH_3)_2NHBH_3 + 3H_2O \longrightarrow 3Ni^0 + (CH_3)_2NH_2^+ + H_3BO_3 + 5H^+ \quad (3.12)$$

$$2[(CH_3)_2NHBH_3] + 4Ni^{+2} + 3H_2O \longrightarrow Ni_2B + 2Ni^0 + 2[(CH_3)_2NH_2^+] + H_3BO_3 + 6H^+ + \frac{1}{2}H_2 \quad (3.13)$$

The electroless deposition process is accelerated in the presence of a catalyst. As shown in Fig. 3.16, the catalyst acts as an electron bridge with the transfer of electrons from the reducing agent to the metal occurring through the catalyst that is present [54].

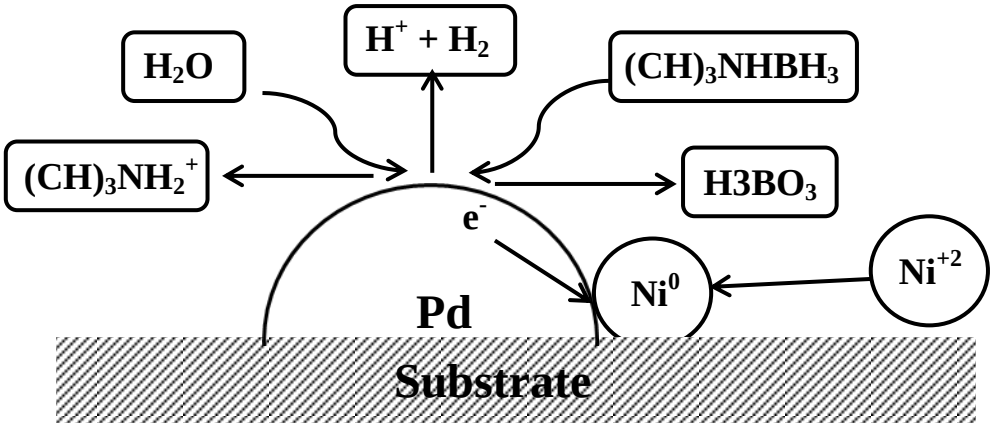

Figure 3.16: Schematic diagram of the electroless deposition process of Ni^{+2} ions with DMAB as the reducing agent. Image adapted from [54].

However, Ni reduction can also occur via a hydrolized nickel mechanism [44]. This process requires two distinct steps before reduction of the metal atom occurs. The first is the formation of nickel hydroxide, $Ni(OH)_2$, which can be created by interaction of free Ni^{+2} ions with OH^- ions in a basic solution. The dissolution of water molecules may also occur and bond with Ni^{+2} ions to form a hydroxide. The second is the adsorption of DMAB onto the deposition surface, followed by cleavage of the N-B bond caused by the Pd catalyst, given by Eqn. 3.14 [55]. The mechanism is illustrated in Fig 3.17 and described by Eqns. 3.14 - 3.20.

N-B bond cleavage at the catalytic site can be described as,

$$2(CH_3)_2NHBH_3 \xrightarrow{\text{Catalyst}} 2(CH_3)_2NH + 2BH_3 \tag{3.14}$$

The electroless deposition process via a hydrolized Ni mechanism is given as,

$$Ni(OH)_2 + BH_3 \longrightarrow Ni^0 + BH(OH)_2 + 2H(ad) \tag{3.15}$$

$$Ni(OH)_2 + BH(OH)_2 \longrightarrow NiOH + B(OH)_3 + H(ad) \tag{3.16}$$

$$NiOH + 2BH_3 \longrightarrow Ni^0 + BH_2(OH) + H(ad) \tag{3.17}$$

$$Ni(OH)_2 + BH_2(OH) \longrightarrow Ni^0 + B(OH)_3 + 2H(ad) \tag{3.18}$$

Summing Eqns. 3.14 - 3.18 gives an overall electroless deposition reaction via a hydrolized Ni mechanism as,

$$2[(CH_3)_2NHBH_3]+3Ni^{+2}+6H_2O \longrightarrow 3Ni^0+2(CH_3)_2NH_2^+ +2B(OH)_3+3H_2 +4H^+ \qquad (3.19)$$

As mentioned previously, the reduction of DMAB also occurs resulting in the co-deposition of B given by Eqn. 3.20.

$$(CH_3)_2NH+BH_3+H_2 +H^+ \longrightarrow (CH_3)_2NH_2^+ +B+\frac{5}{2}H_2 \qquad (3.20)$$

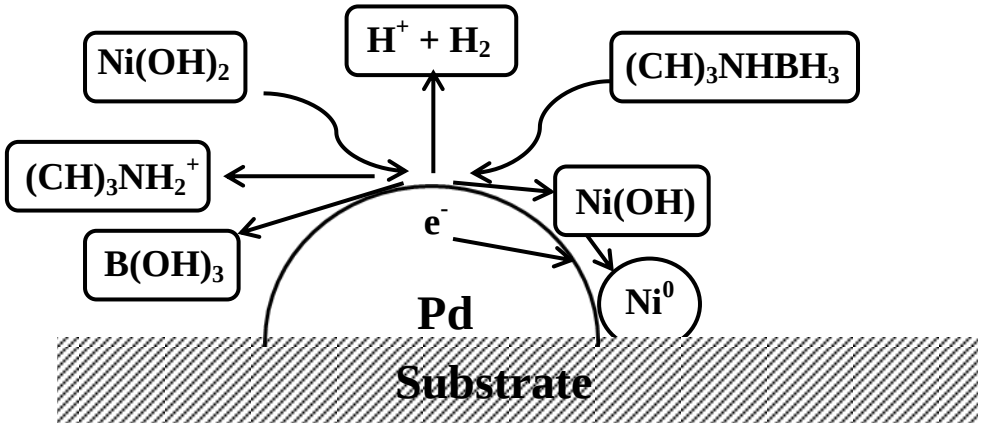

Figure 3.17: Schematic diagram of the hydrolized Ni mechanism for the electroless deposition process of Ni^{+2} ions with DMAB as the reducing agent. Image adapted from [54].

It is known that the pH of the solution affects the rate of reaction and the B content of the deposits [56,57]. Therefore, Eqns. 3.12, 3.13, 3.19 and 3.20 cannot simply be summed to find the relative Ni and B content of the deposit, as the rate of each individual reaction is dependent on the solution pH. Low B contents are reported at large pH values, indicating that the rate at which B is produced in either of the two mechanisms is reduced as the pH of the solution is increased.

3.7 Bath Precipitation

The precipitation of metal salt within the electrolyte can occur spontaneously and results in the precipitation of the electroless deposition bath. Once initial precipitation occurs, the precipitated metal further catalyses the metal ion reduction. This results in

an uncontrollable runaway reaction. During this process, a large amount of hydrogen is given off in a very short space of time and the electrolyte bubbles as if it was boiling, resulting in a large increase in volume. The solution changes to a dark black colour as the metal precipitates out. Once precipitated, the metal sinks to the bottom of the flask and a clear solution remains. As the metal ions cause a colour in solution, this indicates that a majority of the metal ions were reduced in the reaction in a very short space of time. Bath precipitation occurs at high temperatures, high pH values and in baths that have low diammonium citrate concentrations. By controlling each of these parameters, it is possible to ensure that the deposition bath will not decompose.

It has been noted previously that protons disassociate from the water molecules co-ordinated to the Ni complex [44]. Taking the Ni complex shown in Fig 3.11, three complexing sites are co-ordinated with the diammonium citrate molecule and three sites are co-ordinated with H_2O molecules. Only taking into account the water molecules present in the complexed Ni, the precipitation of Ni occurs due to the dissociation of protons within the water molecules and the hydrolysis of Ni to a precipitated Ni salt, as described by Eqn. 3.21. Once the Ni salt has precipitated within solution, it catalysis the reduction of other Ni ions, resulting in a runaway autocatalytic reaction and the spontaneous decomposition of the deposition bath.

$$[Ni(H_2O)_3]^{+2} + 2OH^- \longrightarrow [Ni(H_2O)(OH)_2]^0 + 2H_2O \qquad (3.21)$$

As the pH of the deposition bath increases, the OH^- concentration of the solution increases. This causes a larger number of protons to disassociate from the water molecules co-ordinated to the Ni complex. Due to this process, the deposition bath becomes unstable at high pH values and hydrolysis of the Ni complex occurs, resulting in the precipitation of a metal salt within the electrolyte. At an increased

temperature, the protons can disassociate easier due to the increased energy associated with the deposition bath and so at large temperatures decomposition will occur [58]. The diammonium citrate concentration is also important in preventing the bath decomposition. By increasing the citrate concentration, the number of free Ni^{+2} ions decrease and an increased number of Ni complexes are formed, preventing proton disassociation. By increasing the citrate concentration, deposition baths are stable at higher temperatures and pH values.

3.8 Electroless Deposition Baths

In this research a range of electroless deposition baths were used to achieve our research objectives. The electroless deposition bath determines the composition of the deposit and the deposition rate. In this section, the compositions, temperatures and pH values of all electroless deposition baths that were used throughout this work are given. Placing an activated membrane in any of the deposition baths will result in the catalytic deposition of a metal alloy to form nanostructures.

3.8.1 Research Objective 1 – Ni-B Exemplar

The first research objective of this thesis is to achieve the formation of continuous nanotubes with a uniform wall thickness. To do this, the electroless deposition of Ni was used as an exemplar to investigate the deposition process within a template structure. The electroless deposition bath required as part of this investigation is given in Table. 3.4.

Electrolyte Parameter	Concentration / Value
$NiSO_4.6H_2O$	0.250 M
Lactic Acid	0.143 M
DMAB	0.060 M
Diammonium Citrate	0.074 M – 0.118 M
pH	6 - 12
Temperature	20 ºC - 60 ºC

Table 3.4: Electroless deposition bath used to deposit Ni-B nanotubes to investigate the electroless deposition process within a template structure.

3.8.2 Research Objective 2 – Magnetic Alloys

The second research objective of this thesis is to characterise and control the magentic properties of electrolessly deposited nanotubes with a range of unique compositions. The compositions that we investigated as part of this study were Ni-B, Ni-Fe-B, Co-B and Ni-Cu-B. The electroless deposition baths used to deposit these alloys are given in Tables 3.4 – 3.7. Once deposited, a complete charaterisation of the magnetic nanotubes was carried out.

Electrolyte Parameter	Concentration / Value
$NiSO_4.6H_2O$	0.057 M
$FeSO_4.5H_2O$	0.0125 M - 0.0625 M
DMAB	0.07 M
Lactic Acid	0.143 M
Diammonium Citrate	0.052 M
pH	9
Temperature	25 ºC

Table 3.5: Electroless deposition bath used to deposit Ni-Fe-B nanotubes.

Electrolyte Parameter	Concentration / Value
$CoSO_4.7H_2O$	0.3 M
DMAB	0.07 M
Lactic Acid	0.143 M
Diammonium Citrate	0.052 M
pH	9
Temperature	65 ºC

Table 3.6: Electroless deposition bath used to deposit Co-B nanotubes.

Electrolyte Parameter	Concentration / Value
$NiSO_4.6H_2O$	0.057 M
$CuSO_4.5H_2O$	0.003 M – 0.024 M
DMAB	0.07 M
Lactic Acid	0.143 M
Diammonium Citrate	0.052 M
pH	9
Temperature	65 ºC

Table 3.7: Electroless deposition bath used to deposit Ni-Cu-B nanotubes.

3.8.3 Research Objective 3 – Catalytic Alloys

The third and final research objective of this thesis is to characterise the catalytic properties of the electrolessly deposited nanostructures with the aim of achieving a large hydrogen generation rate from an alkaline $NaBH_4$ solution. Again, a range of compositions are studied including Ni-B and NiCu-B deposited from the baths described in Tables 3.4 and 3.7 respecively. Other compositions investigated include Co-B, NiCo-B and CoNiFe-B, described in Tables 3.8 - 3.10. The as-deposited nanostructures were then used as catalysts for hydrogen generation and their associated activities were investigated.

Electrolyte Parameter	Concentration / Value
$CoSO_4.7H_2O$	0.3 M
DMAB	0.07 M
Lactic Acid	0.143 M
Diammonium Citrate	0.052 M
pH	7-10
Temperature	30 ºC - 65 ºC

Table 3.8: Electroless deposition bath used to deposit Co-B nanotubes.

Electrolyte Parameter	Concentration / Value
$NiSO_4.6H_2O$	0.2 M
$CoSO_4.7H_2O$	0.2 M
DMAB	0.06 M
Lactic Acid	0.143 M
Diammonium Citrate	0.08 M
pH	8
Temperature	60 ºC

Table 3.9: Electroless deposition bath used to deposit Ni-Co-B nanotubes.

Electrolyte Parameter	Concentration / Value
$NiSO_4.6H_2O$	0.019 M
$CoSO_4.7H_2O$	0.016 M
$FeSO_4.7H_2O$	0.013 M
DMAB	0.07 M
Lactic Acid	0.143 M
Diammonium Citrate	0.052 M
pH	9
Temperature	65 ºC

Table 3.10: Electroless deposition bath used to deposit Co-Ni-Fe-B nanotubes.

3.9 Characterisation methods

Characterisation of the electrolessly deposited nanostructures is vital to achieve each of the stated research objectives. To achieve our first research objective, imaging of the deposited nanotube structure is required. To attain these images, scanning electron

microscopy (SEM) and transmission electron microscopy (TEM) are utilized. The second and third research objectives are investigations of the magnetic and catalytic properties of the nanostructures as functions of the structure, composition and crystal structure. To achieve these objectives a compositional and crystal structure characterisation must be carried out. For these, energy dispersive X-ray (EDX), X-Ray photoelectron spectroscopy (XPS) and X-Ray diffraction (XRD) characterisation techniques are used.

3.9.1 Scanning Electron Microscope (SEM)

A Hitachi SU-70 SEM was used to image the deposited nanostructures. The nanotubes were imaged in field free mode at an accelerating voltage of 10 - 30 kV and working distance of 5 - 15 mm depending on the composition and sample type. For high resolution images, a small working distance was used with an upper secondary electron detector. For larger working distances, a mix of lower and upper detectors was used.

The resolution of a microscope is limited by the wavelength of the illumination source. Theoretically, the maximum resolution of a microscope is half the wavelength of the source. In an optical microscope white light, with a wavelength ranging from 500 – 900 nm, is used as the illumination source. Therefore, the maximum theoretical resolution is between 250 nm – 450 nm. When lenses are included in the system due to aberrations and astigmatism, the actual resolution is much lower. As the wavelength of electrons is much smaller than that of light, a higher resolution can be achieved. The wavelength of an electron is given by the de Broglie equation, Eqn. 3.22,

$$\lambda_e = \frac{h}{\sqrt{2m_0E\left(1+\frac{E}{2m_0c^2}\right)}} \tag{3.22}$$

Where λ_e = wavelength of the electron, h = Planks constant, m_0 = rest mass of the electron, c = speed of light and E = energy of the electron.

For an acceleration voltage of 10 – 30 kV, the wavelength of the electrons ranges from 12.25 pm – 7.1 pm. This gives a theoretical maximum resolution of approximately 3.5 pm. In reality however, as the spot size of the electron beam is larger than 1 electron in diameter and other limiting factors such as astigmatism, the maximum achievable resolutions with a scanning electron microscope are in the order of 1 nm.

The main components of an SEM are shown in Fig. 3.18. It consists of a column through which the electron beam is accelerated and focussed and a chamber in which the sample is placed. Both the column and chamber are placed under vacuum to increase the mean free path of the electrons. Electrons are created by a thermionic emission source. The electron current density is given by Richardson's Law, Eqn. 3.23,

$$J = AT^2e^{-\frac{\phi}{kT}} \tag{3.23}$$

where, J = electron beam current density, A = Richardson's constant, T = temperature, ϕ = work function of electron source and k = Boltzmann's constant. Lanthanum hexaboride (LaB_6) is used as the electron source in the Hitachi SU-70 as it has a low work function of 2.3 eV [59].

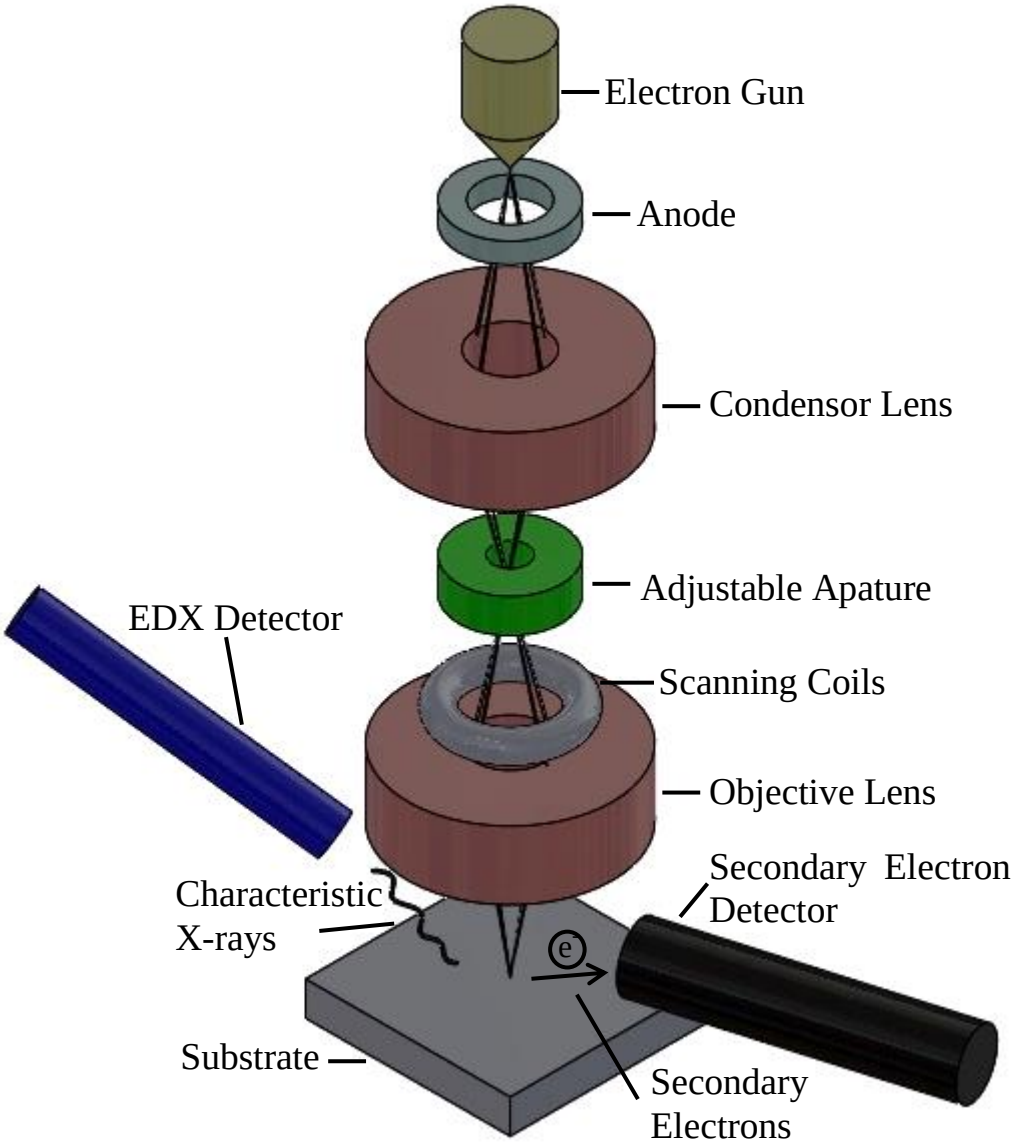

Figure 3.18: Schemtaic diagram of a scanning electron microscope. Image adapted from [60].

The electrons are accelerated through the anode which has a positive charge and travel down through the column. The lenses along the column are electromagnets and cause deflections in the electron beam. The condenser lenses control the size of the beam. A large beam achieves a better signal to noise ratio, but as the beam diameter is larger, there is a lower spatial resolution. A compromise between signal to noise and resolution must be achieved. Apertures are also along the columnar axis. The apertures consist of thin metal plates with a hole in the centre and prevent electrons

that are off the optical axis from passing down through the column of the SEM. The objective lens is used to focus the beam onto the sample while the exact position of the electron beam on the sample surface is controlled by scan coils. These coils allow the beam to be scanned over the sample surface.

When the electron beam hits the sample surface three types of electrons can be recorded coming back off the surface, secondary electrons, back scattered electrons and Auger electrons. Back scattered electrons are reflections of the original incident electrons which have hit an atom nucleus and have been reflected. These electrons can be used to give information of the density and composition of the surface. Auger electrons are produced due to a phenomenon in which energy from an electron which moves to a lower energy level is transferred to a valence electron which is emitted from the sample. However, it is the secondary electrons that are used for SEM imaging. As shown in Fig. 3.19, when a high energy incident electron collides with an electron within the atom, energy is transferred to the electron within the atom and it is emitted from the atom. The emitted electron is known as a secondary electron. Secondary electrons are low energy electrons and the incident electron loses very little energy in the collision. Therefore, a single incident electron can produce thousands of secondary electrons. A positively charged detector within the SEM chamber collects the emitted secondary electrons and different levels of brightness are registered for the image.

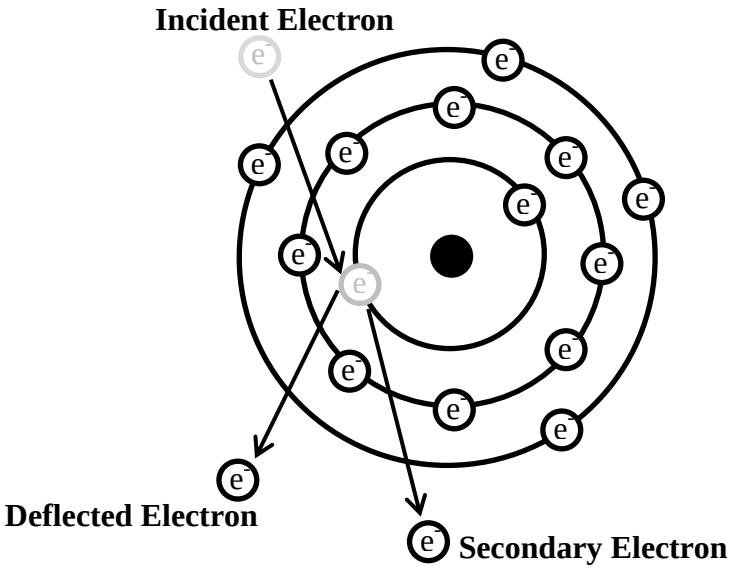

Figure 3.19: Schematic diagram of the process of secondary electron formation. Image adapted from [61].

As the beam scans the sample surface, secondary electrons are emitted from the area on which the beam is focussed. If the beam scans a hole or depression on the surface, very few secondary electrons are released and a dark region is formed on the scanned image [62]. However, if the beam scans across a protruding bump on the surface, a large number of secondary electrons will be recorded, corresponding to a bright spot. A single scan of the surface contains thousands of points and when placed together, a greyscale image of the surface is formed. Utilizing this technique, high resolution images of the deposited nanostructures can be achieved.

3.9.2 Transmission Electron Microscope (TEM)

The structure of the TEM is similar to the SEM. As shown in Fig. 3.20, a beam of electrons are accelerated and focussed down a column in a similar manner to the SEM. However, for TEM imaging the accelerating voltage used is much larger, with an accelerating voltage of 200 kV used to image the nanotubes. This corresponds to an electron wavelength of 2.5 pm. A JOEL 2010 TEM with a camera attached was used in this investigation to image the nanotubes.

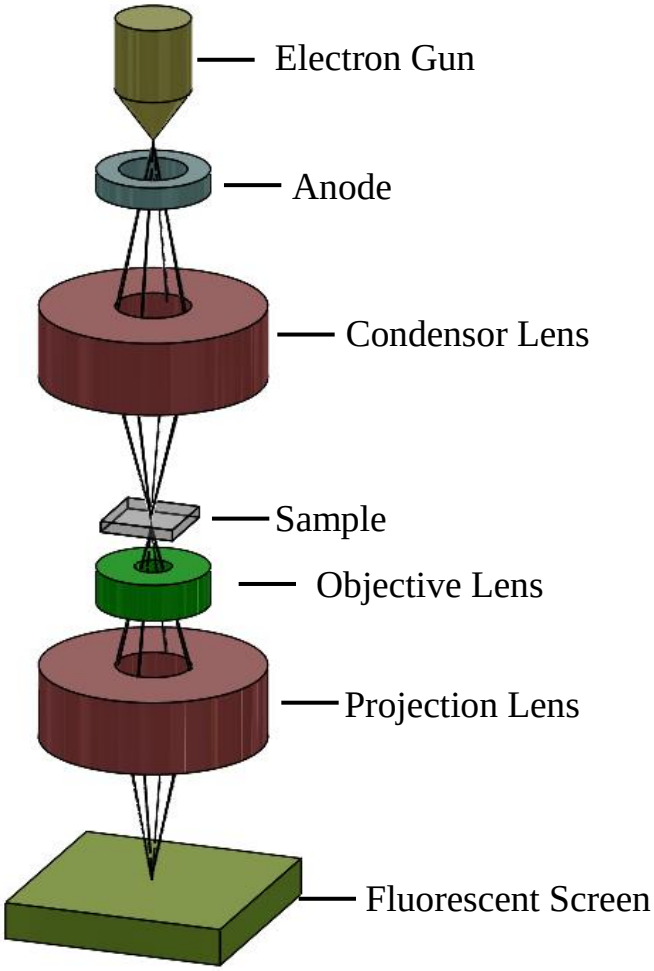

Figure 3.20: Schematic diagram of a transmission electron microscope (TEM). Image adapted from [63].

Unlike an SEM, the sample is placed along the column of the TEM as shown in Fig. 3.20. The high energy electron beam passes through the sample and is focussed onto a fluorescent screen at the bottom of the column with an objective lens. The TEM was used in bright field mode to image the nanotubes. In this mode, a contrast image is formed by occlusion and absorption of the electron beam within the sample. Thick regions or regions with high atomic mass will block electrons from passing through and will appear as dark regions in the image. However, very thin regions or regions comprising of low atomic mass will appear as bright regions on the screen. For TEM imaging, thin samples are required with maximum sizes of hundreds of nanotubes within the imaging range. The nanotubes have an external diameter of 400 nm with

wall thicknesses up to 120 nm. Although, these nanotubes are close to the limiting thickness for TEM imaging, bright field images of the nanotubes can be attained.

3.9.3 Energy Dispersive X-ray (EDX)

An energy dispersive X-ray spectrometer (EDS) is an attachment that can be added to an SEM to do a compositional analysis of a sample. In this study, an Oxford Instruments X-MAX EDS is used. The detector is placed above the sample in the SEM chamber as shown in Fig. 3.18. When the electron beam hits the sample, secondary electrons are knocked out of atomic orbits within the sample, as discussed previously in section 3.9.1. If the electrons are knocked out from the inner shells of the atom, either the K, L or M shells, the atom is unstable and electrons from outer energy levels will drop down to the vacated lower energy level as shown in Fig. 3.21. During this process, the electrons lose energy and the energy is given off in the form of a photon, with an energy corresponding to the wavelength of an X-ray.

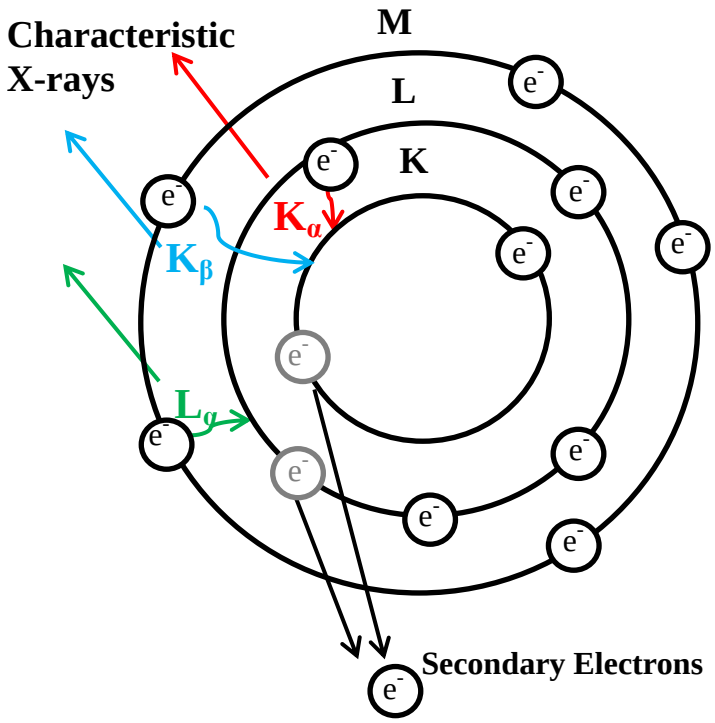

Figure 3.21: Schematic diagram of the production of characteristic X-rays during EDX analysis. Image adapted from [64].

The energy of the X-rays corresponds to the difference in energy of the energy levels. The energy gaps are characteristic of the element and so the X-rays emitted are termed characteristic X-rays. The X-rays with the highest energy correspond to electrons which have been displaced from the inner K shell. These X-rays are the K_α and K_β X-rays as shown in Fig. 3.21. Other characteristic X-rays include the L_α, L_β and M_α. By recording the energy of the emitted X-rays the elements present in the sample can be determined. The energy of the characteristic X-rays as a function of atomic number are determined via Mosley's law shown in Eqn. 3.24,

$$E = K(Z-1)^2 \tag{3.24}$$

where E = energy of X-ray in keV, K = constant for characteristic X-ray lines and Z = atomic number of the atom. A plot of X-ray energy as a function of atomic number is shown for a range of characteristic X-rays in Fig. 3.22.

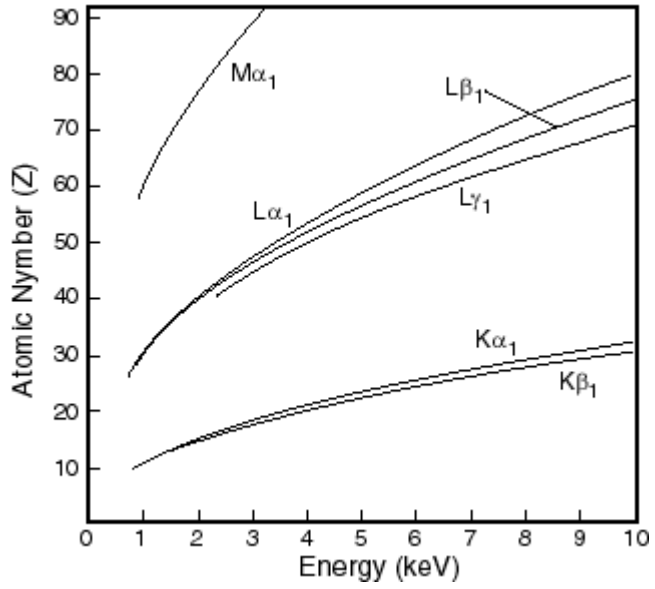

Figure 3.22: Energy of characteristic K, L and M X-rays as a function of atomic number following Moseley's law [64].

The penetration depth of the incident electron beam of an SEM is shown in Fig. 3.23. The exact penetration depth depends on the accelerating voltage the material of the sample though for 20 kV the average penetration depth is approximately 2 µm.

Secondary electrons are only emitted from the top 10 nm of the surface due to their low energy. Back scattered electrons can be emitted from depths of up to 500 nm. Characteristic X-rays are emitted at a depth of up to 2 µm. As the electrolessly deposited alloys in this study are less than 1 µm in thickness, during EDX analysis, X-rays emitted from the polycarbonate template will also be observed.

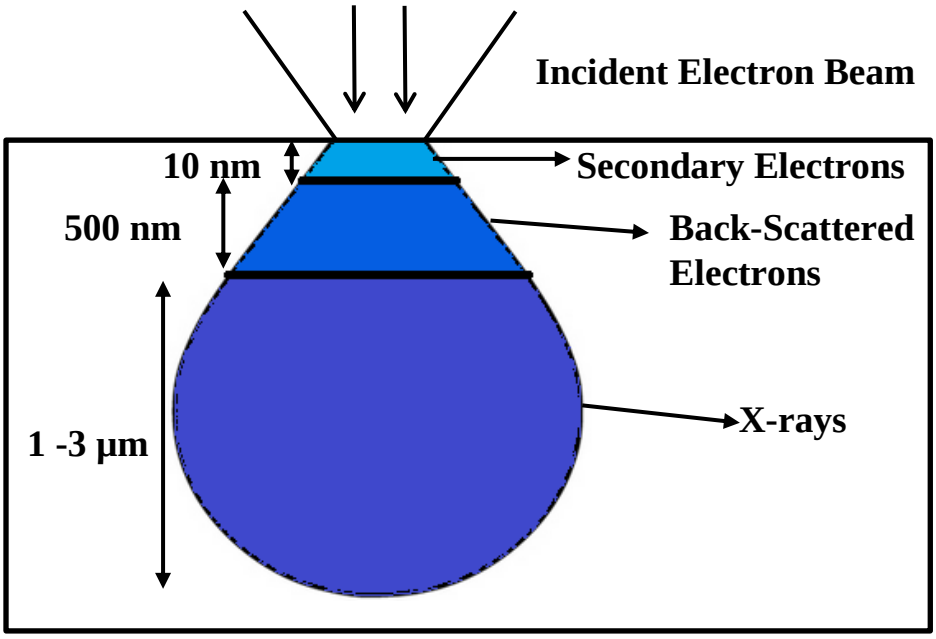

Figure 3.23: Approximate penetration depth of electrons accelerated in an SEM. Image adapted from [60].

Using INCA software an elemental composition of the sample can be determined. An X-ray energy spectrum is recorded from 0 – 20 keV. Each peak corresponds to a characteristic X-ray. During this process the area beneath the individual peaks of each element is recorded. From this an elemental composition of the sample is calculated. Using the scanning coils during EDS analysis, a composition map of the sample can be obtained. The characteristic X-rays emitted are recorded as the electron beam sweeps across the sample surface to form a compositional map of the sample.

3.9.4 X-Ray Photoelectron Spectroscopy (XPS)

XPS relies on the photoelectric effect in which the energy of a photon is transferred to an electron. If the energy of the photon is greater than the binding energy of the electron to the atom, the electron can break free from the atom. The kinetic energy of the released electron is given by the photoelectric effect in Eqn. 3.25,

$$E_K = h\upsilon - E_B \tag{3.25}$$

where E_k = Kinetic energy of the electron, E_B = Binding energy of the electron, h = Planks constant and ν = frequency of the X-ray photon.

In this study, a Kratos Axis 165 X-ray photon spectrometer is used to analyse the composition of the electrolessly deposited nanostructures. The X-ray source is an Al anode which gives characteristic K_α X-rays with a wavelength equal to 0.834 nm. The kinetic energy of the photoelectrons is determined using a concentric hemispherical electron energy analyser, as shown in Fig. 3.24. A charge is placed on both the outer an inner hemispherical plates. Therefore, the photoelectrons are subject to an applied potential perpendicular to the direction in which they are travelling. This causes a deflection in the direction in which the electrons are travelling. Electrons which have a large kinetic energy will be harder to deflect than electrons with a low kinetic energy. Therefore, by controlling the applied potential, electrons of a specific kinetic energy can be focussed onto the detector. An XPS spectrum can be achieved by sweeping the applied potential and counting the number of photoelectrons recorded for each specific value of kinetic energy. Analytic software is used to determine the areas under the peaks and relative intensities. From these values, the composition of the deposited nanostructure can be obtained.

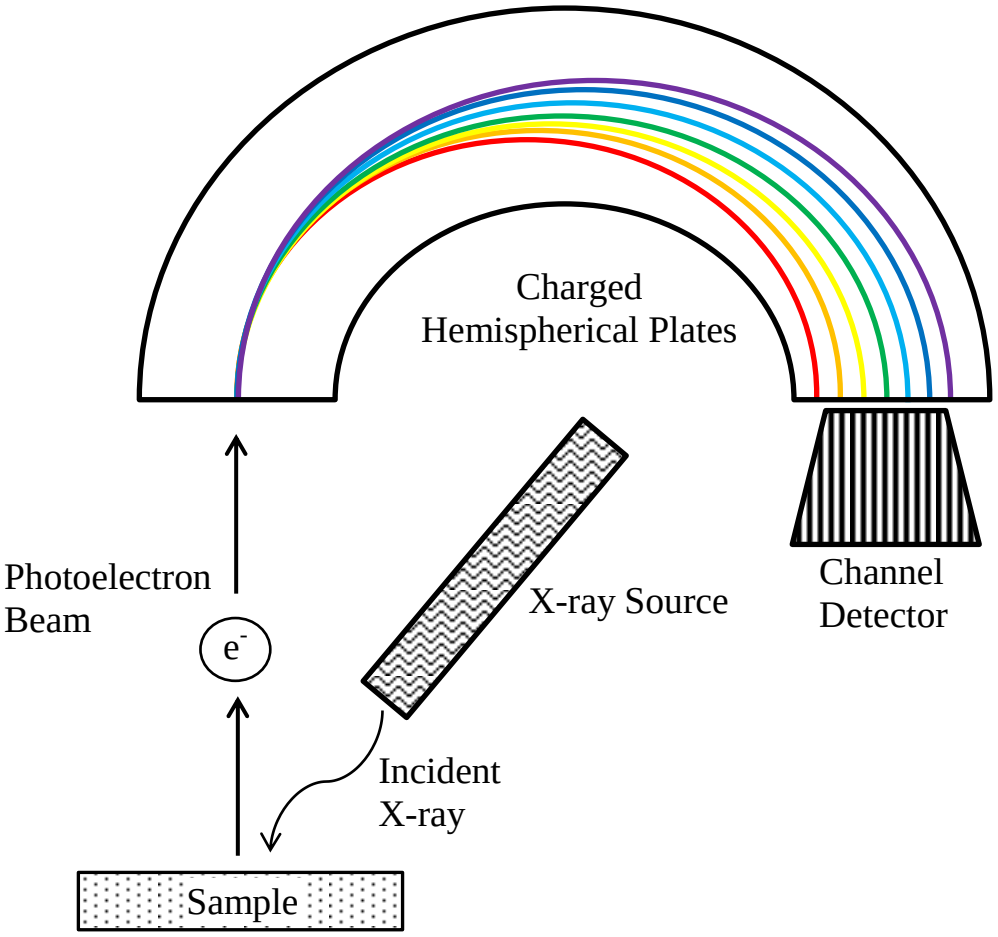

Figure 3.24: Schematic diagram of an X-ray photoelectron spectrometer. Image adapted from [65].

The binding energy, E_B, of the electrons is characteristic to each element. By determining the kinetic energies of the photoelectrons, the binding energies of the photoelectrons can be measured, thus giving the elements present in the sample. However, unlike EDX, the bonding structure of the material may also be determined. The binding energy of an inner electron, such as the 1s or 2s electrons, is determined by the electrostatic interactions between the electron and both the atomic nucleus and outer electrons. When an atomic bond forms within a compound there is a slight change in the electronic configuration of the outer electrons. This causes a minor change in the interactions between the inner and outer electrons, thus causing a small shift in the binding energy of the inner electrons. This is known as chemical shift. For

example, B which is deposited as part of the electroless process has a binding energy for the 1s electron ranging from 188 eV for boron and boride to 192 eV for B_2O_3.

XPS is a surface specific technique. Although X-rays can penetrate deep into the sample and release photoelectrons, the electrons must be released from the sample without losing any energy. The probability of an electron getting scattered as it travels through the material is governed by the Beer-Lambert law given in Eqn. 3.26,

$$I_S = I_0 e^{-\frac{d}{\lambda_i}} \tag{3.26}$$

where I_s = Intensity of electrons at sample surface I_0 = Original initensity of electrons at a depth of d within the sample and λ_i = mean free path of the electron. The sampling depth is defined as the depth from which 95 % of photoelectrons are scattered by the time they reach the surface. This corresponds to a depth of $d = 3\lambda_i$. The average mean free path of an electron within a metal is 1 - 3.5 nm and so the maximum sampling depth of XPS analysis is approximately 10 nm.

3.9.5 X-Ray Diffraction (XRD)

XRD is a technique which is used to investigate the crystal structure of the nanotubes. When an X-ray beam is incident on a crystal, constructive interference between diffracted X-rays can occur. This phenomenon is described by Braggs law, shown in Eqn. 3.25,

$$n\lambda = 2dsin\theta \tag{3.27}$$

where n = integral number representing the order of diffraction peak, λ = wavelength of the X-rays, d = interatomic spacing of crystal structure and θ = diffraction angle. When the X-ray photons collide with electrons of the atoms within the crystal structure, they will be diffracted as shown in Fig. 3.25. If the collision is elastic,

Thompson scattering occurs and the wavelengths of the X-rays remain constant. Depending on the angle of incidence and the wavelength of the X-rays, constructive interference can occur to produce a diffraction pattern. From the diffraction pattern recorded, the d-spacing and crystal structure of the sample can be determined using High Score Plus analytic software.

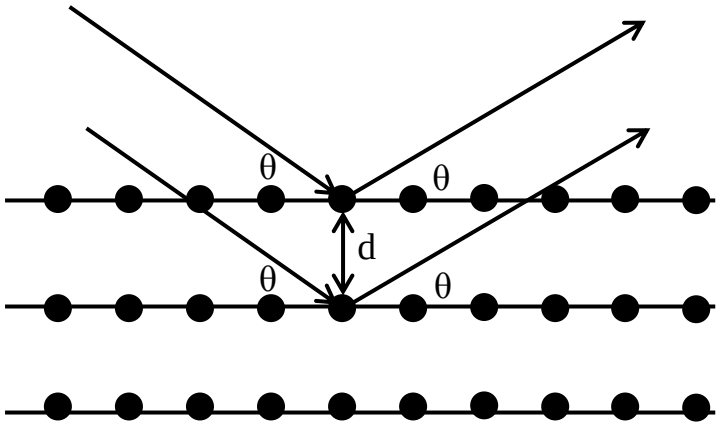

Figure 3.25: Schematic diagram of Bragg diffraction of X-rays occurring within a crystal structure. Image adapted from [63].

We used a Pan Analytic X-Pert MPD Pro XRD instrument to characterise the crystal structure of the electrolessly deposited alloys. The X-rays are produced from a Cu target which has a K_α energy of 8048 eV corresponding to a wavelength of 1.54 Å. The samples are placed on a glass slide for XRD analysis and are analysed using a continuous absolute scan from 20 º to 90 º with a step size of 0.0167 º and a scan speed of 0.071 º s^{-1}.

3.10 Preparation for Characterisation

The as-deposited nanostructures were characterised via a variety of methods. The nanostructure was imaged using SEM and TEM. Compositional data of the nanostructures was acquired using EDX and XPS. The crystal structure of the nanotubes was investigated using XRD while the magnetic properties were measured

with a vibrating sample magnetometer (VSM). Prior to some of these characterisation techniques, the deposited nanostructures had to be prepared in a specified manner.

For SEM imaging of the nanotubes, depending on the exact part of the nanostructure that was to be imaged, different preparation techniques were required. To image the surface of the polycarbonate membrane and investigate the nanotube pore diameter of the surface of the membrane, no preparation was needed. The as-deposited samples were attached to the SEM stub using carbon tape and the polycarbonate surface could be imaged.

To image the nanotubes arrays, the nanotubes had to be removed from the polycarbonate membrane. Polycarbonate dissolves in an alkaline solution. Prior to SEM imaging, the samples were placed in a 7 M KOH solution for up to 48 hours to dissolve the polycarbonate membrane. The nanotube array is held together by a thin metal film that has deposited on the membrane surface. A pipette was used to remove the nanotubes from the KOH solution and they were then placed in a de-ionised water bath to rinse off concentrate KOH. The nanotubes were dropped onto carbon tape on an SEM stub and allowed to dry prior to SEM imaging. As there is a film attached to both sides of the nanotube array, only damaged nanostructures with one of the films removed could be imaged. This damage occurred naturally through agitation during transfer from the KOH solution to the SEM stub.

A method of imaging the as-deposited nanostructure with very little damage is to take a cross sectional image of the nanotube array within the polycarbonate membrane. However, the polycarbonate membrane cannot be cut with a blade as the membrane deforms causing a large amount of damage to the nanotubes. To overcome this challenge, the sample was covered in a film of water and placed in liquid nitrogen.

The frozen sample was then cracked in half, giving a clean cut which allowed for cross sectional SEM imaging. The sample was mounted perpendicular to the SEM stub with silver paint.

For TEM imaging of individual nanotubes, the nanotubes must be removed from both the polycarbonate template and the metal film. Initially, the samples were sanded with fine sand paper to remove the metal film. The nanotubes were then placed in a very low volume of 7 M KOH for up to 48 hours to dissolve the polycarbonate membrane. If KOH solution is dropped onto the copper TEM grids, the copper oxidises preventing TEM imaging. Therefore, the nanotubes must be rinsed with de-ionised water prior to placing on the TEM grids. This leads to a very low concentration of nanotubes spread throughout the grid structure making imaging difficult. However, as the nanotubes are magnetic, a strong magnet was used to attract the nanotubes to the bottom of the solution. The tubes were then rinsed gently with de-ionised water without a reduction in concentration of nanotubes. The nanotubes were then dropped onto a TEM grid using a micropipette. The nanotubes tended to clump along the edges of the grid and a micro needle was used to manoeuvre them into the centre of the grids so that TEM imaging could be accomplished. Cian McKeown, a fellow PhD student, carried out the TEM imaging.

For compositional analysis, EDX and XPS, no further preparation of the deposited structures was needed. EDX analysis was carried out on the same samples that were used for SEM imaging and so EDX analysis of the membrane surface or nanotube structure could be carried out. XPS analysis was done on the nanostructures without the removal of the template structure, as the nanostructures are too fragile when the polycarbonate membrane is dissolved. XPS analysis was carried out by Fathima Laffir, a researcher in the Materials and Surface Science Institute.

XRD analysis was carried out on the as-deposited samples within the template structure. Samples were placed on a glass slide during analysis. Some of the samples were also annealed in a furnace up to 500 °C for 1 hour in a sealed N_2 environment to prevent oxidation. The nanotubes were left in the polycarbonate template structure during the annealing process. However, as the melting point of the polycarbonate membrane is 240 ºC, the membrane melts away from the electrolessly deposited nanostructure. Post annealing, the nanostructures were fragile and so were placed onto a glass slide after annealing and not handled again prior to XRD analysis.

3.11 Magnetic Properties

Our second research objective is to investigate the magnetic properties of the electrolessly deposited nanotubes. The magnetic properties of the nanostructures are recorded with a vibrating sample magnetometer (VSM). The nanotubes have many potential applications in future technologies such as high density data storage, power conversion and nanoscale electronic components. The aim of the research is to control the composition, shape, size and crystal structure of the nanotubes so that their magnetic properties may be altered to suit specific applications.

3.11.1 Vibrating Sample Magnetometer (VSM)

The magnetic properties of the electrolessly deposited nanotubes are measured using a Lake Shore VSM 7410. A hysteresis loop of magnetisation, *M*, as a function of applied magnetic field, *H*, is obtained. The VSM can apply magnetic fields up to 2.0 T (20,000 G) and is capable of measuring moments as low as 0.1×10^{-6} emu. However, in the magnetisation range of 1×10^{-4} emu and below, the measurements we recorded were noisy and the M-H curves required averaging. The 7410 model allows

for the controlled rotation of the sample within the magnetic field. With this feature, it is possible to automatically measure the magnetic properties of the nanotubes both parallel and perpendicular to the nanotube axis. All magnetic measurements were carried out at room temperature. By determining the mass of the magnetic sample, the specific magnetisation, magnetisation per unit mass can be calculated. As discussed previously in section 3.2.4, the mass of the polycarbonate membranes are obtained pre and post deposition. Assuming uniform deposition throughout the whole membrane, the ratio of alloy to membrane can be determined. When a sample is cut for a VSM measurement, the mass of the sample is measured and from the original ratio of alloy mass to membrane mass, the mass of magnetic material within the VSM sample can be determined. From this the specific magnetisation was determined.

Magnetic measurements taken on the VSM were carried out with the nanotubes in situ within the polycarbonate membrane. Polycarbonate has no magnetic properties and so does not interfere with the magnetic measurement. The presence of the membrane structure ensured that the nanotube arrays remained parallel and prevented damage to the nanotube structure. The surface film could be removed by sanding with fine sand paper, similar to that done for TEM preparation, so that only the magnetic properties of the nanotubes were measured. The magnetic measurements of samples post annealing were also taken. Post annealing, the polycarbonate membrane had evaporated and the nanostructure was very fragile. The structure could be loaded onto the VSM sample holder though some damage may be caused. However, as the polycarbonate membrane had been removed, the orientation of the nanotubes was not guaranteed.

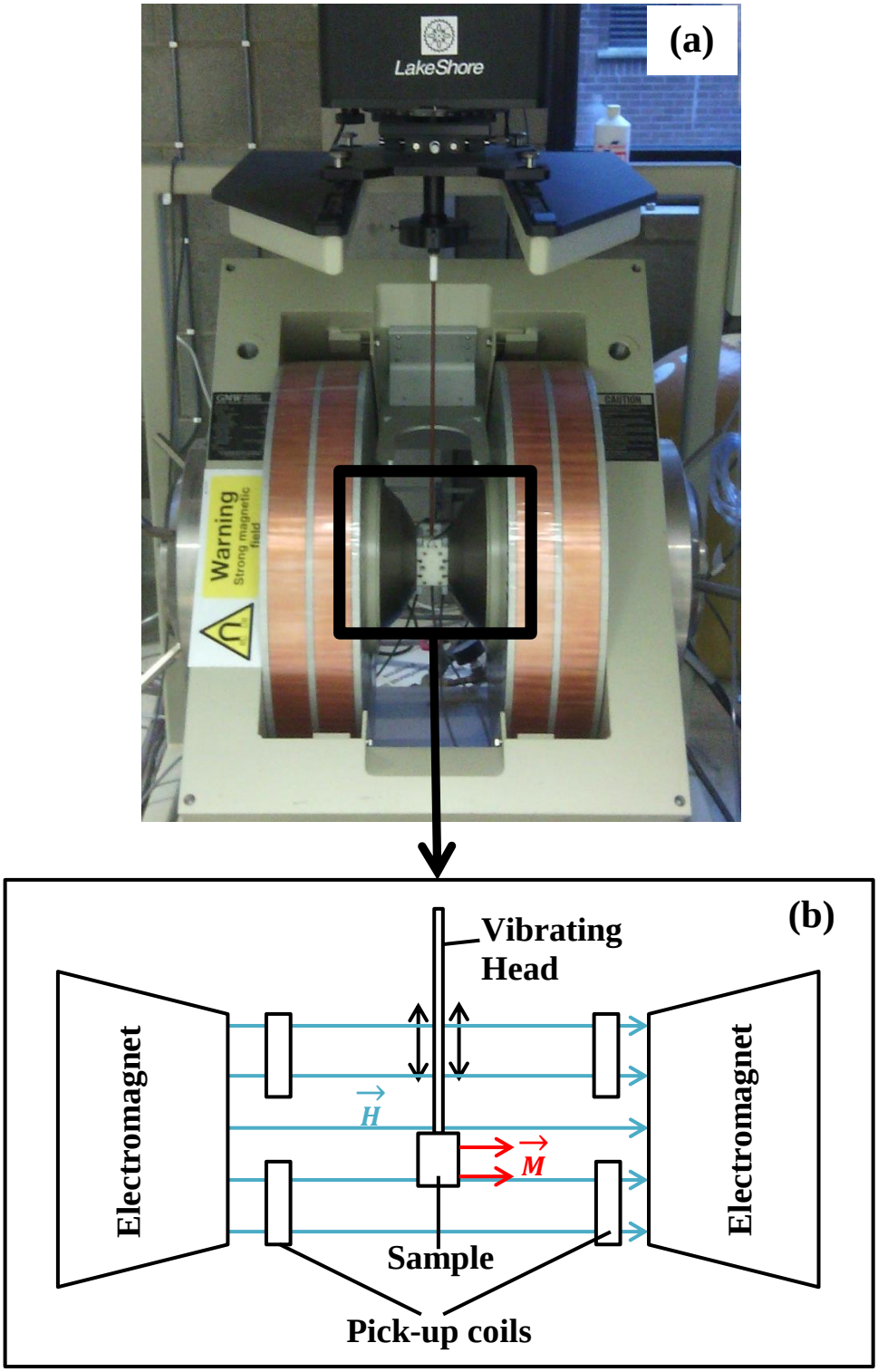

Figure 3.26: (a) Image of the Lakeshore VSM that we used to measure the magnetic properties of the electrolessly deposited nanostructures and **(b)** a schematic diagram of the magnetic fields within the VSM. Image (b) adapted from [66].

A schematic diagram of a VSM is shown in Fig. 3.26. During the measurement, a sample is vibrated in an applied magnetic field, *H*. A magnetic moment, *M*, is produced within the sample due to the aligning of magnetic domains with the applied

magnetic field. The total magnetic flux, *B*, due to the magnetisation of the sample and the applied field is defined given in Eqn. 3.28,

$$B = \mu_0(H + M) \tag{3.28}$$

where μ_0 = permittivity of the medium, in this case air.

The VSM works on the principle of magnetic induction. Faraday induction is used to measure the magnitude of the magnetic moment of the sample. Voltage pick-up coils are placed at either side of the sample to be measured. As the sample vibrates it produces a varying magnetic field across the pick-up coils. According to Maxwell's equation, an EMF will be produced in the coils. Maxwell's equation is given by Eqn. 3.29,

$$\nabla \times E = \frac{\partial}{\partial t} B \tag{3.29}$$

where *E* = Electric Field, *B* = magnetic flux density. For a pick up coil with a number of turns, *N*, and cross sectional area, *A*, the induced voltage can be written as,

$$V = NA \frac{\partial}{\partial t} B \tag{3.30}$$

The VSM oscillates the sample with a sinusoidal angular frequency, ω. Therefore, the magnetic moment of the sample, *M*, can be written as,

$$M = M_0 sin(\omega t) \tag{3.31}$$

Substituting Eqns. 3.28 and 3.31 into Eqn. 3.30 gives,

$$V = NA \frac{\partial}{\partial t} [\mu_0(H + M_0 sin(\omega t))] \tag{3.32}$$

However, the applied magnetic field, *H*, is constant and so differentiating with respect to *t* gives,

$$V = NA\mu_0\omega M_0 cos(\omega t) \tag{3.33}$$

By measuring the induced voltage on the coils, the magnetic moment of the sample can be determined. To reduce the noise associated with the measurement, a lock-in amplifier is used to isolate the signal from the magnetic sample. The software used to take the magnetic measurements is Lake Shore IDEAs Version 3. By measuring the magnetic moment of the sample with respect to applied field, an M-H curve, also known as a hysteresis loop, is obtained.

3.11.2 Hysteresis Curve

A hysterises loop contains a large amount of information about a magnetic material. A typical hysteresis loop, plotting the magnetisation, *M*, against the applied magnetic field, *H*, is shown in Fig. 3.27. The initial magnetisation curve, represented by the open blue circles, plots the change of *M* as a function of *H*, of an initially demagnetised sample. In a demagnetised sample, the magnetic domains of the material are randomly orientated as shown in Fig. 3.27(ii). The randomly orientated domains cancel each other out and there is a net magnetic moment of zero. As the applied magnetic field increases, there is a non-linear increase in the magnetisation of the sample. The magnetic domains of the material rotate and begin to align with the applied field thus inducing a magnetic moment. The net magnetic moment increases until all of the magnetic domains are aligned in the same direction (Fig 3.27(i)). This occurs at the point A on the graph in Fig. 3.27. The applied magnetic field at which this occurs is called the saturation field, H_S. Further increases in the applied field beyond H_S do not increase the magnetic moment. The maximum moment of the

sample is referred to as the saturation magnetisation, M_s. The magnitude of M_S is often quoted as a specific magnetisation, in terms of mass, volume or number of moles. In this study, specific magnetisation, σ_s, refers to magnetisation per unit mass.

After magnetic saturation is reached, the applied magnetic field is reduced. Unless the sample is a perfect hard magnet, there is a decrease in magnetisation as the field decreases to zero. However, at zero applied field, there is still a net magnetisation associated with the sample because the magnetic domains retain a net alignment in the direction of the previously applied magnetic field. This corresponds to point B on the graph in Fig. 3.27 and is referred to as the remanent magnetisation, M_r. This demonstrates the history dependence of magnetisation.

As the applied magnetic field becomes negative, the magnetic domains becomes unaligned and the magnetic moment decreases. There exists a negative field at which the magnetic domains are randomly orientated and there is a net magnetisation of zero, marked as point C in Fig. 3.27. The applied field at which this occurs is referred to as the coercivity, H_c. Coercivity is defined as the negative magnetic field required to completely demagnetise a material after the material has been magnetically saturated. A magnetic material that has a large coercivity is termed a hard magnet. It retains its magnetisation at a low applied field and thus has a corresponding large remanence value. On the other hand, a low coercivity and a low remanence are properties of a soft magnet.

As the field is decreased to negative values, the magnetic domains align in the opposite direction and a negative saturation magnetisation is reached for a negative saturation field at point D in Fig. 3.27. The magnetic domain alignment at this point is shown in Fig 3.27(iii).

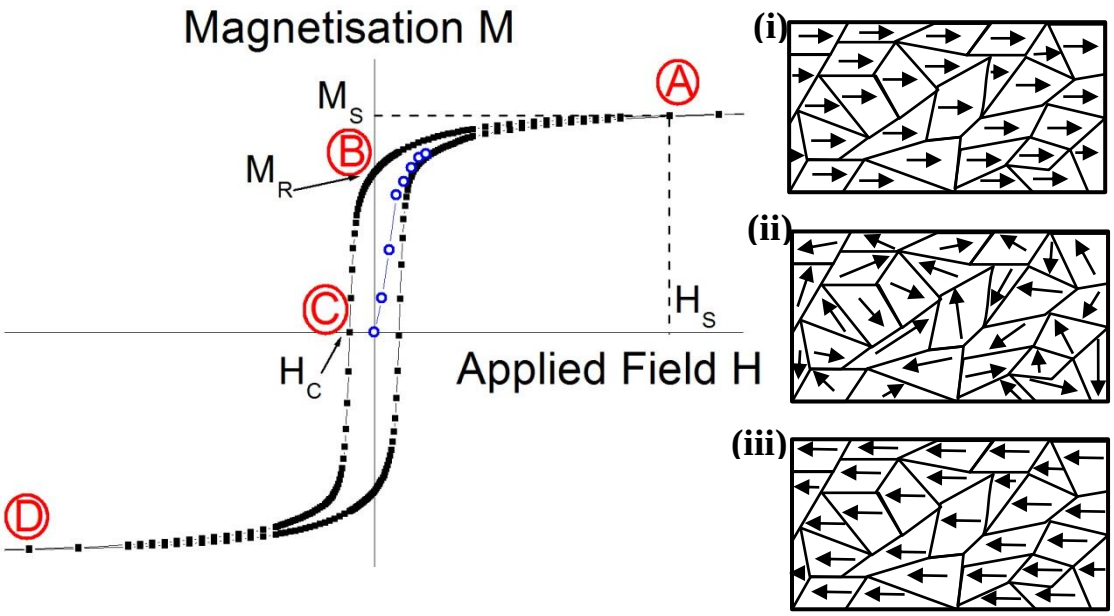

Figure 3.27: Typical hysterises curve that we have obtained from a VSM measurement. Schematic diagrams of the magnetic domain alignments for (i) aligned magnetic domains at saturation in the positive direction (ii) randomly orientated magnetic domains for a net magnetisation of zero and (iii) saturation in the negative direction. Images (i-iii) adapted from [67].

In this study, we will investigate the magnetic properties of magnetic nanotubes. The nanotubes have an associated shape anisotropy. This means that the magnetic properties of the nanotubes depend on the direction in which they are measured, for example, perpendicular or parallel to the nanotube axis. Depending on the orientation of the field with respect to nanostructure, the magnetic field required to reach magnetic saturation changes. The direction at which saturation occurs at the lowest applied field is termed the easy axis, while direction which requires the largest applied field is termed the hard axis.

The hysterises loop in an extrinsic property of the material and depends on many factors including the composition, shape, size and crystal structure. To achieve our second research objective, a VSM will be used to record the magnetic properties of the electrolessly deposited nanostructures. The magnetic properties of the nanotubes will be investigated with respect to the composition, shape, size and crystal structure.

3.12 Hydrogen Generation

3.12.1 Introduction

The third and final research objective of this thesis is to investigate the effectiveness of the electrolessly deposited nanostructures as catalysts for the generation of hydrogen from a $NaBH_4$ solution. In this study, the effect of composition and nanostructure of the metallic alloys on their associated catalytic activity is investigated. The overall aim of this research is to develop nanostructures with enhanced catalytic activities which may have potential for use in future technologies.

3.12.2 Sodium Borohydride ($NaBH_4$)

Sodium borohydride ($NaBH_4$) is an ionic compound which can be used for hydrogen generation. A schematic diagram of the structure of $NaBH_4$ is shown in Fig. 3.28. In the presence of water it undergoes hydrolysis, forming $NaBO_2$ and releasing hydrogen in an exothermic reaction. However, the rate of reaction decreases due to increasing pH of the solution and not all of the potential hydrogen is released.

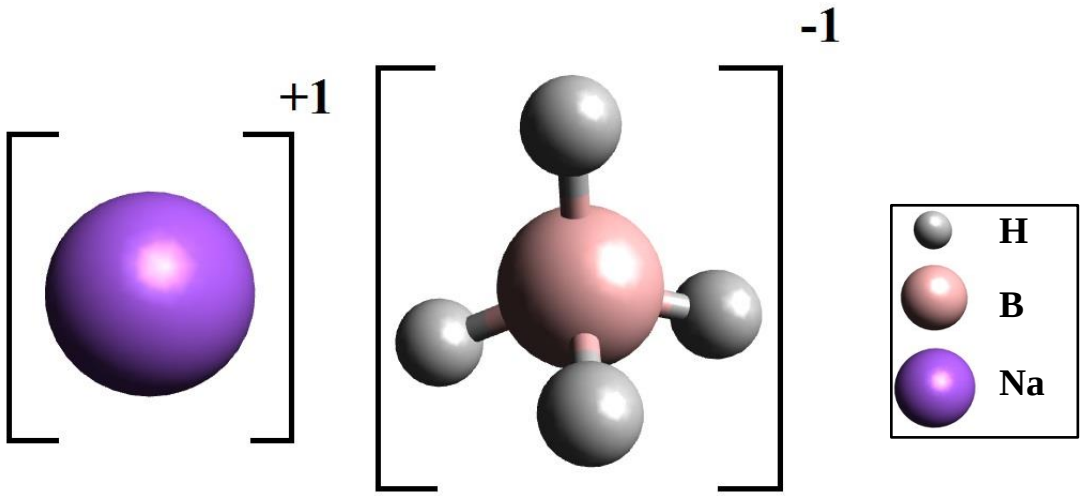

Figure 3.28: Schemtaic diagram of $NaBH_4$. Image adapted from [68].

$NaBH_4$ is stable in an alkaline solution. However, in the presence of a catalyst hydrogen is released in a controlled manner as described in Eqn. 3.34,

$$NaBH_4 + 2H_2O \xrightarrow{\text{catalyst}} NaBO_2 + 4H_2 \quad (3.34)$$

The molecular weight of $NaBH_4$ is 37.83 g mol^{-1}. As 4 g of this is hydrogen, $NaBH_4$ has a hydrogen storage capacity of 10.6 %. 1 g of $NaBH_4$ corresponds to 0.0264 M. Therefore, 1 g of $NaBH_4$ contains 1.59 x 10^{22} molecules of $NaBH_4$, or 3.18 x 10^{22} molecules of H_2. This corresponds to 0.053 M of H_2 gas in 1 g of $NaBH_4$. Using the ideal gas equation, Eqn. 3.35, this corresponds to a volume of 1.185 L of H_2 at standard temperature and pressure (T = 273.15 K and P = 1.01325 x 10^5 Pa).

$$PV = nRT \quad (3.35)$$

where P = Pressure of gas, V = Volume of gas, n = Number of moles of gas, R = Ideal gas constant (8.31 Pa m^3 K^{-1} mol^{-1}) and T = Temperaure. However, as hydrogen is also released from the H_2O molecules in Eqn. 3.34, 1 mole of $NaBH_4$ can generate 4 moles of H_2. Therefore, if 1 g of $NaBH_4$ is used for hydrogen generation with water, 2.37 L of H_2 will be released at STP.

Analogous to the role of Pd in the electroless deposition reaction, the catalyst acts as an intermediate for the transfer of electrons from the BH_4^- ion to the water molecules [68]. The reaction mechanism steps are shown in Fig. 3.29. Initially, in step 1, BH_4^- ions are chemisorbed to the catalyst surface. In step 2, the negative charge on the BH_4^- ion is transferred along with a hydrogen atom to an adjacent complexing site. The charge transfer occurs through the catalyst. Both steps 1 and 2 are reversible reactions and an equilibrium number of chemisorbed BH_4^- ions are reached.

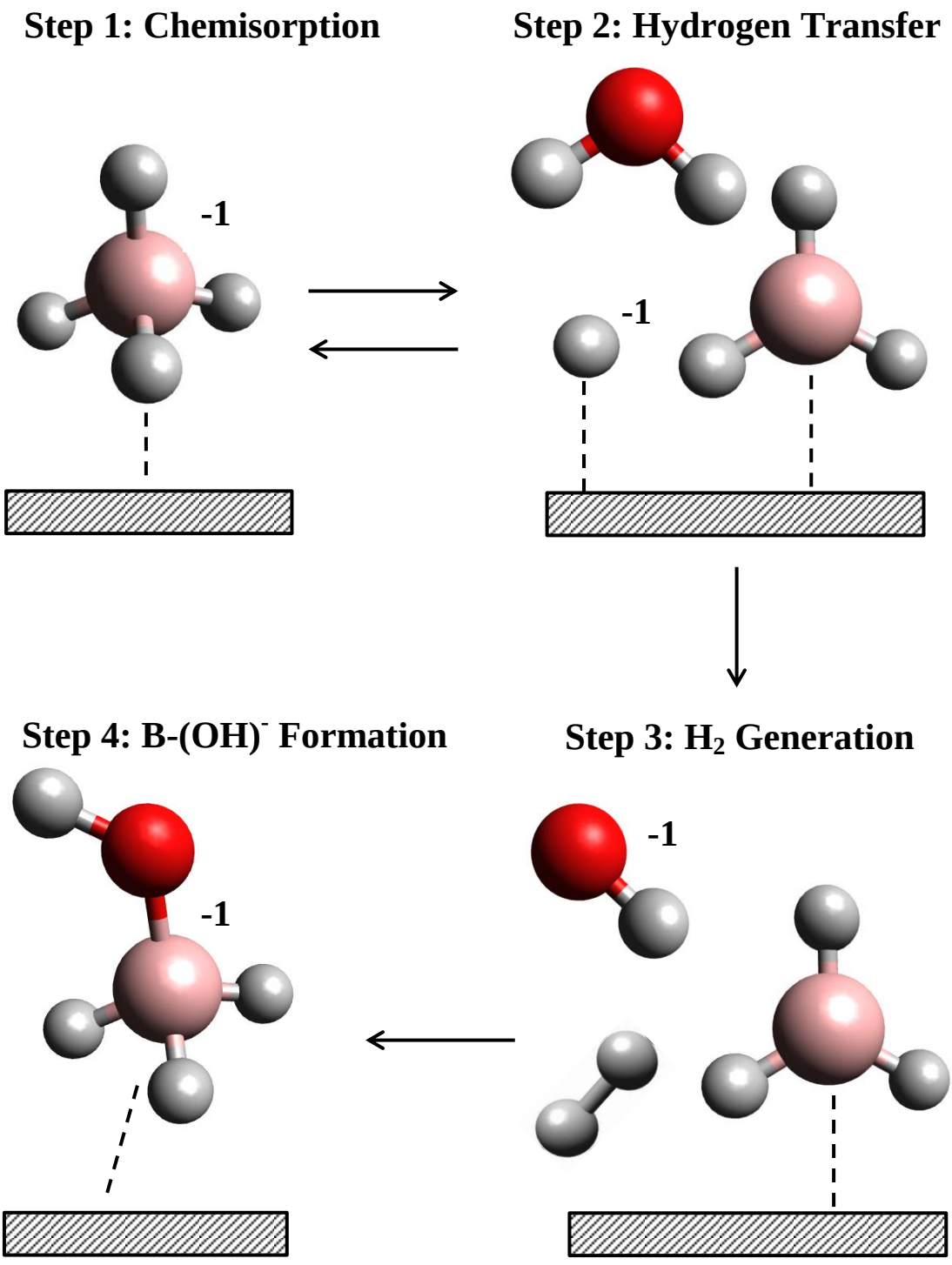

Figure 3.29: Chemical steps involved in hydrogen generation from $NaBH_4$. Image adapted from [68].

In step 3, the charged hydrogen atom reacts with a water molecule to produce H_2 and an OH^- ion. This is an irreversible reaction as hydrogen gas is released from the system. In step 4, the OH^- ion reacts with the BH_3 molecule, which is complexed with the catalyst. This results in the formation of a $BH_3(OH)^-$ ion. However, as there are

still 3 hydrogens bonded to the B atom, steps 2, 3 and 4 can be repeated three more times. In each of these cycles $BH_2(OH)_2^-$, $BH(OH)_3^-$ and $B(OH)_4^-$ are produced. Finally, $B(OH)_4^-$ reacts with Na^+ to produce the by-product $NaBO_2$ [68].

3.12.3 Experimental Set Up

The $NaBH_4$ solution used as a hydrogen source in this experiment comprises of $NaBH_4$ dissolved in an alkaline NaOH solution. The $NaBH_4$ concentration and pH of the solution are varied and their effect on the hydrogen generation rate is studied. The hydrogen generation experimental set-up that is used in this investigation is relatively simple and is shown in Fig. 3.30.

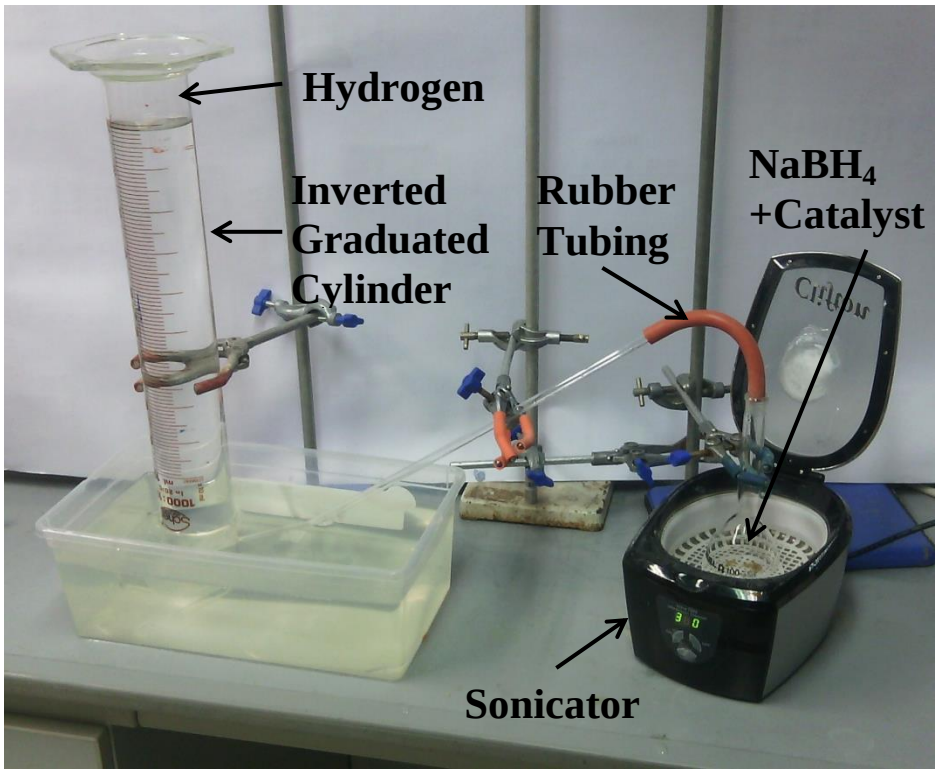

Figure 3.30: Image of the experimental set-up that we used for hydrogen generation testing from a $NaBH_4$ storage material.

A series of electrolessly deposited nanostructures are investigated as potential catalysts for hydrogen release. The template structure is not removed prior to hydrogen generation. The polycarbonate membranes are cut into a number of smaller

pieces and placed at the bottom of the round bottomed flask. A preheated $NaBH_4$ solution is added to the flask and the flask is sealed with rubber tubing. The temperature of the solution is kept constant by controlling the temperature of the bath. A sonicator is used to agitate the catalyst preventing the nucleation of hydrogen bubbles on the membrane surface.

The hydrogen released is collected via a water displacement method. A graduated cylinder full with water is inverted in a water bath and the rubber tubing is fed into the graduated cylinder from below the surface. As hydrogen is generated within the flask, it flows through the rubber tubing and bubbles into the graduated cylinder. From this, the volume of hydrogen produced can be measured.

In this investigation, the effect of catalyst composition, nanostructure, solution concentrations and bath temperature and are all investigated. The hydrogen generation rates are recorded in terms of volume of H_2 produced per minute. The reaction was continued until all of the available hydrogen was released. Depending on hydrogen generation rates, experimental times could range up to a number of hours. Therefore, a camera was set up to record the volume of hydrogen gas released which allowed for long measurements to be easily registered.

3.13 Summary

There are 3 main research objectives associated with this research. The first aim is to understand and control the electroless deposition process so that the formation of continuous nanotubes with a uniform wall thickness can be achieved. To accomplish this objective, the electroless deposition process of Ni-B within a template structure is investigated. The electroless deposition mechanism will be investigated for a range of parameters including electrolyte composition, pH and temperature with the aim of

achieving homogeneous deposition throughout the template structure. The deposited nanostructure will be imaged using SEM and TEM.

The second research objective of the study is to characterise and control the magentic properties of electrolessly deposited nanotubes with unique compositions, so that the properties can be tailored to suit a range of potential applications. The magnetic properties of the nanostructures will be measured using a VSM.

The third research objective is to characterise the catalytic properties of the electrolessly deposited nanotubes with the aim of achieving a large hydrogen generation rate from an alkaline $NaBH_4$ solution. To achieve this research objective, a range of experiments are carried out investigating the rate of hydrogen release using the as-deposited nanostructures. To achieve both the second and third research objectives, a full characterisation of the electrolessly deposited alloys will be carried out using EDX, XPS and XRD techniques.

3.14 References

[1] J. Martín, J. Maiz, J. Sacristan and C. Mijangos, *Polymer*, **53**, 1149 (2012).

[2] X. F. Han, S. Shamaila, R. Sharif, J. Y. Chen, H. R. Liu and D. P. Liu, *Advanced Materials*, **21**, 4619 (2009).

[3] R. Sharif, S. Shamaila, M. Ma, L. D. Yao, R. C. Yu, X. F. Han and M. Khaleeq-ur-Rahman, *Applied Physics Letters*, **92**, 032505 (2008).

[4] A. Azizi, M. Mohammadi and S. K. Sadrnezhaad, *Materials Letters*, **65**, 289 (2011).

[5] J. F. Rohan, D. P. Casey, B. M. Ahern, F. M. F. Rhen, S. Roy, D. Fleming and S. E. Lawrence, *Electrochemistry Communications*, **10**, 1419 (2008).

[6] I. Enculescu, M. Sima, M. Enculescu, E. Matei, M. E. Toimil Molares and T. H. Cornelius, *Optoelectronics and Advanced Materials-Rapid Communications*, **2**, 133 (2008).

[7] G. Z. Cao and D. W. Liu, *Advances in Colloid and Interface Science*, **136**, 45 (2008).

[8] R. L. Fleischer, P. B. Price and R. M. Walker, "*Nuclear Tracks in Solids: Principles and Applications*", Univ of California Press (1975).

[9] N. Hermsdorf, M. Stamm, S. Förster, S. Cunis, S. S. Funari, R. Gehrke and P. Müller-Buschbaum, *Langmuir : the ACS journal of surfaces and colloids*, **21**, 11987 (2005).

[10] V. P. Menon and C. R. Martin, *Analytical Chemistry*, **67**, 1920 (1995).

[11] G. Tourillon, L. Pontonnier, J. P. Levy and V. Langlais, *Electrochemical and Solid-State Letters*, **3**, 20 (2000).

[12] S. Xue, C. Cao and H. Zhu, *Journal of Materials Science*, **41**, 5598 (2006).

[13] R. C. Furneaux, W. R. Rigby and A. P. Davidson, *Letters to Nature*, **337**, 147 (1989).
[14] W. Lee and S. J. Park, *Chemical Reviews*, **114**, 7487 (2014).
[15] S. C. Lin, C. H. Lai and P. W. Wu, *Electrochemical and Solid-State Letters*, **11**, D1 (2008).
[16] X. Ren, C. H. Jiang, X. M. Huang and D. D. Li, *Physica E*, **41**, 349 (2009).
[17] N. Li, X. Li, X. Yin, W. Wang and S. Qiu, *Solid State Communications*, **132**, 841 (2004).
[18] J. Bao, C. Tie, Z. Xu, Q. Zhou, D. Shen and Q. Ma, *Advanced Materials*, **13**, 1631 (2001).
[19] F. Tao, M. Guan, Y. Jiang, J. Zhu, Z. Xu and Z. Xue, *Advanced Materials*, **18**, 2161 (2006).
[20] X. Li, Y. Wang, G. Song, Z. Peng, Y. Yu, X. She and J. Li, *Nanoscale research letters*, **4**, 1015 (2009).
[21] J. Fu, S. Cherevko and C. H. Chung, *Electrochemistry Communications*, **10**, 514 (2008).
[22] C. G. Jin, W. F. Liu, C. Jia, X. Q. Xiang, W. L. Cai, L. Z. Yao and X. G. Li, *Journal of Crystal Growth*, **258**, 337 (2003).
[23] M. M. A. Imran, *Journal of Alloys and Compounds*, **455**, 17 (2008).
[24] F. Tian, J. Zhu and D. Wei, *The Journal of Physical Chemistry C*, **111**, 12669 (2007).
[25] J. B. Shi, Y. C. Chen, C. W. Lee, Y. T. Lin, C. Wu and C. J. Chen, *Materials Letters*, **62**, 15 (2008).
[26] A. B. Emil, "*Surface metallizing method*", U.S. Patent, 2702253, Feb. (1955).
[27] R. L. Meek, *Journal of The Electrochemical Society*, **122**, 1478 (1975).
[28] C. H. de Minjer and P. F. J. vd Boom, *Journal of The Electrochemical Society*, **120**, 1644 (1973).
[29] W. L. Liu, S. H. Hsieh, H. C. Yan and W. J. Chen, *Applied Surface Science*, **258**, 1806 (2011).
[30] L. Hai-Peng, H. Man-Gui, C. Li and D. Long-Jiang, *Chinese Physics B*, **20**, 060701 (2011).
[31] G. Xie, Z. Wang, G. Li, Y. Shi, Z. Cui and Z. Zhang, *Materials Letters*, **61**, 2641 (2007).
[32] R. L. Cohen, J. F. D'amico and K. W. West, *Journal of The Electrochemical Society*, **118**, 2042 (1971).
[33] R. L. Cohen and K. W. West, *Journal of The Electrochemical Society*, **119**, 433 (1972).
[34] N. Feldstein and J. A. Weiner, *Journal of The Electrochemical Society*, **120**, 475 (1973).
[35] B. K. W. Baylis, N. E. Hedgecock, M. Schlesinger and A. van Wijngaarden, *Journal of The Electrochemical Society*, **126**, 1671 (1979).
[36] J. J. Kelly and J. K. Vondeling, *Journal of The Electrochemical Society*, **122**, 1103 (1975).
[37] J. P. Marton and M. Schlesinger, *Journal of The Electrochemical Society*, **115**, 16 (1968).
[38] A. J. Bard and L. R. Faulkner, "*Electrochemical Methods: Fundamentals and Applications*", Wiley India Limited (2004).
[39] F. Delaunois, J. P. Petitjean, P. Lienard and M. Jacob-Duliere, *Surface and Coatings Technology*, **124**, 201 (2000).
[40] K. Stadnicka, A. M. Glazer and M. Koralewski, *Acta Crystallographica Section B*, **43**, 319 (1987).
[41] B. Sharma, "*Instrumental Methods of Chemical Analysis*", Krishna Prakashan Media (2000).
[42] N. Wiberg, A. F. Holleman and E. Wiberg, "*Inorganic Chemistry, 1st Edition*", Academic Press (2001).
[43] A. M. Distler and J. Allison, *J Am Soc Mass Spectrom*, **12**, 456 (2001).

[44] G. O. Mallory, *Plating*, **58**, 319 (1971).
[45] M. Rakap, E. E. Kalu and S. Özkar, *International Journal of Hydrogen Energy*, **36**, 254 (2011).
[46] J. F. Rohan, B. M. Ahern and L. C. Nagle, *ECS Transactions*, **1**, 1 (2006).
[47] Z. Liu, W. L. Li and W. D. Fei, *Modern Physics Letters B*, **27**, 1341006 (2013).
[48] H. B. Dai, Y. Liang, P. Wang, X. D. Yao, T. Rufford, M. Lu and H. M. Cheng, *International Journal of Hydrogen Energy*, **33**, 4405 (2008).
[49] N. Patel, R. Fernandes, N. Bazzanella and A. Miotello, *Thin Solid Films*, **518**, 4779 (2010).
[50] S. Haag, M. Burgard and B. Ernst, *Surface and Coatings Technology*, **201**, 2166 (2006).
[51] S. L. Cheng, T. L. Hsu, T. Lee, S. W. Lee, J. C. Hu and L. T. Chen, *Applied Surface Science*, **264**, 732 (2013).
[52] G. O. Mallory and J. B. Hajdu, "*Chapter 1 - The Fundamental Aspects of Electroless Nickel Plating*", in *Electroless Plating: Fundamentals and Applications*, William Andrew (1990).
[53] N. H. Joshi, "*Treating surface with silver compound before plating; preferably surface is sensitized with a stanous compound before silver treatment*", U.S. Patent, 6645557, Nov. (2003).
[54] B. J. Hwang and S. H. Lin, *Journal of the Electrochemical Society*, **142**, 3749 (1995).
[55] M. Lelental, *Journal of the Electrochemical Society*, **120**, 1650 (1973).
[56] Y. Liu and Q. Zhao, *Applied Surface Science*, **228**, 57 (2004).
[57] W. T. Evans and M. Schlesinger, *Journal of the Electrochemical Society*, **141**, 78 (1994).
[58] M. J. Aleksinas, "*Chapter 3 - Troubleshooting electroless nickel plating solutions*", in *Electroless Plating: Fundamentals and Applications*, William Andrew (1990).
[59] H. Yamauchi, K. Takagi, I. Yuito and U. Kawabe, *Applied Physics Letters*, **29**, 638 (1976).
[60] W. Zhou, R. P. Apkarian, Z. L. Wang and D. Joy, "*Chapter 1: Fundamentals of Scanning Electron Microscopy (SEM)*", in *Scanning Microscopy for Nanotechnology*, Springer (2007).
[61] L. A. Bloomfield, "*How Things Work: The Physics of Everyday Life*", J. Wiley (1997).
[62] D. H. Bruining, "*Chapter 3 - Secondary Electron Emission From Metals; Review of Results*", in *Physics and Applications of Secondary Electron Emission*, Pergamon (1962).
[63] H. D. Young and R. A. Freedman, "*University Physics with Modern Physics 12th Edition*", Pearson (2008).
[64] T. A. Littlefield and N. Thorley, "*Atomic and Nuclear Physics - An Introduction*", Nostrand Reinhold (1979).
[65] H. R. Verma, "*Atomic and Nuclear Analytical Methods*", Springer (2007).
[66] S. Foner, *Review of Scientific Instruments*, **30**, 548 (1959).
[67] A. Hubert and R. Schäfer, "*Magnetic Domains: The Analysis of Magnetic Microstructures*", Springer (1998).
[68] R. Pena-Alonso, A. Sicurelli, E. Callone, G. Carturan and R. Raj, *Journal of Power Sources*, **165**, 315 (2007).

Chapter 4 – Enhancement of Electroless Nanotube Deposition

4.1 Introduction

Although the electroless deposition of nanotubes was previously undertaken [1-3], there are still challenges associated with the deposition process within a template structure. Azizi et al. [4] found that the deposition rate on the membrane surface is larger than within the nanotube pores, resulting in the formation of end-closed nanotubes. A similar effect was also observed by Lin et al. [5] and Enculescu et al. [6] depositing Ni-P nanotubes in an AAO template structure. However, we are still lacking a clear understanding of the deposition process involved. This lack of understanding is addressed in this chapter.

The main challenge associated with the electroless deposition process is the difficulty in producing continuous nanotubes with a uniform wall thickness. The final nanotube structure is controlled by the deposition rate and the size of the nanotube pores. Deposition within the nanostructure can be diffusion limited or kinetically controlled.

A diffusion limited process within the nanotube leads to a larger rate of deposition on the membrane surface than within the nanotube pores. This results in the formation of incomplete end-closed nanotubes with varying wall thicknesses along the tube axis. To achieve the formation of continuous nanotubes with a uniform wall thickness, a kinetically controlled reaction is required. By achieving a kinetically controlled reaction, deposition throughout the template occurs at the same rate, both on the

membrane surface and within the nanotube pores. The result of this will be continuous nanotubes with a uniform wall thickness.

This research has developed a detailed analysis of the deposition process of nanotubes deposited via electroless deposition within a template structure. The four stages of electroless deposition; nucleation, island growth, coalescence and film overgrowth to form end-closed nanotubes, are each discussed in detail in this chapter. A clear understanding of the nanotube deposition process is provided. The final result of electroless deposition within a membrane structure is the formation of a nanotube array connected at both ends by a metal film. In this work, Ni-B deposition is used as an exemplar of this process, to investigate the parameters that affect the deposition rate. By controlling the deposition rate, a kinetically controlled reaction can be achieved to form continuous nanotubes with a uniform wall thickness.

4.2 Stages of Electroless Deposition

In this study we show that there are four main stages involved in the electroless deposition process of nanostructures within a polycarbonate membrane. These are the nucleation of electrolessly deposited metal at catalytic Pd nuclei, Fig. 4.1(a,e), a radially outward island growth from each of these nucleation points, Fig. 4.1(b,f), the coalescence of the islands to form a continuous nanostructure, Fig. 4.1(c,g) and film overgrowth resulting in the formation of end-closed nanotubes, Fig. 4.1(d,h). In this work, a range of alloys have been deposited via electroless deposition. The deposition process associated with each alloy is identical and is discussed in detail in the following sections.

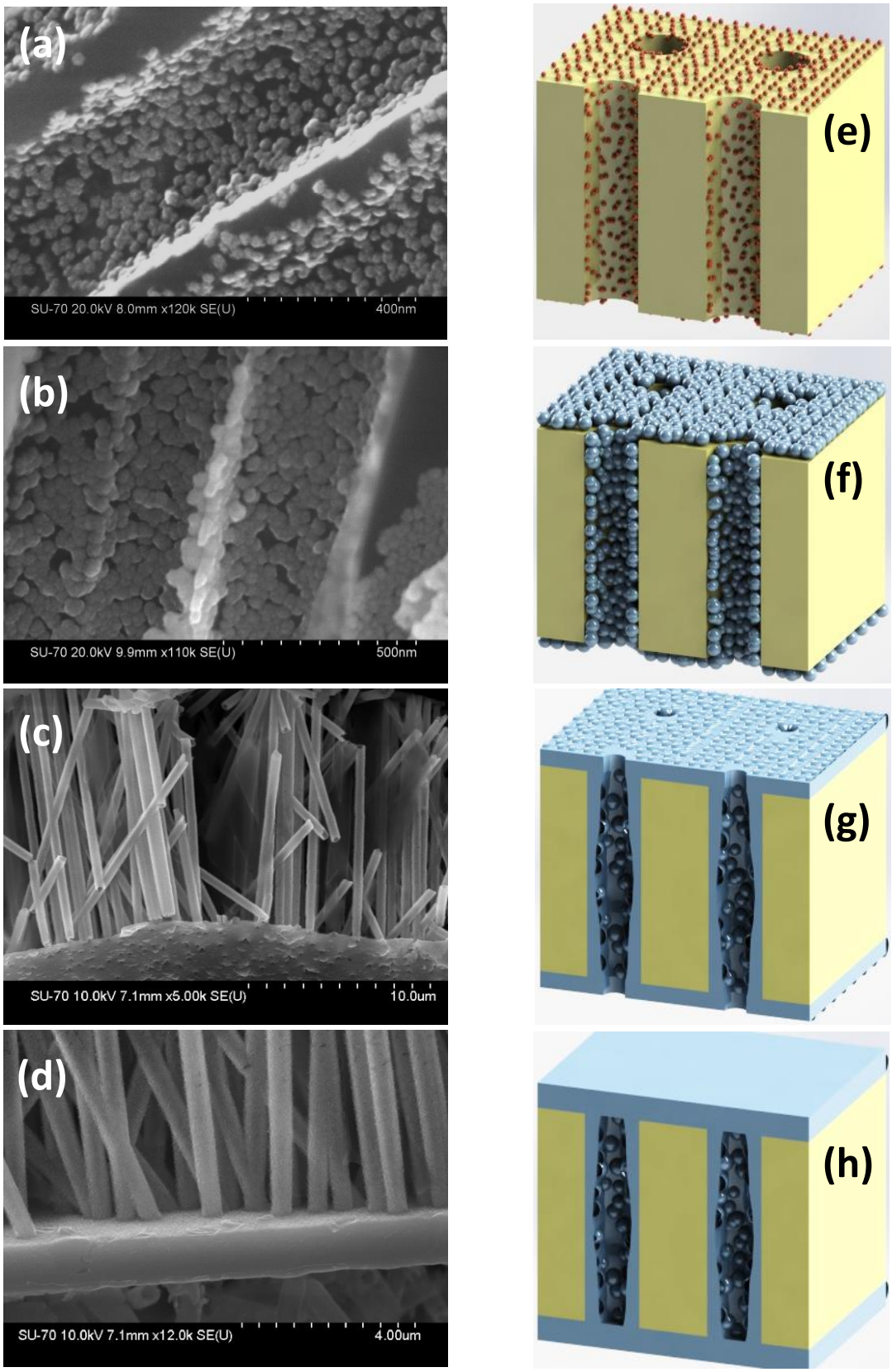

Figure 4.1: (a,b,c,d) SEM images and **(e,f,g,h)** schematic diagrams showing the four stages of electroless deposition. **(a,e)** Initial Ni-B deposition occurs at Pd nuclei to form Ni-B islands. **(b,f)** Island growth occurs at each catalytic nucleation sites, **(c,g)** which coalesce forming continuous nanotubes within the membrane pores and a film on the membrane surface. **(d,h)** Due to a larger deposition rate on the membrane surface than within the nanotube pores, the nanotubes become end-closed and a continuous film is formed**.**

4.2.1 Nucleation

As described in section 3.4.2, during the activation process we deposited Pd nuclei throughout the polycarbonate membrane, along the nanotube walls and on the membrane surface. Meek [7] has shown that during the sensitisation process, the Sn coverage is dependent on the sensitisation time. However, Pd coverage is independent of activation time, but is dependent on the Sn coverage [7]. The deposited Pd nuclei act as catalysts, at which electron exchange between the reducing agent and metal ion occurs. This results in electroless deposition of the metal at catalytic Pd sites [8]. The cross sectional SEM image in Fig. 4.2 shows that initial Ni-B deposition occurs at active Pd nucleation sites. Once coalescence occurs, the thickness of the deposit is independent of grain size and number of nucleation points [9]. Therefore, the uniformity of the nanotube wall thickness or continuity of the tubes will not be affected by the number of catalytic Pd nucleation sites present.

From the amount of fizzing that occurred when an activated polycarbonate membrane was placed in the deposition bath, the initial catalytic nucleation rate could be inferred visually. For deposition baths at high temperatures, > 60 ºC, the reaction begins immediately and aggressively with a large amount of fizzing due to hydrogen evolution. This is the initial catalytic nucleation stage at which electroless deposition is occurring due to catalytic Pd particles. The aggressive reaction can last for up to 20 seconds, after which the fizzing reduces to a more constant rate, indicating that all catalytic Pd nuclei have been covered by the deposit. However, at low temperatures < 40 ºC, the aggressive reaction seen at high temperatures does not occur. Instead, a slow controlled reaction occurs, with small amounts of hydrogen evolution observed. This indicates that the initial nucleation rate is highly dependent on temperature. This

will be discussed further in section 4.5.4, providing a detailed analysis on the effect of temperature on initial nucleation and electroless deposition.

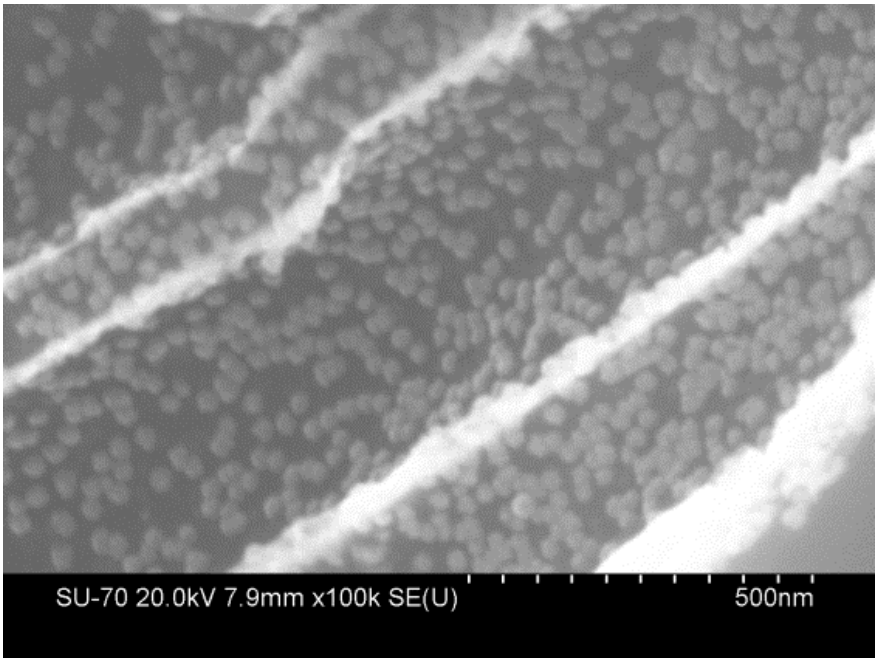

Figure 4.2: Cross-sectional SEM image of Ni-B nanotube after 60 seconds of deposition from the deposition bath described in Table 3.4, showing nucleation of Ni-B at catlytic Pd sites

4.2.2 Island Growth

After initial nucleation occurs at each active Pd site, the electrolessly deposited metal acts as a catalyst for the reaction. This results in an autocatalytic deposition process [10]. Due to the template structure that we have used, deposition occurs radially outward from each nucleation site, forming Ni-B islands along the walls and on the surface of the polycarbonate template [6]. The islands are hemispherical in shape with a Pd particle located at the centre of their base [9]. As shown in the TEM image in Fig. 4.3, islands formed along the internal walls of the template structure after a short period of deposition. The size to which the islands grow before coalescence appears to be dependent on the density of nucleation points. If the distance of separation between nucleation points is small, the islands will have a small diameter at the point at which coalesce occurs. However, for sparsely populated nucleation points, much larger

islands will be formed prior to coalescence [9]. However, provided the deposition rate is constant, the nanotube wall thickness is independent on the density of nucleation points.

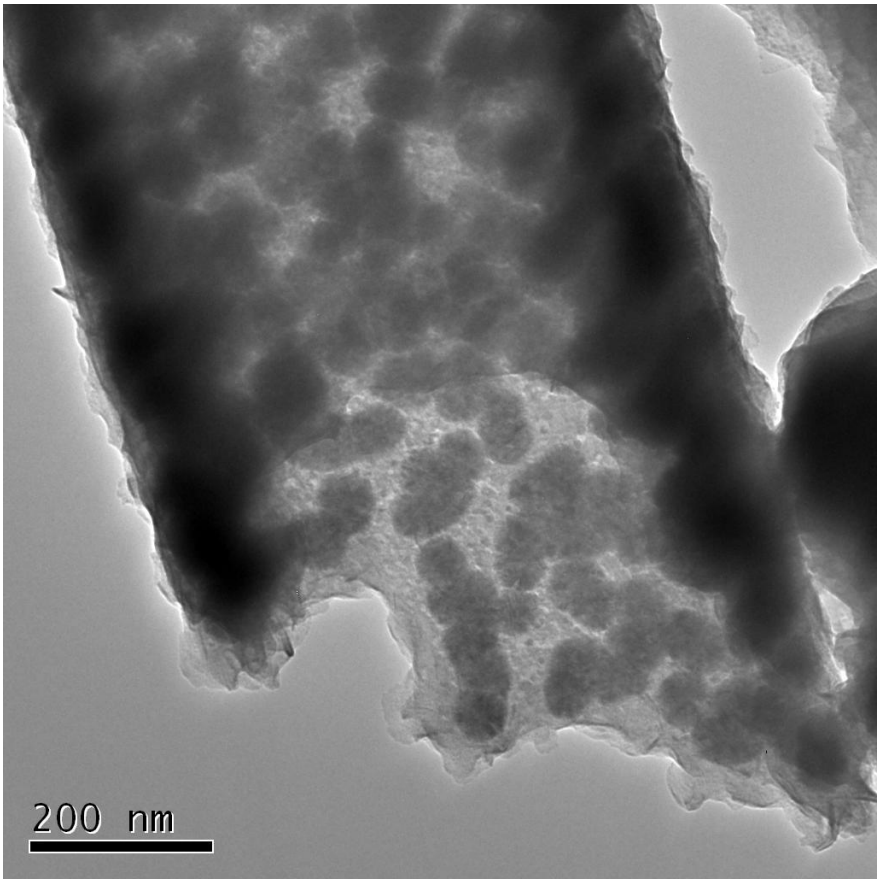

Figure 4.3: TEM image of Ni-B nanotube deposited from the deposition described in Table 3.4, showing the formation of Ni-B islands along the tube structure.

4.2.3 Coalescence

As electroless deposition continues, the diameter of the islands increases and neighbouring islands grow into each other as shown in Fig. 4.4. This process is known as coalescence. The time it takes for coalescence to occur depends on two main factors; the deposition rate and the distance of separation of nucleation sites. For large deposition rates, the time taken until coalescence is small as the islands will grow at a large rate. However, if the separation between adjacent sites is large, the time taken for coalescence is larger. To ensure that islands grow at the same rate throughout the

nanotube structure, a homogeneous deposition rate is required. This will guarantee the formation of nanotubes with a uniform wall thickness.

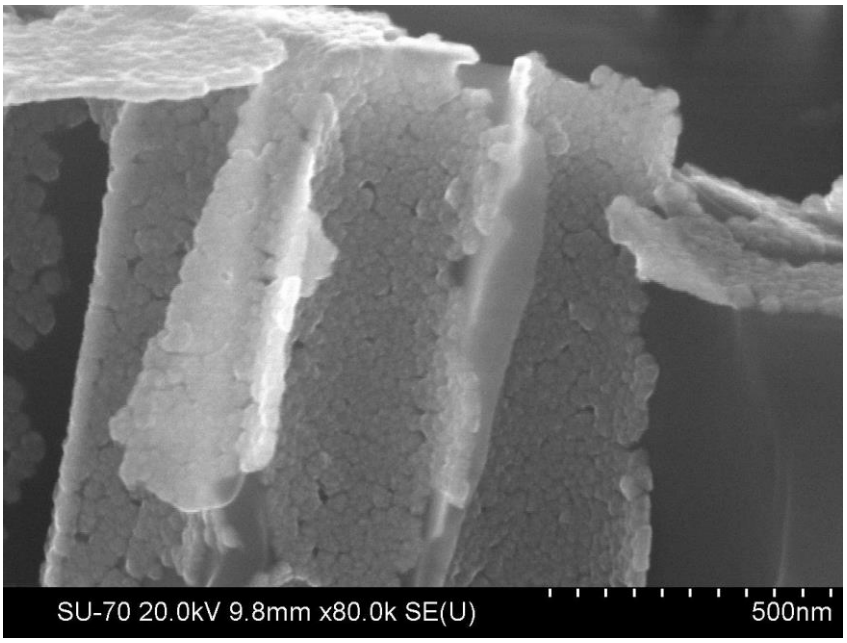

Figure 4.4: SEM image of Ni-B nanotubes after 2 minutes of deposition from the bath described in Table 3.4, showing Ni-B islands coalescing to form a continuous Ni-B nanotube.

Coalescence of the electrolessly deposited islands within the template structure results in the formation of continuous nanotubes along the membrane walls and a film on the surface on the membrane, as shown in Fig. 4.5.

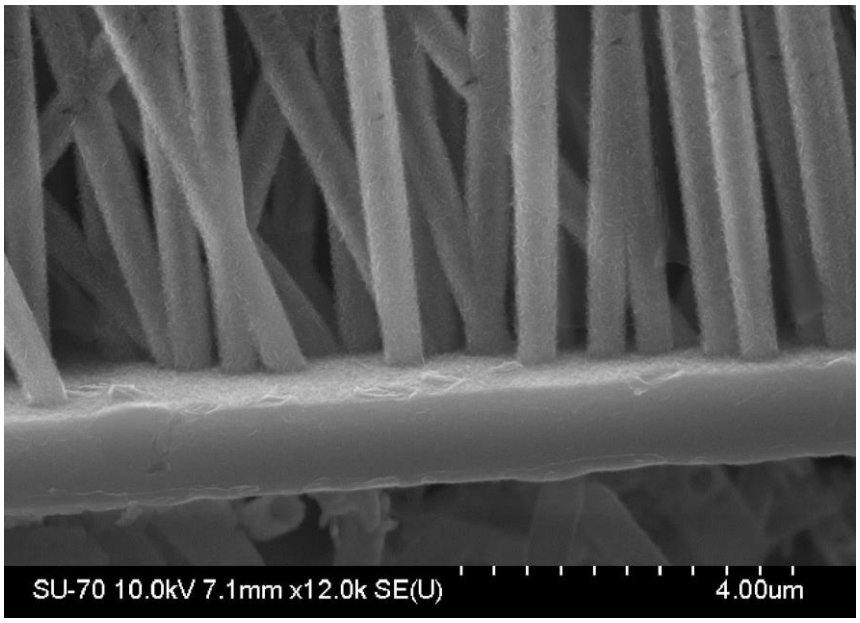

Figure 4.5: SEM image of Ni-B island coalescence on nanotubes within the membrane pores and a thin film on the membrane surface deposited from the deposition bath described in Table 3.4.

As deposition occurs in the form of hemispherical islands, the deposit is uneven and is characterised by spherical type grains which correspond to the size and shape of the electrolessly deposited islands. An SEM image of the internal surface of a Ni-B nanotube, shown in Fig. 4.6, reveals that the inner tube wall is composed of spherical grains which have coalesced. As the deposit thickness increases, the surface becomes smoother due to a decrease in the spherical nature of the Ni-B islands as coalescence occurs.

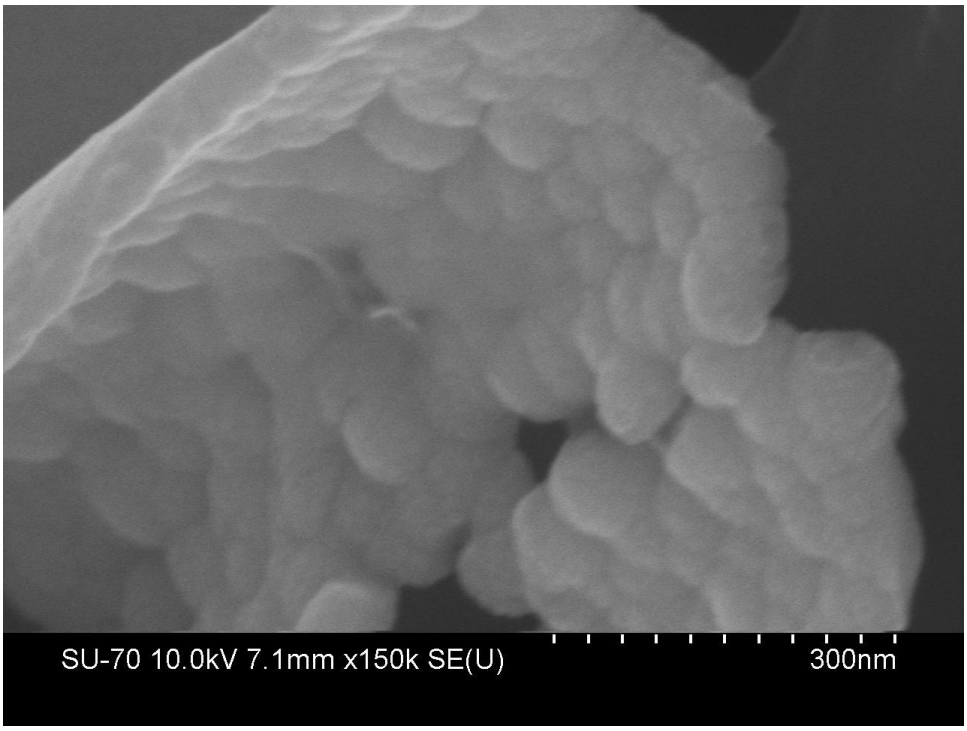

Figure 4.6: SEM image of a Ni-B nanotube after 5 minutes of deposition from the deposition bath described in Table 3.4 showing the formation of a continuous nanotube from the coalescence of Ni-B islands.

4.2.4 End-Closed Nanotubes

Once coalescence occurs, end-opened nanotubes are formed, as shown in Fig. 4.7. However, we have observed that as deposition continues, the pore openings of the nanotube decrease in size, resulting in the formation of end-closed nanotubes. This is similar to the results described previously by Azizi et al. [4]. These results indicate

that electroless deposition occurs at a faster rate on the membrane surface than within the nanotube pores, resulting in the formation of end-closed nanotubes. In this research, we investigate the electroless deposition process to gain an understanding of the origin of the differing deposition rates on the membrane surface and within the nanopores.

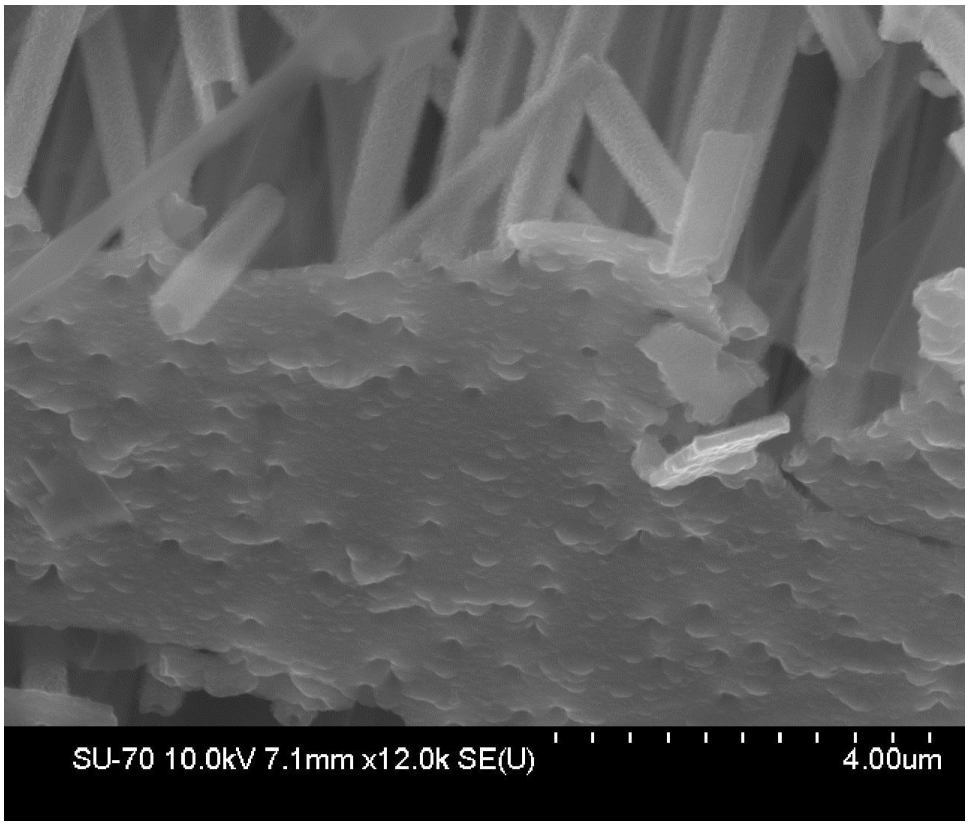

Figure 4.7: SEM image of Ni-B nanotubes after 5 minutes deposition with end-opened pores deposited from the deposition bath described in Table 3.4.

The difference between deposition rates of the film on the membrane surface and nanotubes within the membrane pores results in a thicker deposit at the nanotube pore openings than along the nanopore walls. As the film grows, it completely covers the pore opening of the nanotube. This results in the formation of end-closed nanotubes as shown in Fig. 4.8. Once the nanotubes are end-closed, no further deposition takes place within the nanotube structure, thus preventing the formation of nanotubes with a

large wall thickness. Electroless deposition will continue on the membrane surface and a film in the order of microns thick can be formed.

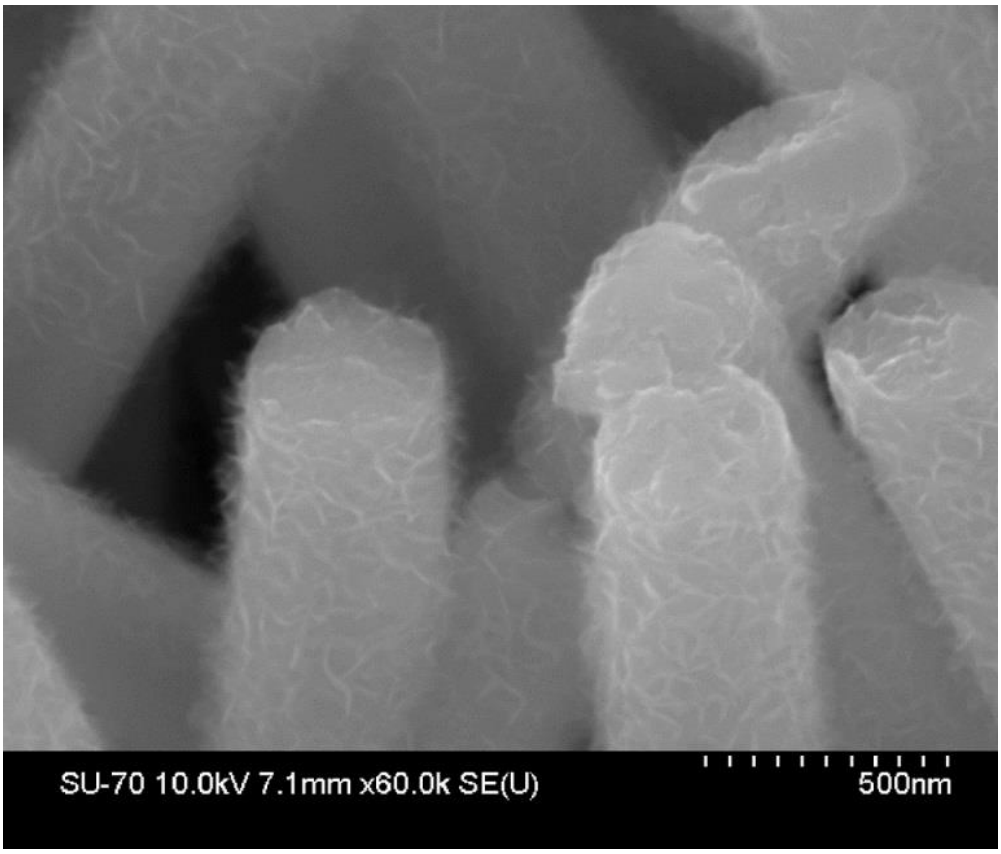

Figure 4.8: SEM image of end-closed Ni-B nanotubes after a deposition time of 20 minutes from the deposition bath described in Table 3.4.

4.2.5 Final Structure

Electroless deposition occurs on the pore walls of the polycarbonate membrane forming nanotubes. Electroless deposition also occurs on the top and bottom surfaces of the membrane to form thin films. Therefore, the final result of the electroless deposition process within a polycarbonate membrane is a nanotube array connected at both ends by a thin film as shown in Fig. 4.9. The synthesised nanotubes have a length of 20 μm and an outer diameter of 400 nm, matching the diameter and length of the pores of the polycarbonate membrane. This corresponds to an aspect ratio of 50

for the deposited nanotubes. The thicknesses of the film and nanotube walls are dependent on the deposition bath conditions and the total deposition time.

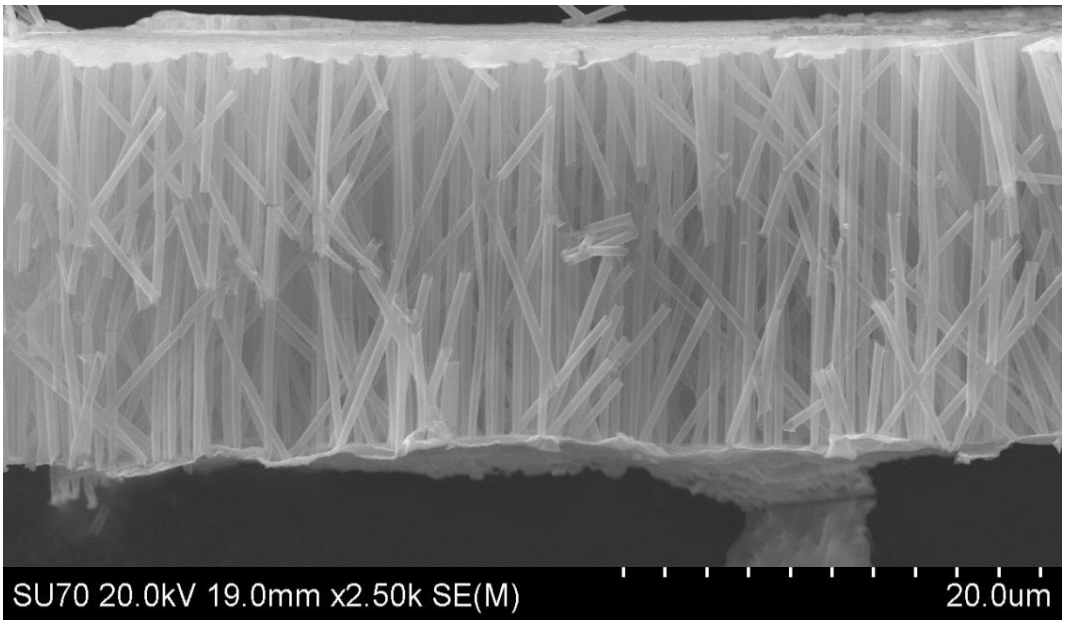

Figure 4.9: SEM image of Ni-B nanotube array connected together at both ends by a thin film deposited from the deposition bath described previously in Table 3.4.

The pores of the polycarbonate membrane are not all perpendicular to the membrane surface. Although the majority of the nanotubes in Fig. 4.9 are perpendicular to the film surface, there are also nanotubes present which deviate from the perpendicular at angles of up to 30 º and are typical of the polycarbonate membrane due its manufacturing process [11]. However, the density of these defects is negligible and the majority of the deposited nanotubes grow perpendicular to the membrane surface. Another defect that is present due to the manufacturing process is the growth of pores into each other as discussed in section 3.2.1. This leads to the formation of nanostructures, which consist of multiple tubes all sharing the same wall. Examples of double (i), triple (ii) and quadruple (iii) tubes all sharing the same wall, are shown in Fig. 4.10. However, these defects are relatively rare and the vast majority of the deposited structures consist of uniform single walled nanotubes. Other defects include

nanotubes which do not grow to the full length of the membrane and nanotubes that grow through each other.

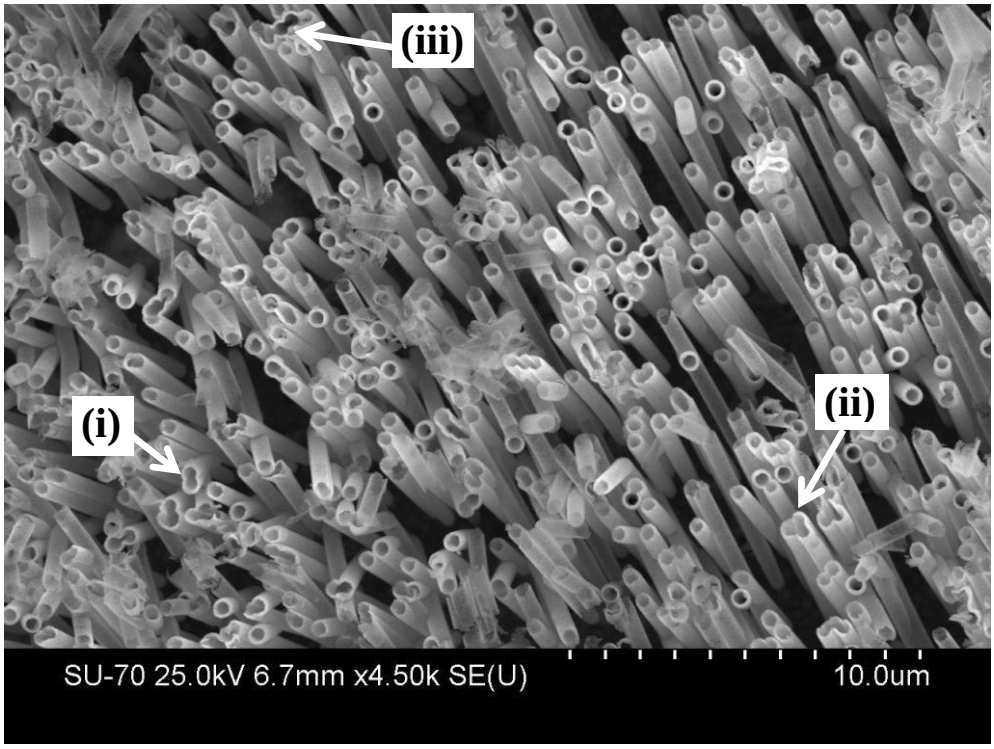

Figure 4.10: Cross-sectional SEM image of Ni-Cu-B nanotube array deposited after a deposition time of 5 minutes from the deposition bath described in Table 3.7.

4.3 Challenges Associated with the Deposition Process

We have identified many challenges associated with the electroless deposition of nanostructures due to differing deposition rates throughout template structure. As shown in Fig. 4.11, the differing deposition rates can result in the formation of incomplete nanotube structures. A continuous nanotube is formed close to the nanotube base, Fig. 4.11(b). However, only 3 μm from the nanotube base, incomplete nanotubes consisting of un-coalesced islands are present Fig. 4.11 (c) and (d). This indicates that the deposition rate also varies along the nanotube axis. Therefore, it is important that the deposition rate is controlled throughout the nanotube structure,

because large fluctuations in the deposition rate result in the formation of incomplete nanotubes.

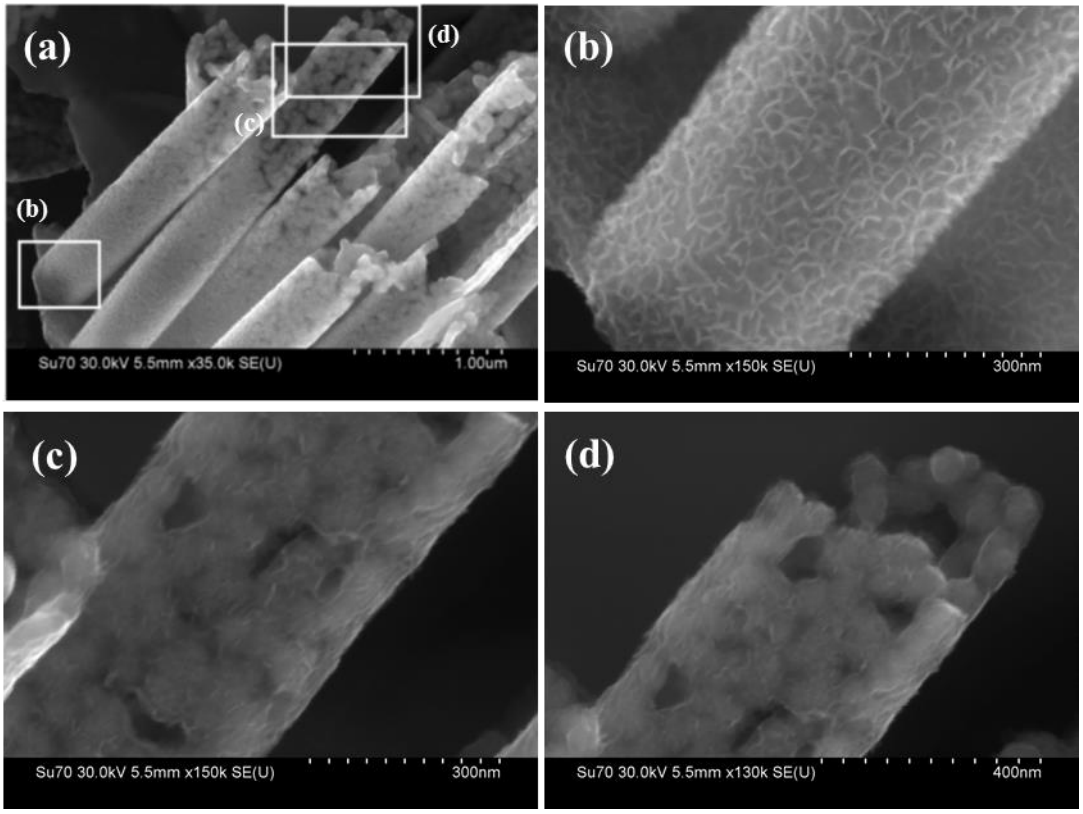

Figure 4.11: (a) SEM image of Co-Ni-Fe-B nanotubes with a deposition time of 5 minutes deposited from the deposition bath described in Table 3.10. **(b)** Complete continuous deposit present at base of tube **(c)** mixture of nucleation sites and grains as the islands coalesce **(d)** Fragmented nature of nucleation sites 3 µm along tube length.

Another challenge associated with the elctroless deposition process within a template structure is the variation between the deposition rate on the membrane surface and within the nanotube pores. As shown in Fig. 4.12 for a Ni-B deposit after 1 minute of deposition, the nanotube growth and film growth are at different stages of formation. An almost complete film has already been formed on the membrane surface as shown in Fig. 4.12(a). Here, Ni-B islands are clearly visible with sizes up to 80 nm in diameter. These islands have already coalesced and there is complete surface coverage of the membrane. However, measurements of the islands close to the top of the nanotube in Fig. 4.12(b) show that they are no greater than 30 nm in size and have

not coalesced to form a continuous nanotube. This indicates that the deposition rate on the membrane surface is larger than the deposition rate within the nanotube pores.

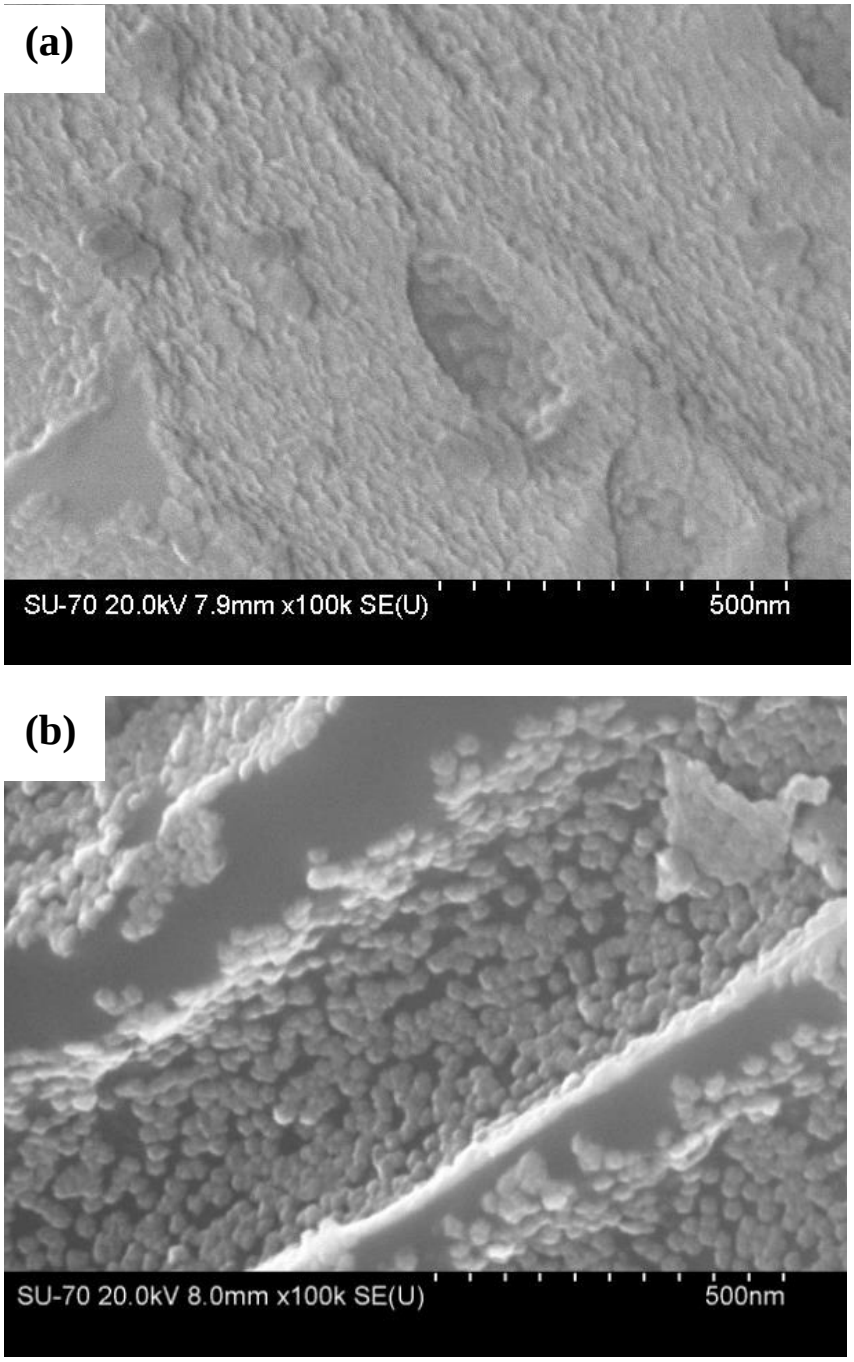

Figure 4.12: Ni-B deposition on **(a)** the membrane surface and **(b)** within the nanopore after 1 minute of deposition from the deposition bath described in Table 3.4.

A large variation between the deposition rate on the membrane surface and within the nanotube pores can lead to the closing of the membrane pores before a continuous

nanotube is formed as shown in 4.13. Here, continuous nanotubes of less than 2 μm in length are deposited before the nanotubes become end-closed. Therefore, to achieve the formation of continuous nanotubes, it is important that the deposition on the membrane surface and along the nanotube axis occurs at the same rate.

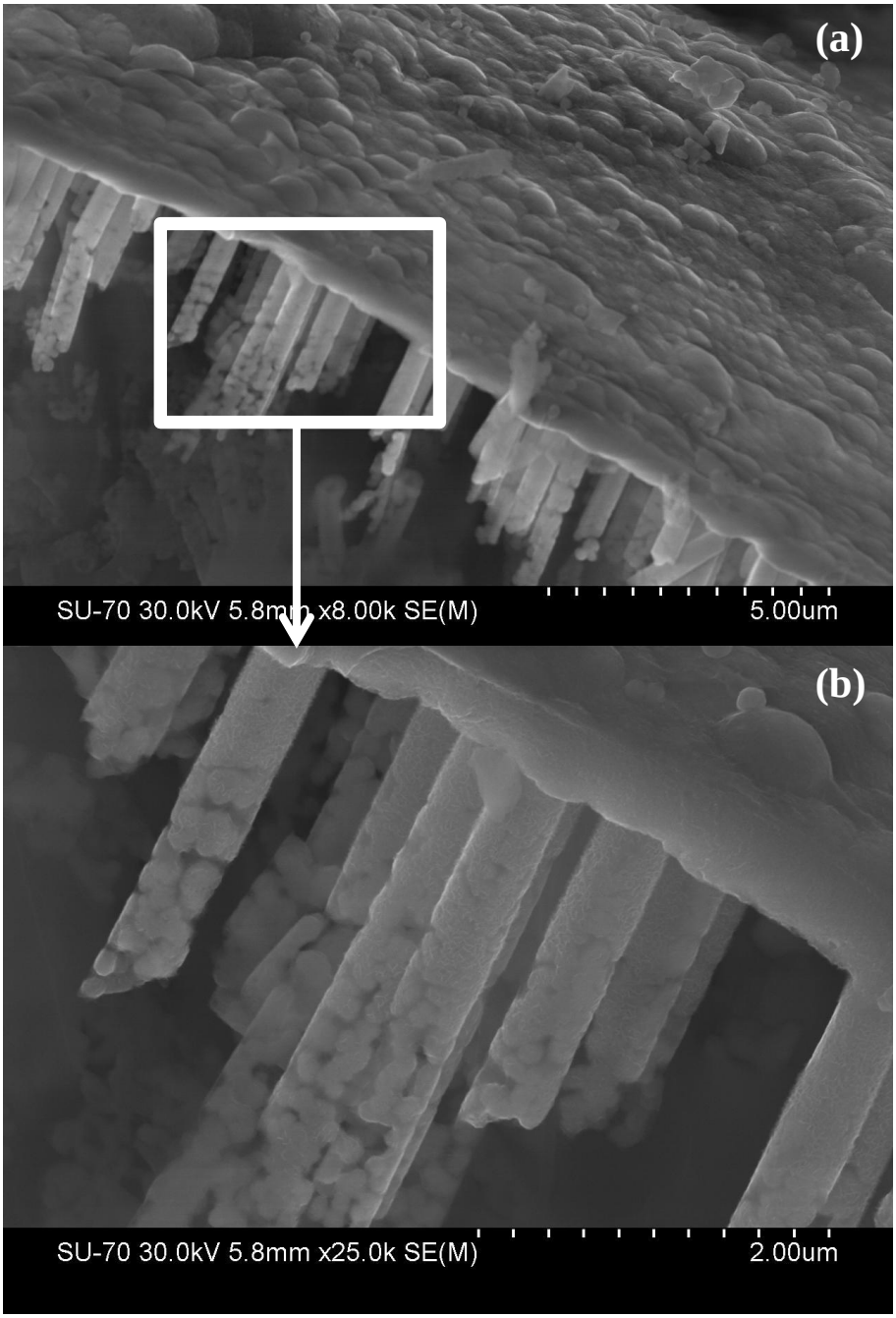

Figure 4.13: (a) SEM image of end-closed incomplete Co-Ni-Fe-B nanotubes connected at the base by a film deposited from the deposition bath described in section 3.10 **(b)** High magnification image of the incomplete nanotubes and film approximately 400 nm thick.

All of the challenges are a result of the same problem; differing deposition rates throughout the template structure. We propose that the differing rates along the tube axis are due to a diffusion limited deposition process occurring within the nanotube pores and a kinetically controlled process occurring on the membrane surface. To achieve our research objective of synthesising continuous nanotubes with a uniform wall thickness, a kinetically controlled deposition rate is required throughout the template structure. To achieve this, we must investigate the reaction kinetics of the deposition process.

4.4 Deposition Kinetics

4.4.1 Introduction

Before the deposition kinetics of electroless nanotube deposition are considered, it is important to note some factors that govern the electroless deposition process. There are five different stages associated with the electroless deposition process [10], each of which may control the rate of electroless deposition. Firstly, the reactants consumed in the electroless deposition process such as the metal ions and the reducing agent must diffuse through the electrolyte to the catalytic surface. Secondly, before a chemical reaction can take place, adsorption of the reactants onto the deposition surface must occur. Thirdly, once the reactants have adsorbed onto the surface, a chemical reaction involving the transfer of electrons from the reducing agent to the metal ions occurs. Fourthly, after the metal has been reduced and deposited onto the surface, the products of the reaction including the oxidised agent, salts, H_2 and H^+ ions, must all desorb from the surface before the adsorption of fresh reactants onto the surface. The final step in the process is the diffusion of the products

away from the surface. This allows for a replenished solution to diffuse towards the surface and the five stages of the process are then repeated.

As discussed in section 4.1, the reaction may be limited by one of two mechanisms. If the diffusion of reactants and products to and from the surface occur at a slower rate than the chemical reaction, then the process is said to be diffusion limited. However, if the chemical steps, the adsorption, the reaction or the desorption, occur at the slowest rate, then the chemical reaction is said to be kinetically controlled.

4.4.2 Experimental

Prior to an investigation of experimental results, let us consider a polycarbonate template structure placed in the Ni-B deposition bath described in Table 3.4. The electrolyte contained a concentration of 0.25 M $NiSO_4$ as the active source of Ni^{+2} ions and 0.06 M DMAB as the reducing agent. This corresponds to 1.51 x 10^{23} Ni ions and 3.61 x 10^{22} DMAB molecules per litre of solution. The membrane pores have a diameter of 400 nm and a length of 20 μm which corresponds to a volume of 2.51 x 10^{-18} m^3 and a surface area of 2.51 x 10^{-11} m^2. When filled with electrolyte, a single membrane pore contains 3.78 x 10^8 Ni atoms and 9.08 x 10^7 B atoms. The atomic radius of a Ni atom is 124 pm and the atomic radius of a B atom is 85 pm. Assuming perfect spheres, this gives a volume of of 7.99 x 10^{-30} m^3 for a Ni atom and 2.57 x 10^{-30} m^3 for a B atom. The total volume of Ni atoms within the nanotube structure is 3.02 x 10^{-21} m^3 and the total volume of B atoms is 2.34 x 10^{22} m^3. Assuming that all the atoms present can be electrolessly deposited along the pore walls to form a Ni-B alloy, the total volume of deposit will be 3.26 x 10^{-21} m^3. If these atoms are deposited uniformly along the membrane walls which have a total surface area of 2.51 x 10^{-11} m^2, the achieved deposit will have a thickness of 1.29 x 10^{-10} or

129 pm, approximately half a Ni atom thick. This indicates that not even a single layer of atoms would be deposited along the pore walls. Therefore, from these results we conclude that diffusion of electrolyte throughout the nanotube is vital for a sustainable electroless reaction to take place. Even if the concentrations were increased by a multiple of 10, due to the extremely small volume of the nanotube structure, a nanotube with a wall thickness of only 1 nm would be deposited without diffusion.

Diffusion of the electrolyte along the nanotube axis is governed by Fick's Law in one-dimension as shown in equation 4.1,

$$J = D\frac{\partial \phi}{\partial x} \tag{4.1}$$

where J = diffusion flux, the amount of substance that will flow through a unit area per unit time, D = diffusion coefficient, ϕ = the concentration per unit volume and x = position along the tube axis. The rate at which the Ni ions, DMAB molecules and OH^- ions will diffuse through the nanotube is dependent on J, the diffusion flux. The diffusion flux is directly proportional to both the diffusion co-efficient and the concentrations of the reactants. The diffusion co-efficient of a liquid can be estimated from the Stokes-Einstein equation for diffusivity and is given by,

$$D = \frac{k_B T}{3\pi\mu d} \tag{4.2}$$

where, D = diffusion co-efficient , k_B = the Boltzmann constant, T = temperature, μ = viscosity of the liquid and d = molecule size. Electroless deposition takes in the range of 20 °C - 60 °C (293 K – 333 K). While the diffusion coefficient is directly proportional to temperature it is also inversely proportional to viscosity. The viscosity of water at 60° C is approximately half that at 20 °C. Therefore, the rate of diffusion

at 60° C is just over twice that at 20 °C. As temperature increases there is also an increased deposition rate resulting in diffusing particles being electrolessly deposited on the nanotube walls close to the pore opening. As this deposition process occurs at a large rate, further diffusion along the tube axis is prevented and nanotubes with a non-uniform wall thickness are formed. The pore opening diameter of the nanotube decreases as deposition occurs, thus further reducing the diffusion rate, preventing deposition from occurring within the nanotube structure.

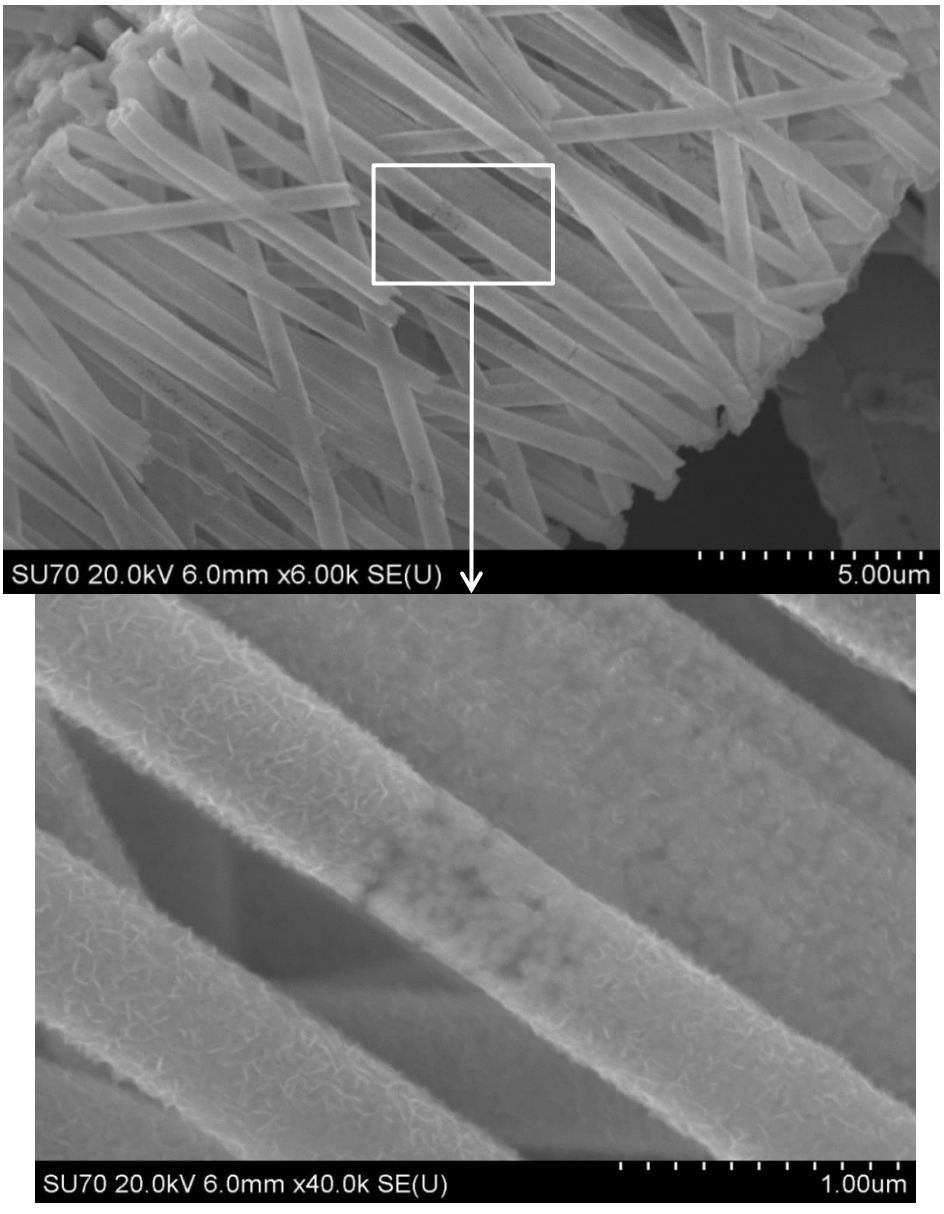

Figure 4.14: SEM image of a Ni-B nanotube array deposited from the deposition bath described in Table 3.4. Inset: Incomplete nanotube at the centre of the nanotube axis.

We propose that the challenges associated with the electroless deposition of nanotubes within a template structure described in section 4.3 are due to a diffusion limited reaction occurring within the nanotube. Theoretically, a kinetically controlled reaction can be obtained if the electroless deposition rate is reduced, so that electrolyte diffusion along the nanotube axis no longer limits the deposition process. A kinetically controlled reaction is desired because it will lead to the formation of continuous nanotubes with a uniform wall thickness.

Although deposition may start as a kinetically controlled reaction, due to a constantly decreasing pore diameter, it is possible that the deposition reaction may change from kinetically controlled to diffusion limited. As shown in Fig. 4.14, an almost fully continuous nanotube array has been formed. However, at the exact centre of the nanotube 10 µm from both ends a 1µm section of nanotube is incomplete, see inset of Fig. 4.14. Although deposition along most of the nanotube axis may have been kinetically controlled, deposition at the centre of the nanotube is diffusion limited. This prevents the formation of a 20 µm long continuous nanotube. Therefore, achieving a completely kinetically controlled reaction along the full length of the nanotube axis is vital for the formation of continuous nanotubes with uniform wall thickness.

4.4.3 Summary

From these results we have established that a kinetically controlled reaction is required to achieve the formation of continuous end-opened nanotubes with a uniform wall thickness. In order to understand and control the kinetics of the deposition process, electroless deposition of a Ni-B alloy is used as an exemplar of this process.

Ni-B is chosen because there is a relatively simple deposition mechanism with only one type of metal ion being deposited.

4.5 Bath Parameters

4.5.1 Introduction

In order to achieve a kinetically controlled reaction, the electroless Ni-B deposition rate has to be minimised. By fully understanding the conditions that result in a kinetically controlled electroless deposition process, the model process can be used to deposit nanostructures of more complex alloys. In this section, the effect of citrate concentration, pH and temperature of the deposition bath on the electroless deposition process will be investigated.

4.5.2 Diammonium Citrate Concentration

As discussed previously in section 3.5.4, a complexing agent, diammonium citrate is used in the deposition bath. Citrate ions in solution bind with Ni ions in the electrolyte to form Ni complexes, reducing the concentration of free Ni^{+2} ions which can be reduced in the electroless deposition reaction. While diammonium citrate prevents the precipitation of Ni within solution and the decomposition of the electrolyte, it also has an effect on the electroless deposition rate.

Fig. 4.15 displays the total Ni-B mass deposited on the polycarbonate membrane with respect to deposition time for a range of diammonium citrate concentrations. Using the deposition bath described in Table 3.4 at a temperature of 40 ºC and pH 8, a diammonium citrate concentration of 0.074 M had a total deposited mass of 9.1 mg after 10 minutes of deposition. However, as citrate concentration increased, the total

deposited mass decreased, indicating that the presence of diammonium citrate reduces the rate at which Ni-B is deposited. At a diammonium citrate concentration of 0.118 M, the total deposited mass of Ni-B on the polycarbonate membrane was reduced to 7.6 mg.

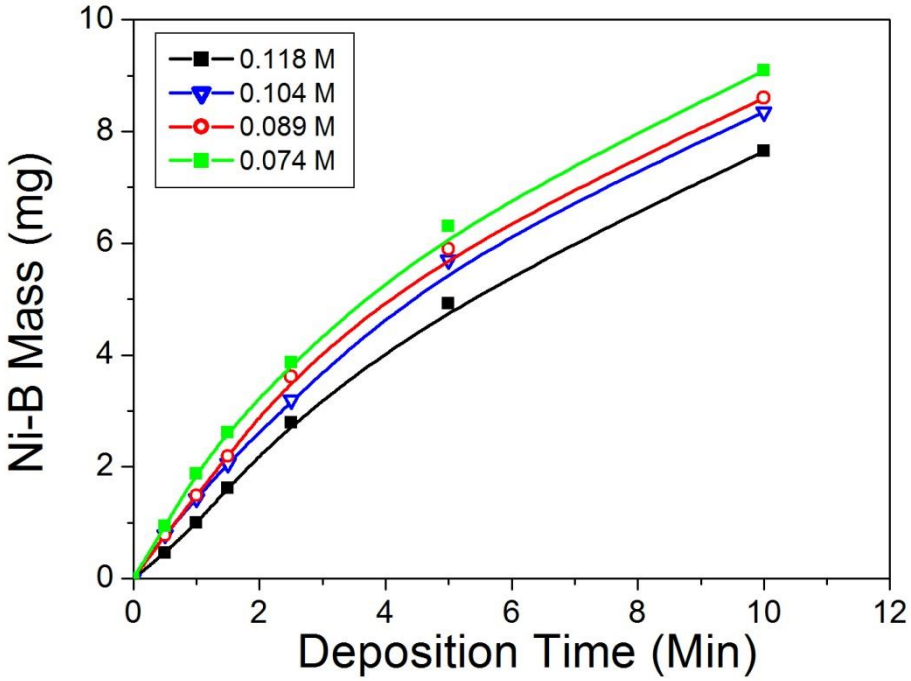

Figure 4.15: Total deposited Ni-B mass with respect to deposition time for a range of diammonium citrate concentrations carried out at a deposition bath temperature of 45 ° C.

The differential of the total deposited mass with respect to time gives the Ni-B deposition rate as a function of time. Fig. 4.16 shows the deposition rate as a function of deposition time for a large diammonim citrate concentration of 0.118 M. Matsubara et al. [9,12] recorded four distinct regions of deposition. An initial induction period during which very little deposition occurs was followed by an acceleration period during which the deposition rate increased as catalytic deposition occured at the Pd nucleation points and Ni-B islands began to grow. The maximum deposition rate recorded in their work corresponded to the point at which a continuous film is formed. This was followed by a deceleration period during which time the

deposition rate decreases. Finally a stationary period is observed during which steady state deposition was recorded. Fig. 4.16 shows the deposition rate as a function of time for a diammonium citrate concentration of 0.118 M. Only three regions of deposition are observed; the acceleration, deceleration and stationary regions. The initial induction region was not observed as it occurred at a time of less than 30 seconds.

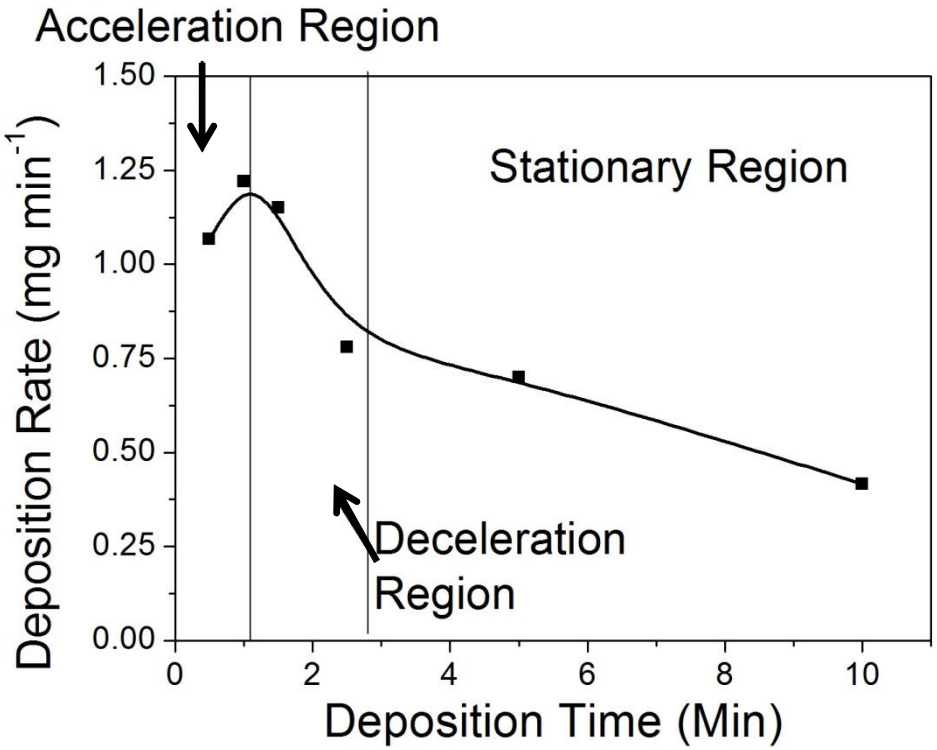

Figure 4.16: Ni-B deposition rate as a function of deposition time for a diammonium citrate concentration of 0.118 M deposited from the deposition bath described in Table 3.4.

After a deposition time of 30 seconds, a deposition rate of 1.07 mg min^{-1} is recorded. However, this is already within the acceleration region and the deposition rate continues to increase up to a deposition time of 60 seconds. During this acceleration period, catalytic deposition is occurring at the Pd nuclei and Ni-B islands are growing out from each nucleation site. As the deposition surface area increases, a corresponding increase in the deposition rate is recorded. We recorded a maximum deposition rate of 1.25 mg min^{-1} at a deposition time of 60 seconds.

Matsubara et al. [12] indicate that this maximum corresponds to the point at which complete surface coverage is achieved.

The theory proposed by Matsubara et al. [12] is that initial Ni-B deposition occurs at Pd nucleation sites, which have a large catalytic activity. As the Ni-B islands grow the surface area at which electroless deposition can occur increases and a corresponding increase in the deposition rate is observed. However, Ni-B has a lower catalytic activity than Pd. Therefore, as the Pd sites become covered by Ni-B a decrease in the deposition rate is observed until a continuous Ni-B film is formed. At this point, a stationary region is observed at which the deposition rate becomes constant. We believe that a similar process in occurring here.

In the stationary region, the deposition rate is expected to reach a constant value. However, as observed in Fig. 4.16, we observe a constant decrease in the Ni-B deposition rate within the stationary region. This may be due to a number of factors. Within this region, Ni-B deposition is occurring both on the membrane surface and within the nanotube structure. As the nanotube wall thickness increases, the internal radius of the nanotube decreases, resulting in a decreased internal nanotube surface area. This could explain the observed decrease in the deposition rate. Deposition also occurs on the surface of the membrane causing a decrease in the pore diameters at both ends of the nanotube. This limits diffusion of the electrolyte within the nanotubes, resulting in a decreased deposition rate. Small changes in the concentrations of Ni^{+2}, DMAB and changes in the pH of the electrolyte may also contribute to the reducing deposition. However, a decreasing rate was not observed in previous studies [12,13]. Therefore, although steady state deposition is expected

within the stationary region, we can attribute the decreasing deposition rate to the use of a nanostructured template.

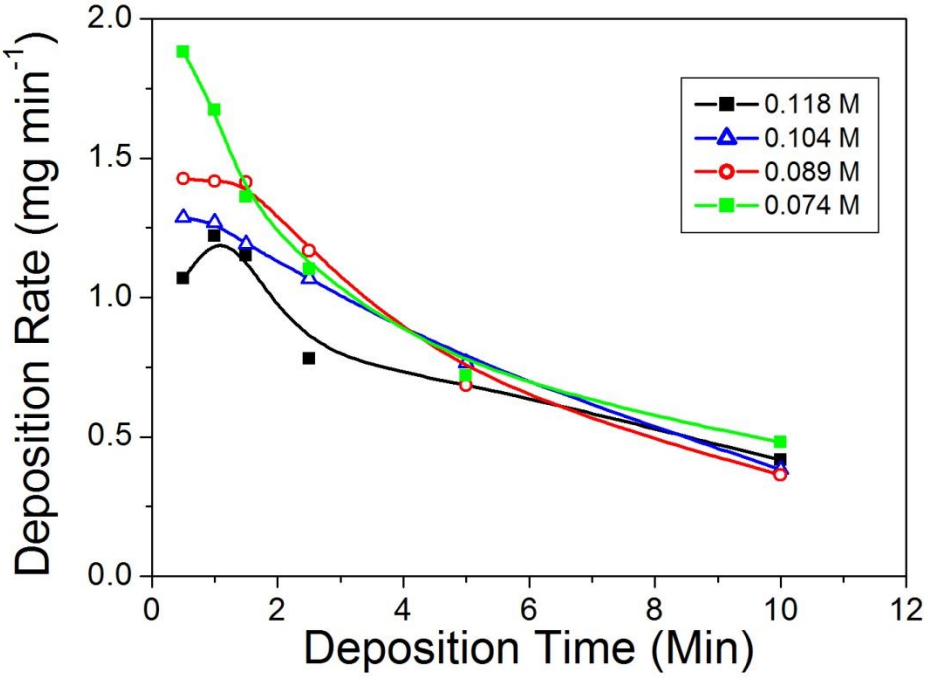

Figure 4.17: Deposition rate as a function of deposition time for a variety of diammonium citrate concentrations found by differentiating the graph in Fig. 4.15.

The deposition rates as a function of deposition time for a range of diammonium citrate values are shown in Fig. 4.17. For diammonium citrate concentrations between 0.074 M and 0.104 M, the induction and acceleration regions are not observed as they occur at deposition times of less than 30 seconds. As the deposition rate is constantly decreasing with respect to deposition time, only the deceleration and stationary regions are observed. This indicates that at diammonium citrate concentrations below 0.104 M, the initial catalytic reaction occurs at a fast rate resulting in a maximum deposition rate at deposition times of less than 30 seconds. As the diammonium citrate concentration increases, the maximum deposition rate decreases. This is due to a decrease in the number of free Ni^{+2} ions available to take part in the reaction. However, after 10 minutes of deposition, little difference is observed between the

deposition rates with respect to diammonium citrate concentration as all deposition converge to a value of approximately 0.5 mg min^{-1} after 10 minutes of deposition. This indicates that within the stationary region, the deposition rate becomes independent of citrate concentration.

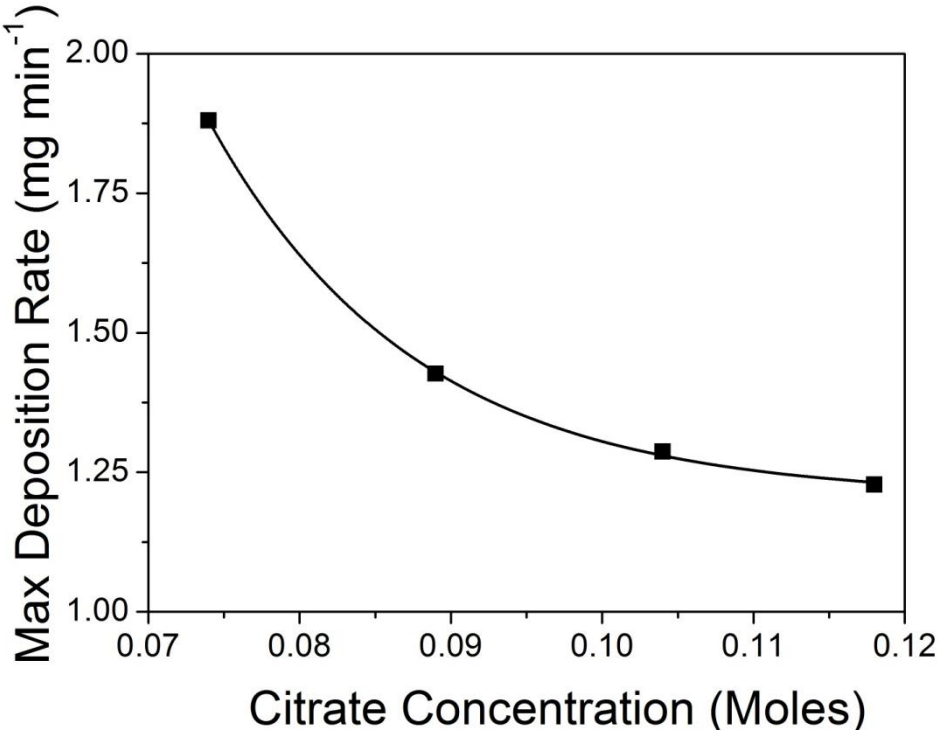

Figure 4.18: Maximum Ni-B deposition rate as a function of diammonium citrate concentration. The displayed curve acts as a guide to the eye.

The maximum deposition rate achieved as a function of diammonium citrate concentration is shown in Fig. 4.18. The maximum deposition rate corresponds to the point at which the electroless deposition process changes from the acceleration region to the deceleration region. As the diammonium citrate concentration increases there is a corresponding decrease in the maximum Ni-B deposition rate. For a low citrate concentration of 0.074 M, the maximum deposition rate is 1.9 mg min^{-1}. An increased citrate concentration of 0.118 M has a corresponding maximum deposition rate of 1.1 mg min^{-1}. However, the change in deposition rate with respect to citrate concentration is not linear. As the citrate concentration increases above 0.1 M, large

changes in citrate concentration result in small changes in the deposition rate. Previously for Ni-P deposition from a deposition bath that contained diammonium citrate, decreases in deposition rate were observed up to 0.25 M concentration at which point almost no deposition occurred [14].

The maximum deposition rate is a function of the free Ni^{+2} ion concentration within the electrolyte. As mentioned previously in section 3.5.4, diammonium citrate molecules bind with Ni ions to form a Ni complex as shown in Fig. 3.11. The nickel complex can dissociate to form free nickel ions and an equilibrium state of complexed and uncomplexed Ni^{+2} ions are formed as shown in Eqn. 4.3, where the citrate molecule is represented by the letter *L*.

$$NiL \leftrightharpoons Ni^{+2} + L \tag{4.3}$$

A state of equilibrium is achieved for Eqn. 4.3, with a number of free Ni^{+2} ions released and available for deposition. Therefore, the observed decrease in deposition rate with an increasing citrate concentration is due to a reduction in the number of free Ni^{+2} ions available for reaction. By controlling the citrate concentration, the free nickel ion concentration can be regulated. The equilibrium constant K_m, also known as the instability constant for equation 4.3 is given by,

$$K_m = \frac{[Ni^{+2}][L]}{[NiL]} \tag{4.4}$$

This is often also referred to as the stability constant K_s, given as,

$$K_s = \frac{1}{K_m} = \frac{[NiL]}{[Ni^{+2}][L]} \tag{4.5}$$

As the citrate concentration increases the number of free Ni^{+2} ions on the right hand side of Eqn. 4.3 will reduce and the NiL concentration on the left hand side of the equation will increase. An increased NiL concentration and reduced Ni^{+2}

concentration increase the value of the stability constant, which corresponds to a decreased deposition rate.

In my experiments, a low Ni-B deposition rate was achieved for a diammonium citrate concentration of 0.118 M. Therefore, an electrolyte containing 0.118 M diammonium citrate will be used to achieve a kinetically controlled deposition process within the template structure.

4.5.3 Effect of pH

The pH of the electrolyte has a large influence on the kinetics of the Ni-B deposition process. If the deposition bath is acidic, with a pH of 4 or below, no deposition will occur. However, in very alkaline solutions with a pH of 12 and above, the solution may become unstable and decompose with the precipitation of Ni-B within the electrolyte, as described previously in section 3.7.

Fig 4.19(a) shows the total deposited Ni-B mass on a polycarbonate membrane as a function of deposition time for a range of pH values, using the deposition bath described previously in Table 3.4 at a temperature of 45 ºC. As the pH of the deposition bath increases, there is a corresponding increase in the total mass of Ni-B deposited on the polycarbonate membrane. For a pH of 6, the total Ni-B mass deposited was 13.7 mg after 60 minutes of deposition. For a pH of 10, the total deposited mass was 16.2 mg. As the deposition had been allowed to occur for an hour, end-closed nanotubes were formed and much of the deposit exists as a thin film and not a nanotube structure. At a pH of 4, no deposition occurred as DMAB does not oxidise in a very acidic solution. Conversely, above a pH of 12, the solution was unstable and decomposition of the deposition bath occurred. This was due to the

precipitation of Ni within the electrolyte. At a pH of 12, the solution was stable for a short period of time after which the precipitation of Ni occurred.

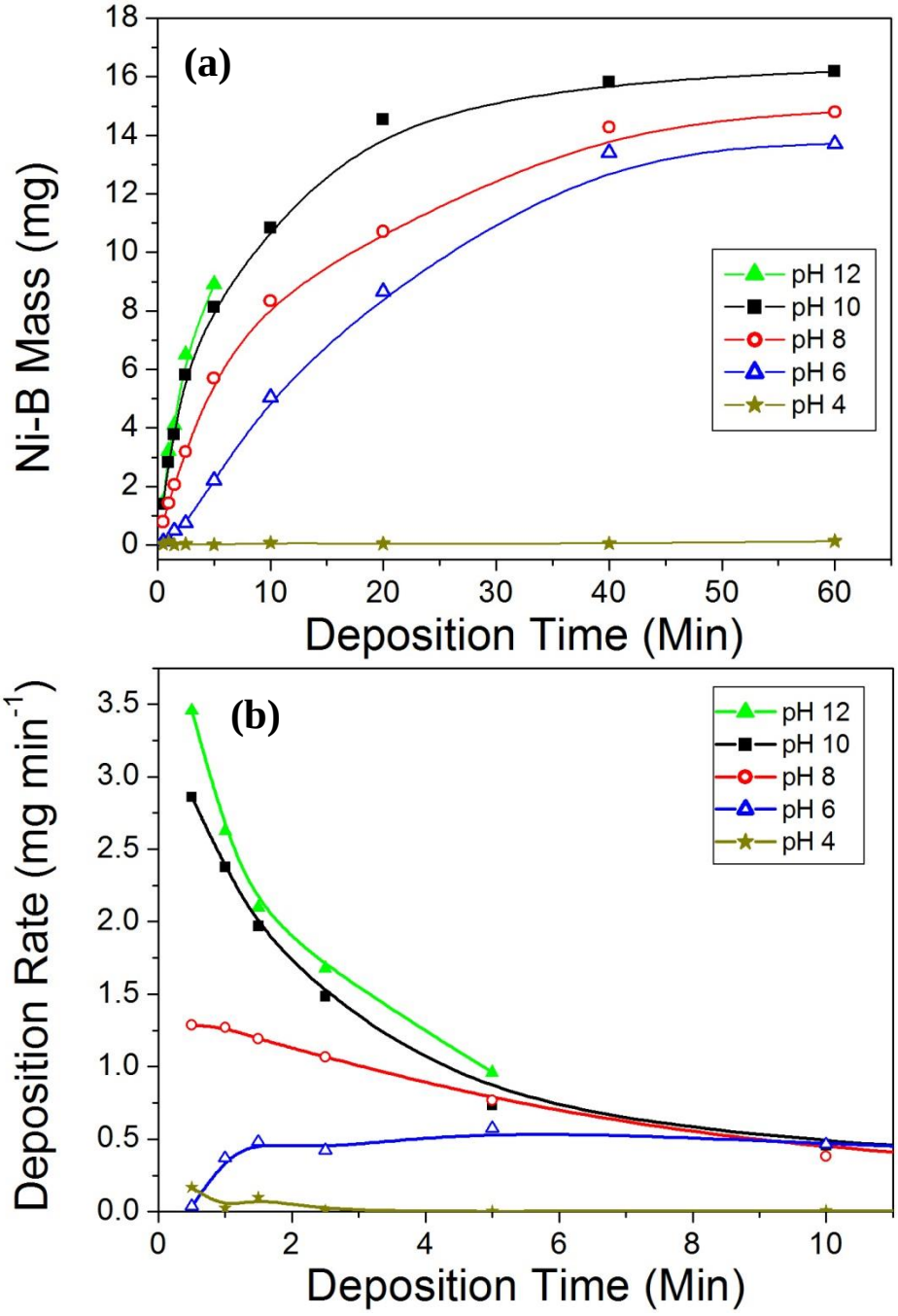

Figure 4.19: (a) Total deposited Ni-B mass with respect to deposition time for a range of pH values carried out at a deposition bath temperature of 45 ° C. **(b)** Deposition rate as a function of deposition time for a range of pH values found by differentiating the graph in (a).

The deposition rate as a function of deposition time for a range of pH values is shown in Fig. 4.19(b) and was obtained by differentiating the curves in Fig. 4.19(a). The

main deviations in deposition rate for each pH value occur at low deposition times, during the initial acceleration period which involves the nucleation of Ni-B islands at catalytic Pd atoms. For pH values of 12 and 10, the initial acceleration region is not observed as it occurs at a deposition time of less than 30 seconds. As discussed previously in section 4.5.2, this indicates that a continuous deposit has been formed on the membrane surface at a deposition time of less than 30 seconds. The maximum deposition rates recorded were 3.5 mg min^{-1} and 2.8 mg min^{-1} for pH values of 12 and 10 respectively. At a pH of 8, the maximum deposition rate is recorded at a time of 30 - 60 seconds. However, for a pH of 6, the induction, acceleration and stationary regions are all visible. For the first 30 seconds, no deposition occurs, corresponding to the initial stationary period. An acceleration region is observed between 30 and 90 seconds as initial Ni-B nucleation occurs. However, the slope of the acceleration region is small, indicating that Ni-B nucleation at catalytic Pd atoms occurs at a very slow rate. This was observed visually as, unlike large pH values of 10 and 12, an aggressive reaction with a large amount of fizzing due to hydrogen evolution did not occur. Instead, a smoother transition to a constant bubbling rate was observed. No clear maximum deposition rate is observed and the deceleration region is not present. Instead, an almost stationary period of deposition occurs after the acceleration region corresponding to the constant bubbling rate observed. This indicates that there is a very low number of free Ni^{+2} ions within solution, which limit the deposition rate and as a result, a maximum value is never reached.

During the stationary period between deposition times of 4-10 minutes, the deposition rates at pH values of 8, 10 and 12 decrease. However, the deposition rate at a pH of 6 remains constant. As discussed previously in section 4.5.2, this decrease is attributed

to a decrease in free Ni^{+2} ion concentration and the closing of the nanotube pores, preventing deposition from occurring within the nanotube structure. This indicates that at pH 6, the number of free Ni^{+2} ions does not decrease, as the rate at which deposition is occurring is lower than the rate at which free Ni^{+2} ions are produced within the solution. As the deposition rate does not decrease, it can also be deduced that the pores of the nanotubes do not close, indicating that deposition is occurring at a constant rate throughout the nanostructure. From these results, we can deduce that a kinetically controlled reaction is achieved at a pH value of 6.

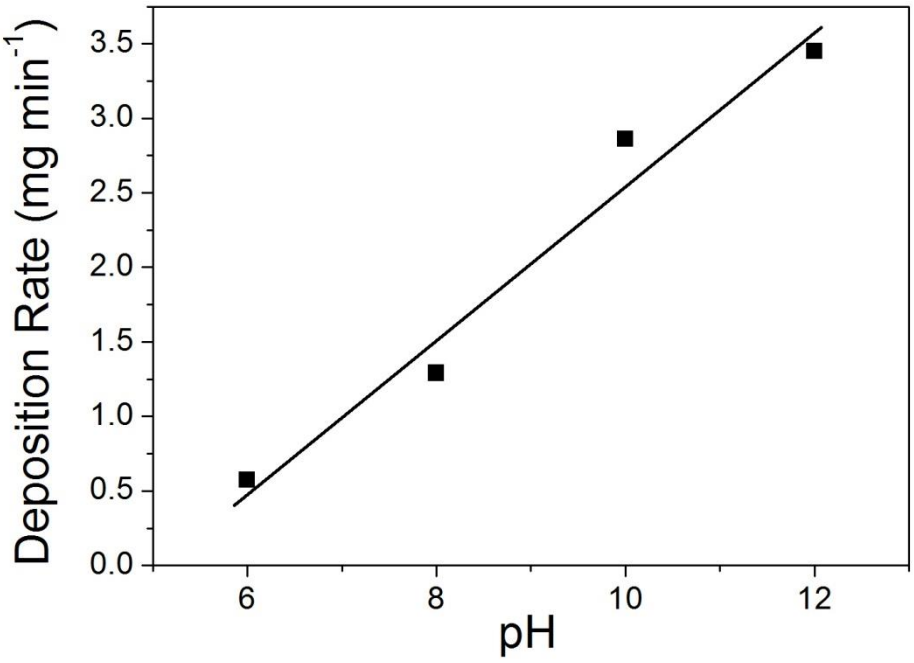

Figure 4.20: Maximum Ni-B deposition rate as a function of electrolyte pH. The trendline acts as a guide to the eye.

As discussed previously in section 3.6, electroless Ni deposition can occur via hydrolysed Ni mechanism. It is important to note that this hydrolysed deposition mechanism is a separate process from Ni hydrolysis that results in the precipitation of Ni and the decomposition of the deposition bath. As the pH of the electrolyte increases, there is an excess amount of OH^- ions present with which Ni^{+2} can break free from the citrate complex and hydrolyse to form $Ni(OH)_2$. In this hydrolysed

form, Ni is reduced by DMAB, depositing Ni-B on the polycarbonate membrane. Fig. 4.20 shows the maximum deposition rate achieved with respect to bath pH. A maximum recorded deposition rate of 3.5 mg min^{-1} for a pH of 12 is due to the large concentration of OH^- ions present within the solution. A much lower maximum deposition rate of 0.57 mg min^{-1} is observed at a pH of 6 due to the limited number of OH^- ions available in solution.

From these results, it is clear that there is a relatively linear relationship between deposition rate and electrolyte pH. The ideal pH to achieve a kinetically controlled deposition reaction within the template structure is pH 6. However, as discussed previously in chapter 2, the bath pH also controls the composition of the deposit with a large boron content recorded at low pH values [15,16]. The composition and associated properties of the deposited Ni-B nanostructures with respect to pH will be discussed in detail in chapter 5. Therefore, although controlling the pH can achieve the low deposition rate required for a kinetically controlled reaction, pH is not a suitable parameter to control, as only certain alloys can be deposited.

4.5.4 Temperature

Although a large decrease in deposition rate can be achieved through the variation of pH, large B contents are undesirable as they result in non-magnetic nanostructures. Therefore, a more suitable parameter to control the Ni-B deposition rate is the bath temperature. To investigate the effect of temperature on the deposition rate, an electrolyte pH of 10 was used. This ensured that the nanotubes were magnetic with a high Ni content. At pH 10, a $Ni_{80}B_{20}$ alloy is deposited. This will be discussed in detail in Chapter 5.

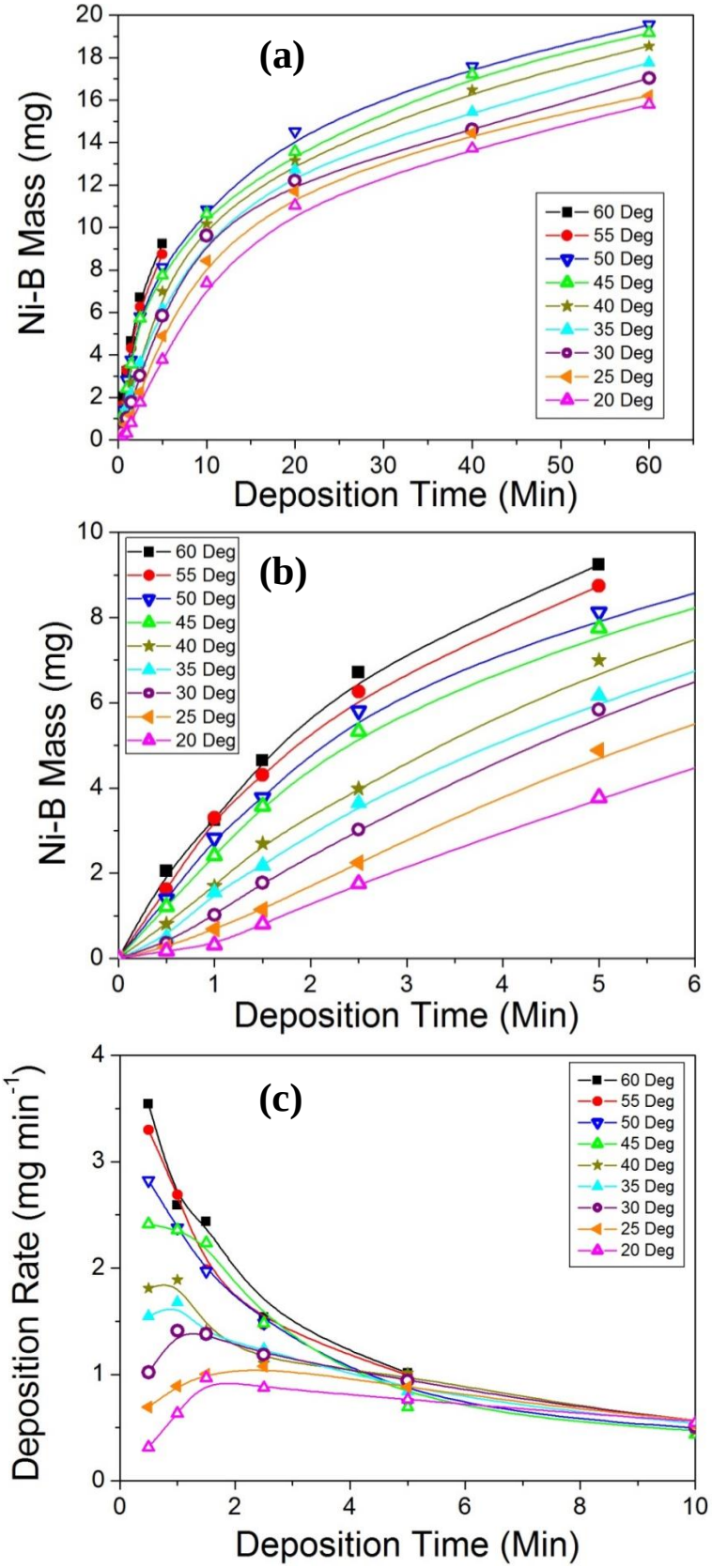

Figure 4.21: (a) Total deposited Ni-B mass with respect to deposition time for a range of temperatures using the deposition bath described in Table 3.4 at a pH of 10. **(b)** High magnification of graph (a) showing the total deposited mass with respect to time for the first 5 minutes of deposition. **(c)** Ni-B deposition rates with respect to deposition time found by differentiating the graph in 4.21(a).

For a range of temperatures from 20 to 60 °C, the total deposited Ni-B mass on the polycarbonate as a function of deposition time is shown in Fig. 4.21(a). The total deposited mass after a deposition time of 60 minutes ranges from 15.8 mg at 20 ºC to 19.5 mg at 50 ºC. At high temperatures above 50 ºC, decomposition of the deposition bath occurs due to the hydrolysis of Ni as discussed in section 3.7. Due to the increased energy of the deposition bath, the hydrolysis reaction occurs easily at elevated temperatures. Therefore, using the deposition bath described in Table 3.4, deposition must be carried out at a temperature of 50 ºC or below. However, as discussed previously in sections 4.5.2 and 4.5.3, if the pH of the deposition bath was reduced, or the concentration of citrate increased, deposition could be carried out at larger temperatures.

Fig. 4.21(b) is a zoomed in image of Fig. 4.21(a), showing the initial 5 minutes of change in mass with respect to deposition time. It is clear that initial Ni-B deposition is highly dependent on the bath temperature. For a deposition bath temperature of 20 °C, only 0.5 mg of Ni-B is deposited after 90 seconds, while for a deposition temperature of 50 ºC, 3.8 mg has been deposited after 90 seconds. This corresponds to a difference of 3.3 mg between a 50 ºC and 20 ºC deposition baths after only 90 seconds. After 60 minutes of deposition, the difference in mass was 3.8 mg. This indicates that temperature has a large influence on the initial Ni-B deposition rate, but after the initial nucleation period it has a reduced effect on the deposition rate.

The first derivative of mass with respect to deposition time gives the deposition rate as shown in Fig. 4.21(c). For temperatures greater than 45 °C, the acceleration region and maximum deposition rates occur within the first 30 seconds and are not observed. At 45 ºC, the maximum deposition rate possibly occurs between 30 and 60 seconds of

deposition. For temperatures between 30 - 40 ºC, the maximum deposition rate occurs at a deposition time of about 60 seconds and below 30 ºC this has increased to above 90 seconds of deposition. This indicates that, as the temperature decreases, the time taken for a continuous film to form increases.

For temperatures above 40 ºC, sharp decreases in deposition rate are recorded during the deceleration period. For the 60 ºC deposition bath, a deposition rate of 3.6 mg min^{-1} was recorded after 30 seconds which decreased to 1.2 mg min^{-1} after 5 minutes of deposition. There was a large initial deposition rate at the catalytic Pd nuclei at high temperatures. This was due to the energy associated with the deposition bath overcoming the activation energy of the electroless deposition process. At these initial elevated deposition rates, deposition within the nanotubes is diffusion limited which leads to the closing of the nanotube pores. This further decreases the deposition rate.

However, at temperatures below 40 °C, the initial acceleration period occurs at a slow rate. As the thermal energy of the bath is close to the activation energy required for Ni-B reduction at the catalytic Pd nuclei, the spontaneous catalytic reaction becomes a very slow process and Ni-B deposition occurs at a low rate. For a temperature of 20 ºC, a large deceleration after a maximum deposition rate is not observed. A maximum value of 0.96 mg min^{-1} is recorded after a deposition time of 90 seconds. This decreases to a value of 0.77 mg min^{-1} after a deposition time of 5 minutes. This indicates that deposition is occurring at a constant low rate throughout the deposition process and achieving a kinetically controlled reaction within the nanotube structure will be possible by reducing the temperature of the deposition bath.

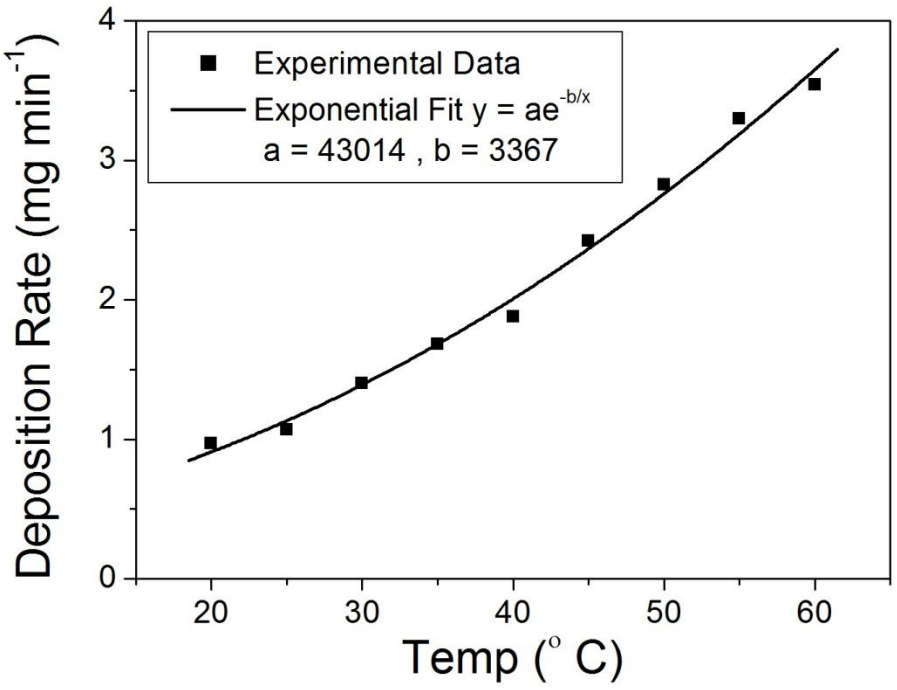

Figure 4.22: Maximum Ni-B deposition rates as a function of deposition bath temperature. The exponential fit corresponds to Eqn. 4.6. From the fitting we obtain k_0 4.30 x 10^4 mol min^{-1} g^{-1}, E = 28.0 kJ mol^{-1} where R = ideal gas constant 8.31 J K^{-1} mol^{-1}.

The maximum deposition rate achieved as a function of temperature is shown in Fig 4.22. Although the maximum rates occur at different deposition times, there is an increase in the maximum deposition rate achieved with respect to temperature. The correlation between deposition rate and bath temperature is described by the Arrhenius equation shown in Eqn. 4.6;

$$r = k_0 e^{-\frac{E_a}{RT}} \tag{4.6}$$

where, k_0 = reaction rate constant, A = pre-factor constant, E_a = activation energy of the reaction, R = ideal gas constant (8.31 J K^{-1} mol^{-1}), and T = temperature in Kelvin. Taking the natural logarithm of the Arrhenius equation yields;

$$\ln(r) = \frac{E_a}{R}\frac{1}{T} + \ln(k_0) \tag{4.7}$$

This can be written in the form of $y = mx + c$. An Arrhenius plot of the maximum deposition rates is shown in Fig. 4.23 .

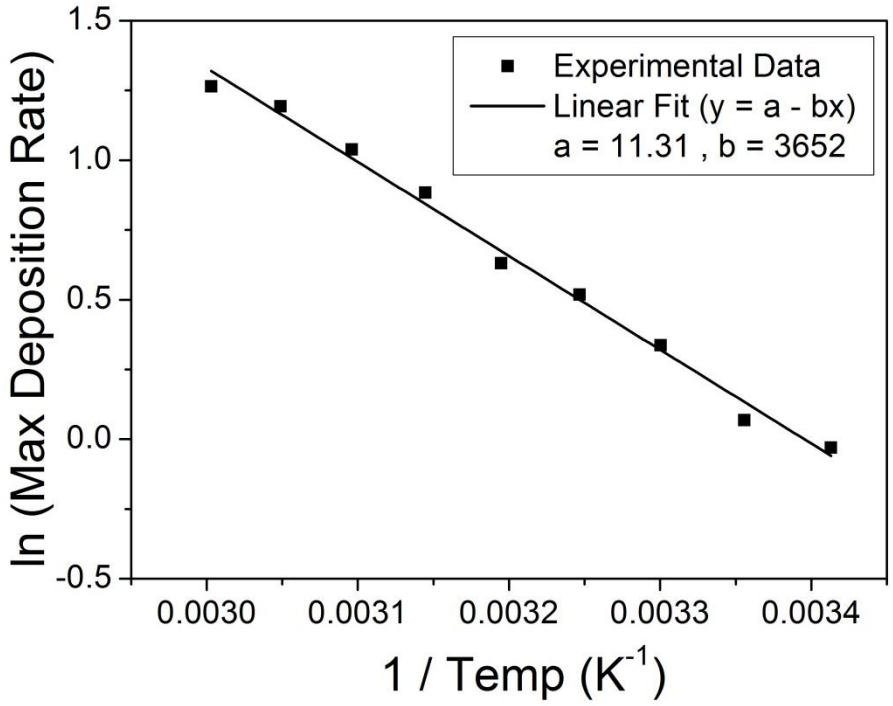

Figure 4.23: Arrhenius plot for maximum Ni-B deposition rates as a function of temperature. The linear fit corresponds to the Arrhenius equation shown in Eqn. 4.7 where a = 11.31 and b = 3652 K.

The values of *m* and *c* for the Arrhenius plot are – 3652 K and 11.31 respectively. This gives an activation energy of 30.3 kJ Mol^{-1} for the initial electroless Ni deposition reaction. This is similar to activation energies reported in the literature of 41 kJ Mol^{-1} for a Pd catalyst and 35 kJ Mol^{-1} for a Ni catalyst for the electroless deposition process with DMAB as a reducing agent [17].

As shown in Fig. 4.21(c), the deposition rates appear to converge after a deposition time of 10 minutes and become independent of temperature. They reach a value of 0.5 mg min^{-1}, similar to the rates observed after 10 minutes for a variety of pH values and citrate concentrations in sections 4.6.1 and 4.6.2 respectively. However, as shown in Fig. 4.24, the deposition rate continues to decrease after a deposition time of 10 minutes. For deposition times greater than 40 minutes, the nanotubes have become end-closed for all temperatures and the observed deposition rates are the deposition rates associated with an electrolessly deposited film on both sides of the

polycarbonate membrane. After 60 minutes of deposition, the rate has decreased to approximately 0.1 mg min^{-1}. The slow decrease in deposition rate observed is attributed to a decreasing Ni^{+2} concentration within the electrolyte, a decrease in the DMAB concentration and a decreasing pH. This is due to the by-product of H^{+} ions released during the reaction.

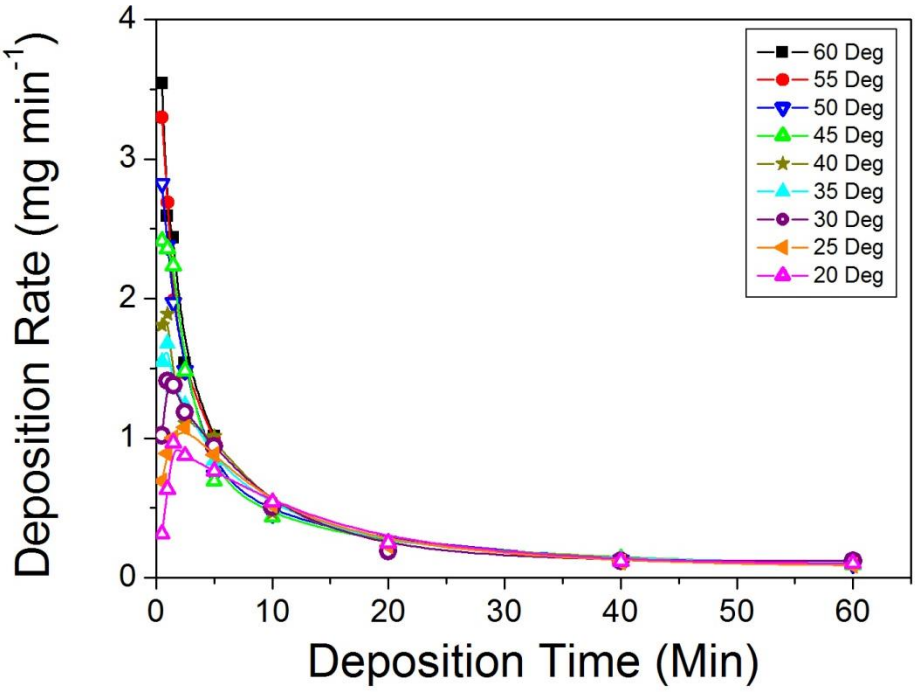

Figure 4.24: Ni-B deposition rates with respect to deposition time found by differentiating the graph in Fig. 4.21(a).

4.6 Pore Diameter

We have found that a relatively simple but effective way of establishing if a uniform deposition has occurred is to investigate the pore diameter of the nanotube with respect to both deposition time and total d eposited mass. For diffusion limited reactions, the deposition rate on the membrane surface is larger than within the nanotube pores and the nanotube pore will close quickly. However, at low deposition rates the pore will close slowly and a large amount of Ni-B will be deposited on the internal membrane walls to form nanotubes.

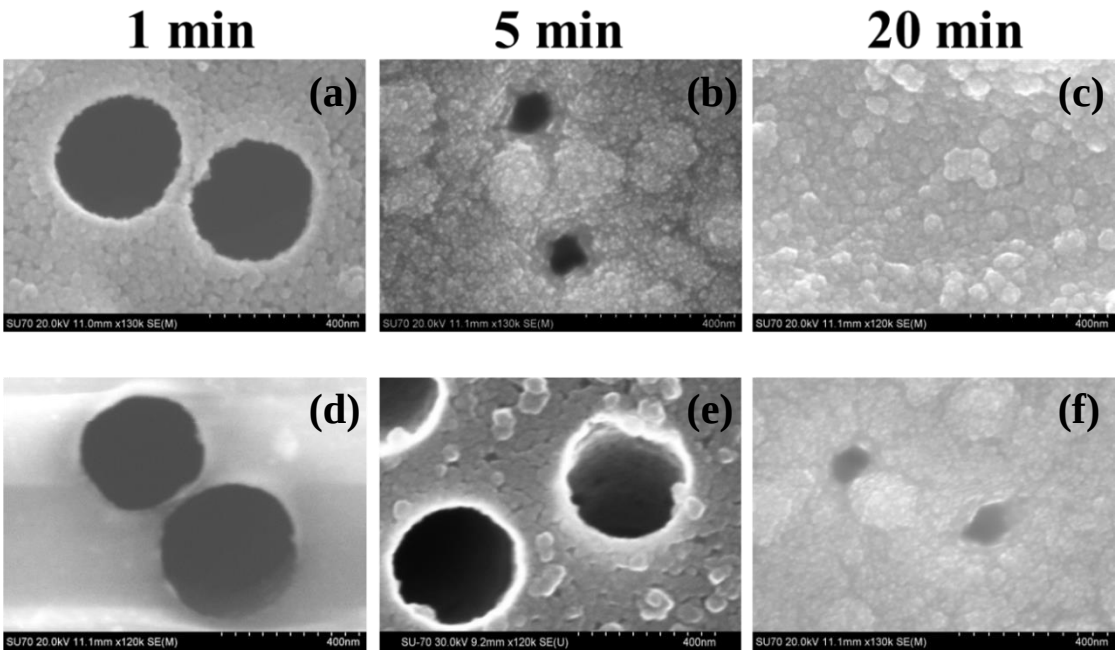

Figure 4.25: SEM images of the membrane pore diameters of Ni-B nanotubes taken for deposition times of 1, 5 and 20 minutes at temperatures of **(a, b, c)** 45 ° C and **(d, e, f)** 20 ° C**.**

SEM images of the pore diameters recorded at varying deposition times are shown for deposition temperatures of 45 °C (a,b,c) and 20 °C (d,e,f) in Fig. 4.25. The pore diameters of the nanotubes are larger at lower deposition temperatures for similar deposition times. After one minute of deposition at 45 °C, the pore diameter is approximately 300 nm and Ni-B islands have coalesced on the surface of the membrane to form a film. The time taken correlates with the observed maximum deposition rate for 45 °C as presented Fig. 4.21(c). This occurs between 30 and 60 seconds of deposition. However, at 20 °C a similar film formation is not observed until approximately 5 minutes of deposition, again correlating with the maximum deposition rate in Fig. 4.21(c). The pore diameter of the nanotube deposited at 20 °C for 5 minutes is approximately 300 nm, the same diameter as 1 minute of deposition at 45 °C. The total Ni-B masses deposited on the polycarbonate membrane are 2.5 mg after 1 minute at 45 °C and 3.5 mg after 5 minutes at 20 °C. As the pore diameters and surface morphologies are very similar for each sample, a larger mass of Ni-B is

deposited on the internal nanotube walls at 20 °C than 45 °C. This indicates that a kinetically controlled deposition may be occurring within the nanotube pores at low deposition temperatures.

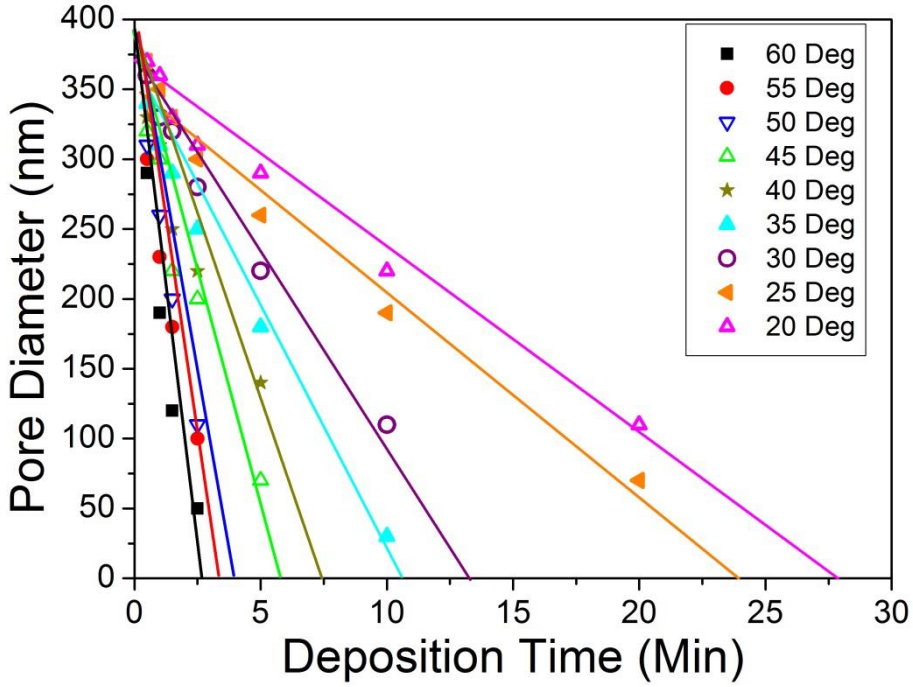

Figure 4.26: Ni-B nanotube pore diameters for a range of temperatures as a function of deposition time.

The pore diameter of the nanotubes as a function of deposition time is shown in Fig. 4.26 for a range of temperatures. For all temperatures, the change in pore diameter with respect to deposition time is approximately linear, indicating that the growth rate of the Ni-B film is constant. The deposition rate on the membrane surface is therefore constant and is kinetically controlled. For bath temperatures above 50 °C, with large deposition rates, the pore diameter decreases quickly with respect to time and the nanotubes become end-closed after deposition times of less than 5 minutes. However, as bath temperature is reduced, the deposition rate decreases and the time taken for end-closed nanotubes to form is increased. A deposition time of approximately 27.5 minutes is needed to create end-closed nanotubes at a deposition temperature of 20 °C. However, the time taken for end-closed nanotubes to form does

not give any insight into the kinetics of deposition within the pores of the template and the structure of the nanotubes.

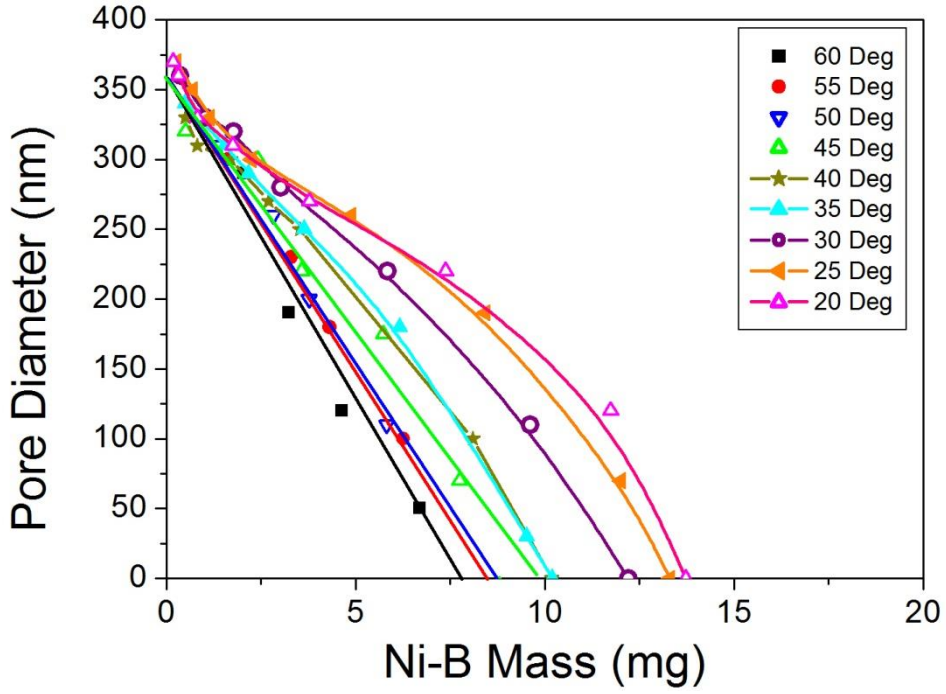

Figure 4.27: Ni-B nanotube pore diameters for a range of temperatures as a function of total deposited Ni-B mass.

The change in pore diameter with respect to total deposited mass is shown in Fig. 4.27. At high temperatures of 45 °C and greater, the rate of change of pore diameter with respect to total deposited mass is almost constant. This indicates that the vast majority of deposition is occurring on the membrane surface. Very little Ni-B is deposited within the nanotube structure because the deposition rate within the pores is diffusion limited. However, at low temperatures, the change in pore diameter with respect to time is not linear. This indicates that there is a change in deposition kinetics at lower temperatures.

Due to the hemispherical shape of the Ni-B island growth, the deposition rate on the membrane surface is equal in all directions. Therefore, it can be assumed that when the Ni-B film on the surface of the membrane is 200 nm thick, the pores, which have

an external diameter of 400 nm, will be covered and the nanotubes will become end-closed. As the membranes have a surface area of 0.000491 m^2 and the density of $Ni_{80}B_{20}$ is 7540 kg m^{-3}, a film thickness of 200 nm on both sides of the membrane corresponds to a total film mass of 1.5 mg. For depositions at temperatures above 45 °C, the Ni-B nanostructures have become end-closed after less than 5 minutes of deposition. A total deposited mass of between 7.5 mg and 8.5 mg is deposited on the polycarbonate membrane depending on the exact temperature. This corresponds to 1.5 mg of Ni-B on the template surface and up to 7 mg of Ni within the nanotube pores. Initially, the total surface area of the nanotubes is 20 times larger than the total surface area of film, though as the tube thickness increases the internal surface area decreases. As less than 5 times more Ni-B is deposited within the nanotube pores than on the surface, the deposition kinetics within the nanotube are diffusion limited and deposition occurs at a much lower rate than within the tubes. A total Ni-B mass of 7 mg deposited within the nanotube pores corresponds to a nanotube wall thickness of 52 nm calculated from Eqn. 4.9. However, due to a diffusion limited reaction within the pores, the wall thickness of the nanotube varies along the tube axis.

At a bath temperature of 20 ºC, a total Ni-B mass of 14 mg is deposited before the nanotubes become end-closed. This corresponds to 12.5 mg of Ni-B deposited within the nanotube pores and 1.5 mg deposited on the membrane surface. As over 8 times more Ni-B is deposited within the nanotubes than on the surface, deposition within the nanotube structure is kinetically controlled. A total nanotube mass of 12.5 mg corresponds to a nanotube wall thickness of 115 nm. Therefore, deposition at a low temperature of 20 ºC will result in a large amount of Ni-B deposited within the nanotube structure.

4.7 Deposition Kinetics Model

For a perfectly kinetically controlled deposition process throughout the template structure, the nanotube wall thickness and film thickness would be equal throughout the deposition process. The nanotubes would continue to grow radially inward to form nanowires and a film of thickness 200 nm would form on the membrane surface. The theoretical mass as a function of pore diameter can be calculated from Eqn. 4.8,

$$m = [(\pi R^2 - \pi r^2)Nl + 2A_s(R - r)]\rho \quad (4.8)$$

where, m = total deposited mass, R = external tube radius (400 nm), r = internal tube radius which is equal to the pore radius, l = length of the nanotubes (20 μm), N = number of nanotubes within the polycarbonate membrane (8.05 x 10^8), A_s = surface area of the membrane (4.9 x 10^{-4} m^2) and ρ = density of the $Ni_{80}B_{20}$ deposit (7540 kg m^{-3}). The theoretical mass of the Ni-B deposit is assumed to be equal to the total volume of the nanotubes, $(\pi R^2 - \pi r^2)Nl$, plus the volume of the films on both sides of the membrane surface, $2A_s(R-r)$, multiplied by the density of the deposit ρ.

For our experimental polycarbonate membrane template structure, this corresponds to a maximum deposited mass of 16.8 mg for which continuous nanowires connected at both ends by a 200 nm film are formed. The total mass of the nanotube structure without a film present is given by;

$$m_{tubes} = (\pi R^2 - \pi r^2)Nl\rho \quad (4.9)$$

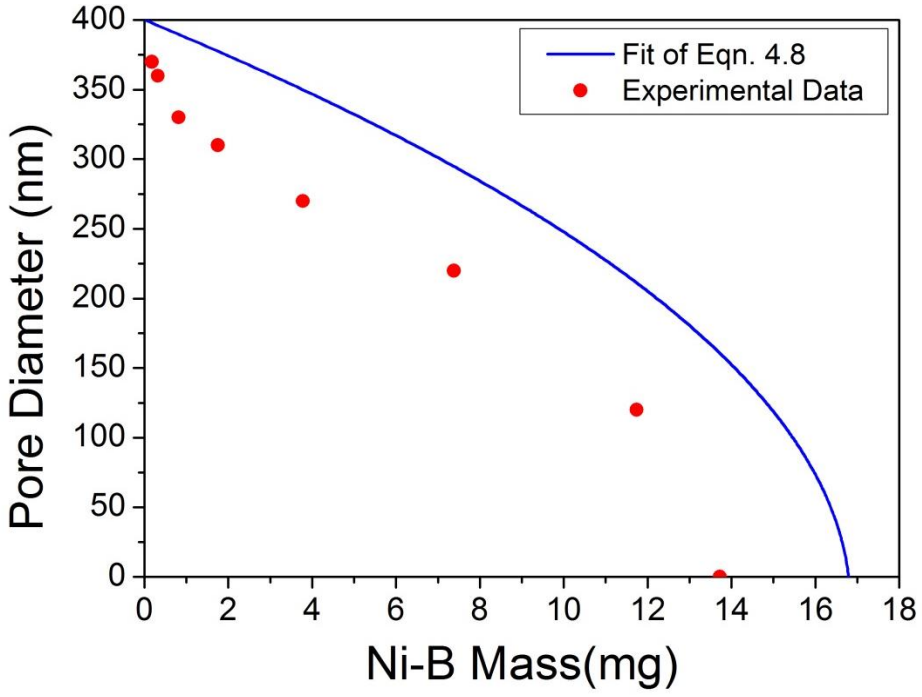

Figure 4.28: Pore diameter with respect to total deposited mass for Ni-B deposited onto a polycarbonate membrane at a bath temperature of 20 ºC (red curve) and a theoretical fit (blue curve) for completely kinetically controlled deposition.

A theoretical fit of this idealised deposition process compared to deposition carried out at 20 ºC is shown in Fig. 4.28. It is clear that the experimental data measured does not match the theoretical fit. The total Ni-B mass obtained is much lower than the expected theoretical value for each corresponding pore diameter. However, the experimental curve matches the shape of the theoretical fit with very little variation observed after a Ni-B mass of 2 mg has been deposited. Initially, the nanotube pores close quickly for deposited masses of less than 2 mg. From Fig. 4.21(b), this corresponds to deposition times of less than 2 and half minutes. This region corresponds to the catalytic activation period during which an increasing deposition rate is observed as shown in Fig. 4.21(c). An SEM image of Ni-B deposition on the membrane surface and within the membrane pores is shown in Fig. 4.29(a) and (b) respectively, for a deposition time of 90 seconds. A complete Ni-B film is present on the membrane surface, whereas incomplete Ni-B islands are present within the

membrane pores. This shows that a kinetically controlled deposition process is not taking place during the initial catalytic reaction because deposition occurs at a faster rate on the membrane surface than within the nanotube pores.

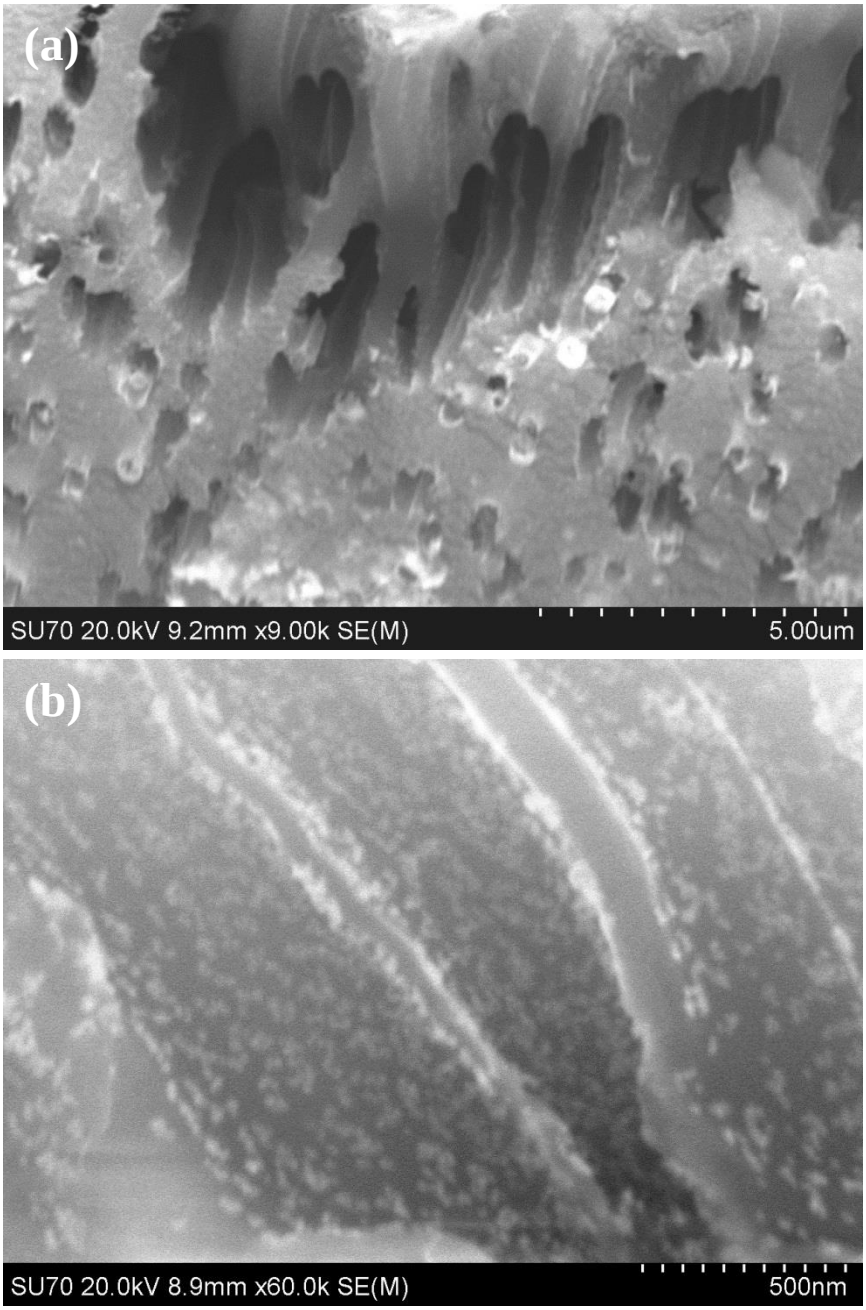

Figure 4.29: SEM image of **(a)** membrane surface and **(b)** internal nanotube pores of electrolessly deposited Ni-B from the deposition bath described in Table. 3.4 at a temperature of 20 °C for a deposition time of 90 seconds.

Therefore, the theoretical fit must be altered to allow for the initial catalytic process occurring on the membrane surface. It is approximated that, initially, a 30 nm Ni-B layer is deposited on the membrane surface with minimal deposition occurring within the nanotube pores. After this point, deposition will be assumed to occur at an equal rate on both the membrane surface and within the nanotube pores. With this modification, the pore radius is not equal to the internal tube radius, but instead is equal to (r – 30 nm). Eqn. 4.8 remains almost identical with only 1 small modification; an extra 30 nm film thickness is added to the original equation and is given by,

$$m = [(\pi R^2 - \pi r^2)Nl + 2A_s(R - (r - 30nm))]\rho \quad (4.10)$$

Ni-B mass as a function of pore diameter is plotted in Fig. 4.30(a) for the experimentally obtained data for nanotubes deposited at 20 ºC and the modified theoretical plot. At a deposition temperature of 20 ºC, three distinct regions of deposition type are observed. Initial deposition occuring at the Pd nuclei is a catalytic reaction and occurs at a fast rate. During this initial catalytic deposition phase, deposition within the nanotube is diffusion limited and there is a large initial decrease in pore diameter with respect to total deposited mass. After the initial activated Pd catalytic phase, the slope reduces and the pore diameter decreases slowly with respect to deposited mass. In this region, deposition within the nanotube structure closely matches the theoretical data, which indicates that a kinetically controlled reaction is occurring. For a kinetically controlled reaction, deposition is occurring at a constant rate throughout the nanostructure.

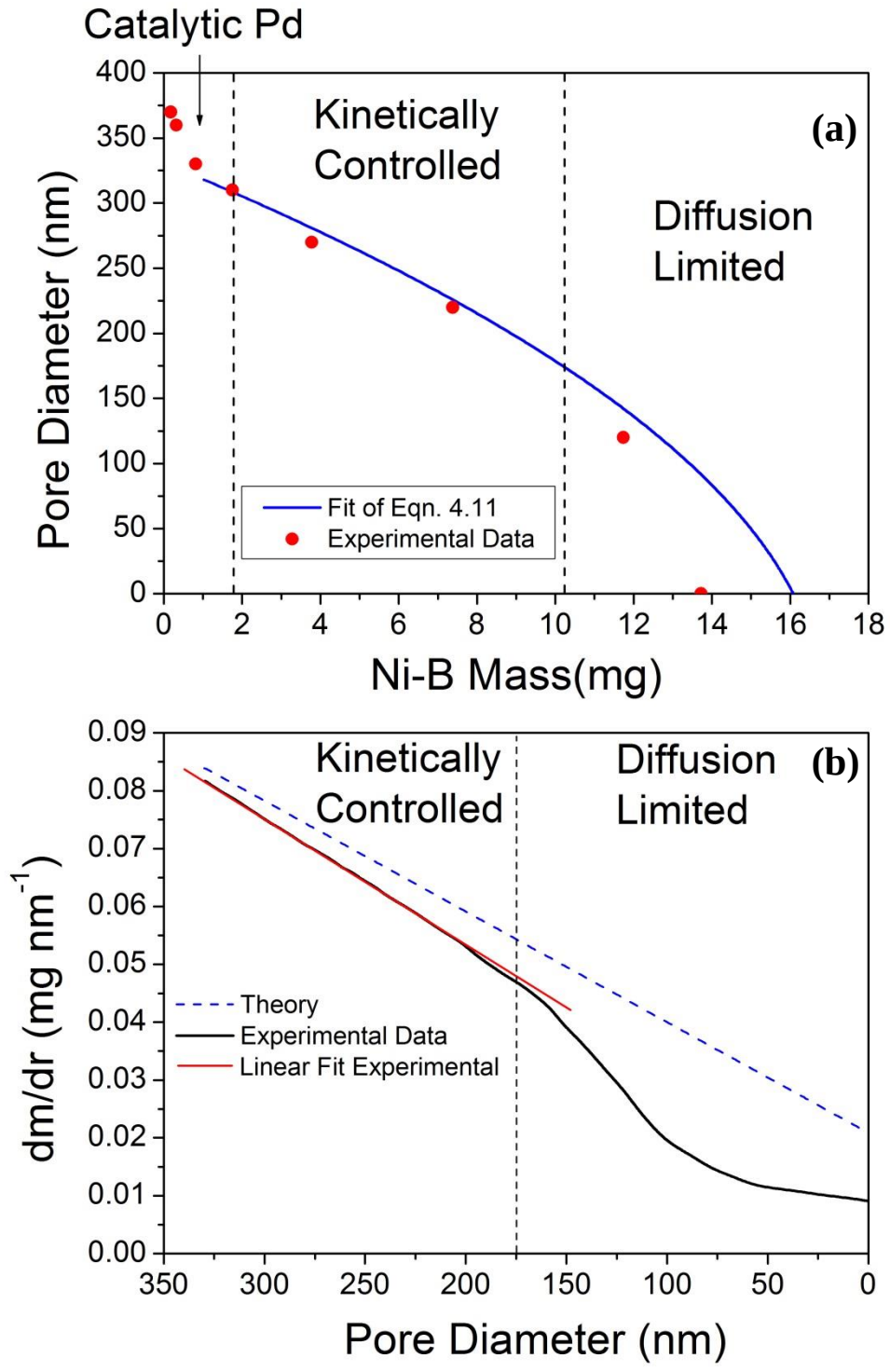

Figure 4.30: Pore diameter of Ni-B nanotubes deposited at 20 ºC versus total deposited mass, displaying 3 distinct regions of deposition within the nanotube structure – initial Pd catalytic, kinetically controlled and diffusion limited, compared against an idealised kinetically controlled reaction with corrections for initial catalytic process. **(b)** Rate of change of mass with respect to pore diameter plotted as a function of pore diameter.

The rate of change of mass with respect to pore diameter is plotted as a function of pore diameter for Ni-B deposition at 20 ºC and for the modified theoretical fit in

Fig. 4.30(b). The theoretical curve gives a constant deposition rate per unit surface area throughout the deposition process as would be expected for a kinetically controlled reaction. The experimental data also displays a constant deposition rate until a minimum diameter of 175 nm. At this diameter, there is a sharp change in the slope of the 20 ºC deposition, indicating that deposition within the nanotube pores has changed from kinetically controlled to diffusion limited. This matches the deviation from the theoretical curve seen previously in Fig. 4.30(a). The small difference between the slopes of the experimental and theoretical data is attributed to defects within the polycarbonate membrane such as incomplete pores and double or triple walled tubes. As a kinetically controlled reaction is achieved up to a pore diameter of 175 nm, continuous open-end nanotubes with a uniform wall thickness of approximately 110 nm can be achieved.

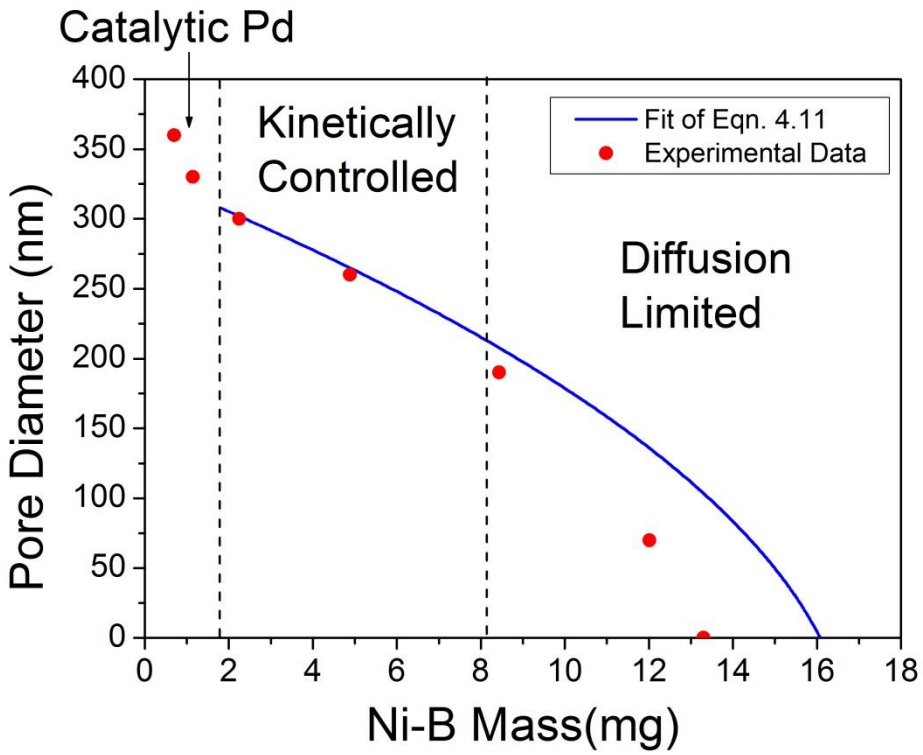

Figure 4.31: Pore diameter of Ni-B nanotubes deposited at 25 ºC versus total deposited mass, compared against an idealised kinetically controlled reaction with corrections for initial catalytic process.

As the temperature increases, the size of the kinetically controlled region observed decreases. At a deposition temperature of 25 ºC, there is a change from a kinetically controlled reaction to a diffusion limited reaction at a pore diameter of 200 nm as shown in Fig. 4.31. Therefore, it should be possible to form continuous end-open nanotubes with a wall thickness of 100 nm at 25 ºC. At 30 ºC, the kinetically controlled region is reduced further, with a pore diameter of approximately 250 nm, showing a change from kinetically controlled to a diffusion limited region. However, for temperatures of 35 ºC and above, no kinetically controlled region matching the theoretical fit is observed. For a bath temperature of 45 ºC, there is almost no resemblance to the theoretical fit, shown in Fig. 4.32, indicating that diffusion limits the deposition process. At temperatures of 50 ºC and above, the change in pore diameter with respect to mass is almost linear. This indicates that the vast majority of deposition is occurring on the membrane surface and very little deposition within the nanotube structure occurs due to a diffusion limited reaction.

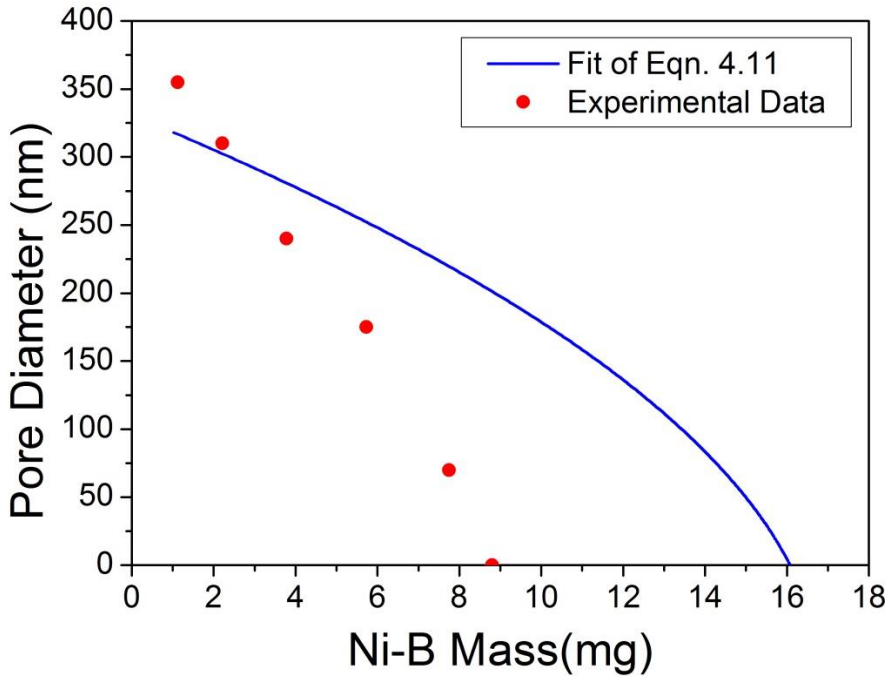

Figure 4.32: Pore diameter of Ni-B nanotubes deposited at 45 ºC versus total deposited mass compared against an idealised kinetically controlled reaction with corrections for initial catalytic process.

A plot of total deposited mass on the polycarbonate membrane as a function of deposition bath temperature is shown in Fig. 4.33. Between a temperature of 35 ºC and 60 ºC, there is an almost linear relationship between temperature and total deposited mass. In this region, deposition is diffusion limited and no match to the theoretical curve is observed. However, between a deposition temperature of 35 ºC and 30ºC, there is an increase in the slope of the graph. This increase in slope corresponds to the point at which deposition changes from a kinetically controlled deposition process at low temperatures to a diffusion limited reaction at high temperatures. Therefore, by maintaining a relatively low temperature of 20 – 30 ºC within the deposition bath, kinetically controlled deposition within the nanostructure can be achieved. By achieving a kinetically controlled deposition, we have overcome the previous challenges associated with the deposition process.

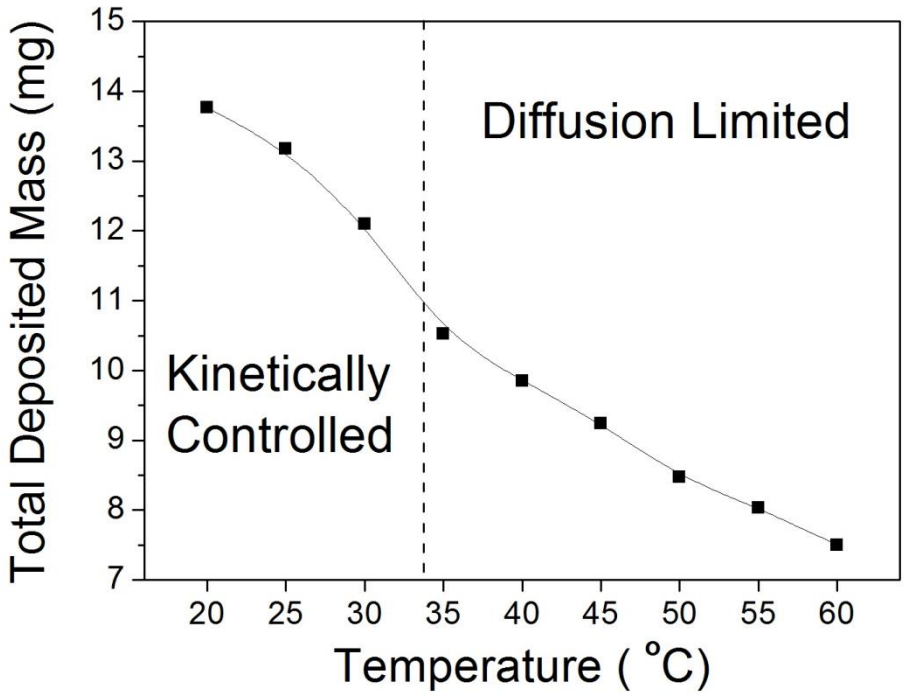

Figure 4.33: Total deposited Ni-B mass at the point at which the nanotubes become end-closed.

4.8 Continuous Uniform Nanotubes

As deposition at low temperatures is kinetically controlled and deposition at high temperatures is diffusion limited, the nanostructures obtained are compared to investigate the differences between the deposited nanostructure for a kinetically controlled reaction and a diffusion limited reaction. Fig. 4.34 shows SEM images of nanostructures formed at 50 ºC and 20 ºC for a deposition time of 40 minutes and compares the film and wall thicknesses.

For deposition at 50 °C, there is a considerable non-uniformity associated with the deposited nanostructures due to a diffusion limited reaction within the nanotubes and a kinetically controlled reaction on the membrane surface. The synthesised nanotubes have a wall thickness of 175 nm close to the nanotube base while the wall is only 60 nm thick at the centre of the nanotube as shown in Fig. 4.34(c) and (d) respectively. This confirms that deposition within the nanotube structure is diffusion limited at 50 ºC as the nanotube wall thickness decreases along the nanotube axis. The associated film has a thickness of 900 nm after 40 minutes of deposition as shown in Fig. 4.34(a). This is due to the large deposition rate on the membrane surface.

However, for low deposition temperatures, a more homogeneous nanostructure deposition is achieved. At 20 °C, the nanotube wall thickness is relatively uniform with a wall thickness of approximately 120 nm at the base of the tube and 100 nm at the centre of the tube as shown in Fig. 4.34(e) and (f). This indicates that for a low deposition rate, the deposition is occurring at the same rate throughout the nanotube structure, thus proving that a kinetically controlled deposition process is occurring. As

shown in Fig. 4.31, a kinetically controlled reaction was observed up until a pore diameter of 175 nm was reached, indicating that a wall thickness of 110 nm was deposited. These values also match the calculated wall thickness of 115 nm for a nanotube array with a mass of 12 mg as described in section 4.6.

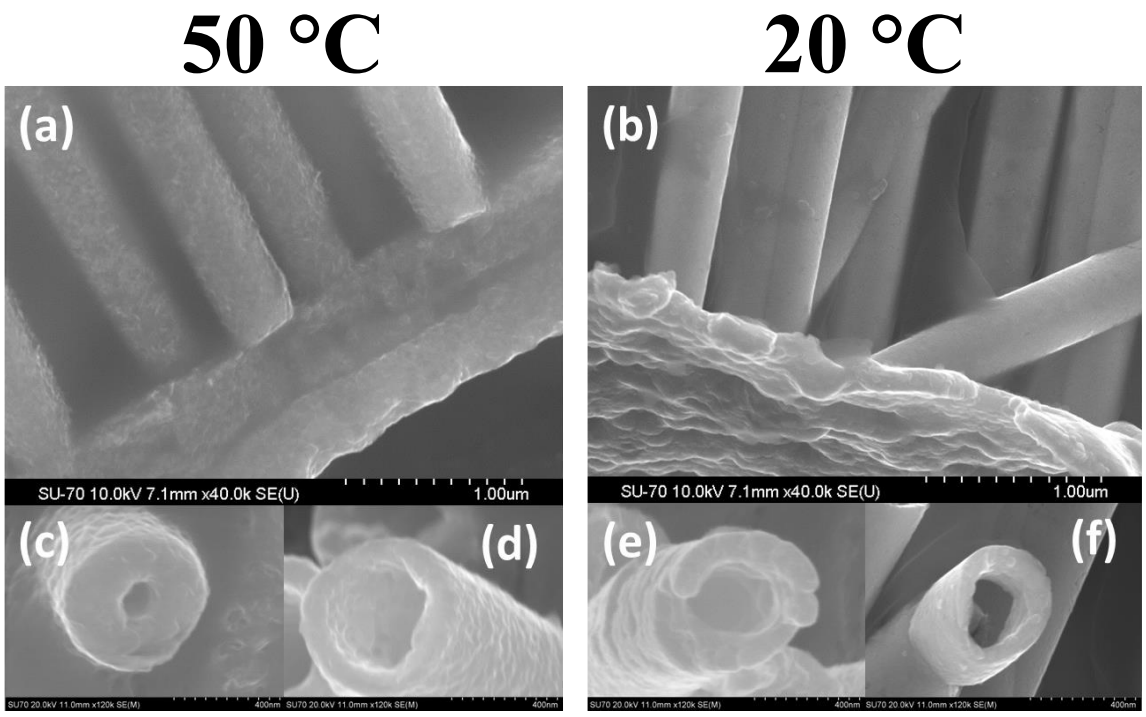

Figure 4.34: SEM images of Ni-B nanotubes deposited using the deposition bath described in Table 3.4 for 40 minutes at temperatures of (a) 50 °C with a film thickness of approximately 900 nm and (b) 20 °C with a film thickness of 200 nm. Wall thicknesses of nanotubes deposited at 50 °C (c) close to the nanotube base of 150 nm and (d) at the centre of the nanotube of 70 nm and nanotubes deposited at 20 °C (e) close to the nanotube base of 100 nm and (f) at the centre of the nanotube 80 nm.

However, TEM imaging is a more comprehensive method of observing the wall thickness of the nanotube structure. Unlike SEM, TEM imaging allows for measurement of both the position along the nanotube axis and the wall thickness of the nanotube. The TEM image in Fig. 4.35 provides conclusive evidence that a continuous nanotube with a uniform wall thickness is obtained at temperatures of 30 ºC and below. This image shows nanotubes 20 µm in length deposited at 30 ºC with a uniform wall thickness. The wall thickness remains at a constant value of

approximately 80 nm throughout the nanostructure. This indicates that a uniform kinetically controlled deposition process has occurred within the nanotube structure.

At 50 ºC a non-uniform deposit is formed along the walls of the membrane pores. This results in nanotubes with a non-uniform wall thickness as shown in Fig. 4.36. A thick wall is deposited at the nanotube ends close to the membrane pore. However, just a short distance along the nanotube axis, the nanotube wall has become thinner indicating that deposition within the nanotube is diffusion limited at high temperatures. Close to the centre of the nanotube, the nanotubes are not fully complete and Ni-B islands that have not fully coalesced are still visible. This further proves that deposition at high temperatures is diffusion limited and nanotubes with non-uniform wall thicknesses will be formed.

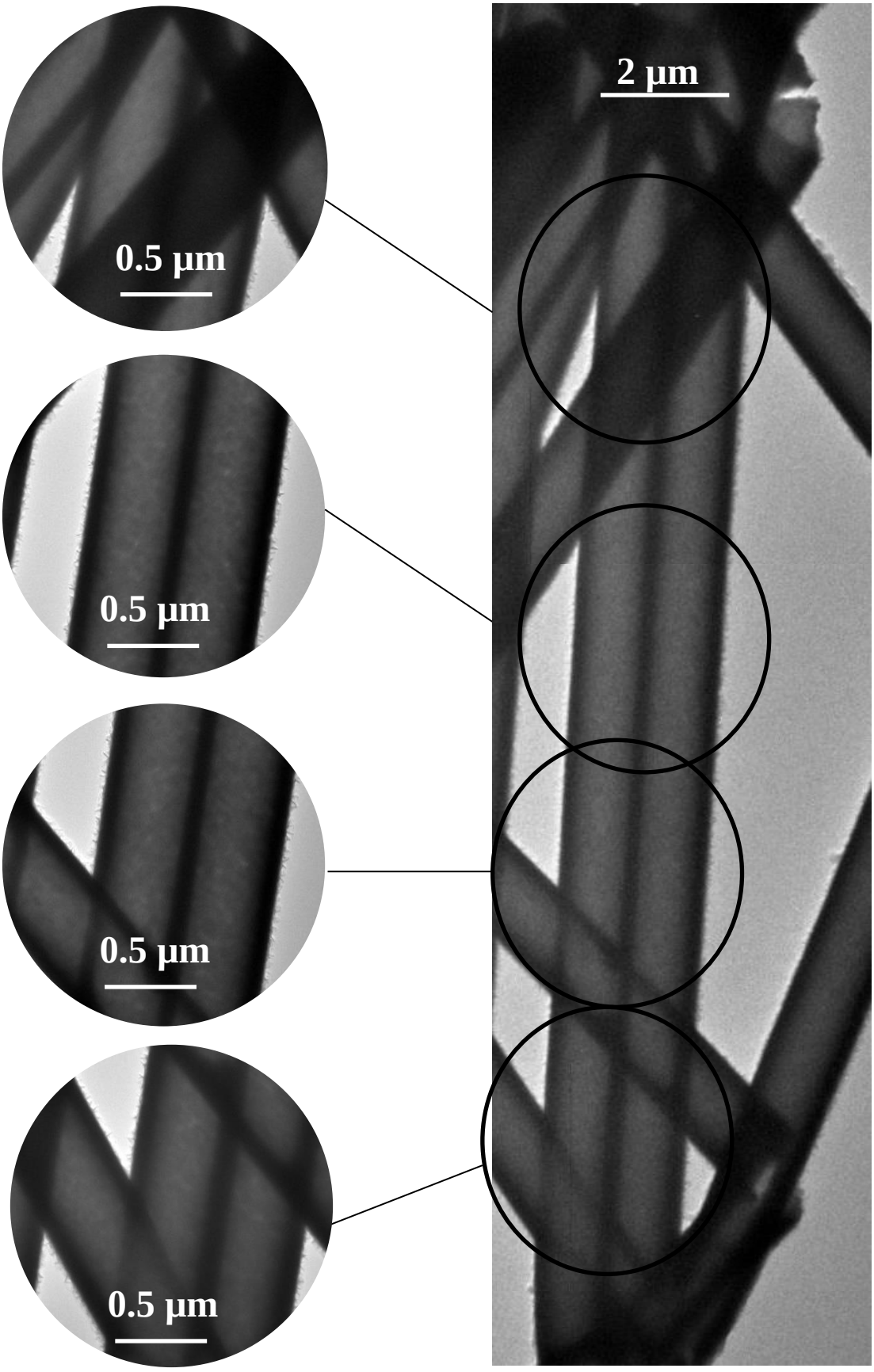

Figure 4.35: TEM image of continuous nanotube with uniform wall thickness deposited at 30 ºC for a deposition time of 10 minutes deposited from the deposition bath given in Table 3.4.

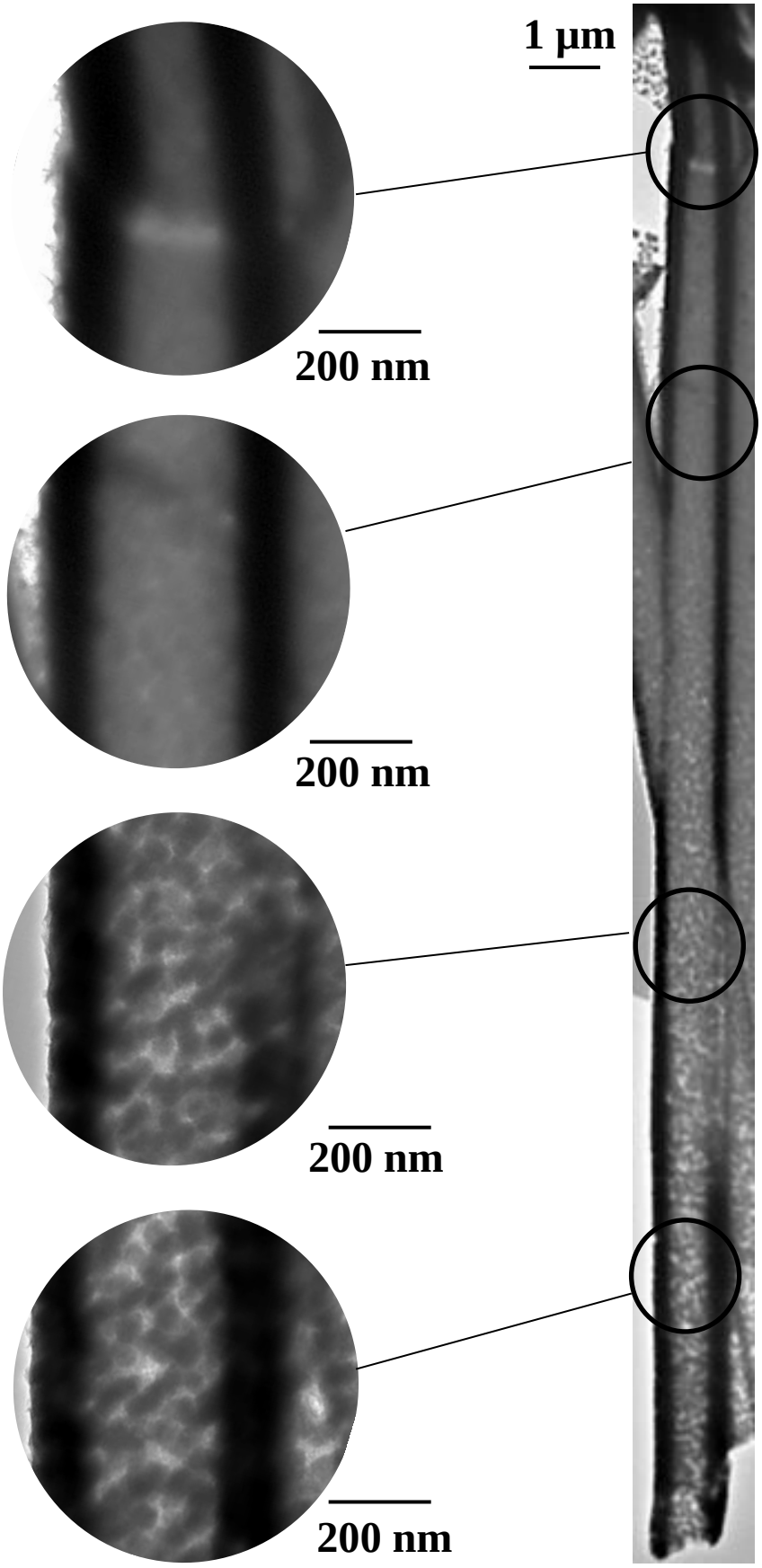

Figure 4.36: TEM image of continuous nanotube with uniform wall thickness deposited at 50 ºC for a deposition time of 10 minutes deposited from the bath given in Table 3.4.

4.9 Conclusion

In this chapter, we have shown that the deposited nanostructure depends on the type of deposition process that is occurring within the nanotube, either diffusion limited or kinetically controlled. Due to a pore diameter of 400 nm, diffusion throughout the nanotube structure is limited. Therefore, if the deposition rate is large, reactant concentration within the nanotube pore will be reduced resulting in a diffusion limited reaction. However, if the deposition rate can be lowered so that deposition occurs at the same rate as diffusion of the reactants throughout the nanotube structure, a kinetically controlled reaction can be achieved. We have presented a relatively simple method to determine if a kinetically controlled deposition process is occurring. By varying bath parameters such as the citrate concentration, pH or bath temperature the deposition rate can be controlled. A kinetically controlled deposition was successfully achieved with deposition bath parameters of 0.118 M citrate concentration, a pH of 10 and a temperature of less than 30 ºC. Using this deposition bath, end-open continuous nanotubes, 20 µm in length, with a uniform wall thickness of up to 110 nm have been successfully fabricated.

4.10 References

[1] W. Wang, N. Li, X. Li, W. Geng and S. Qiu, *Materials Research Bulletin*, **41**, 1417 (2006).

[2] N. Li, X. Li, X. Yin, W. Wang and S. Qiu, *Solid State Communications*, **132**, 841 (2004).

[3] J. F. Rohan, D. P. Casey, B. M. Ahern, F. M. F. Rhen, S. Roy, D. Fleming and S. E. Lawrence, *Electrochemistry Communications*, **10**, 1419 (2008).

[4] A. Azizi, M. Mohammadi and S. K. Sadrnezhaad, *Materials Letters*, **65**, 289 (2011).

[5] S. C. Lin, C. H. Lai and P. W. Wu, *Electrochemical and Solid-State Letters*, **11**, D1 (2008).

[6] I. Enculescu, M. Sima, M. Enculescu, E. Matei, M. E. Toimil Molares and T. H. Cornelius, *Optoelectronics and Advanced Materials-Rapid Communications*, **2**, 133 (2008).

[7] R. L. Meek, *Journal of The Electrochemical Society*, **122**, 1478 (1975).

[8] B. J. Hwang and S. H. Lin, *Journal of the Electrochemical Society*, **142**, 3749 (1995).
[9] H. Matsubara, T. Yonekawa, Y. Ishino, N. Saito, H. Nishiyama and Y. Inoue, *Electrochimica Acta*, **52**, 402 (2006).
[10] G. O. Mallory and J. B. Hajdu, "*Chapter 1 - The Fundamental Aspects of Electroless Nickel Plating*", in *Electroless Plating: Fundamentals and Applications*, William Andrew (1990).
[11] P. Apel, *Radiation Measurements*, **34**, 559 (2001).
[12] H. Matsubara, T. Yonekawa, Y. Ishino, H. Nishiyama, N. Saito and Y. Inoue, *Electrochimica acta*, **47**, 4011 (2002).
[13] H. Ashassi-Sorkhabi, A. Mirmohseni and H. Harrafi, *Electrochimica Acta*, **50**, 5526 (2005).
[14] H. Ashassi-Sorkhabi, H. Dolati, N. Parvini-Ahmadi and J. Manzoori, *Applied Surface Science*, **185**, 155 (2002).
[15] T. Saito, E. Sato, M. Matsuoka and C. Iwakura, *Journal of Applied Electrochemistry*, **28**, 559 (1998).
[16] W. T. Evans and M. Schlesinger, *Journal of the Electrochemical Society*, **141**, 78 (1994).
[17] I. Ohno, O. Wakabayashi and S. Haruyama, *Journal of The Electrochemical Society*, **132**, 2323 (1985).

Chapter 5 – Magnetic Properties

5.1 Introduction

Magnetic nanostructures are of great interest as their magnetic properties differ from those of the bulk material [1]. They are being explored in emerging areas of energy, power-technologies, data storage and bio-magnetics [2]. Due to the diverse potential applications, a large amount of research is being conducted to find new nanostructures with suitable magnetic and electrical properties. Nanotubes are of particular interest due to their diverse potential applications and unique properties [3-5]. The most common methods of magnetic nanotube synthesisation are electrochemical [1,6] and electroless deposition [7,8]. In the literature, electroless deposition has been used to deposit a variety of magnetic nanotube compositions including Ni-P [9-11], Co-P [12], Co-Fe-B [13] and Co-Ni-Fe-B [7,8]. The magnetic properties of electrolesssly deposited nanotubes depend on a number of factors including the composition, crystallinity and structure. It has been found that the addition of alloying metals into the magnetic nanostructures can enhance their associated magnetic properties [14].

Our research objective is to characterise and control the magnetic properties of electrolessly deposited nanotubes with unique compositions, so that the properties can be tailored to suit a range of potential applications. To achieve this aim, we investigated the magnetic properties of a variety of unique nanotube compositions including Ni-B, Co-B, Ni-Cu-B and Ni-Fe-B. In this work, we investigate the effect of nanotube wall thickness on the reversal mechanism and on the magnetic properties of the electrolessly deposited nanotubes. We also discuss the specific magnetisation, coercivity and remanence values of the as-deposited nanostructures and nanotubes, as a function of composition and crystallinity. The overall aim of this study is to

understand and control the magnetic properties of the electrolessly deposited nanostructures, so that they can be considered as potential candidates for a wide range of future applications.

5.2 Shape Anisotropy

The end result of electroless deposition on a porous polycarbonate membrane is the formation of nanotubes connected together at both ends by a thin film. The shape anisotropy of the deposited nanostructure depends on the dimensions of the nanotubes and of the film. If the majority of the magnetic material is deposited within the nanotube structure, the nanotubes will dominate the magnetic measurements. However, if the majority of deposition occurs on the membrane surface, the magnetic film formed on the membrane surface will dominate the magnetic measurements. In this section, we present our investigation into the shape anisotropy associated with the electrolessly deposited nanostructures and nanotubes and the magnetic reversal mechanisms involved.

5.2.1 Magnetic Film

The hysteresis curve of an electrolessly deposited Ni-Fe-B film with a thickness of less than 100 nm that we have deposited on a flat substrate is shown in Fig. 5.1. In this case, measurements are made parallel and perpendicular to the film surface. There is a large anisotropy in the magnetic measurements recorded for the film with squareness values of 0.05 and 0.85 obtained for measurements made parallel and perpendicular to the film surface. Therefore, the hard axis of the film corresponds to measurements made perpendicular to the film surface while an easy axis is observed for measurements made parallel to the film surface. The coercivity of the hard axis is 0.0140 T, while that of the easy axis is only 0.0022 T. A large anisotropy is observed

because in-plane orientations of magnetic moments are favoured within a magnetic film. For our electrolessly deposited nanostructure, we want to minimise the magnetic contributions from the film and focus on the magnetic properties of the nanotubes.

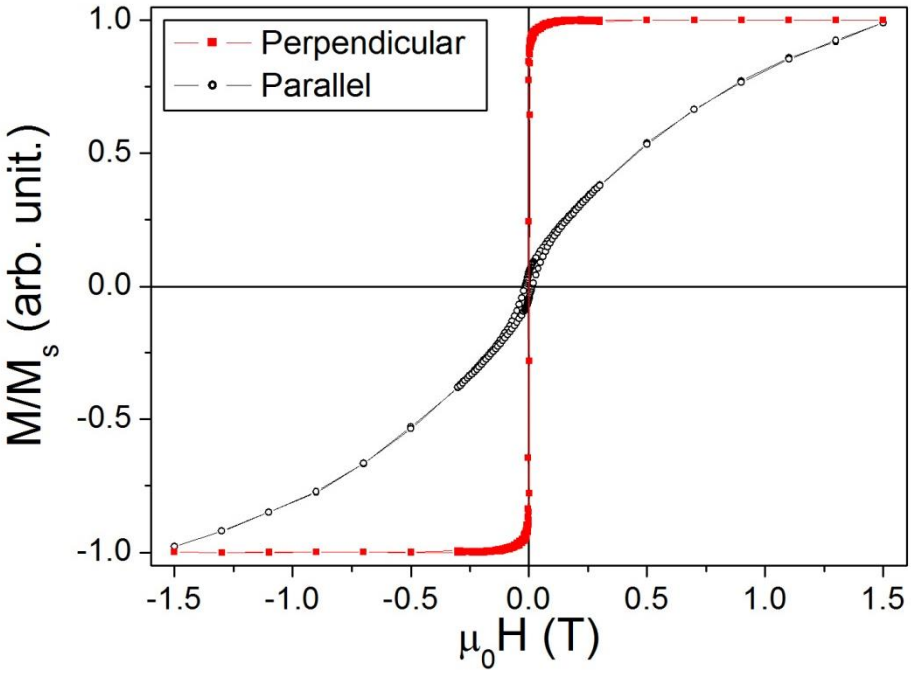

Figure 5.1: Hysteresis curve of a $(Ni_{75}Fe_{25})_{74}B_{26}$ film electrolessly deposited on an acetate surface for 3 minutes using the deposition bath described previously in Table 3.5. Measurements are made parallel and perpendicular to the film surface.

5.2.2 Kinetically Controlled Deposition

As discussed in Chapter 4, the electroless deposition process for Ni-B nanotubes is highly dependent on the deposition bath temperature. A kinetically controlled reaction occurs at low deposition temperatures below 35 ºC. This results in a large amount of Ni-B deposition within the membrane pores which forms Ni-B nanotubes. However, at high temperature, deposition within the membrane pores is diffusion limited and a smaller amount of magnetic material is deposited within the nanotube pores. Therefore, differences in the magnetic anisotropy between deposition at high temperature and low temperature are expected. For magnetic measurements carried out on the electrolessly deposited nanostructures, parallel will refer to measurements carried out parallel to the nanotube axis (perpendicular to the film), while

perpendicular refers to measurements carried out perpendicular to the nanotube axis (parallel to the film).

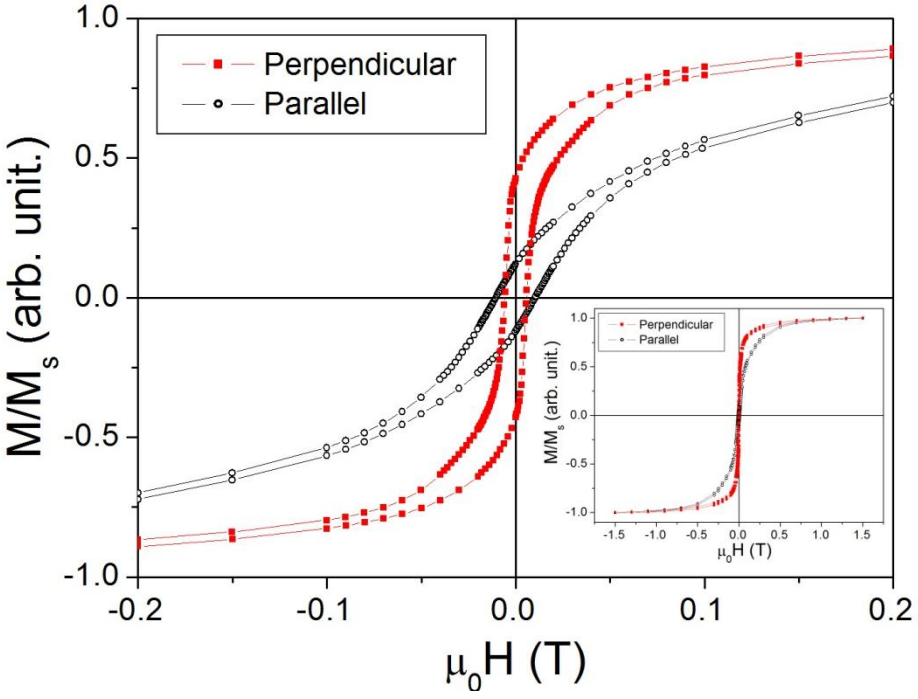

Figure 5.2: Close up of the hysteresis curves of Ni-B nanotubes deposited at a pH of 10 and temperature of 50 ° C for a deposition time of 20 minutes. Inset: Complete hysteresis curve.

The hysteresis curve of an electrolessly deposited Ni-B nanostructure deposited at 50 ºC for 20 minutes is shown in Fig. 5.2. The nanotubes became end-closed after a deposition time of less than 5 minutes and have a varying wall thickness along the nanotube axis. Therefore, a large amount of deposition has occurred on the membrane surface. The magnetic response displayed is somewhat similar to that observed for a thin film as measurements carried out perpendicular to the nanotube axis (parallel to the film surface) act as an easy axis while measurements carried out parallel to the nanotube axis act as a hard axis. After 20 minutes of deposition, from Fig. 4.21(a), a total of 14.4 mg of Ni-B is deposited throughout the polycarbonate membrane. From our analysis in section 4.6 we determine that 7 mg of Ni-B is deposited within the nanotube structure and 7.4 mg is deposited as a film on the membrane surface. This gives a ratio of Ni-B deposit on the membrane surface to Ni-B deposit within the

nanotube structure to be 51 : 49. The observed magnetic response is a combination of the magnetic response of the nanotubes and of the film. Therefore the magnetic properties of neither the nanotubes nor the film can be distinguished. A coercivity of 0.0057 T and a squareness of 0.46 are recorded perpendicular to the nanotube axis. Parallel to the nanotube axis, the nanostructure displays a coercivity of 0.0104 T and a squareness of 0.12.

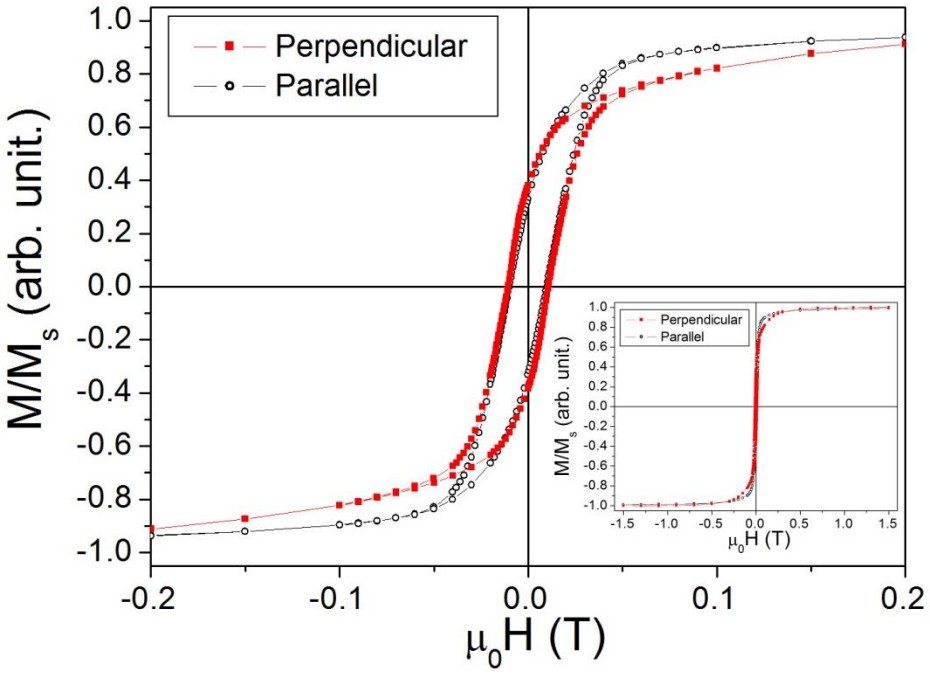

Figure 5.3: Close up of the hysteresis curves of Ni-B nanotubes deposited at a pH of 10 and temperature of 20 ° C for a deposition time of 5 minutes. Inset: Complete hysteresis curve.

However, for a deposition temperature of 20 °C, deposition within the membrane pores is no longer diffusion limited. For a deposition time of 5 minutes, we obtain a total deposited mass of 3.3 mg. Of this, 0.5 mg corresponds to a film structure while 2.8 mg corresponds to a deposit within the nanotube structure. Therefore, a much larger fraction of magnetic material is deposited within the nanotube structure with a ratio of Ni-B on the membrane surface to Ni-B within the nanotube structure of approximately 15 : 85. The magnetic properties of the as-deposited nanostructure, deposited at 20 °C for a deposition time of 5 minutes, are shown in Fig. 5.3. For a

deposition time of 5 minutes, nanotubes with a wall thickness of approximately 30 nm are formed with a similar film thickness. There is very little observable anisotropy present for the nanostructures with a measured coercivity of 0.0108 perpendicular to the nanotube axis and 0.0098 T parallel to the nanotube axis. Squareness values of 0.37 and 0.34 were measured in the perpendicular and parallel direction respectively. The recorded hysteresis curves are not similar to that recorded for a thin film in Fig. 5.1. Therefore, in this case, the magnetic response of the nanotube structure dominates the observed magnetic properties.

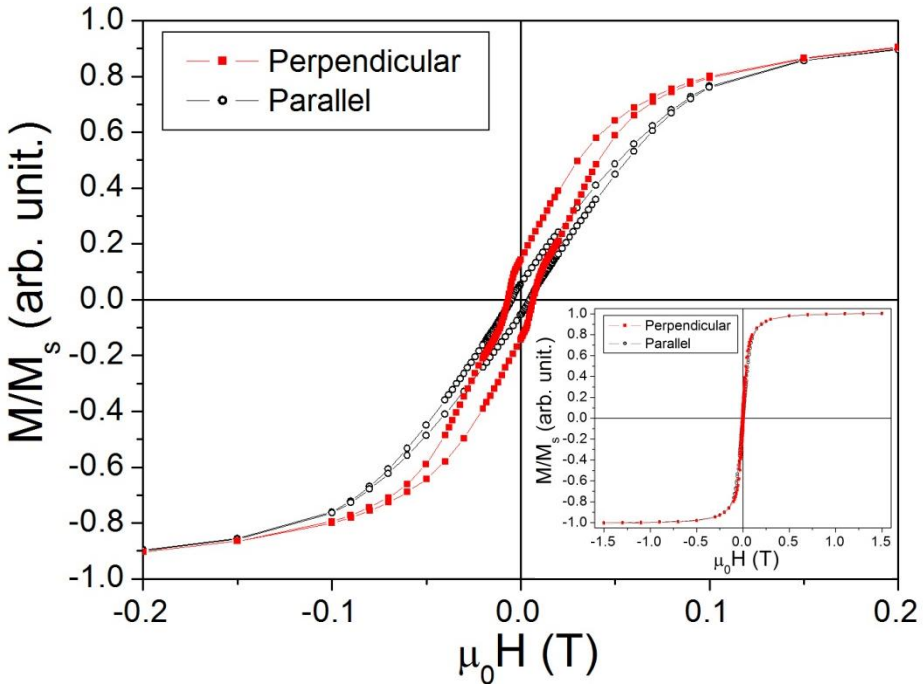

Figure 5.4: Close up of the hysteresis curves of Ni-B nanotubes deposited at a pH of 10 and temperature of 20 ° C for a deposition time of 40 minutes. Inset: Complete hysteresis curve**.**

For a deposition time of 40 minutes, the nanotube has become end-closed with a wall thickness of 100 nm. The film thickness has increased to 200 nm. As shown in Fig. 5.4, there is a small anisotropy associated with the nanotube structure. The coercivity of nanotubes is decreased with values of 0.0070 T recorded perpendicular to the nanotube axis and 0.0046 T recorded parallel to the nanotube axis. Due to the presence of a continuous film and a ratio of Ni-B on the membrane surface to Ni-B

within the nanotube structure of approximately 22 : 78, the recorded magnetic measurement is a superposition of the magnetic response of the nanotubes and the magnetic response of the thin film. This results in the unusual shape observed in the magnetic hysteresis curve.

Due to the in-plane anisotropy associated with the thin film, measurements made perpendicular to the nanotube axis act as a slightly easier axis. However, the anisotropy observed is smaller than that recorded for the nanotube structure at a deposition temperature of 50 ºC. This proves that by lowering the temperature at which electroless deposition occurs, the amount of magnetic material deposited within the nanotube pores is increased. Here we have shown that by optimizing the deposition process, it is possible to record the magnetic properties of the deposited end-opened and end-closed nanotubes with a minimal influence from the deposited film. This is important as the magnetic properties of the nanotubes must be recorded separately from the magnetic film.

5.2.3 As-deposited Nanostructure

In this section we investigate the reversal mechanisms of end-open nanotubes connected at both ends by a thin film and end-closed nanotubes covered at both ends by a continuous thin film. Due to the presence of a continuous and discontinuous film on the membrane surface a change in reversal process is likely to be present.

An end-open nanotube structure is formed at low deposition times and corresponds to the presence of a film less than 200 nm thick. The initial magnetisation curve of an end-open Ni-B nanotube array is shown in Fig. 5.5 for a magnetic field applied perpendicular to the nanotube axis. The initial magnetisation curve aligns itself to the hysteresis curve at an applied magnetic field of 0.02 T and a magnetisation value of

0.2 M_s. The alignment of the initial hysteresis curve to the hysteresis loop at a low magnetisation value indicates that a pinning type reversal mechanism is present. A pinning mechanism occurs when magnetic domain motion is impinged by the presence of defects or voids in the structure of the material. Magnetic domain walls moving through regions with very large defect densities will experience a large damping. Therefore, large applied magnetic fields are required to induce a magnetic moment in the material. The magnetic film on the membrane surface is incomplete, due to the presence of nanotube pores. These act as pinning points and due to the large pore density, a pinning mechanism is present.

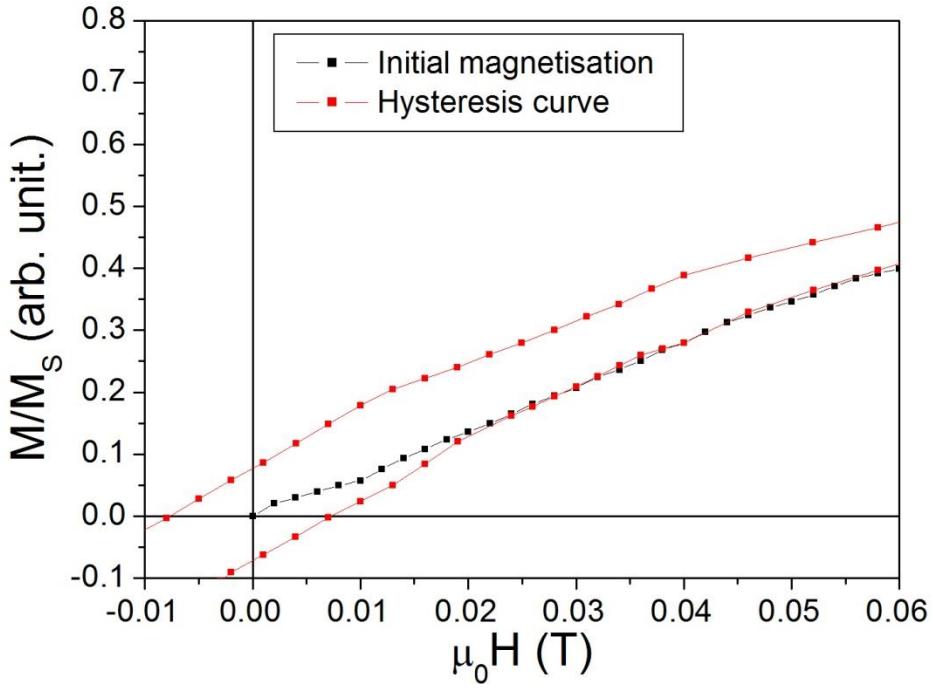

Figure 5.5: Initial magnetisation curve of end-open $Ni_{73}B_{27}$ nanotubes deposited from the deposition bath described in Table 3.4 for deposition time of 5 minutes.

As shown in Fig. 5.6, when the nanotubes become end-closed, a change in the magnetic reversal mechanism is observed. The initial magnetisation curve rises sharply with respect to magnetic field and reaches a value of 0.2 M_s at an applied field of less than 0.005 T. The required applied field to reach this magnetisation value is over 4 times smaller for end-closed nanotubes than for end-open nanotubes. The

initial magnetisation curve aligns with the hysterises curve at a magnetisation value of approximately 0.6 M_s, corresponding to an applied magnetic field of 0.015 T. This indicates a change in the magnetic reversal mechanism from a pinning type mechanism to a nucleation mechanism, though some pinning also occurs. A nucleation mechanism occurs when magnetic reversal occurs in a small volume of the magnetic structure and the domain wall propagates out from these sites with relative ease due to a lack of pinning sites. As the nanotubes are end-closed, the number of void defects is reduced. However, pinning is not eliminated due to the presence of grain boundaries and other defects present within the nanostructure. The reversal mechanisms observed are predominantly due to the film that is present on the surface of the membrane and magnetic properties of the nanotubes are not observed.

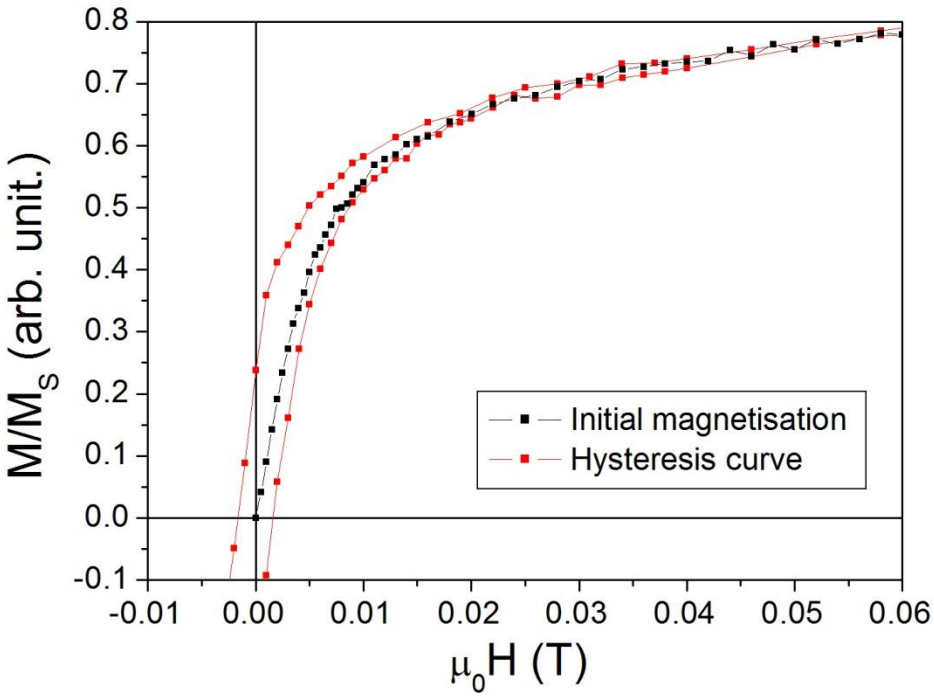

Figure 5.6: Initial magnetisation curve of end-closed $Ni_{73}B_{27}$ nanotubes deposited from the deposition bath described in Table 3.4 for deposition time of 20 minutes.

5.2.4 Nanotube Only Measurements

To attain the magnetic properties of only the nanotube structure, the film must be removed from the surface of the membrane. We mechanically polished the deposited nanostructures with fine sand paper to remove the magnetic film. This enables the measurement of the properties of the electrolessly deposited nanotubes without any influence from the magnetic film. A hysterises curve before and after polishing of a $(Ni_{74}Fe_{26})_{74}B_{26}$ nanostructure deposited for 40 minutes is shown in Fig. 5.7.

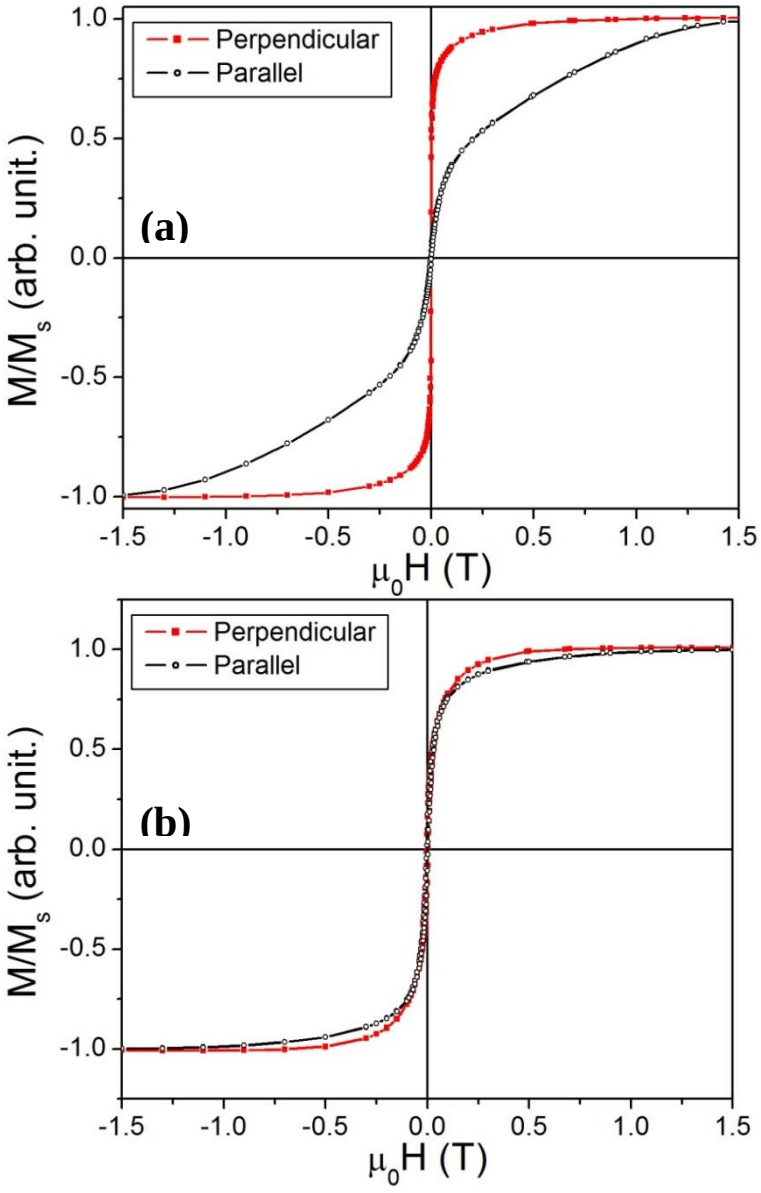

Figure 5.7: Hysteresis curve of an electrolessly deposited $(Ni_{74}Fe_{26})_{75}B_{25}$ nanostructure **(a)** As deposited **(b)** Mechanically polished with the thin film removed showing the magnetic properties of only the as-deposited nanostructure.

It is clear that the anisotropy associated with the deposited nanostructure is much larger than that of the nanotube structure. The anisotropy observed for the as-deposited nanostructure is due to the presence of a magnetic film on the membrane surface. However, once the film is removed the anisotropy decreases and measurements made parallel and perpendicular to the nanotube axis are similar. This indicates that the anisotropy recorded for the as-deposited nanostructures is due to the presence of a magnetic film. With the film removed, there is very little anisotropy associated with the as-deposited nanostructures and the magnetic properties of the electrolessly deposited nanotubes can be obtained.

5.3 Co-B Nanotubes

Co-B nanotubes were deposited via an electroless deposition method identical to that of the Ni-B nanotubes described in chapter 3. Deposition was carried out using the electrolyte described in Table 3.7 at a temperature of 65 ºC and pH 9. This resulted in the deposition of a $Co_{70}B_{30}$ alloy. The Co-B deposit has a specific magnetization of 65.6 J T^{-1} kg^{-1}, which is approximately 40 % of the specific magnetization of pure Co of 161 J T^{-1} kg^{-1}. The deposited nanostructure is identical to that of Ni-B deposition with nanotubes connected at both ends by a thin film. We have also investigated the effect of nanostructure on the magnetic properties of Co-B.

The hysteresis curves in Fig. 5.8(a,c,e) show that a large anisotropy is present for the as-deposited nanostructures. However, the data suggests that the observed anisotropy is due to the presence of the Co-B thin film. As the deposition time increases, the anisotropy becomes more evident. For a deposition time of 5 minutes, the film thickness is approximately 200 nm and a small anisotropy is observed between the magnetic measurements made perpendicular and parallel to the nanotube axis.

However, as the film thickness increases, the anisotropy becomes more pronounced. For a deposition time of 40 minutes, the film thickness has increased to approximately 800 nm and a very large anisotropy is recorded. Therefore, as recorded previously for Ni-B nanotubes, contributions from the film dominate the magnetic measurements when the amount of magnetic material deposited on the membrane surface is larger than the amount within the membrane pores.

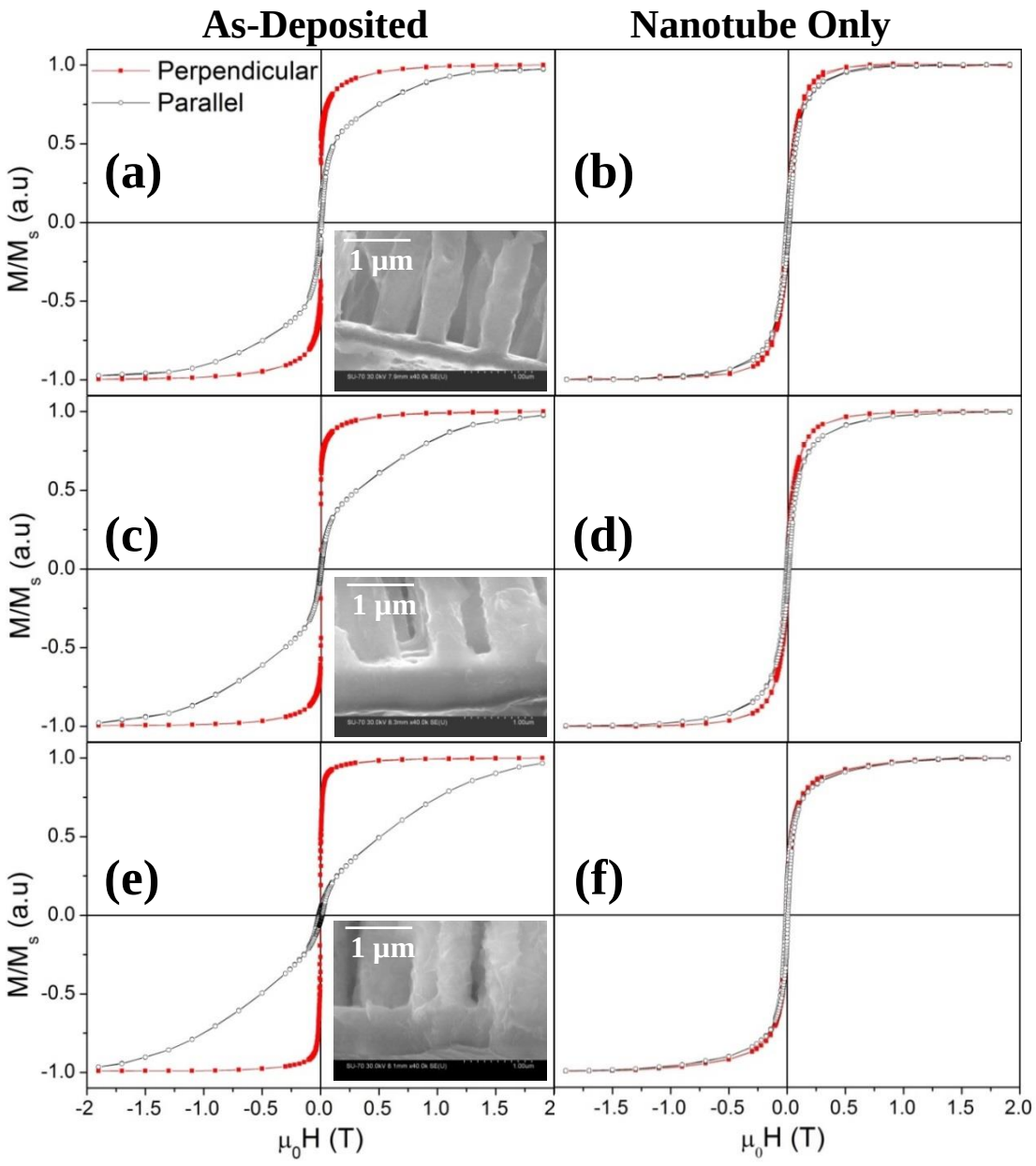

Figure 5.8: Room temperature magnetization curves of $Co_{65}B_{35}$ nanostructures measured perpendicular (solid squares) and parallel (open circles) to the nanotube growth of the as depsoited nanostructure after (a) 5 minute (c) 15 minute and (e) 40 minute deposition and of the nanotubes with the film removed after (b) 5 minute (d) 15 minute and (f) 40 minute deposition. The insets show SEM images of the nanostructure before the removal of the top and base films.

Due to the anisotropy associated with the deposited film, large differences in the squareness of the as-deposited nanostructure, perpendicular and parallel to the nanotube axis, have been recorded as shown in Fig. 5.9. Measurements made perpendicular to the nanotube axis have a squareness values between 0.4 and 0.6. However, measurements made parallel to the nanotube axis have squareness values of less than 0.2. Therefore, measurements made perpendicular to the nanotube axis act as an easy magnetic axis, while measurements made parallel to the nanotube axis act as a hard axis. These results are similar to those obtained in section 5.2.1 for a thin film. This indicates that the magnetic properties of the as-deposited nanostructure are dominated by the deposited thin film.

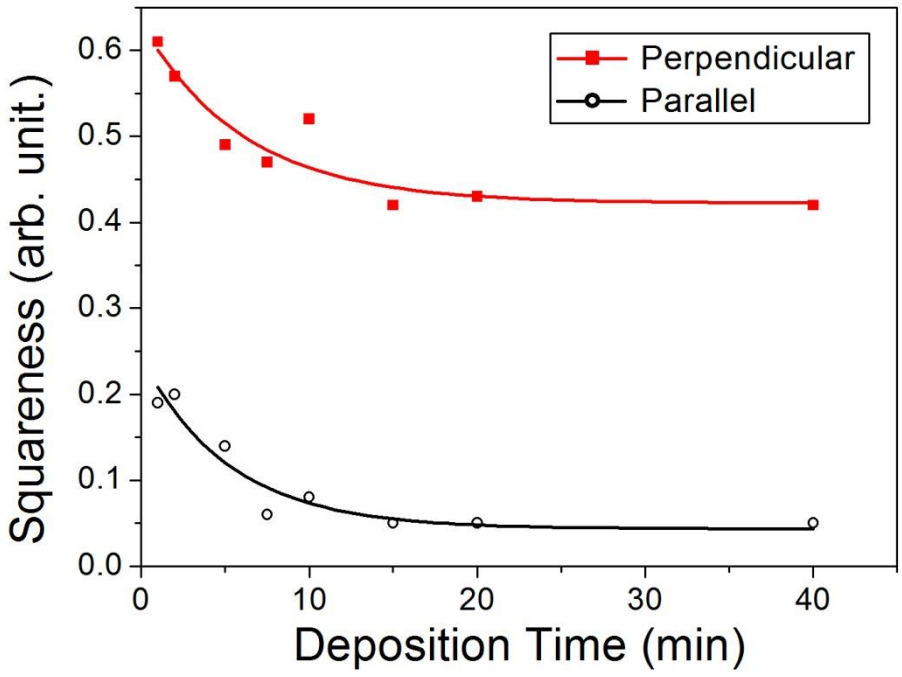

Figure 5.9: Squareness values of as deposited $Co_{70}B_{30}$ nanostructures, measured perpendicular and parallel to the Co-B nanotube axis plotted against deposition time. Displayed curves act as a guide to the eye.

Large differences in the coercivities of the as deposited nanostructure have also been recorded and are shown in Fig. 5.10. Initially, for a deposition time of 60 seconds, the coercivity of the as deposited nanostructures is large - 0.0220 T parallel to the nanotube axis and 0.0105 T perpendicular to the nanotube axis. This is due to the

presence of an incomplete nanostructure and thus the magnetic properties of electrolessly deposited Co-B islands are recorded. After 2 minutes of deposition, a continuous structure is formed and a decrease in the coercivities is observed. Coercivities of 0.0128 T and 0.0044 T are recorded parallel and perpendicular to the nanotube axis for a deposition time of 2 minutes.

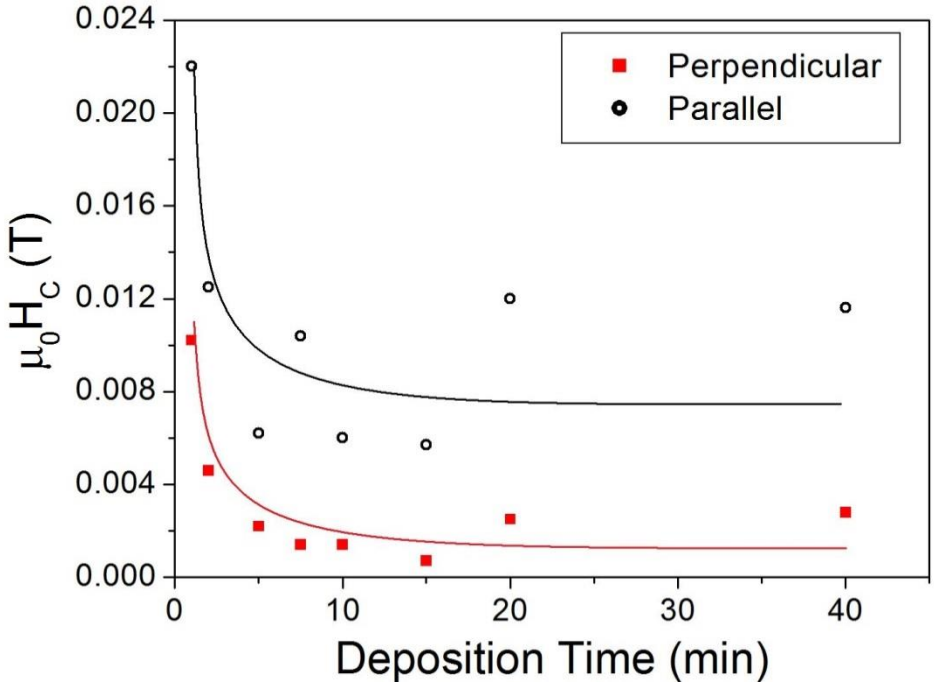

Figure 5.10: Coercivities of as deposited $Co_{70}B_{30}$ nanostructures, measured perpendicular and parallel to the Co-B nanotube axis plotted against deposition time. Displayed curves act as a guide to the eye.

The nanotubes become end-closed after a deposition time of approximately 5 minutes. Once this occurs, a continuous thin film forms and there is a further decrease in the coercivity of the nanostructures. Minimum coercivities of 0.0057 T parallel and 0.0007 T perpendicular to the nanotube axis are recorded for a deposition time of 15 minutes. This corresponds to a film thickness of approximately 500 nm. For all deposition times, the coercivity recorded parallel to the nanotube axis is more than double that of the coercivity perpendicular to the nanotube axis. The coercivity values recorded are similar to those recorded in section 5.2.1 for a thin film. This indicates

that the large anisotropy associated with the deposited nanostructure can be attributed to the presence of a relatively thick film on the membrane surface.

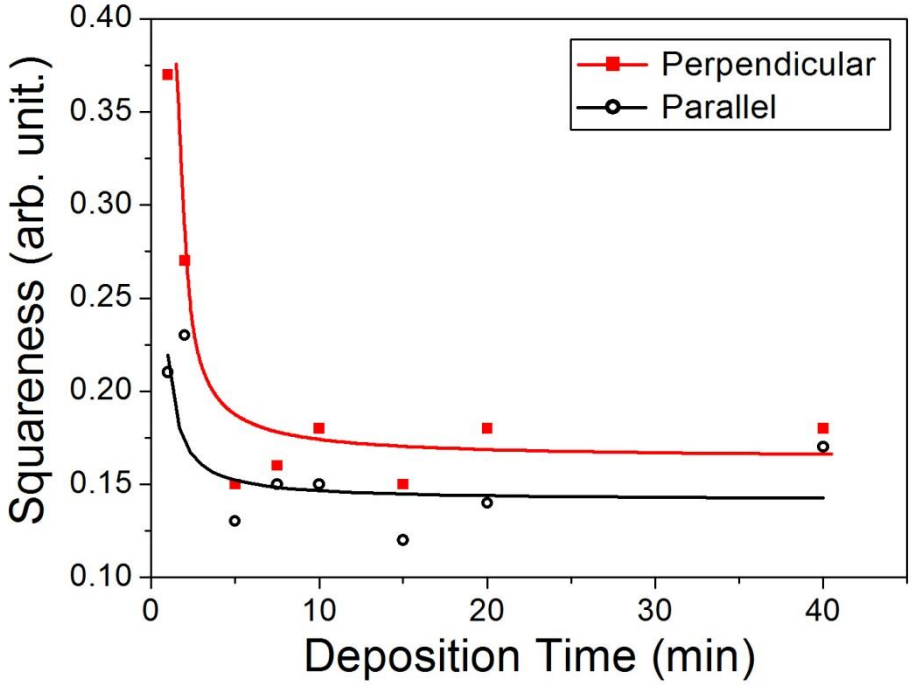

Figure 5.11: Squareness values of $Co_{70}B_{30}$ nanotubes with the film removed, measured perpendicular and parallel to the Co-B nanotube axis as a function of deposition time. Displayed curves act as a guide to the eye.

To enable the measurement of the magnetic properties of end-opened nanotubes without any contribution from the thin film, we removed the thin film by mechanically polishing the sample. As shown in Fig. 5.8(b,d,f), the magnetic measurements taken parallel and perpendicular to the tube growth are similar. Therefore, preferential anisotropy caused by the film is no longer significant. This supports the idea that the anisotropy recorded previously was due to the thin film on the surface of the membrane.

The electrolessly deposited nanotubes display a far lower anisotropy than the as-deposited nanostructures as shown in Fig. 5.11. Squareness values of the Co-B nanotube are similar, irrespective of the direction of the applied field. For deposition times of less than 2 minutes, squareness values greater than 0.2 are recorded. Due to the low deposition time, the nanotubes are incomplete. However, once continuous

nanotubes are formed, the squareness decreases with values ranging from 0.12 and 0.19 being recorded. Measurements made perpendicular to the nanotube axis have a slightly higher squareness value than measurements made parallel to the nanotube axis. This indicates that a minor anisotropy is present for the nanotube structure, with an easy axis present perpendicular to the nanotube axis.

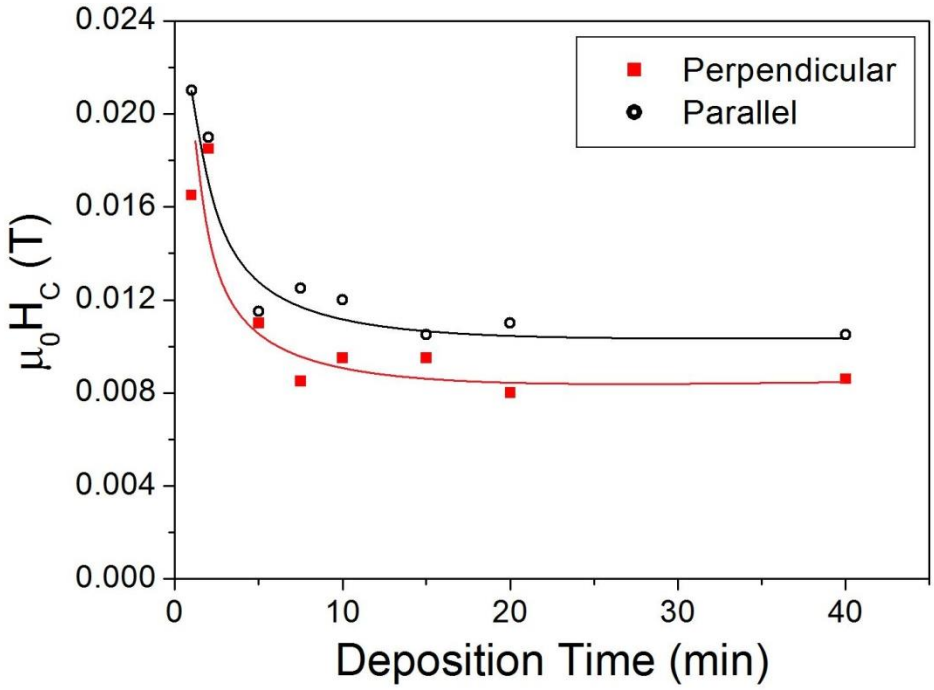

Figure 5.12: Coercivities of $Co_{70}B_{30}$ nanotubes with the top and base film removed, measured perpendicular and parallel to the Co-B nanotube axis plotted against deposition time. Displayed curves act as a guide to the eye.

Unlike the as-deposited nanostructure, differences in the coercivity values perpendicular and parallel to the nanotube axis are small. This indicates that the anisotropy of the electrolessly deposited nanotubes is much lower than that of the film. The coercivity values recorded at a range of deposition times are shown in Fig. 5.12. At low deposition times, the coercivities of the nanotubes are large due to the presence of an incomplete nanostructure. However, once continuous nanotubes are formed, the coercivity reaches constant values of approximately 0.011 T parallel and 0.009 T perpendicular to the nanotube axis. The coercivity perpendicular to the

nanotube axis is slightly lower than coercivities parallel to the nanotube axis and will be discussed further in section 5.7.

5.4 Specific Magnetisation of Ni-B Nanotubes

In chapter 4, we described a method to electrolessly deposit continuous nanotubes with a uniform wall thickness. We used DMAB as a reducing agent during the deposition process resulting in the co-deposition of Ni and B, thereby forming a Ni-B alloy. However, it has previously been shown that the presence of P results in a reduced specific magnetisation [15]. Therefore, we expected to achieve a similar result for the co-deposition of B. As nanotubes with a relatively large specific magnetisation are desired, we investigate the effect of the electroless deposition process on the specific magnetisation of the Ni-B nanotubes. We also discuss a method of increasing the specific magnetisation of the electrolessly deposited Ni-B nanotubes by annealing without altering the nanostructure. In this section our results are analysed in comparison to bulk Ni metal which has a specific magnetisation of 55.4 J T^{-1} kg^{-1}. Our aim is to achieve a similar value for the electrolessly deposited nanostructures.

5.4.1 Composition

Electroless Ni-B deposition using DMAB as a reducing agent can occur via a number of reactions shown in Eqns. 5.1-5.4 [16]. Each reaction occurs at a different rate and the resultant composition of the Ni-B nanostructure is dependent on the reaction rate of each process.

$$3Ni^{+2}+(CH_3)_2NHBH_3+3H_2O \longrightarrow 3Ni^{0}+(CH_3)_2NH_2^{+}+H_3BO_3+5H^{+} \quad (5.1)$$

$$2[(CH_3)_2NHBH_3]+4Ni^{+2}+3H_2O \longrightarrow Ni_2B+2Ni^{0}+2\left[(CH_3)_2NH_2^{+}\right]+H_3BO_3+6H^{+}+\frac{1}{2}H_2 \quad (5.2)$$

$$2[(CH_3)_2NHBH_3]+3Ni^{+2}+6H_2O \longrightarrow 3Ni^{0}+2(CH_3)_2NH_2^{+}+2B(OH)_3+3H_2+4H^{+} \quad (5.3)$$

$$(CH_3)_2NH+BH_3+H_2+H^{+} \longrightarrow (CH_3)_2NH_2^{+}+B+\frac{5}{2}H_2 \quad (5.4)$$

In Chapter 4, we showed that variations in the pH of the deposition result in large variations in the deposition rate of the Ni-B alloy. This indicates that the reaction rates of Eqns. 5.1-5.4 are dependent on the pH of the electrolyte. However, the relative rates as a function of pH are not constant and thus variations in the B content of the Ni-B alloy are recorded.

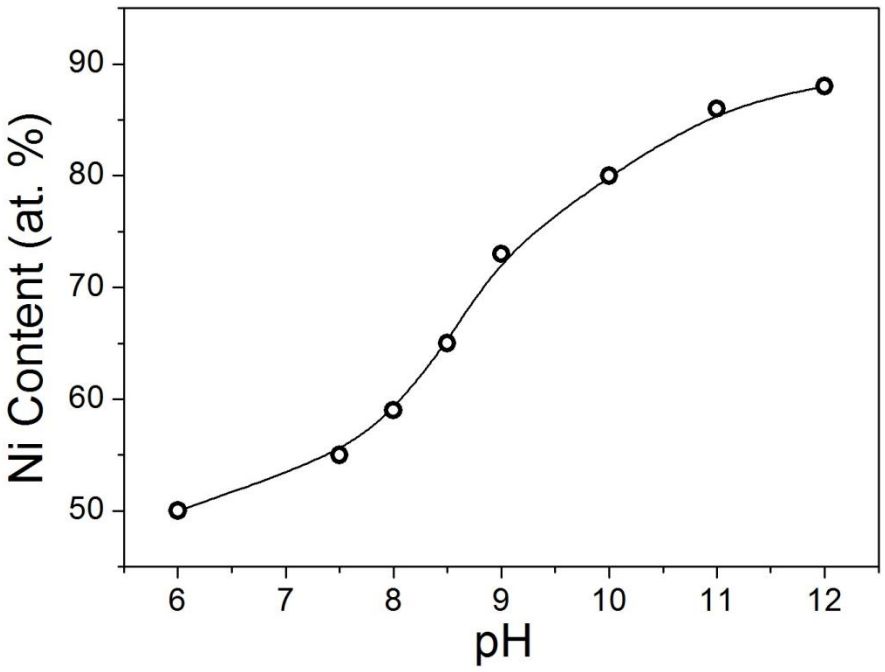

Figure 5.13: The Ni content of the Ni_x-B_{100-x} nanotubes as a function of electrolyte pH deposited from the deposition bath described in Table 3.4. Displayed curve acts as a guide to the eye.

Fig. 5.13 displays the Ni content of the Ni_xB_{100-x} as a function of bath pH. Deposition at pH 6 results in the formation of a $Ni_{50}B_{50}$ alloy. As the pH of the deposition bath increases, a corresponding increase in the Ni content is observed. At pH 8.5 the

composition of the deposited Ni-B alloy is $Ni_{65}B_{35}$ and by pH 12 this has increased to $Ni_{88}B_{12}$. Large increases in the mass of the Ni-B deposit with respect to pH were also observed previously in Chapter 4. These results indicate that the rate at which Ni is deposited increases with pH. Therefore, by controlling the pH of the electrolyte, we are able to control the composition of the Ni-B nanotubes.

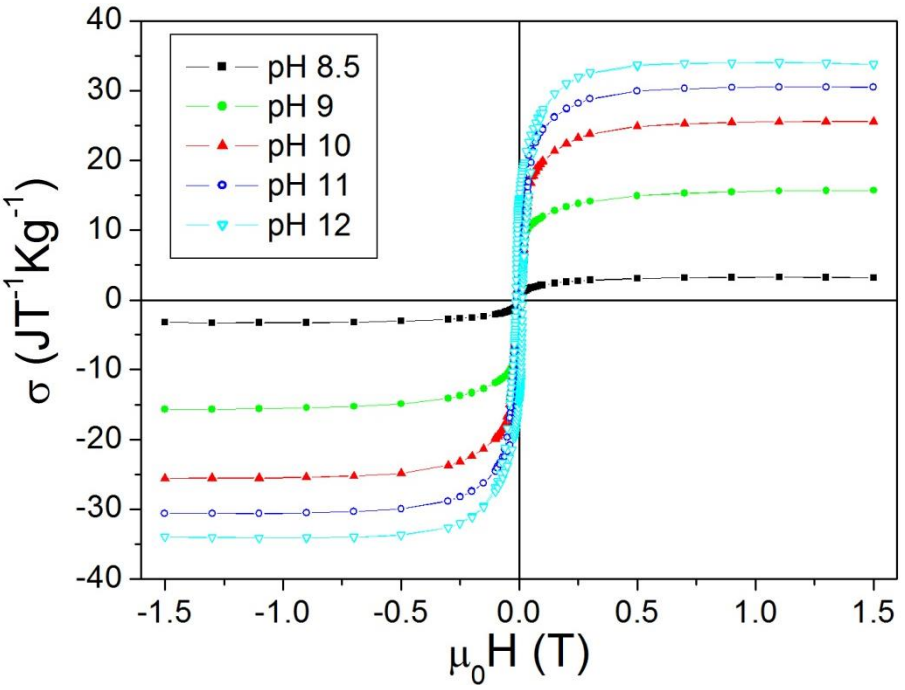

Figure 5.14: Hysteresis curves of the as-deposited Ni-B nanotube arrays for a range of compositions with the applied field parallel to the nanotube axis.

The specific magnetisation, σ, of the electrolessly deposited nanotubes is dependent on the composition of the nanostructure. Hysteresis curves of the as-deposited nanostructures measured perpendicular to the nanotube axis are shown in Fig. 5.14. We have found that nanotubes with a B content of at least 40 at. % display a negligible associated magnetic moment. These compositions are achieved at electroless deposition pH values of 8 and below. The nanostructures were deposited at a temperature of 30 ^{o}C for a deposition period of 5 minutes. This ensured the formation of continuous open-end nanotubes with a uniform wall thickness. These deposition parameters correspond to a wall thickness of approximately 80 nm and

external pore diameter of 240 nm, though slight differences are observed due to the variations of electrolyte pH, which result is differing deposition rates.

Fig. 5.15 shows that the electrolyte pH has a large influence on the specific magnetisation of the electrolessly deposited Ni-B nanostructures. For a pH of 8.5, corresponding to a $Ni_{65}B_{35}$ alloy, the specific magnetisation of the deposit is 3.5 J T^{-1} kg^{-1}. A small increase in pH from 8.5 to 9 results in a factor of 5 change in specific magnetisation which increased to 15.7 J T^{-1} kg^{-1}. Another large increase to 25.6 J T^{-1} kg^{-1} is observed between pH 9 and pH 10. However, above pH 10, the rate of increase slows considerably with a value of 30.5 J T^{-1} kg^{-1} recorded at pH 11. The maximum specific magnetisation recorded for the as-deposited Ni-B nanostructures corresponds to pH 12, at which the specific magnetisation increases to 33.7 J T^{-1} kg^{-1}. This is approximately 60 % of the theoretical maximum value that can be obtained for a Ni deposit of 55.4 J T^{-1} kg^{-1}.

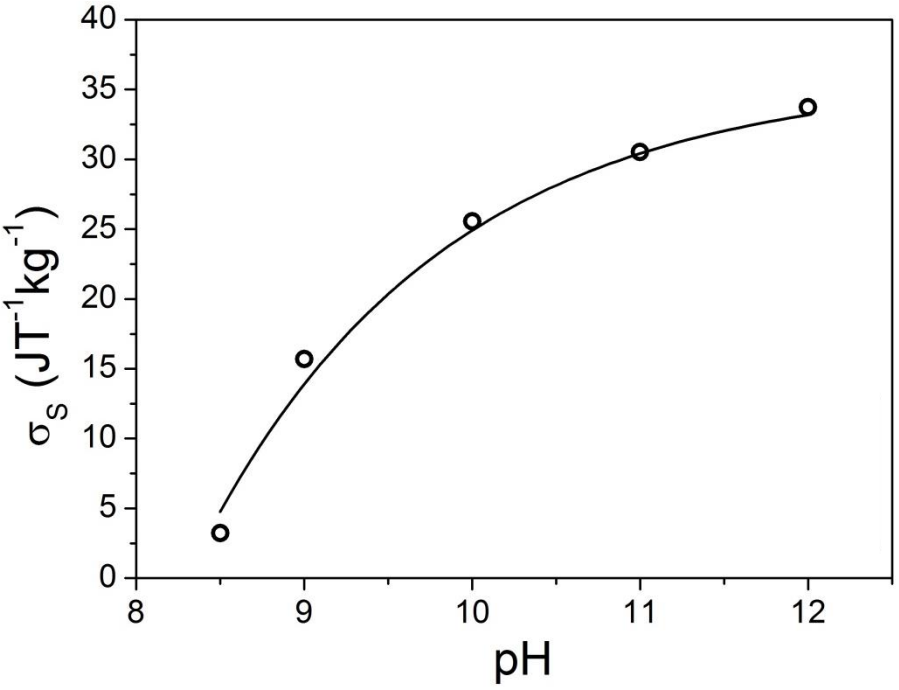

Figure 5.15: Specific saturation magnetisation (σ_S) of Ni-B nanotubes measured as a function of electrolyte pH. Displayed curve acts as a guide to the eye.

Due to the variations in boron content of the Ni-B nanostructures, the specific magnetisation of the nanotubes is dependent on the solution pH. Fig. 5.16 shows the specific magnetisation of the nanostructures as a function of B content. There is an almost linear decrease in specific magnetisation with respect to B content.

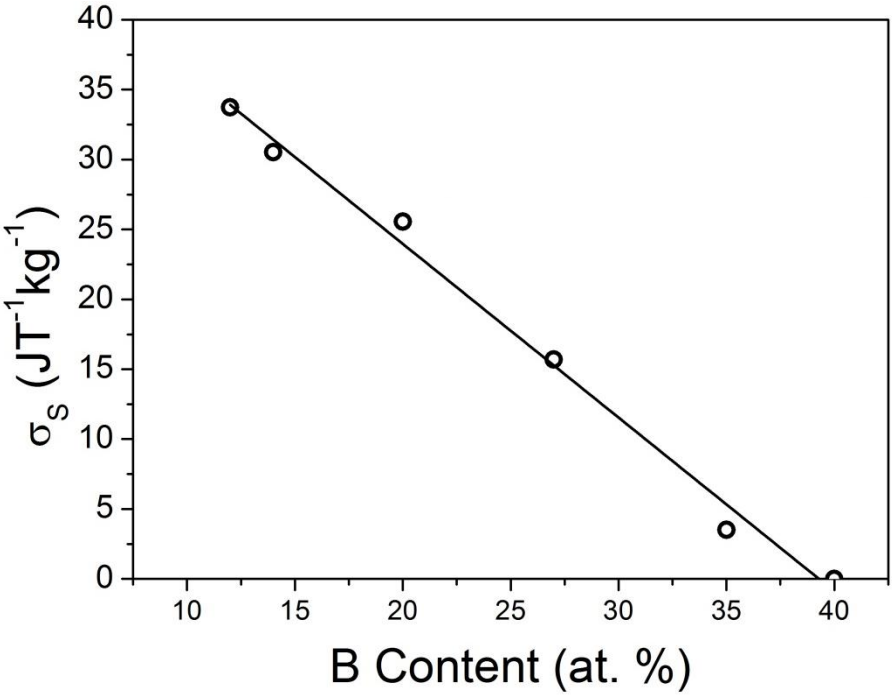

Figure 5.16: Specific saturation magnetisation (σ_S) of Ni-B nanotubes as a function of B content. Linear fit acts as a guide to the eye.

For a B content of 12 at. %, the specific magnetisation of the Ni-B nanostructure is 33.7 J T^{-1} kg^{-1}, while a B content of 40 at. % corresponds to an almost non-magnetic material. As the atomic B content increases there is a corresponding decrease in the atomic Ni content. However, the specific magnetisation is measured as a function of mass and not of atomic percentage. At pH 8, the Ni content is 60 at. %. This corresponds to a Ni-B composition containing 89 wt. % Ni. The Ni content increases to a maximum of 88 at. %, which corresponds to 97.5 wt. % Ni. The difference in wt. % Ni content, from pH 8 to pH 12, is less than 10 %. Therefore, if the changes in specific magnetisation were solely due to a decrease in the Ni content, the maximum change expected in the specific magnetisation between pH 8 and pH 12 would be less

than 10 %. Therefore, the large decrease in specific magnetisation cannot be attributed to a decrease in the Ni content alone.

From these results it is clear that B must play a significant role in controlling the specific magnetisation of the Ni-B deposit. The magnetic properties of Ni and other magnetic materials stem from the fact that electrons have a net magnetic moment due to the associated spin of the electron. When electrons within the atom are unpaired in a partially filled shell, the material can display a magnetic moment. However, once the shells are filled with 2 electrons, their spins align with opposing magnetic fields resulting in no net magnetic moment. For ferromagnetic materials such as Ni, Co and Fe, the unpaired electrons are in the d-orbital and display a quantum mechanical effect known as exchange interaction. Exchange interaction causes the spins of electrons from neighbouring atoms to align resulting in a net magnetic moment.

Previously, it has been identified that, when Ni and B are co-deposited via electroless deposition, B interacts with Ni by transferring electrons to a vacant d-orbital of the metallic Ni [17]. Therefore, the B is electron deficient and the Ni is electron enriched. These electrons fill unoccupied states within the d-orbital band structure, thus reducing the magnetisation of the Ni atom [18].

To investigate this, XPS analysis of the boron peaks was performed on the B 1s orbital spectrum around 190 eV as shown in Fig. 5.17. We observed two peaks, one at 192.0 eV and a second at 187.9 eV. According to the National Institute of Standards and Technology X-ray Photoelectron Spectroscopy (NIST-XPS) database, the peak at 192 eV corresponds to boron-oxide (B_2O_3). The recorded oxide is due to the oxidation of the surface post deposition. The database also indicates that a B peak should be observed at 187.1 eV. However, we observe a shift of 0.8 eV in this peak to 187.9 eV. An increase in the binding energy of the B 1s photoelectron indicates that the B atom

has become electron deficient, thus supporting the idea that B transfers electrons to vacant sites of the Ni atom. A similar increase of approximately 1 eV in the binding energy of the B 1s electron was recorded previously for electrolessly deposited Ni-B particles [19].

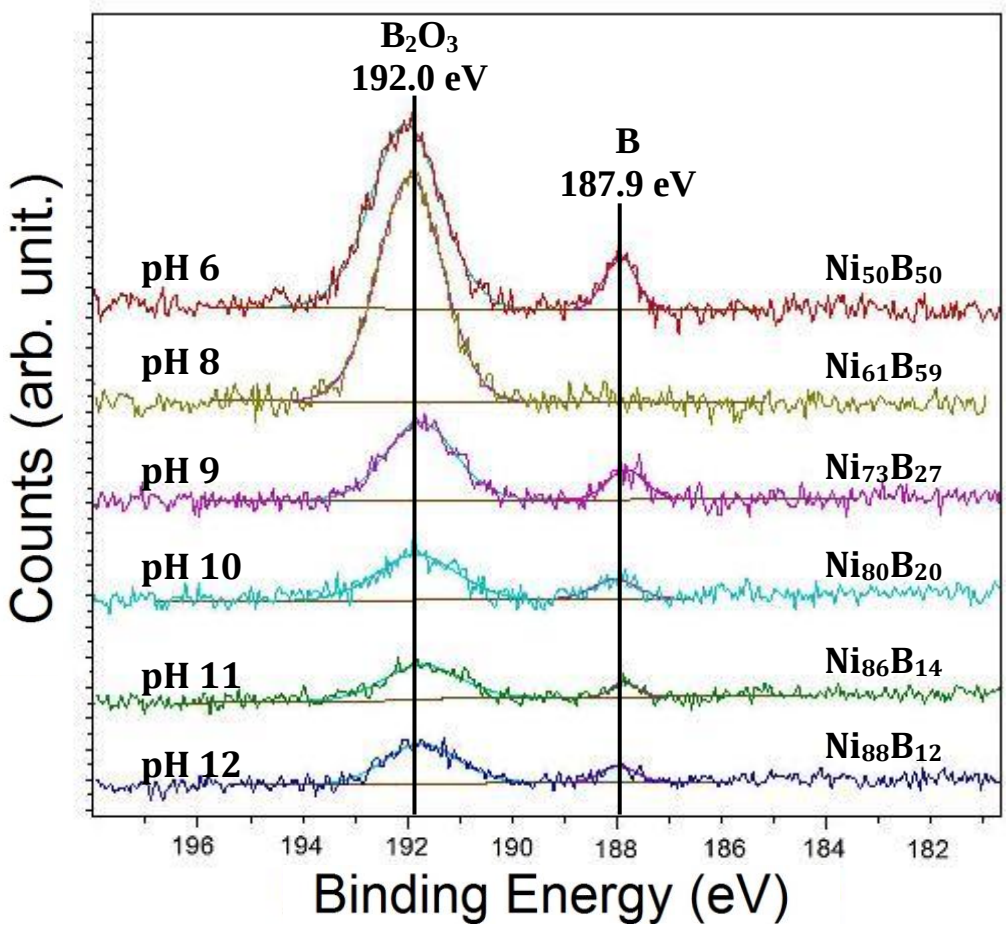

Figure 5.17: B 1s peaks observed in the XPS spectra of Ni-B nanostructures deposited at a range of pH values from the deposition bath described in Table 3.4.

At a pH of 6 and 8, large peaks are recorded for a binding energy of 192 eV, indicating that a large amount of B_2O_3 has formed. The presence of B_2O_3 within the Ni-B structure would also decrease the specific magnetisation of the alloy, although it is likely that the B_2O_3 only exists on the surface of the alloy. No XPS peak was recorded at 187.9 eV for the sample deposited at pH 8. However, as XPS is a surface specific technique, this is likely due to the formation of a large B_2O_3 layer on the surface, which prevented the release of B photoelectrons from within the Ni-B alloy.

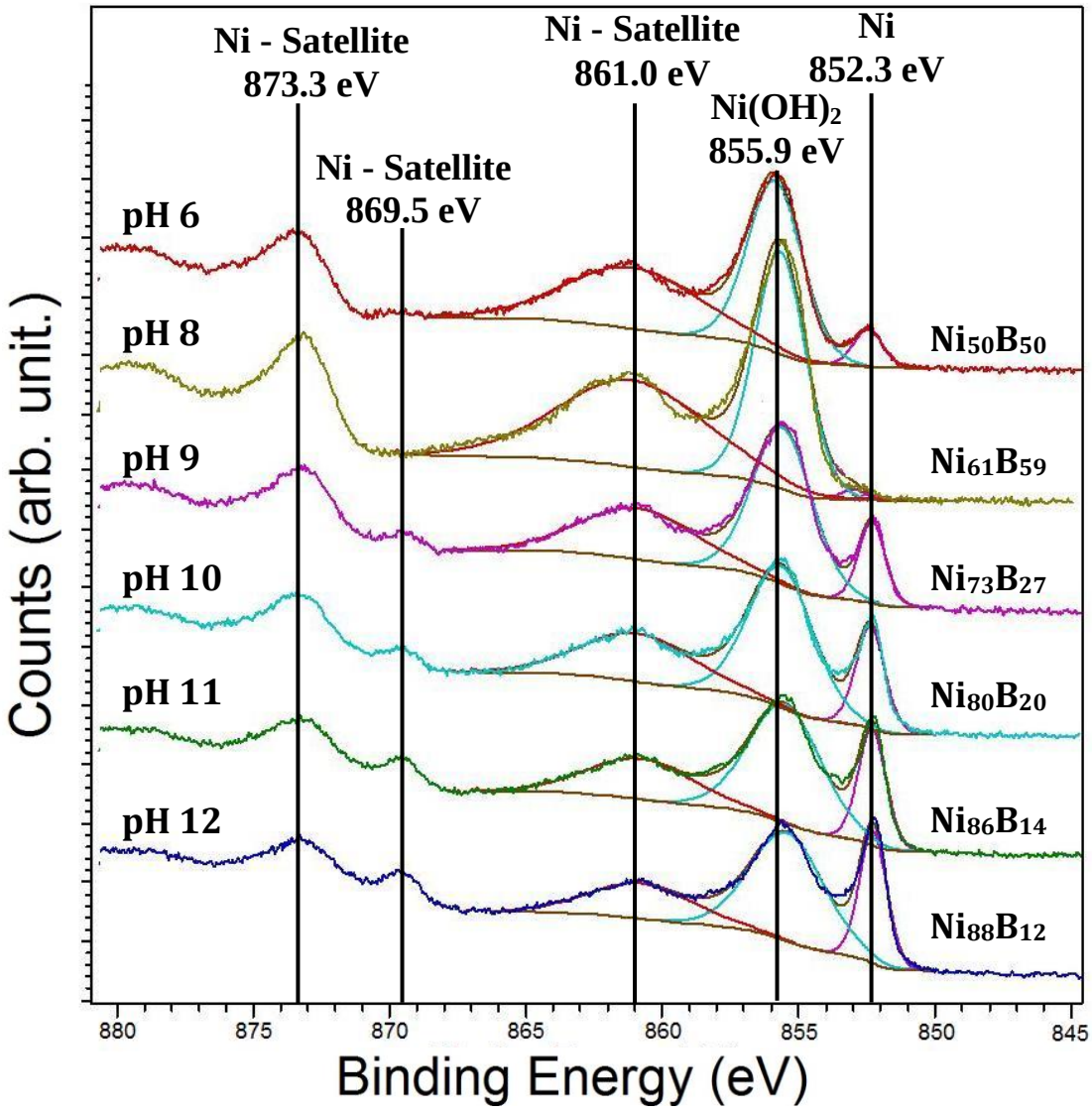

Figure 5.18: Ni 2p peaks observed in the XPS spectra of Ni-B nanostructures deposited at a range of pH values from the deposition bath described in Table 3.4.

We have found at a B content > 40 at. %, the electrolessly deposited Ni-B nanotubes become nonmagnetic. It is likely that this corresponds to the B content required to fill all the un-occupied states within the d-orbital of the Ni atom. As the B content decreases the number of un-occupied states within the d-orbitals of the Ni atoms increase, thus increasing the specific magnetisation of the Ni-B alloy. Therefore, by adjusting the B content we can control the specific magnetisation of the electrolessly deposited nanotubes.

The XPS spectrum of the Ni 2p peaks, shown in Fig. 5.18, provides further evidence for the results established from the B 1s peaks. The peak at 852.3 eV corresponds to Ni metal, while the peak at 855.9 eV corresponds to nickel hydroxide, $Ni(OH)_2$. The peak at 861 eV is a satellite peak while the peaks close to 870 eV are due to the energy level doublet within the 2p orbital. The two peaks which contain the most information are the first two peaks recorded at 852.3 eV and 855.9 eV.

The NIST-XPS database gives the binding energy of the Ni 2p electron to be 852.6 eV. In this study, a small decrease in the binding energy to 852.3 eV is observed. This indicates that the Ni atom becomes electron enriched. The decrease in binding energy is only 0.3 eV; less than the 0.8 eV recorded for B. This smaller change in binding energy is recorded due to extra shielding from the inner shells of the Ni atom. As the pH of the solution bath increases, the height of the Ni peak increases. This shows an increased Ni content. Again at pH 8, a large $Ni(OH)_2$ peak is recorded with no Ni peak present. This strongly indicates that a larger oxide layer has formed on the alloy surface, thus preventing the observation of electrons from within the Ni-B alloy.

XPS analysis is a surface sensitive technique and may not represent the composition of the bulk structure. The shift observed in the Ni peak position is small and may not be completely accurate. However, the theory that electron transfer occurs between B and Ni is consistent with our experimental results and are similar to those of previous studies [17,18]. From this we conclude that the specific magnetisation of the nanostructures is highly dependent on B content. By controlling the pH of the deposition bath, we can control the B content of the electrolessly deposited alloy and thus control the specific magnetisation. However, the maximum value achieved of 33.7 J T^{-1} kg^{-1} for a composition of $Ni_{88}B_{12}$ is still much lower than that of pure Ni.

Therefore, due to the low specific magnetisation obtained, annealing was carried out with the aim of increasing the specific magnetisation.

5.4.2 Crystal Structure

Pure Ni has face centered cubic (FCC) crystal structure. However, as shown in Fig. 5.19, X-ray diffraction patterns of the as-deposited Ni-B alloy indicate that an amorphous structure is present irrespective of the deposition pH and B content. A weak broad peak is visible at 45 º for samples deposited at pH values of greater than 9. This peak corresponds to the (111) plane of a FCC Ni structure. This indicates that there is a slight crystallisation of the Ni within the Ni-B alloy for large Ni contents.

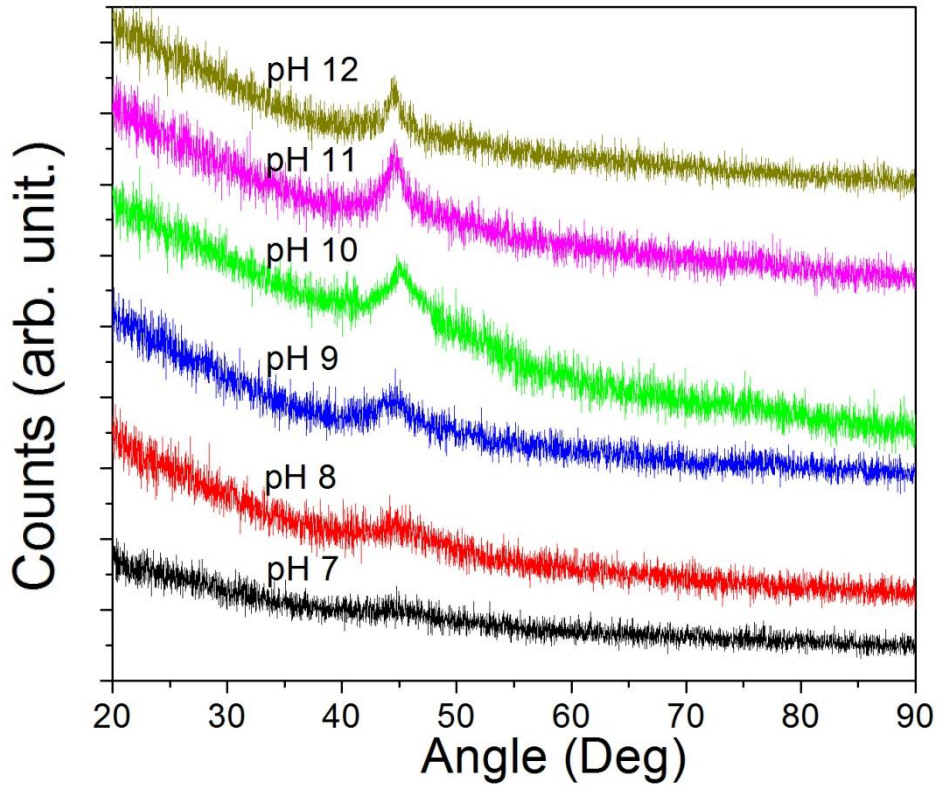

Figure 5.19: XRD spectra of as-deposited Ni-B nanostructures deposited at a range of pH values from the deposition bath described in Table 3.4.

It is likely that the B acts as a grain growth inhibitor within the Ni-B structure thus preventing the crystallization of the deposited Ni. This will also prevent magnetic interaction between adjacent Ni atoms thus decreasing the magnetic moment

recorded. Therefore, as the pH of the electrolyte increases, the B content decreases and a small amount of grain growth is possible. This results in a weak Ni FCC peak on the XRD spectrum. However, the alloy is still considered to be amorphous or possibly polycrystalline, as no clear crystal structure can be observed.

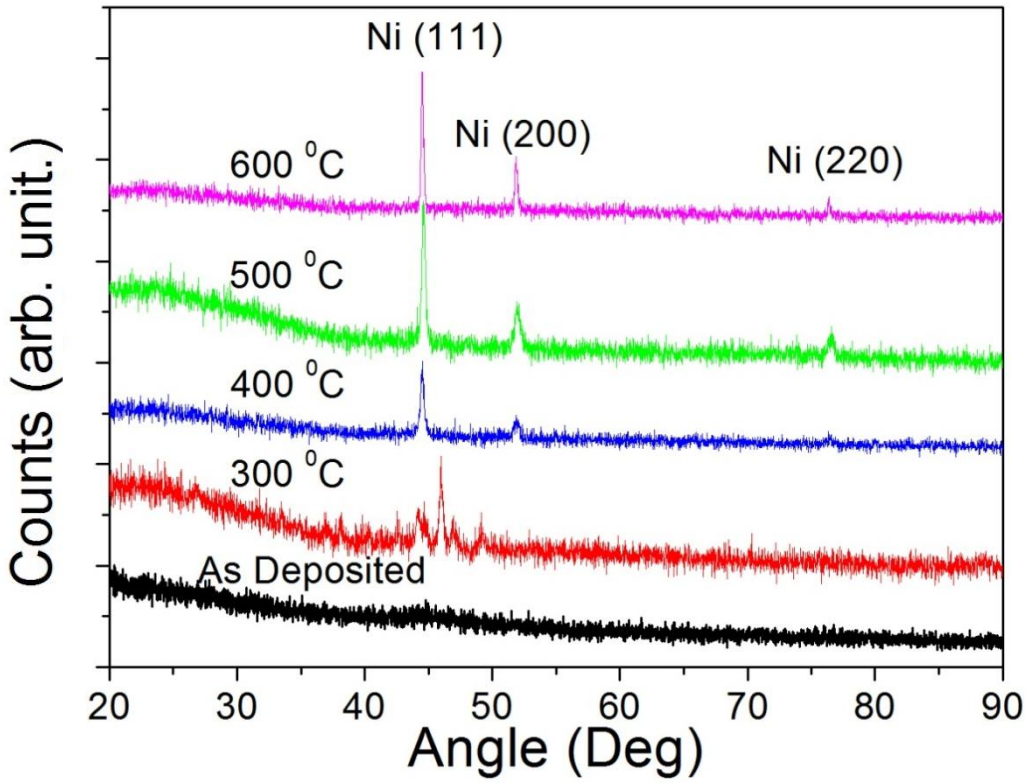

Figure 5.20: XRD spectra of $Ni_{55}B_{45}$ nanostructure post-annealing for 1 hour at a range of temperatures.

However, annealing of the electrolessly deposited nanotube structure results in the formation of a crystalline structure. The XRD spectra of a $Ni_{55}B_{45}$ nanostructure deposited at pH 7.5 are shown in Fig. 5.20, for a range of annealing temperatures. The samples were annealed for 1 hour in a N_2 atmosphere. For an annealing temperature of 300 ºC, a number of XRD peaks are recorded between 40º and 50º. This indicates that there is a transition from an amorphous Ni-B phase to a polycrystalline phase. At a temperature of 400 ºC, three distinct XRD peaks are recorded. These peaks correspond to a Ni FCC structure with a (111) plane recorded at 45 º, (200) at 52 º and (220) at 76.5 º. For annealing temperatures above 400 ºC, the peak intensity increases.

It is clear that as the annealing temperature increases, the crystallinity of the Ni-B alloy increases. Previously in an investigation of mechanical properties, it was shown that annealing of Ni-B films results in a large amount of boron diffusing to the surface [20]. As boron diffuses towards the surface of the deposit, it no longer prevents the formation of a Ni FCC structure within the deposit. Therefore, the crystallinity of the bulk deposit increases. It is likely that a similar mechanism is occurring here and regions rich in Ni content with an FCC structure are formed within the nanostructure.

SEM images of the nanotube structure both pre and post-annealing are shown in Fig. 5.21(a-d). Broken nanotubes are observed due to breaking the nanostructure post-annealing so that cross sectional imaging can be undertaken. As the polycarbonate membrane has evaporated during the annealing process, the nanostructure is fragile resulting in damage to the nanotube structure.

Even with the damage present, it is clear from Fig. 5.21(b) that, post-annealing at 400 ºC, the nanostructure remains with continuous nanotubes connected at both ends by a thin film. Post-annealing at 500 ºC, Fig. 5.21(c), the nanotube structure remains though a small amount of bending in some of the nanotubes is observed. This indicates that, at 500 ºC, the metallic nanotubes become ductile and those under stress may bend slightly, though the majority of nanotubes retain their original structure. However, post-annealing at 600 ºC, Fig. 5.21(d), the nanotubes have melted and very little of the deposited nanostructure remains. This indicates that the maximum annealing temperature that can be used for the Ni-B nanotubes is 500 ºC.

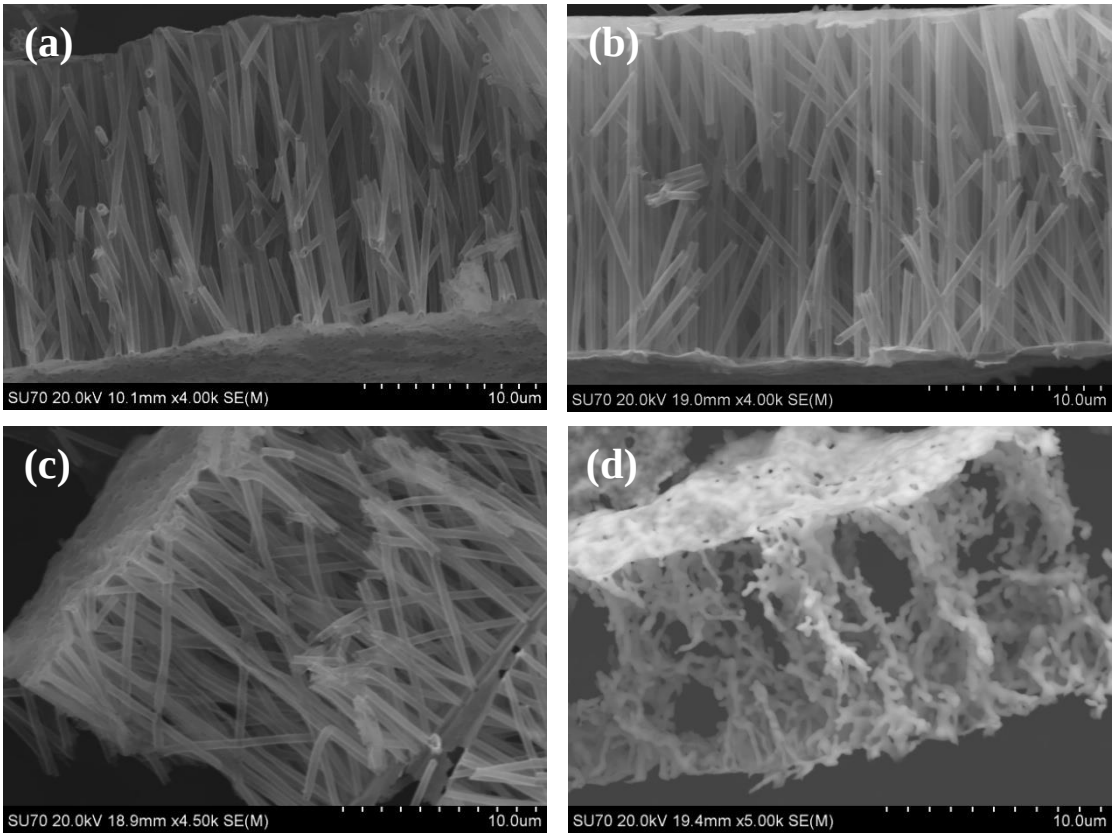

Figure 5.21: SEM images of $Ni_{55}B_{45}$ nanotubes (a) as-deposited (b) post-annealing at 400 ºC (c) 500 ºC and (d) 600 ºC.

The magnetic hysteresis loops obtained for nanotubes deposited at pH 7.5 post-annealing at a range of temperatures are shown in Fig. 5.22. Due to the large boron content in the $Ni_{55}B_{45}$ alloy Ni-B deposited at a pH of 7.5 has a negligible magnetic moment. However, post-annealing at 300 ºC, a specific magnetisation of 6.1 J T^{-1} kg^{-1} was recorded. This temperature corresponds to a transition between an amorphous Ni-B structure and a FCC Ni crystalline structure. This indicates that a crystalline structure has a larger specific magnetisation than an amorphous structure. At 400 ºC, a crystalline FCC phase is present resulting in a specific magnetisation of 23 J T^{-1} kg^{-1}. The specific magnetisation of the Ni-B nanotubes, annealed at 500 °C, reaches a value of 46.3 J T^{-1} kg^{-1}. This corresponds to 84 % of the specific magnetisation of pure Ni. Although the as-deposited nanotubes displayed no associated magnetic moment, the annealing process increased magnetisation values.

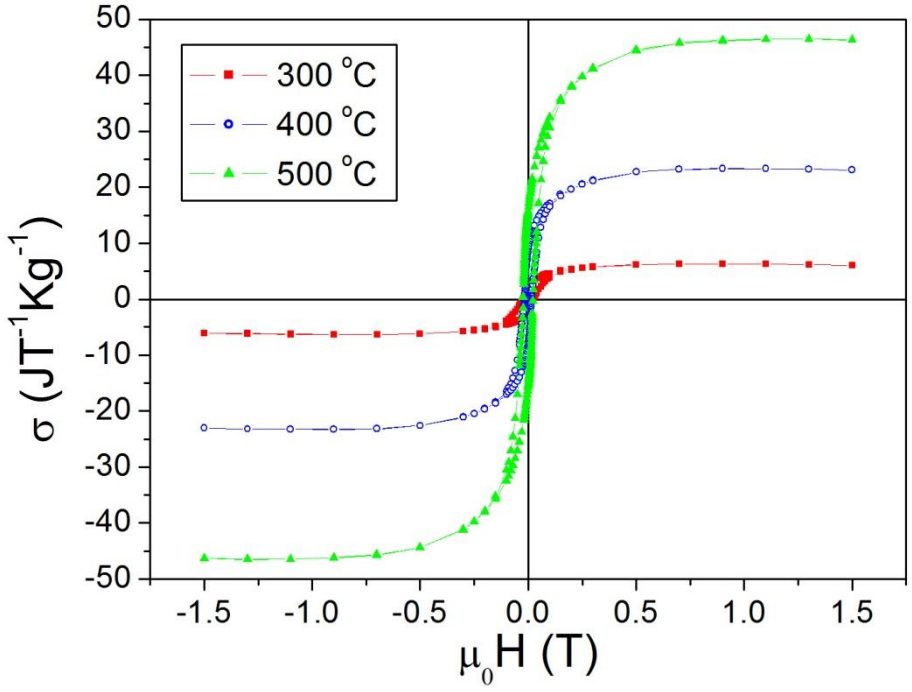

Figure 5.22: Hysteresis curves of $Ni_{55}B_{45}$ nanotube array post-annealing at a range of temperatures with the applied field parallel to the nanotube axis.

The large increase in specific magnetisation is attributed to the diffusion of B out of the Ni-B alloy. Instead of an amorphous Ni-B alloy, Ni rich regions are formed within the nanostructure. In an amorphous Ni-B structure, Ni was nonmagnetic due to the donation of electrons from the B atoms. However, once the B has diffused towards the surface away from the Ni atoms, the Ni forms a crystalline structure and a large magnetic moment is recorded for the annealed nanotubes.

Hysteresis curves for a $Ni_{88}B_{12}$ nanotube array deposited at pH 12 are shown in Fig. 5.23. Unlike the $Ni_{55}B_{45}$ the nanotubes are strongly magnetic in their as deposited form with a specific magnetisation of 33.7 J T^{-1} kg^{-1}. Again a Ni FCC crystal structure is formed post-annealing up to 500 ºC. However, there is only a small change in the specific magnetisation of the nanotubes with a value of 37.9 J T^{-1} kg^{-1} recorded post-annealing at 300 ºC. A maximum specific magnetisation of 48.6 J T^{-1} kg^{-1} is recorded post-annealing at 500 ºC. This value is similar to that recorded for $Ni_{55}B_{45}$ post-annealing at 500 ºC of 46.3 J T^{-1} kg^{-1}. From these experiments, we have found

that the specific magnetisation of the electrolessly deposited nanotubes post-annealing is independent of both deposition bath pH and atomic composition.

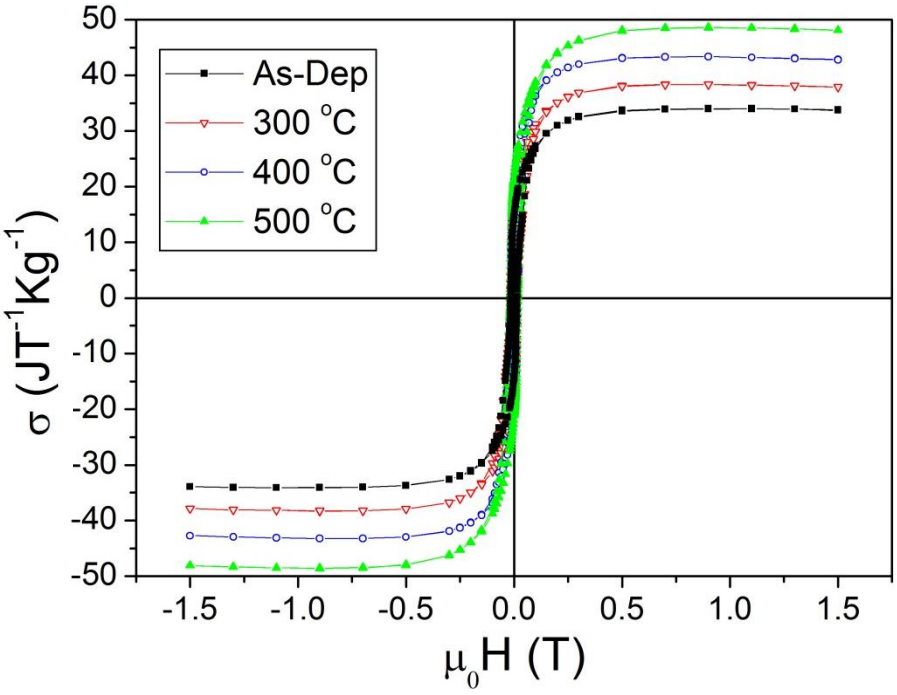

Figure 5.23: Hysteresis curves of $Ni_{88}B_{12}$ nanotube array post-annealing at a range of temperatures with the applied field parallel to the nanotube axis.

Achieving similar specific magnetisations irrespective of bath pH and B content is a significant result in relation to the electroless deposition process which was discussed in Chapter 4. To attain continuous nanotubes with a uniform wall thickness, a kinetically controlled electroless deposition process within the polycarbonate template structure is required. To achieve this, a low deposition rate is necessary. As discussed in section 4.5.3, the pH of the deposition bath has a considerable effect on the deposition rate, with a high pH resulting in an undesirably large deposition rate. However, a large pH is required to attain electrolessly deposited nanotubes with a low B content and large specific magnetisation. Here, we have described a method to overcome this challenge. To ensure ideal kinetically controlled nanotube growth occurs, nonmagnetic nanotubes can be deposited at the desired low pH. A large

specific magnetisation can then be obtained through annealing post deposition, while the nanotubes retain their original structure.

5.4.3 Summary

In this section we have discussed two different methods of increasing the specific magnetisation of electrolessly deposited nanostructures. By controlling the pH of the deposition the B content of the Ni-B can be controlled. Using this method we have achieved a maximum specific magnetisation of 33.7 J T^{-1} kg^{-1} for a composition of $Ni_{88}B_{12}$. This is approximately 60 % of the specific magnetisation of pure Ni. However, through annealing the specific magnetisation can be increased further without altering the nanotube structure. We achieved a maximum specific magnetisation of of 48.6 J T^{-1} kg^{-1} post-annealing at 500 ºC. This is approximately 80 % of the specific magnetisation of pure Ni. Therefore, we have achieved part of our research objective by forming nanotube structures with a large specific magnetisation via electroless deposition.

5.5 Coercivity

Similar to saturation magnetisation, the coercivity of the magnetic nanotubes is also dependant on the composition and crystal structure of the electrolessly deposited Ni-B alloy. Alloying magnetic materials with B affects the magnetic properties of the material with variations in coercivity and squareness recorded previously for thin films [14,21]. In this section, we present the results of our investigation on the effect of composition and crystal structure on the magentic properties of electrolessly deposited Ni-B nanotubes. By understanding these effects, it should be possible to control the magnetic properties of the nanostructures.

5.5.1 Composition

The magnetic properties of the as-deposited Ni-B nanostructures are investigated as a function of B content. Fig. 5.24(a) shows a close-up image of the hysterises curves recorded for the as-deposited nanostructures, from which the coercivity and remanence values can be determined. For a large B content a very low coercivity is observed. $Ni_{65}B_{35}$ displays a coercivity of less than 1 mT. As the B content decreases, the coercivity increases with values of 8 mT and 14.5 mT recorded for compositions of $Ni_{80}B_{20}$ and $Ni_{88}B_{12}$ respectively. These results indicate that the B content has a large effect on the coercivity of the magnetic nanostructures. The remanent magnetisation of the nanostructures increases as the B content decreases. A remanent magnetisation of less than 1 J T^{-1} kg^{-1} is recorded for $Ni_{65}B_{35}$, while this increases to 15 J T^{-1} kg^{-1} for $Ni_{88}B_{12}$ nanotube structure.

As the specific magnetisation of the nanotube structures varies with B content, the ratio of the remanent magnetisation, M_r, to the saturation magnetisation, M_s, also varies with B content. This value is known as the squareness of the material and can be found by normalising the magnetic moment and recording the ratio of M_r/M_s at zero applied magnetic field. A normalised hysteresis curve is shown in Fig. 5.24(b). The squareness of the $Ni_{65}B_{35}$ nanostructure is 0.03. A small decrease in the B content has a large effect on the squareness. For example, a decrease in the B content to a composition of $Ni_{73}B_{27}$ results in a squareness value of 0.28, almost a factor of 10 increase. The maximum squareness recorded was 0.43 for a composition of $Ni_{88}B_{12}$. Due to the relatively low coercivities and squareness values of less than 0.5, the as-deposited nanostructures are classified as magnetically soft materials.

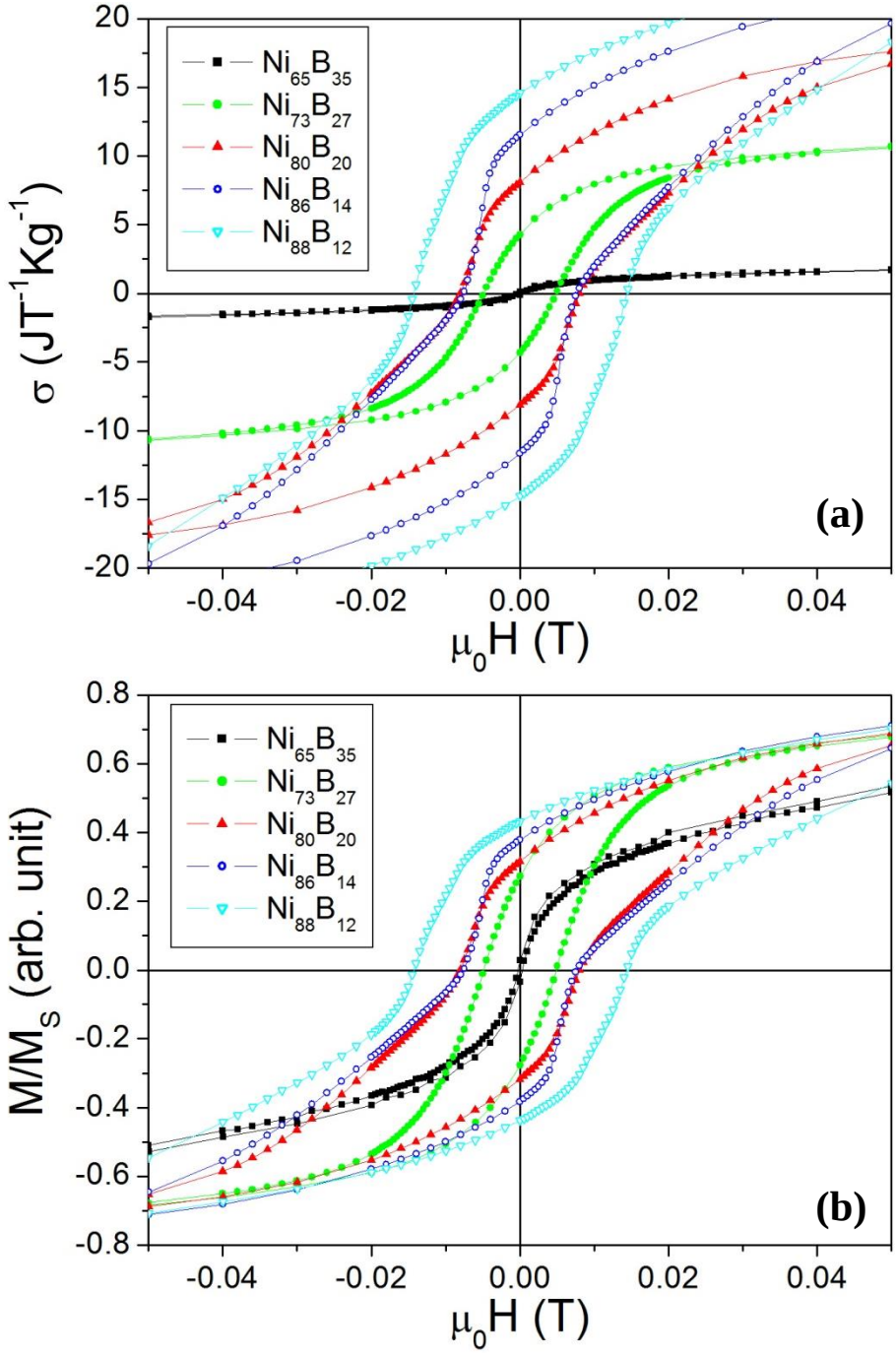

Figure 5.24: (a) Close up of the hysterises curves in Fig. 5.14 of Ni-B nanotube arrays for a range of compositions with the applied field parallel to the nanotube axis. **(b)** Hysteresis curves with normalised magnetisation values.

The magnetic properties recorded for all the as-deposited nanostructures are shown in Table. 5.1. For all Ni-B compositions the coercivity is in the order of mT and the squareness is below 0.5. These results indicate that the deposited Ni-B nanostructures are soft magnetic materials irrespective of composition. $Ni_{65}B_{35}$ has lowest coercivity

and remanence values. As the B content decreases there is a corresponding increase in the coercivity and remanence values of the Ni-B nanostructures.

pH	Composition	Specific Saturation Magnetisation σ_s ($J\ T^{-1}\ kg^{-1}$)	Coercivity $\mu_0 H_c$ (mT)	Remanent Magnetisation M_r ($J\ T^{-1}\ kg^{-1}$)	Squareness M_r/M_s
8.5	$Ni_{65}B_{35}$	3.5	0.5	0.1	0.03
9	$Ni_{73}B_{27}$	15.7	4.8	4.2	0.27
10	$Ni_{80}B_{20}$	25.6	8	8.1	0.32
11	$Ni_{86}B_{14}$	30.5	7.8	11.6	0.38
12	$Ni_{88}B_{12}$	33.7	14.5	14.6	0.43

Table 5.1: Magnetic properties of the as-deposited nanotube structures.

The increase in coercivity as a function of B content can be understood if we consider the crystallinity of the Ni-B alloy. The effect of magnetic domain size on the coercivity of magnetic materials is well understood. On the macroscopic scale there is an inverse relationship between the coercivity and the magnetic domain size proportional to D^{-1}, where D = approximate domain size. However, when D is similar to the size of the domain wall thickness, an alternative relationship is observed. The coercivity increases as the domain size increases with a D^6 relationship proposed in [22] and given by Eqn. 5.5,

$$H_C = P_C \frac{K_r^4 D^6}{M_S A^3} \tag{5.5}$$

where, H_c = Coercivity, P_c = Constant, K_r = Anisotropy constant , M_s = Saturation Magnetisation and A = Exchange stiffness constant. The D^6 relationship is recorded for grain sizes below a value of approximately 40 nm, with minimum coercivities recorded for amorphous materials [23]. The XRD data in Fig. 5.19 shows that Ni-B alloys with a large B content are completely amorphous. Thus taking Eqn. 5.5 into

consideration, these Ni-B alloys have a low associated coercivity. As the B content decreases, small peaks are recorded on the XRD spectrum in Fig. 5.19 indicating the formation of a nanocrystalline material. Therefore, the size of the grains and thus the size of magnetic domains within the material increase as B content decreases. Therefore, an increase in coercivity is recorded with decreasing B content.

As the electrolessly deposited nanotubes are soft magnetic materials, they cannot be used as future data storage media which will require hard magnetic materials with a large coercivity and remanence. However, soft materials have potential applications in the read-write heads of magnetic recording media. The soft magnetic nanotubes also have potential applications in future power technologies for use in components such as nano-inductors and nano-transformers in future electronic devices. Other potential applications include use in sensor application and bio-technology in areas such as targeted drug delivery. We have shown, that by varying the boron content of the nanotubes, the magnetic properties can be altered. Hence, the magnetic properties of the nanotubes can be tailored to suit each potential application. Again, these results contribute to our overall research objective of controlling the magnetic properties of the electrolessly deposited nanostructures.

5.5.2 Crystal Structure

The magnetic properties of the Ni-B nanotubes are also affected by the crystallinity of the nanostructure. A zoomed in image of the hysteresis curves for $Ni_{55}B_{45}$ post-annealing is shown in Fig. 5.25(a). Although, nanotubes with a large B content are soft magnetic materials with a low coercivity and remanence, the coercivity increases post-annealing. The coercivity recorded post-annealing between 300 ºC and 500 ºC is approximately 20 mT.

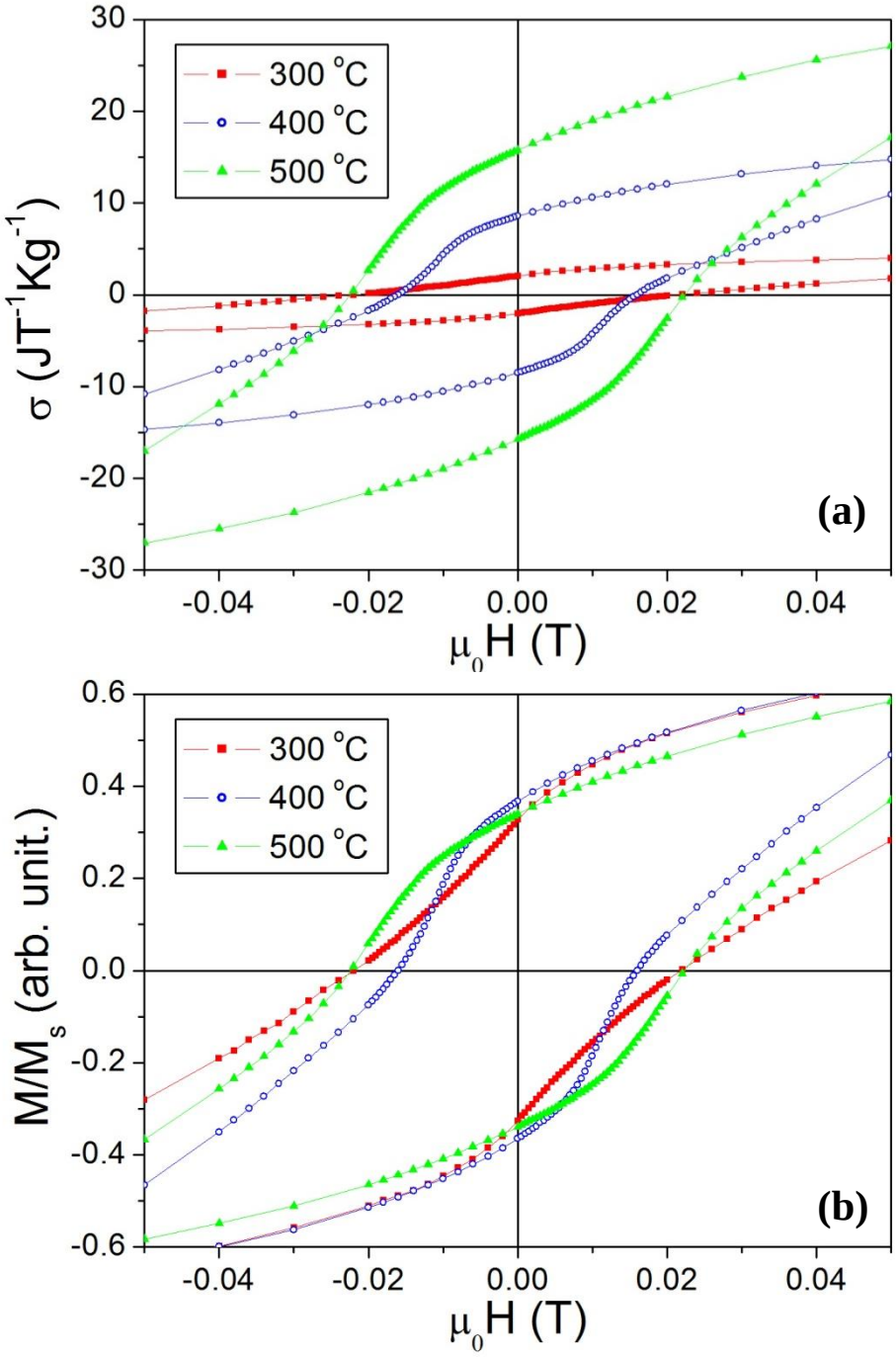

Figure 5.25: (a) Close up of the hysteresis curves in Fig. 5.22 showing the coercivity and remanence values for $Ni_{55}B_{45}$ nanotubes post-annealing with the applied field parallel to the nanotube axis. **(b)** Hysteresis curves with normalised magnetisation values.

The coercivity of the annealed nanotubes is larger than the as deposited nanotubes irrespective of composition. $Ni_{55}B_{45}$ had a negligible magnetic moment prior to annealing. However, a coercivity of 23 mT recorded post-annealing. The maximum coercivity recorded prior to annealing was 14.5 mT for $Ni_{88}B_{12}$. This increased to 20 mT post annealing. As the grain size of the Ni-B alloy increases during the

annealing process, there is a corresponding increase in the size of the magnetic domains. Therefore, the increase in coercivity observed post-annealing can be attributed Eqn. 5.5.

The remanent magnetisation of the $Ni_{55}B_{45}$ nanotubes shown in is 2.0 J T^{-1} kg^{-1}, 8.7 J T^{-1} kg^{-1}, and 15.6 J T^{-1} kg^{-1} for annealing temperatures of 300 ºC, 400 ºC and 500 ºC respectively. The squareness, M_r/M_s, for each of these nanostructures is between 0.32 and 0.36 as shown in Fig. 5.25(b). These values are very similar to those of the as-deposited nanotubes with a low B content, with squareness values of 0.32 and 0.38 recorded for $Ni_{80}B_{20}$ and $Ni_{86}B_{14}$ respectively. The increase in remanent magnetisation of the annealed nanostructures is attributed to the diffusion of B out of the Ni-B structure, allowing for magnetic interactions between adjacent Ni atoms and the retaining of the induced magnetic moment at zero field. The saturation field of the annealed nanotubes is approximately 1 T, similar to that recorded for an as-deposited $Ni_{80}B_{20}$ sample.

The hysteresis curves of annealed $Ni_{88}B_{12}$ nanotubes are shown in Fig. 5.26. Although the boron content of the as-deposited nanostructure is low, annealing results in a change in the magnetic properties. The remanent magnetisation increases from 14.6 J T^{-1} kg^{-1} for the as-deposited nanostructure to 21.1 J T^{-1} kg^{-1} post-annealing at 500ºC. The squareness values range from 0.43 to 0.46 for all samples. This indicates that within the bounds of experimental error, no significant change in the squareness of the $Ni_{88}B_{12}$ nanotubes is recorded. A small increase in the coercivity from 14.3 mT to 17.0 mT is observed post-annealing at 500 ºC. A decrease in the saturation field of the nanotubes is also recorded and magnetic saturation occurrs at approximitally 0.5 T post-annealing at 500 ºC. Due to an increase in the grain size of

the Ni-B alloy, annealing results in an increased coercivity associated with the magnetic structure.

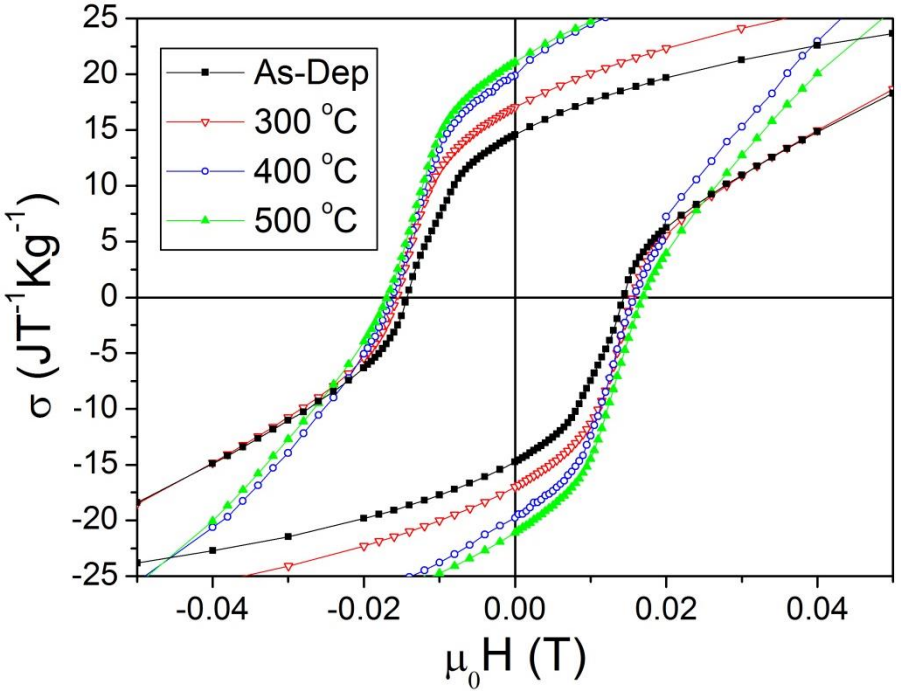

Figure 5.26: Hysterises curves of $Ni_{88}B_{20}$ nanotubes both as deposited and post-annealing at various temperatures with the applied field parallel to the nanotube axis.

5.5.3 Summary

In this section, we have shown that we have control over the magnetic properties of the nanostructures by altering the composition and annealing temperature. The grain size is effected by the B content within the Ni-B alloy. The saturation magnetisation, coercivity and remanence can all be controlled by varying the B content of the deposit. The magnetic properties of the magnetic nanostructure can also be controlled through annealing of the magnetic nanostructures. Post-annealing, the magnetic properties of alloys with a large B content are similar to those of as-deposited nanostructures with low B contents.

Therefore, it is possible to deposit continuous nanotubes with a uniform wall thickness at a low pH and then anneal the nanostructures to enhance their magnetic

properties. This allows for a controllable electroless deposition reaction for which kinetically controlled deposition will occur within the nanostructure. Therefore, continuous nanotubes can easily be formed and bath decomposition will not be an issue. To maintain a supportive template structure, it may be beneficial to use a template structure that does not evaporate during the annealing process thus preventing nanotube damage and making the sample easier to handle. This is an important contribution to this research, as it is possible to achieve a kinetically controlled deposition process then anneal the nanotubes to increase the specific magnetisation. This overcomes the challenges associated with the electroless deposition of magnetic nanotubes.

However, some challenges remain with this process. We have described two methods to increase the specific magnetisation of the electrolessly deposited Ni-B nanotubes, either decreasing the B content or annealing up to 500 ºC. However, these processes resulted in an increased coercivity and squareness of the nanotubes. Therefore, we also attempted to increase the specific magnetisation of the Ni-B structures with the addition of Fe and investigated the corresponding effect on the magnetic properties.

5.6 Ni-Fe-B Nanotubes

5.6.1 Specific Magnetisation

Ni-Fe-B nanotubes were deposited from the deposition bath described previously in section 3.5 at a pH of 9. By adding Fe to the Ni-B nanotubes we aim to increase the specific magnetisation of the deposited nanostructures and alter the associated magnetic properties. The specific magnetisation of Fe is 217.6 J T^{-1} kg^{-1}, almost four times larger than of Ni, which has a specific magnetisation of 55.4 J T^{-1} kg^{-1}. Therefore, it is expected that as the iron content increases a corresponding increase in

the specific magnetisation will be recorded. Also, as Fe is a soft magnetic material we aim to form soft magnetic nanotubes. For future applications, soft magnetic nanotubes with an increased specific magnetisation would be beneficial.

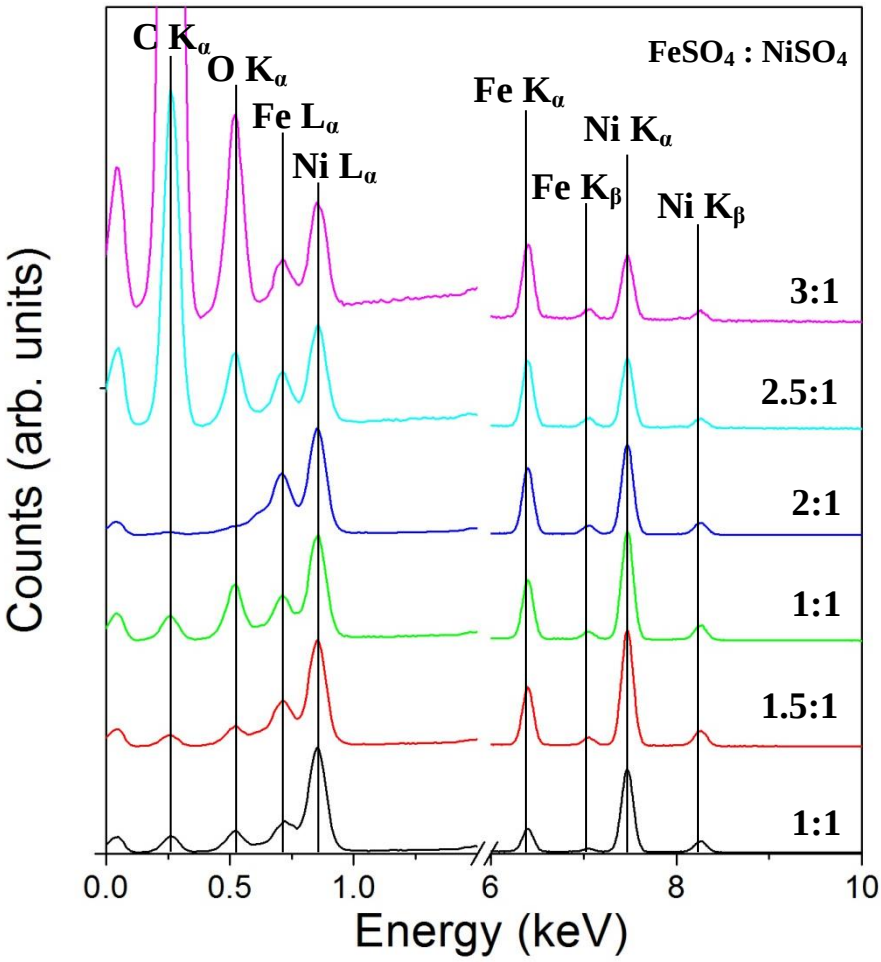

Figure 5.27: EDX spectrum of Ni-Fe-B nanotubes deposited for 40 minutes from the electroless deposition bath described in section 3.5 for a range of $FeSO_4$ concentrations.

Through variations of the $FeSO_4$ concentration from 0.0125 M - 0.0625 M in the electroless deposition bath, we were able to control the Fe content of the electrolessly deposited alloy. We determined the Fe : Ni ratio of the electrolessly deposited alloy via EDX analysis. The EDX spectrum of electrolessly deposited Ni-Fe-B alloys that we recorded is shown in Fig. 5.27. As the $FeSO_4$ concentration increases, there is a corresponding increase in the relative intensity of the Fe peaks. These results indicate that the iron content of the deposited alloy increases as $FeSO_4$ concentration increases.

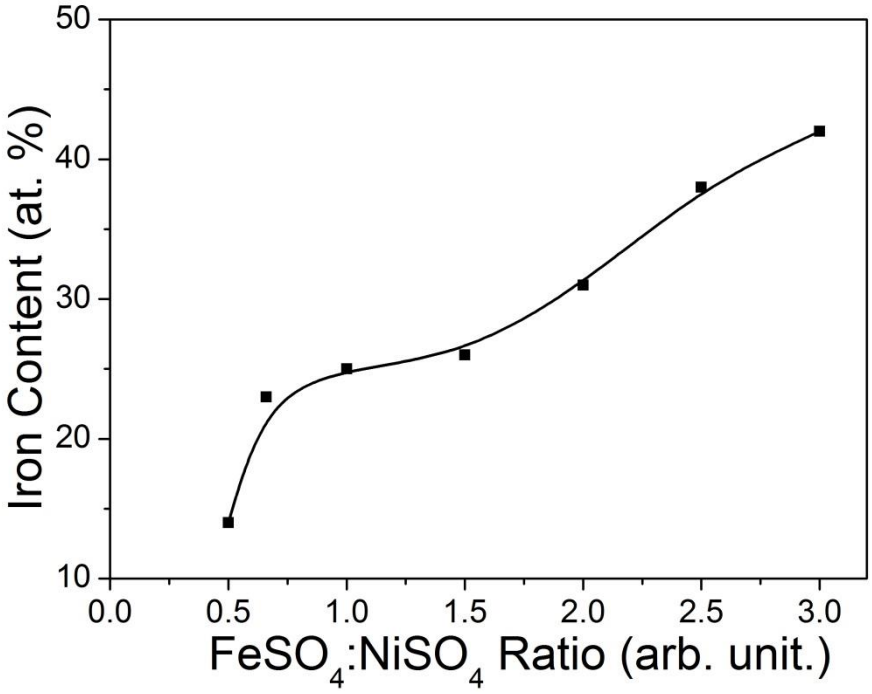

Figure 5.28: Relative iron content determined by EDX analysis for an $Ni_{100-x}Fe_x$-B alloy deposited via electroless deposition from the deposiiton bath described in section 3.5 for a range of $FeSO_4$ concentrations. Displayed curve acts as a guide to the eye.

The iron content as a function of the ratio of Ni and Fe sulphates in the deposition bath is shown in Fig. 5.28. The $NiSO_4$ concentration remained constant at 0.025 M. The composition of $Ni_{100-x}Fe_x$ ranges from x = 13 for a $FeSO_4$: $NiSO_4$ ratio of 1:2, to x = 42 for a ratio of 3:1. For relatively low $FeSO_4$ concentrations below a ratio of 2:1, the largest peaks observed on the EDX spectrum correspond to Ni and Fe. However, for large $FeSO_4$ concentrations, the largest peaks observed correspond to C and O. These peaks are recorded from the polycarbonate membrane and indicate that above an $FeSO_4$: $NiSO_4$ ratio of 2:1, limited deposition occurs and a very thin Ni-Fe-B film is formed on the membrane surface. Fe does not catalyse the electroless deposition process [24,25]. Therefore, for large Fe contents, the autocatalytic reaction required for electroless deposition occurs at a very slow rate and a minimal deposit is attained. In this case, due to the limited amount of deposition that occurs, incomplete nanotubes are formed for an $FeSO_4$:$NiSO_4$ ratio of 3:1. The B content of the nanotubes has been determined via XPS analysis. As the pH of the solution is

constant for all deposition baths, a constant B content of 26 at. % is recorded. Therefore, the overall composition of the nanotubes is written as $(Ni_{100-x}Fe_x)_{74}B_{26}$.

The magnetisation curves of the as-deposited nanostructures that we obtained are shown in Fig. 5.29. A specific magnetisation of 33.5 J T^{-1} kg^{-1} is recorded for a composition of $(Ni_{86}Fe_{14})_{74}B_{26}$ which increases to 84.3 J T^{-1} kg^{-1} for a composition of $(Ni_{62}Fe_{38})_{74}B_{26}$. Due to the small amount of magnetic material deposited for a $FeSO_4$:$NiSO_4$ ratio of 3:1, the error in the specific magnetisation of $(Ni_{58}Fe_{42})_{74}B_{26}$ is large and is not shown. Through alloying of Ni with small amounts of Fe, a larger specific magnetisation can be achieved for the deposited nanotubes than from a Ni-B nanostructure. The use of Fe also prevents the requirements of annealing or the use of a high pH to achieve large specific magnetisations.

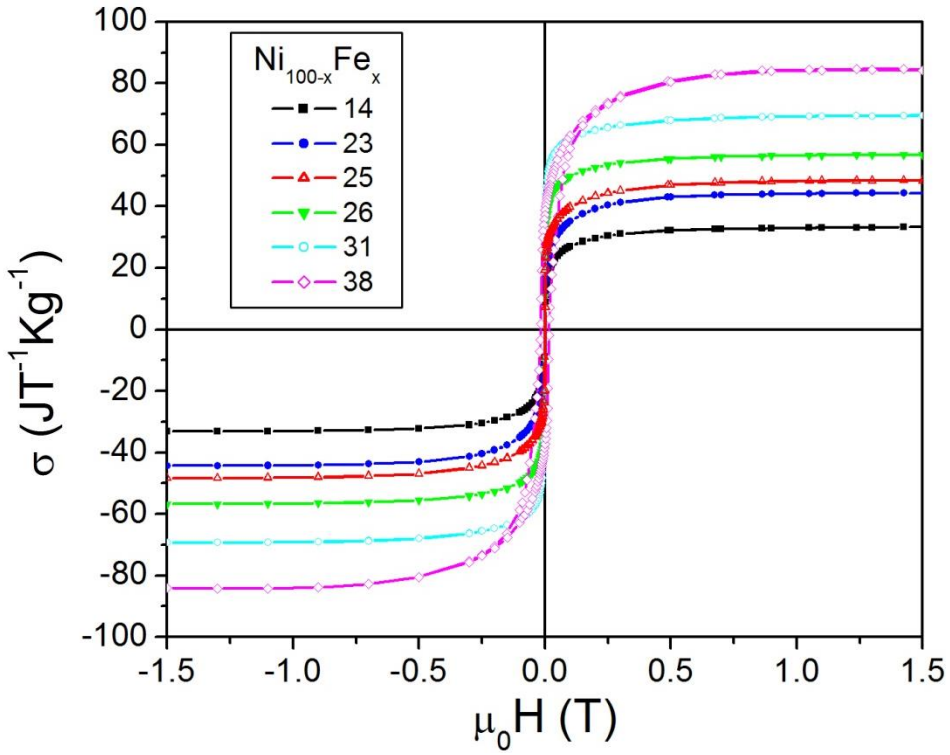

Figure 5.29: Hysterises curves of electrolessly deposited $(Ni_{100-x}Fe_x)_{74}B_{26}$ nanostructures with the applied field parallel to the nanotube axis.

5.6.2 Magnetic Properties

We have also investigated the magnetic properties of the Ni-Fe-B nanotubes as a function of iron content. The coercivity as a function of Fe content is shown in Fig. 5.30. As the Fe content of the nanotubes increases, there is a corresponding decrease in the coercivity of the nanotubes both parallel and perpendicular to the nanotube axis. A minimum coercivity of 2.9 mT is recorded for the $(Ni_{32}Fe_{68})_{74}B_{26}$ alloy. This is much lower than the coercivities recorded for Ni-B nanotubes with large specific magnetisations. These results can be explained by the fact that Fe is a magnetically soft material. Therefore, increases in the Fe content of the nanotubes results in nanotubes with reduced values of coercivity and increased values of specific magnetisation.

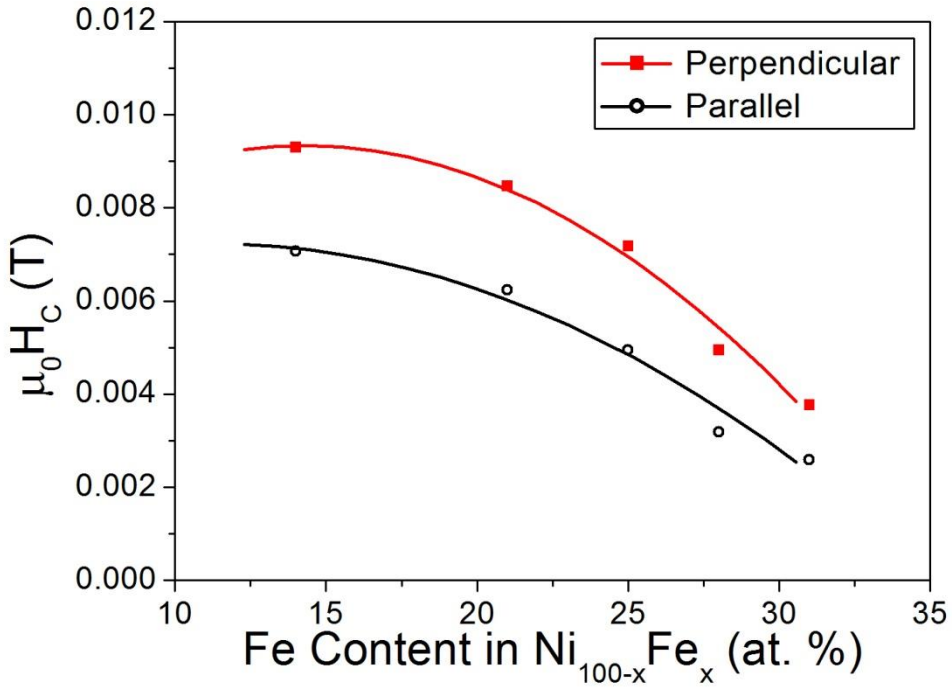

Figure 5.30: Coercivity of the Ni-Fe-B nanotubes as a function of iron content. Displayed curves act as a guide to the eye.

The coercivity perpendicular to the nanotube axis is larger than the coercivity parallel to the nanotube axis for all nanotube compositions. This indicates that there is a slight anisotropy associated with the nanotube structure with the nanotube axis acting as a

hard axis. The anisotropy present in the nanotube structure is due to the presence of a vortex reversal mechanism discussed previously in Section 5.7.1.

The squareness of the nanotubes as a function of Fe content is shown in Fig. 5.31. For a composition of $(Ni_{86}Fe_{14})_{74}B_{26}$, squareness values of 0.23 and 0.20 are recorded perpendicular and parallel to the nanotube axis. As the Fe content increases, the squareness of the nanotubes decreases with minimum values of 0.12 and 0.09 recorded perpendicular and parallel to the nanotube axis for a composition of $(Ni_{69}Fe_{31})_{74}B_{26}$. These values are much lower than those observed for Ni-B nanotubes with squareness values in the region of 0.3. The anisotropy observed is attributed to the presence of a vortex reversal mechanism.

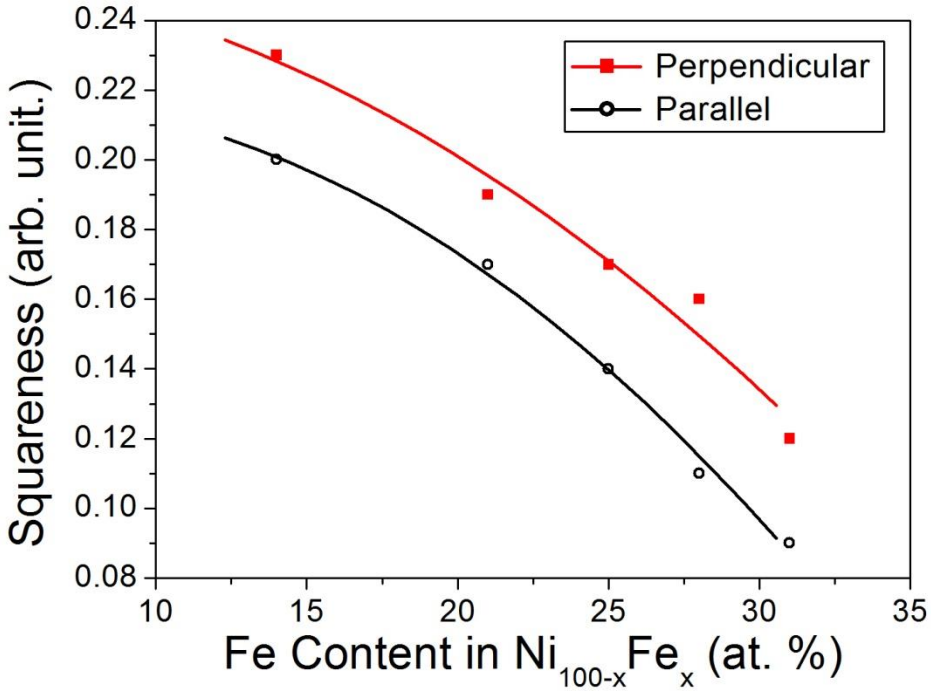

Figure 5.31: Squareness of Ni-Fe-B nanotubes as a function of iron content. Displayed curves act as a guide to the eye.

Here, we have shown that through alloying the Ni-B nanotubes with Fe the specific magnetisation of the alloy is increased while the coercivity and squareness is decreased. Therefore, the Ni-Fe-B nanotubes have lower coercivities and squareness

values than the Ni-B alloys. Therefore, the Ni-Fe-B nanotubes have more potential applications in future power technologies due to their lower energy losses. Ideally, larger Fe contents would be achieved as these should lead to lower coercivities. To achieve this further research into the electroless deposition of Fe is required.

5.7 Magnetic Reversal Mechanism

As discussed previously in section 2.9.1, magnetic nanotubes have three possible reversal mechanisms, coherent rotation, vortex wall reversal and transverse wall reversal. The coherent reversal mechanism can only occur for very short nanotubes where the domain wall thickness is of the same order as the nanotube length. As our nanotubes are 20 μm in length, this reversal mechanism can be discounted. Therefore, our nanotubes can reverse via vortex or transverse mechanisms. The nanotubes will reverse via the most energetically favourable mechanism. That is the mechanism which has the lowest associated coercivity. The coercivity values for each mechanism depend on a number of magnetic and structural properties. For Co-B nanotubes we recorded a minimum coercivity perpendicular to the nanotube axis. These results differ from those obtained for Ni-B and Ni-Fe-B nanotubes, for which a minimum coercivity was obtained parallel to the nanotube axis. This suggests that the magnetic reversal modes of Ni-B and Ni-Fe-B nanotubes differ from Co-B nanotubes.

5.7.1 Vortex Reversal Mechanism

For vortex wall reversal, also known as a curling reversal mechanism, the magnetic moments of the nanotube reverse via the propagation of a vortex wall along the nanotube axis [26]. The moments are aligned as they are if rotating around the centre of the nanotube axis. Curling mode predicts that the lowest coercivity will be recorded parallel to the nanotube axis, while the largest coercivity will be recorded

perpendicular to the nanotube axis [27]. Although other reversal mechanisms have been recorded previously for nanotubes with outer diameters up to 600 nm [6], because our nanotubes have a large external diameter of 400 nm, a vortex reversal mode is predicted [26].

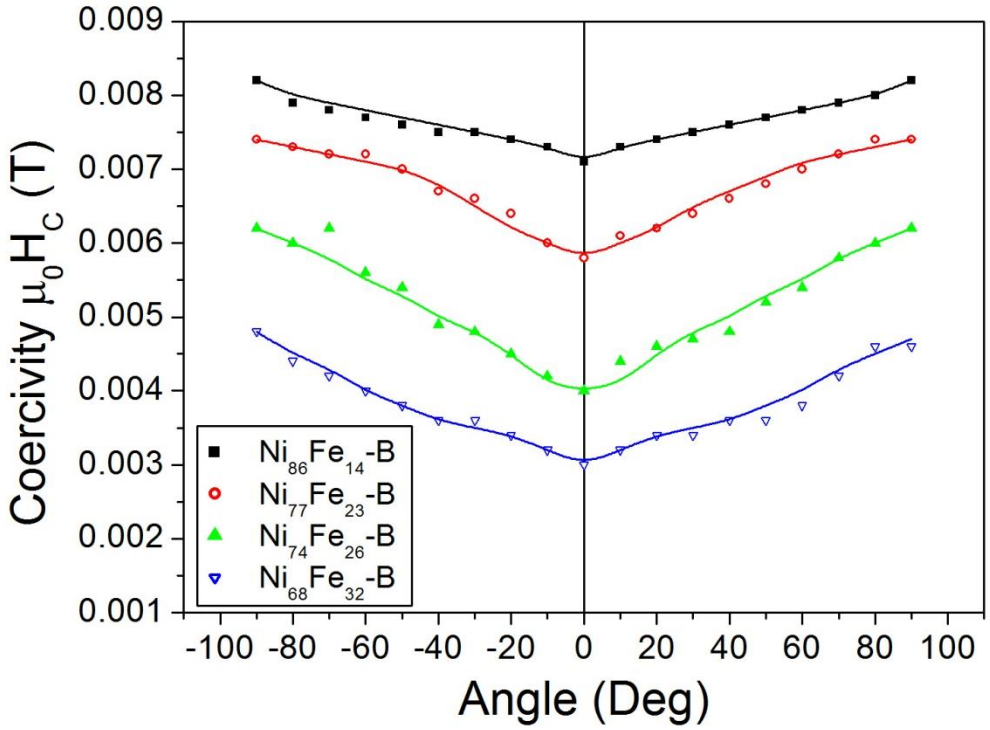

Figure 5.32: Coercivity as a function of angle for Ni-Fe-B nanotubes deposited at 20 ºC for a range of nanotube wall thickness. Displayed curves act as a guide to the eye.

As shown in Fig. 5.32, a U-shaped curve is obtained for coercivity plotted as a function of angle for all Ni-Fe-B nanotube compositions deposited at a low temperature. The nanotubes have been deposited for 40 minutes and thus they have a large wall thickness of approximately 100 nm. Due to the large wall thickness and large outer diameter a vortex reversal mode is expected. The small difference in coercivity values between the parallel and perpendicular measurements are due to vortex mode reversal mode as reversal occurs slightly easier parallel to the nanotube axis [28]. As the Fe content increases there is an associated decrease in the coercivity observed. This will be discussed further in Section 5.6.2.

A formula for nanotube nucleation field parallel to the nanotube axis is given by Escrig et al. [26] as shown in Eqn. 5.6,

$$H_n^V = \alpha(\beta)\frac{(L_{ex})^2}{R^2}M_S \tag{5.6}$$

where, H_n^V = nucleation field for vortex mode reversal, $\alpha(\beta)$ = constant which depends on β, the ratio of the internal nanotube radius divided by the external nanotube radius, L_{ex} = exchange length, R = external nanotube diameter and M_s = saturation magnetisation.

The exchange constant is given by Eqn. 5.7,

$$L_{ex} = \sqrt{\frac{2A}{\mu_0 {M_S}^2}} \tag{5.7}$$

where, A = exchange stiffness, μ_0 = permeability of free space.

Substituting Eqn. 5.7 into Eqn. 5.6 leads to Eqn. 5.8,

$$H_n^V = \frac{2\alpha(\beta)}{\mu_0 R^2}\left(\frac{A}{M_0}\right) \tag{5.8}$$

It has been stated that the nucleation field is a good approximation of the coercivity for magnetic nanotubes reversing via a vortex mechanism [27]. Therefore, the coercivity is directly proportional to the exchange constant and inversely proportional to the saturation magnetisation. The exchange stiffness of Fe is 2.1 x 10^{-11} J m^{-1} and of Ni is 0.9 x 10^{-11} J m^{-1}, while the exchange stiffness of NiFe lies in between the two with a value of 1.3 x 10^{-11} J m^{-1} [29]. Therefore, we assume that for our Ni-Fe nanotubes the exchange stiffness will lie between 0.9 x 10^{-11} J m^{-1} and 1.3 x 10^{-11} J m^{-1} for compositions ranging from $Ni_{86}Fe_{14}$ to $Ni_{68}Fe_{32}$. The effect of B on the exchange stiffness is not known though it is assumed that the exchange

stiffness remains relatively constant for all Fe contents even when alloyed with B. However, as discussed previously in section 5.6.1 the specific magnetisation for these nanotubes ranges from 33.5 J T^{-1} kg^{-1} to 69.8 J T^{-1} kg^{-1} for compositions of $(Ni_{86}Fe_{14})_{74}B_{26}$ and $(Ni_{68}Fe_{32})_{74}B_{26}$ respectively.

Therefore, as the Fe content increases the saturation magnetisation increases, while the exchange stiffness remains relatively constant. According to Eqn. 5.8 this should result in a decreasing nucleation field. These results agree with the observed experimental measurements in Fig. 5.32, with a decreasing coercivity observed for an increasing Fe content.

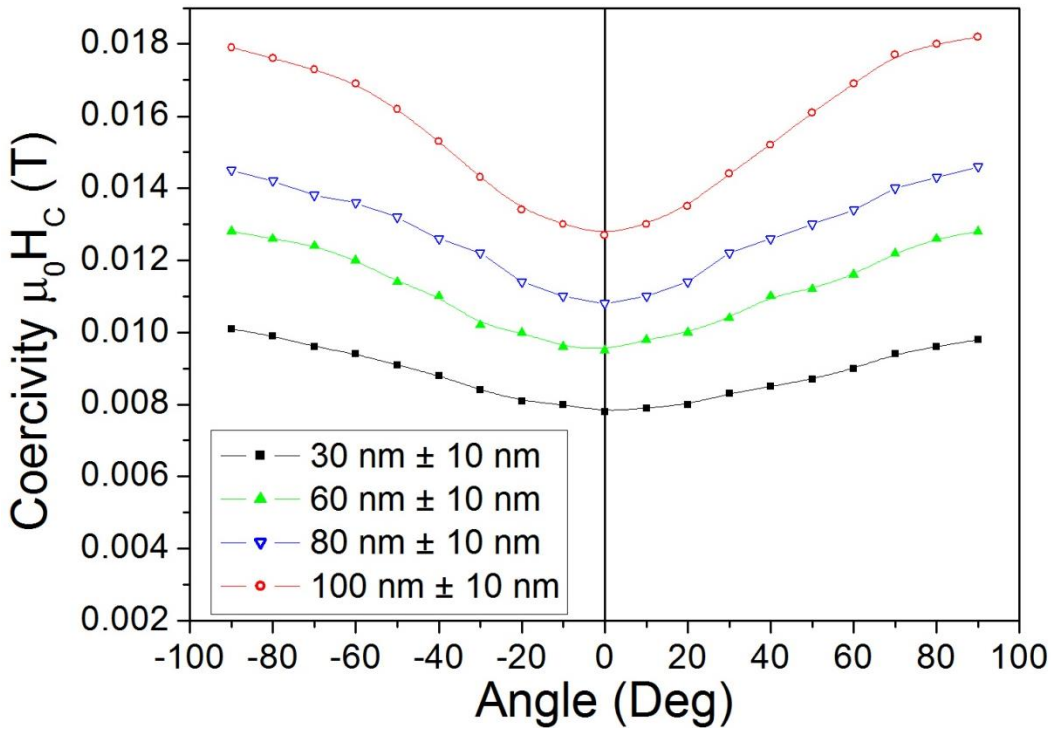

Figure 5.33: Coercivity as a function of angle for Ni-B nanotubes deposited at 20 °C for a range of nanotube wall thickness.

As shown in Fig. 5.33, a vortex reversal mechanism has also been observed for Ni-B nanotubes deposited via a kinetically controlled deposition process. The reversal mechanism has been investigated for a range of deposition times, each corresponding to a different nanotube wall thickness. In all cases, a vortex mode reversal mechanism

was observed. As the wall thickness of the nanotubes increases there is an associated increase in the coercivity. These results match the theoretical calculations of Chang et. al., who proposed an increased in coercivity as the wall thickness of the nanotubes increases due to increases in the associated nucleation field [30]. These also match the calculations of Escrig et al. [26] and Albrecht et al. [27].

From these results we can conclude that, for wall thicknesses ranging from 30 nm to 100 nm, Ni-Fe-B and Ni-B nanotubes have an associated vortex mode reversal mechanism. By altering the composition and wall thickness of the nanotubes, changes the in the coercivity of the nanotubes can be controlled.

5.7.1 Transverse Reversal Mechansim

A plot of coercivity as a function of angle for the Co-B nanotubes is shown in Fig. 5.34. A minimum coercivity is obtained for magnetic measurements perpendicular to the nanotube axis. As the angle of applied field decreases, the coercivity of the nanotubes increases. However, the maximum coercivity does not occur parallel to the nanotube axis. The maximum coercivity is recorded at an angle of approximately 10 º. This results in an M shaped graph. Similar results have been obtained previously for electrodeposited Co, Ni and Fe nanotubes with an external radius of 600 nm and wall thickness of 50 nm [6] and for Fe_3O_4 nanotubes with an external radius of 70 nm and a wall thickness of 10 nm [27]. Sharif et. al. [6], described this as a change from a coherent reversal mechanism at large angles to a vortex reversal mechanism at low angles. However, since then, it has been shown that the increase in coercivity at large angles is due to a transverse reversal mechanism [27]. The maximum coercivity recorded corresponds to the angle at which the

magnetic reversal mechanism of the nanotubes switches from a transverse reversal mechanism at large angles to a vortex reversal mechanism at low angles.

As shown previously in Eqn. 5.8, the coercivity associated with the vortex reversal mechanism is directly proportional to the exchange stiffness and inversely proportional to the specific magnetisation. However, the exchange stiffness of Co is 3.0 x 10^{-11} J m^{-1} almost 3 times larger than that of Ni-Fe and Ni [29]. Therefore, assuming the nanotube structue is similar for all compositions, Co-B has the largest nucleation field for a vortex reversal mechanism. Due to the increased coercivity of the Co-B nanotubes for vortex mode, the energetically favorable reversal mechanism is transverse mode reversal. The nucleation field associated with a transverse reversal mechanism is given by Escrig et al. [26]as shown in Eqn. 5.9,

$$H_n^T = \frac{2K(\omega_T)}{\mu_0 M_S} \tag{5.9}$$

where,

$$K(l) = \frac{1}{4}\mu_0 {M_S}^2[1 - 3N_z(l)] \tag{5.10}$$

and ${H_n}^T$ = nucleation field for transverse mode reversal, ω_T = transverse mode domain wall thickness, μ_0 = permeability of free space, M_s = saturation magnetisation N_Z = demagnetisation factor which depends on β, the ratio of the internal nanotube radius divided by the external nanotube radius. Inserting Eqn. 5.10 into Eqn. 5.9 leads to directly proportional relationship between coercivity and specific magnetisation. Previously, Sharif et. al. [6] found that Ni, Fe and Co nanotubes all displayed the same reversal mechanism which was dependent on the tube wall thickness. However, as these were pure metals, the large specific magnetisations may have prevented a transverse reversal mode from occurring. In this case the specific magnetisation is

reduced due to the presence of B and thus, a transverse reversal mode may be the energetically favourable mechanism for Co. The Co-B nanotubes became end-closed after 5 minutes of deposition and so the wall thicknesses of each deposition time are similar, with a value of approximately 40 nm.

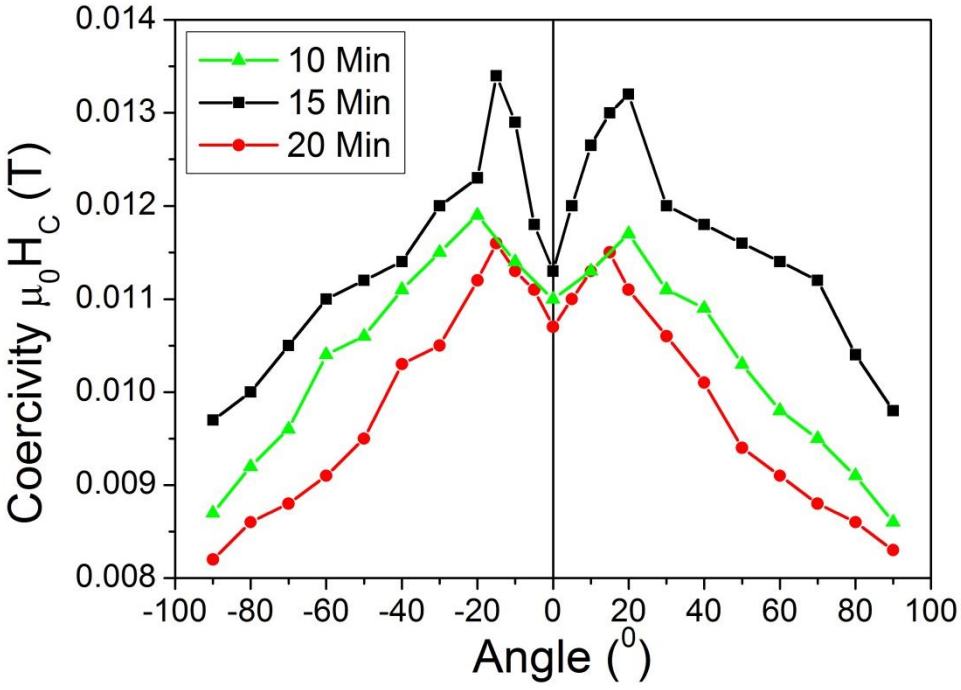

Figure 5.34: Coercvity as a function of angle for Co-B nanostrcutures with a wall thickness of approximately 40 nm deposited for a variety of deposition times at 65 C from the deposition bath described previosuly in Table 3.6.

For the Co-B nanotubes the reversal mechanism changes from a transverse reversal mechanism to a vortex reversal mechanism at an angle of approximately 20 °. This angle corresponds to point at which the maximum coercivity is recorded. At this angle the vortex mode becomes the energetically favoured mechanism and the reversal mode switches from a transverse to a vortex mode.

5.8 Ni-Cu-B Nanotubes

Electroless deposition of Ni-Cu-B nanostructures is extremely challenging. An electrolyte containing $CuSO_4$ was extremely unstable and bath decomposition occurred easily. As discussed previously, the deposition of magnetic nanostructures

occurs best at a pH of greater than 9. However, an electrolyte containing this pH favours the precipitation of copper. On the other hand, a low pH results in a nanostructure with a very low magnetisation. We found that the optimum deposition pH at which the deposition of both Cu and Ni occurred was between 6.5 and 8.5. The pH was kept as large as possible to have a magnetic moment associated with the nanostructure. The greatest specific magnetisation achieved using this deposition process was 0.6 J T^{-1} kg^{-1} for $Ni_{85}Cu_{15}$-B. This is over 50 times smaller than the specific magnetisation of bulk Ni. A minimum detectable magnetisation of 0.2 J T^{-1} kg^{-1} was recorded for $Ni_{60}Cu_{40}$-B. The B content of the nanotubes was approximately 40 at. % for all Ni-Cu compositions. As discussed previously, the large reduction in moment observed is associated with the large amount of boron that is present in the nanotube alloy.

5.8.1 Structure and Composition

The composition of the nanotubes was controlled by varying the $CuSO_4$ molarity between 0.003 M – 0.024 M within the electrolyte as described in Table 3.7. At molarities greater than 0.024 M, the solution was unstable and precipitation of metal within the electrolyte occurred. The Ni-Cu ratio was investigated using EDX analysis. An EDX spectrum of the deposited alloy is shown in Fig. 5.35. A summary of the compositions of the deposited Ni-Cu-B nanotubes is given in Table. 5.2 for a range of $CuSO_4$ concentrations. As the $CuSO_4$ molarity increases the Cu content of the nanotubes increases with a maximum Cu content of $(Ni_{60}B_{40})_{60}B_{40}$ recorded for a $CuSO_4$ molarity of 0.024 M.

An EDX compositional mapping of Cu (Fig. 5.36(b)) and nickel (Fig. 5.36(c)) indicates that electroless deposition of Ni and Cu is relatively uniform across the entire membrane surface. However, some bright deposits are visible on an SEM

image of the membrane surface as shown in Fig. 5.36(a). The compositional mapping shows that the bright deposits consist of a Ni-Cu alloy. Further EDX analysis of the bright deposits show the presence of a large amount of Pd. These bright deposits are probably Pd clusters that have attached to the membrane surface thus resulting in increased deposition in this area. The nanotubes were deposited for 5 minutes at 65 ºC. The nanostructure which formed consisted of nanotubes with a wall thickness of approximately 60 nm connected at both ends by a thin film 200 nm thick. In this case, an ideal kinetically controlled reaction did not occur and the nanotubes were slightly thinner at the centre of the nanotube than at the base.

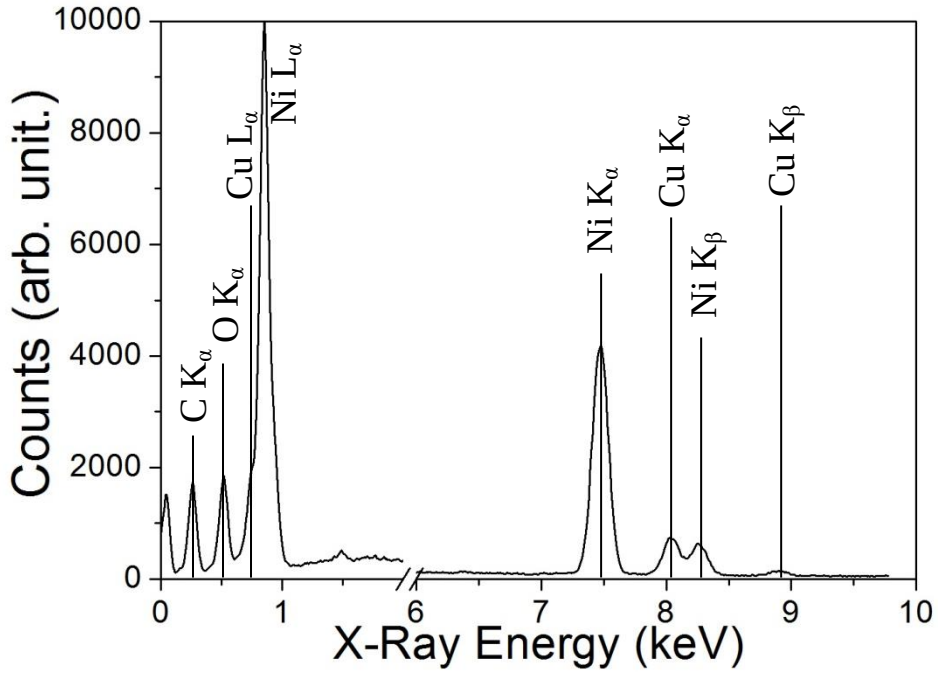

Figure 5.35: EDX spectrum of $(Ni_{80}Cu_{20})_{60}B_{40}$ nanotubes.

$CuSO_4$ Concentration (Mol L^{-1})	Composition
0	$Ni_{60}B_{40}$
0.003	$(Ni_{85}Cu_{15})_{60}B_{40}$
0.012	$(Ni_{80}Cu_{20})_{60}B_{40}$
0.024	$(Ni_{60}Cu_{40})_{60}B_{40}$

Table 5.2: Composition of the electrolessly deposited $(Ni_XCu_{100-X})_{60}B_{40}$ nanotubes.

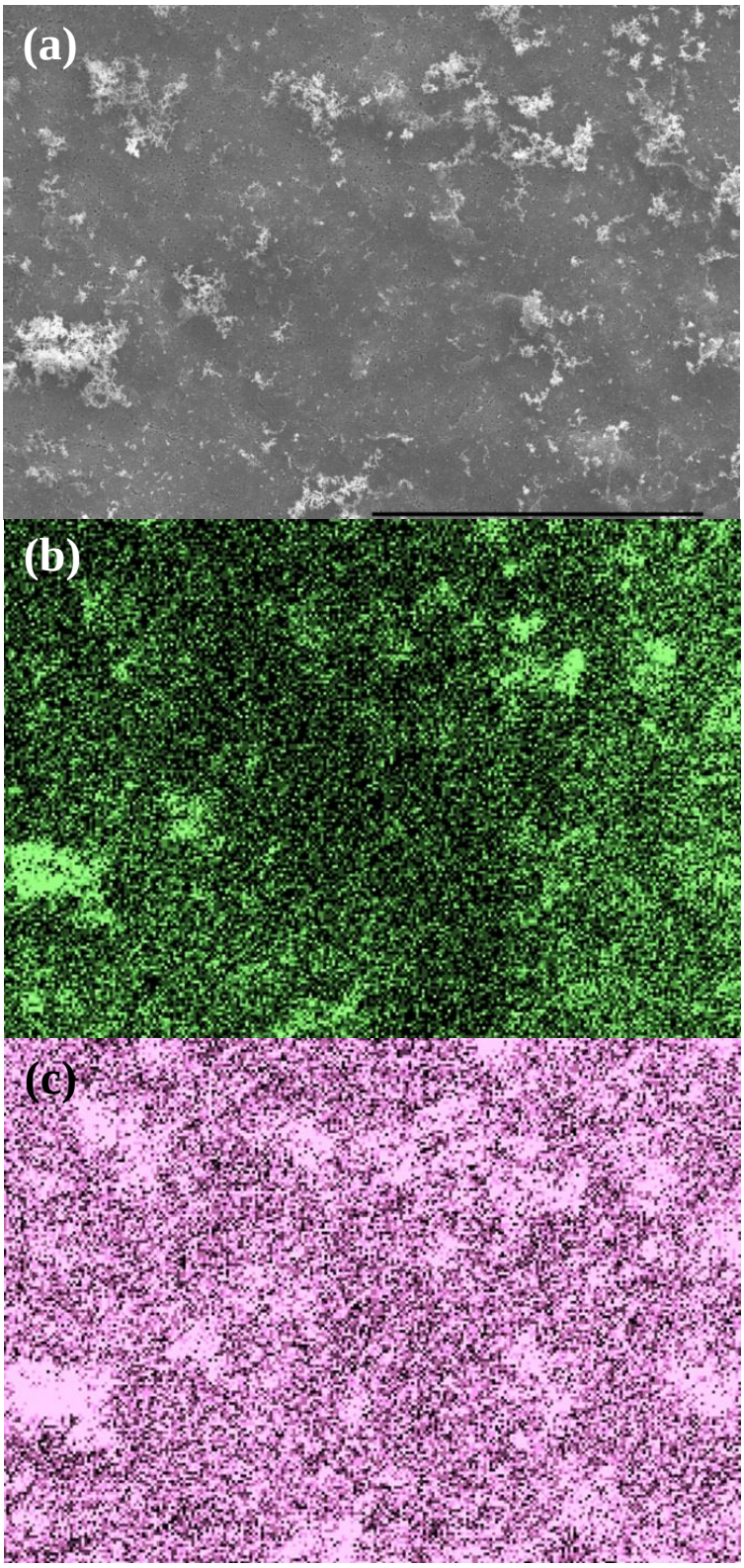

Figure 5.36: (a) SEM image of the membrane surface of electrolessly deposited $(Ni_{60}Cu_{40})_{60}$-B_{40}. EDX mapping of the polycarbonate membrane surface of **(b)** Cu and **(c)** Ni.

5.8.2 Magnetic Properties

Due to the low magnetic moment associated with the Ni-Cu-B nanotubes, a large noise was present in the VSM measurements. The maximum moment recorded was in the range of 0.1 memu. The VSM is capable of measuring as low as 1 x 10^{-6} emu. The values we recorded were well above this range. Therefore, the hysteresis curves can still be clearly defined. Averaging of the VSM measurements was calculated to reduce the noise detected. One half of the hysteresis curve for a $(Ni_{85}Cu_{15})_{60}B_{40}$ nanotube array is shown in Fig. 5.37. Using the data analysis software, a good hysteresis curve fit can be achieved. The remanence and coercivity values can easily be recorded as a good approximation of the saturation field. From this curve a coercivity of 7 mT and a squareness of 0.07 are recorded for the $(Ni_{85}Cu_{15})_{60}B_{40}$ nanotube array.

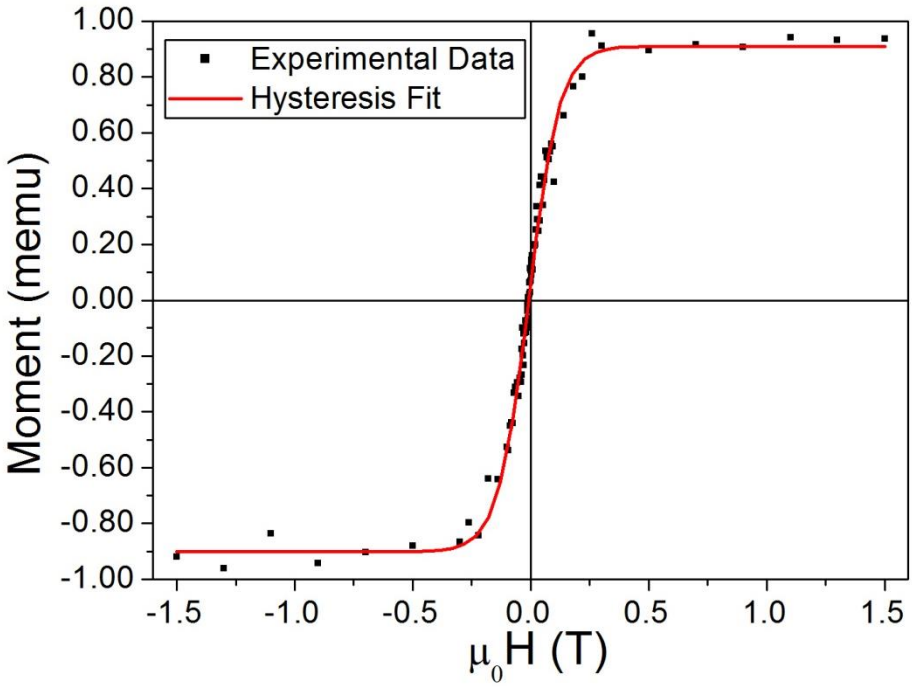

Figure 5.37: As measured hysterises curve for a $(Ni_{85}Cu_{15})_{60}B_{40}$ nanotube array with a curve fitted to smooth the data.

A full hysteresis curve for a $(Ni_{80}Cu_{20})_{60}B_{40}$ nanotube array is shown in Fig. 5.38. The coercivity recorded was 7 mT and the squareness was 0.07. The coercivity and squareness values for $(Ni_{60}Cu_{40})_{60}B_{40}$ were also very similar. Similar to the end-open

nanotubes discussed previously, we observed that the magnetic reversal is dominated by a pinning type mechanism for all nanotube compositions. These results indicate that a copper content of less than 40 % in the Ni-Cu alloy has no effect on the coercivity, remanence or the magnetic reversal mechanism of the nanotubes.

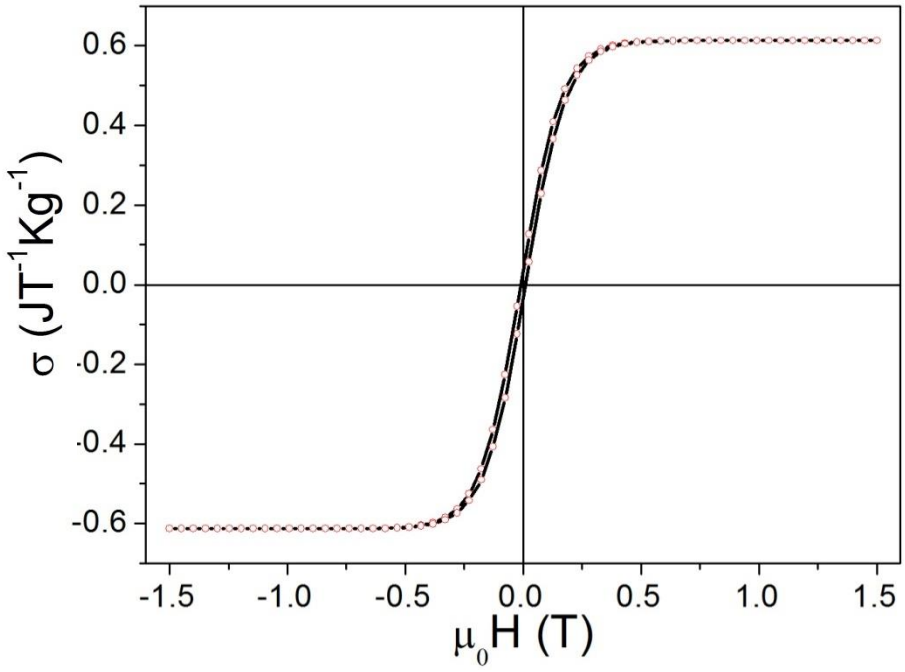

Figure 5.38: Averaged hysteresis curve of a $(Ni_{80}Cu_{20})_{60}B_{40}$ nanotube array carried out parallel to the nanotube axis.

Due to an increase in the saturation field of the deposited nanotubes, normalised initial magnetisation curves in Fig. 5.39 show that there is an increase in magnetic anisotropy of the nanostructures as the copper content increases. Pure Ni-B deposits have the lowest anisotropy with a saturation field of 0.5 T. As the copper content of the nanotubes increases, there is a corresponding increase in the saturation field of the nanotube array. A saturation field of 0.7 T is recorded for a $(Ni_{80}Cu_{20})_{60}B_{40}$ nanotube array, while this value increases to 1.4 T for $(Ni_{60}Cu_{40})_{60}B_{40}$. By controlling the amount of non-magnetic Cu in the Ni-Cu-B alloy, we can control the anisotropy and saturation field while holding the associated coercivity constant.

The magnetic properties of nanotube arrays are dependent on magnetocrystalline anisotropy, shape anisotropy, aspect ratio of the nanotubes and the dipolar interactions between the nanotubes [31]. We can rule out the effect of shape and size as all deposited nanotubes have the same dimensions with identical aspect ratios. The dipolar interaction is expected to reduce with decreasing saturation magnetization, which is inconsistent with an increase in anisotropy. Therefore, it is likely that the anisotropy in the deposits is associated with magnetocrystalline anisotropy, which is dependent on the Cu content of the nanostructure. Although XRD analysis shows a dominant amorphous nature of the deposits, the technique cannot rule out the presence of a nanocrystalline component, which is likely to be responsible for the observed anisotropy. Hence, increasing the copper and decreasing the nickel content has an effect on the anisotropy of the deposited nanostructures, by increasing the saturation field, with no effect on the coercivity or squareness of the nanostructures.

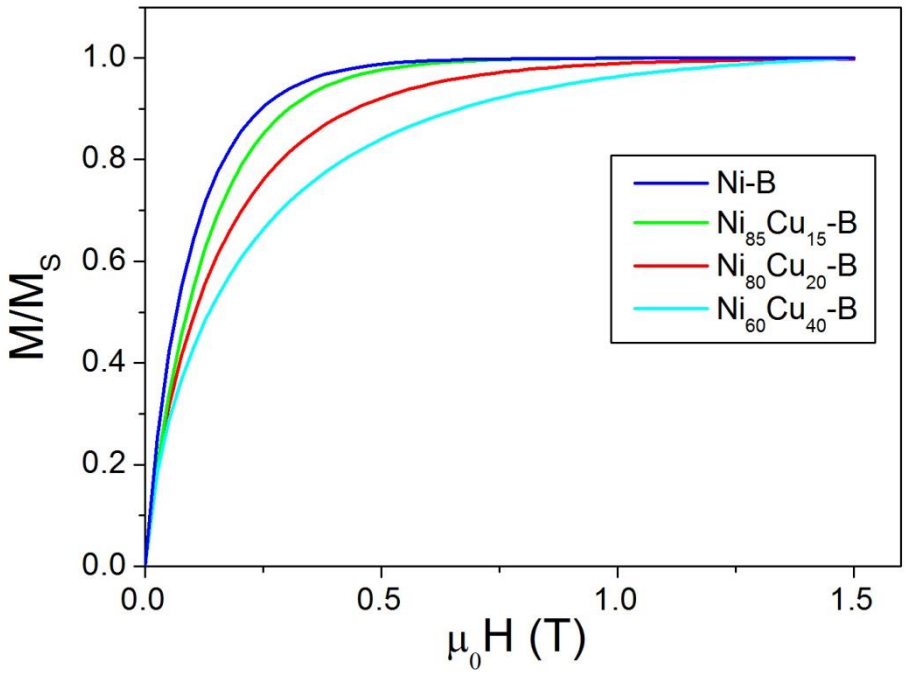

Figure 5.39: Normalised initial magnetization (M/M_S) curves carried out on DC demagnetised Ni-B and (Ni_XCu_{100-X})-B nanotubes.

This is an important result as we show that, it is possible to fine tune the composition of the nanostructures and synthesise nanotubes which have different saturation fields, while maintaining a constant coercivity. This result provides many potential future applications for magnetic nanotubes. By controlling the addition of alloys to the magnetic nanostructures, we show that it may be possible to vary the magnetic properties of the nanostructures. We have achieved the aim of having the ability to control the magnetic properties of the electrolessly deposited nanostructures. However, the electroless deposition of Ni-Cu-B nanotubes results in a very low specific magnetisation. Therefore, other alternatives with large magnetic moments, such as Fe or Co alloys, should be used to create nanostructures with large specific magnetisations.

5.9 Conclusions

By carrying out a wide range of experiments, we have found that the magnetic properties of electrolessly deposited nanostructures depend on a wide variety of parameters including alloy composition, boron content, crystallinity and nanostructure. The deposited nanostructures are soft magnetic materials with low coercivities and low remanent magnetisation. We have investigated the magnetic properties of a wide variety of novel nanotube compositions including Ni-B, Ni-Fe-B, Co-B and Ni-Cu-B.

We have found that there is a large anisotropy associated with the as-deposited nanostructure. This is attributed to the magnetic film formed on the membrane surface. We observed that an end-open nanotube array connected at both ends by a thin film reverses via a pinning type mechanism. However, once the nanotubes become end-closed, the reversal mechanism switches to a nucleation type mechanism.

Through removal of the thin film, the magnetic properties of the electrolessly deposited nanotube structure can be observed. There is a small anisotropy recorded for the nanotube arrays. Ni-B and Ni-Fe-B nanotubes deposited via a kinetically controlled deposition process reverse via a vortex mode. In this case a minimum coercivity is recorded parallel to the nanotube axis. However, for Co-B nanotubes, we have recorded a change from a vortex reversal mechanism to a transverse reversal mechanism. A minimum coercivity is observed perpendicular to the nanotube axis. A transverse reversal mechanism occurs because the transverse reversal mode becomes energetically favourable for Co-B nanotubes.

An investigation to maximise the specific magnetisation of an electrolessly deposited Ni-B nanotube structure led to the conclusion that B plays a vital role in the determining the specific magnetisation of the electrolessly deposited nanostructure. Variations in the deposition bath pH control the B content of the deposit. Large pH values correspond to a low B content, which results in a large specific magnetisation. Therefore, by depositing nanostructures at large pH values, we have achieved the electroless deposition of a $Ni_{88}B_{12}$ alloy with a specific magnetisation of 33.7 J^{-1} T^{-1} kg^{-1}. This is 60 % of the maximum possible value of 55.4 J^{-1} T^{-1} kg^{-1} for pure Ni. Annealing is another method that can be used to increase the specific magnetisation of the nanotube structure. During annealing B diffuses out of the Ni-B structure. This leads to the formation of a Ni FCC structure with an increased magnetic moment. Annealing for 1 hour at 500 °C led to a maximum magnetisation of 48.6 J^{-1} T^{-1} kg^{-1}. The addition of ferromagnetic alloys with large specific magnetisations also increases the specific magnetisation of the deposited alloy. A maximum value of 84.3 J T^{-1} kg^{-1} is recorded for a composition of $(Ni_{62}Fe_{38})_{60}B_{40}$.

We have found that, as the B content of the nanostructures decreases, larger coercivities and squareness values are recorded. This is due to an increase in the size of the grain structure as the B content decreases. During annealing, the magnetic properties of the magnetic nanostructure are altered. Due to increases in the size of the crystal grains, there is a corresponding increase in the coercivities of the magnetic nanotubes.

We have also investigated the effect of alloy composition on the magnetic properties of the electrolessly deposited nanostructures. We have found that for Ni-Fe-B nanotubes, as the iron content increases, decreases in the coercivity and squareness of the nanotubes are recorded. The addition of Cu to Ni-B nanotubes increases the anisotropy of the nanotube structure while holding the coercivity constant. Therefore, through the use of additives such as Fe and Cu, we have altered the associated magnetic properties of the electrolessly deposited nanostructures.

Soft magnetic nanotubes have many potential applications in areas such as magnetic recording media, power technologies, electronic components and bio-technology. Here, we have shown that, through the use of electroless deposition, nanotubes and nanostructures with a wide range of magnetic properties can be deposited. Through alterations of the composition, crystallinity and nanostructure, the magnetic properties of the nanotubes can be varied. Therefore, using the electroless deposition method we have shown that it is possible to fine tune the magnetic properties of the electrolessly deposited nanotubes to suit a wide range of potential applications.

5.10 References

[1] X. F. Han, S. Shamaila, R. Sharif, J. Y. Chen, H. R. Liu and D. P. Liu, *Advanced Materials*, **21**, 4619 (2009).

[2] X. W. Wang, Z. H. Yuan, S. Q. Sun, Y. Q. Duan and L. J. Bie, *Materials Chemistry and Physics*, **112**, 329 (2008).
[3] J. Bao, C. Tie, Z. Xu, Q. Zhou, D. Shen and Q. Ma, *Advanced Materials*, **13**, 1631 (2001).
[4] F. Tao, M. Guan, Y. Jiang, J. Zhu, Z. Xu and Z. Xue, *Advanced Materials*, **18**, 2161 (2006).
[5] W. Lee, R. Scholz, K. Nielsch and U. Gösele, *Angewandte Chemie*, **117**, 6204 (2005).
[6] R. Sharif, S. Shamaila, M. Ma, L. D. Yao, R. C. Yu, X. F. Han and M. Khaleeq-ur-Rahman, *Applied Physics Letters*, **92**, 032505 (2008).
[7] J. F. Rohan, D. P. Casey, B. M. Ahern, F. M. F. Rhen, S. Roy, D. Fleming and S. E. Lawrence, *Electrochemistry Communications*, **10**, 1419 (2008).
[8] A. Azizi, M. Mohammadi and S. K. Sadrnezhaad, *Materials Letters*, **65**, 289 (2011).
[9] I. Enculescu, M. Sima, M. Enculescu, E. Matei, M. E. Toimil Molares and T. H. Cornelius, *Optoelectronics and Advanced Materials-Rapid Communications*, **2**, 133 (2008).
[10] L. Hai-Peng, H. Man-Gui, C. Li and D. Long-Jiang, *Chinese Physics B*, **20**, 060701 (2011).
[11] S. C. Lin, C. H. Lai and P. W. Wu, *Electrochemical and Solid-State Letters*, **11**, D1 (2008).
[12] W. Wang, N. Li, X. Li, W. Geng and S. Qiu, *Materials Research Bulletin*, **41**, 1417 (2006).
[13] Z. Liu, W. L. Li and W. D. Fei, *Modern Physics Letters B*, **27**, 1341006 (2013).
[14] I. Kim, J. Kim, K. H. Kim and M. Yamaguchi, *IEEE Transactions on Magnetics*, **40**, 2706 (2004).
[15] A. Bai and C. C. Hu, *Materials Chemistry and Physics*, **79**, 49 (2003).
[16] G. O. Mallory, *Plating*, **58**, 319 (1971).
[17] N. Patel, R. Fernandes and A. Miotello, *Journal of Power Sources*, **188**, 411 (2009).
[18] B. Szpunar, U. Erb, G. Palumbo, K. Aust and L. J. Lewis, *Physical Review B*, **53**, 5547 (1996).
[19] H. Li, Y. Wu, H. Luo, M. Wang and Y. Xu, *Journal of Catalysis*, **214**, 15 (2003).
[20] W. T. Evans and M. Schlesinger, *Journal of the Electrochemical Society*, **141**, 78 (1994).
[21] M. M. Rico, J. M. Greneche and G. A. Pérez Alcázar, *Journal of Alloys and Compounds*, **398**, 26 (2005).
[22] B. Cantor, "*Novel Nanocrystalline Alloys and Magnetic Nanomaterials*", CRC Press (2004).
[23] G. Herzer, *Physica Scripta*, **T49**, 307 (1993).
[24] G. O. Mallory and J. B. Hajdu, in *Electroless Plating: Fundamentals and Applications*, William Andrew (1990).
[25] F. Delaunois, J. P. Petitjean, P. Lienard and M. Jacob-Duliere, *Surface and Coatings Technology*, **124**, 201 (2000).
[26] J. Escrig, J. Bachmann, J. Jing, M. Daub, D. Altbir and K. Nielsch, *Physical Review B*, **77**, 214421 (2008).
[27] O. Albrecht, R. Zierold, S. Allende, J. Escrig, C. Patzig, B. Rauschenbach, K. Nielsch and D. Görlitz, *Journal of Applied Physics*, **109**, 093910 (2011).
[28] J. Bachmann, J. Escrig, K. Pitzschel, J. M. Montero Moreno, J. Jing, D. Görlitz, D. Altbir and K. Nielsch, *Journal of Applied Physics*, **105**, 07B521 (2009).
[29] C.-Y. You, *Applied Physics Express*, **5**, 103001 (2012).
[30] C. R. Chang, C. M. Lee and J. S. Yang, *Physical Review B*, **50**, 6461 (1994).
[31] X. Z. Li, X. W. Wei and Y. Ye, *Materials Letters*, **63**, 578 (2009).

Chapter 6 – Hydrogen Generation

6.1 Introduction

The heat of combustion of hydrogen is 3 times larger than that of hydrocarbons, 142 MJ kg^{-1} compared to 47 MJ kg^{-1} [1]. Additionally, the by-product of hydrogen combustion is water. This makes hydrogen an environmentally friendly energy source. However, the viability of hydrogen technology as a future alternative to non-renewable energy sources requires low cost fuel cells, safe and cheap storage media and efficient methods of hydrogen generation.

Hydrogen storage for portable applications is currently an important area of research. Due to the relatively large amount of stored hydrogen and the stability in an alkaline solution, metal hydrides, such as sodium borohydride ($NaBH_4$), are one such possible storage mechanism [2]. Hydrogen from an alkaline metal hydride solution is released only in the presence of a catalyst. The chemical reaction that occurs is shown in Eqn. 6.1,

$$NaBH_4 + 2H_2O \xrightarrow{\text{catalyst}} NaBO_2 + 4H_2 \qquad (6.1)$$

A variety of noble metal catalysts [3-5] have been shown to generate hydrogen from a $NaBH_4$ solution at a large rate. However, due to the cost involved they are not suitable for large scale catalysis in future technologies. Therefore, alternative cheap non-noble transition metal catalysts are currently the focus of research in this area [6-8]. Nanostructured transition metal catalysts, such as nanoparticles or catalysts deposited on a Ni-foam substrate, have been shown to catalyse hydrogen release from $NaBH_4$ at the largest rates of all of the transition metal catalysts [9-12].

To be considered as a viable alternative technology for future energy requirements, the Department of Energy (DOE) in the USA have set hydrogen storage targets of 5.5 wt. % H2 by the year 2015 with an ultimate target of 7.5 wt. %. For an aqueous $NaBH_4$ solution, these targets correspond to $NaBH_4$ concentrations of 6.87 M (26 wt. % $NaBH_4$) and 9.38 M (35.5 wt. % $NaBH_4$) respectively. The hydrogen generation system needs to meet these targets in order to be considered viable for future technologies. The largest storage values achieved previously for aqueous $NaBH_4$ solutions with large hydrogen generation rates include 4.2 wt. % hydrogen (20 wt. % $NaBH_4$ solution) [10] and 3.2 wt. % hydrogen (15 wt. % $NaBH_4$ solution) [11]. The catalyst must possess a large activity, so that hydrogen can be released from the system and used to power a fuel cell as it is produced. It is also important that the catalyst can be recovered from the solution and recycled.

In this chapter an electrolessly deposited nanotube structure is investigated as a potential catalyst for hydrogen generation from a $NaBH_4$ solution. Due to the large surface area associated with the nanostructure, our hypothesis is that transition metal catalysts, electrolessly deposited on a polycarbonate template structure, will display a large catalytic activity. Our experiments establish the hydrogen generation rates of the nanostructured catalysts as a function of composition, structure, solution temperature and $NaBH_4$ concentration. The recyclability of the catalyst and its potential use in future technologies is also investigated as part of our experiments. From the results obtained, we consider whether an electrolessly deposited nanotube structure is suitable as a potential catalyst for hydrogen release from an alkaline $NaBH_4$ solution.

6.2 Preliminary Study

6.2.1 Control Experiment

Prior to a comprehensive investigation of the effectiveness of a nanostructured catalyst, a control experiment was undertaken to ensure there was no release of hydrogen from the system without the presence of a catalyst. When $NaBH_4$ was placed in de-ionised water, hydrogen was released instantly. However, by placing $NaBH_4$ in a NaOH solution with a pH greater than 10, the $NaBH_4$ solution was stable for times of greater than 12 hours. The alkaline $NaBH_4$ solution was placed in a 250 ml round bottom flask. This was placed in the experimental set-up as shown in Fig. 3.30. A polycarbonate membrane with no electrolessly deposited material was added to the solution and no hydrogen was released. However, occasionally an air bubble was released from the system. The negative flow of water back into the outlet was also occasionally observed. We proposed that these effects were due to volume changes of the air within the round bottom flask, attributed to small fluctuations in temperature. The effect of temperature on the volume of a gas is described by Charles's law which states that the volume of a gas at constant pressure is directly proportional to its temperature. Using Charles's law, the change in volume with respect to a change in temperature is given by Eqn. 6.2,

$$\Delta V = \frac{T_f}{T_i} V_i - V_i \tag{6.2}$$

where ΔV = change in volume, V_i = initial volume, T_i = initial temperature and T_f = final temperature. Our experiments were carried out between 30 ºC and 50 ºC. For example, a temperature increase from 30 ºC (303 K) to 33 ºC (306 K), for a 250 ml volume of gas would correspond to a change in volume of 2.5 ml. For catalysts with a large hydrogen generation rate this volume is negligible. However, for

catalysts with a low generation rate this change in volume may be appreciable. Therefore, stabilising the temperature of the solution was deemed important.

6.2.2 Sonication Requirement

When a suitable catalyst is placed in an aqueous $NaBH_4$ solution, hydrogen gas is released. However, during initial testing, it was noticed that hydrogen bubbles stuck to the catalyst on the polycarbonate membrane. These bubbles prevent $NaBH_4$ from coming into contact with the catalytic surface. We used agitation of the solution to remove hydrogen from the catalytic surface and this resulted in an increase of the hydrogen generation rate.

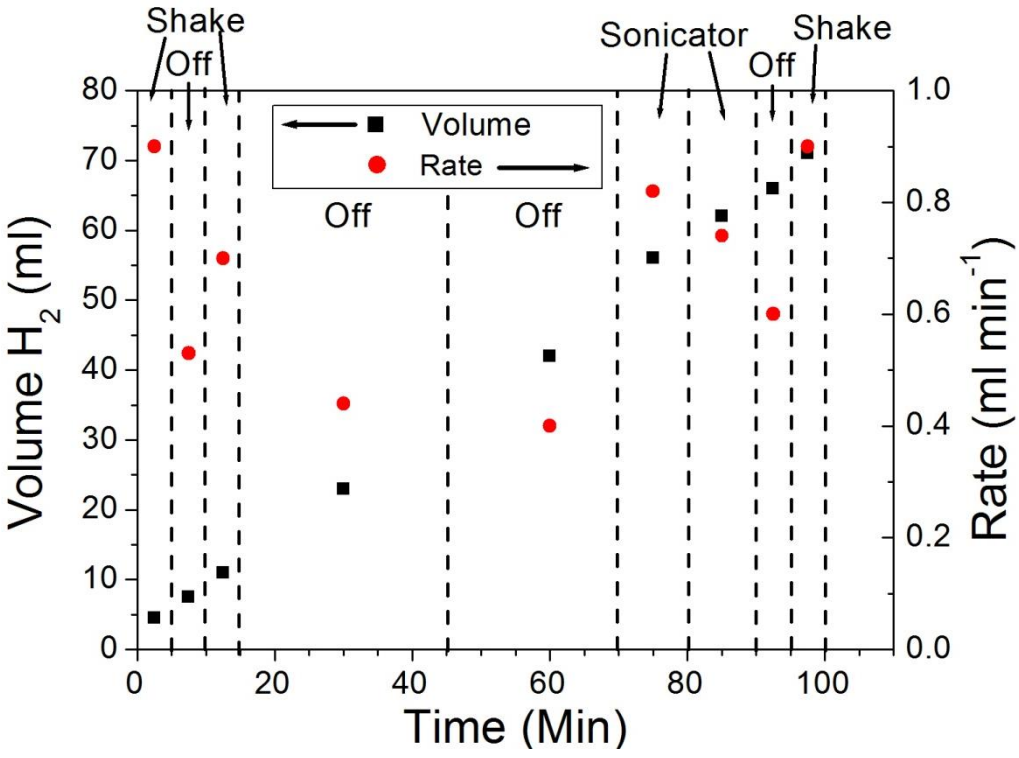

Figure 6.1: Hydrogen generation rates achieved with different levels of agitation using a Co-B catalyst in a $NaBH_4$ solution at 25 ^{o}C. Shake - Shaking the $NaBH_4$ solution by hand. Sonicator - Placing the $NaBH_4$ solution in a sonicating bath. Off - No aggitation.

The solution was agitated via two different mechanisms, by shaking the solution by hand and by placing the solution in a sonicator. Fig. 6.1 shows the volume of hydrogen generated with respect to time and the hydrogen generation rate of a

nanostructured Co-B catalyst for a range of agitation periods. Initially, for the first 5 minutes of hydrogen generation, the solution was shaken by hand, resulting in a hydrogen generation rate of 0.9 ml min^{-1}. For the time period of 5 – 10, minutes the solution was left undisturbed and the hydrogen generation rate decreased to 0.5 ml min^{-1}. When the solution was shaken again, the hydrogen generation rate increased to 0.7 ml min^{-1}. Again, when the solution was left undisturbed for the time period 15 – 70 minutes, hydrogen generation continued to occur at a steady rate of between 0.4 ml min^{-1} and 0.5 ml min^{-1}. This indicates that while it is not necessary for hydrogen generation to occur, agitation increases the hydrogen generation rate. When placed in a sonicator after 70 minutes, the hydrogen generation rate increased from 0.5 ml min^{-1} to 0.8 ml min^{-1}. Once the sonicator was turned off, a decrease in the hydrogen generation rate to 0.6 ml min^{-1} was observed. For the final 5 minutes, the solution was shaken by hand and a large increase in the hydrogen generation rate to 0.9 ml min^{-1} was observed.

From this, it is clear that agitation of the catalyst within the $NaBH_4$ solution results in an increased hydrogen generation rate. Shaking the solution by hand results in the largest hydrogen generation rate of approximately 0.9 ml min^{-1}. However, apart from the impracticality of this for tests running for hours at a time, the solution must be kept in a water bath to control the temperature. A sonicator provides a suitable alternative with hydrogen generation rates of up to 0.8 ml min^{-1}. Sonication of the hydrogen generation bath releases hydrogen bubbles from the surface of the catalyst. This increases the catalytic surface area in contact with the $NaBH_4$ solution, thus increasing the hydrogen generation rate.

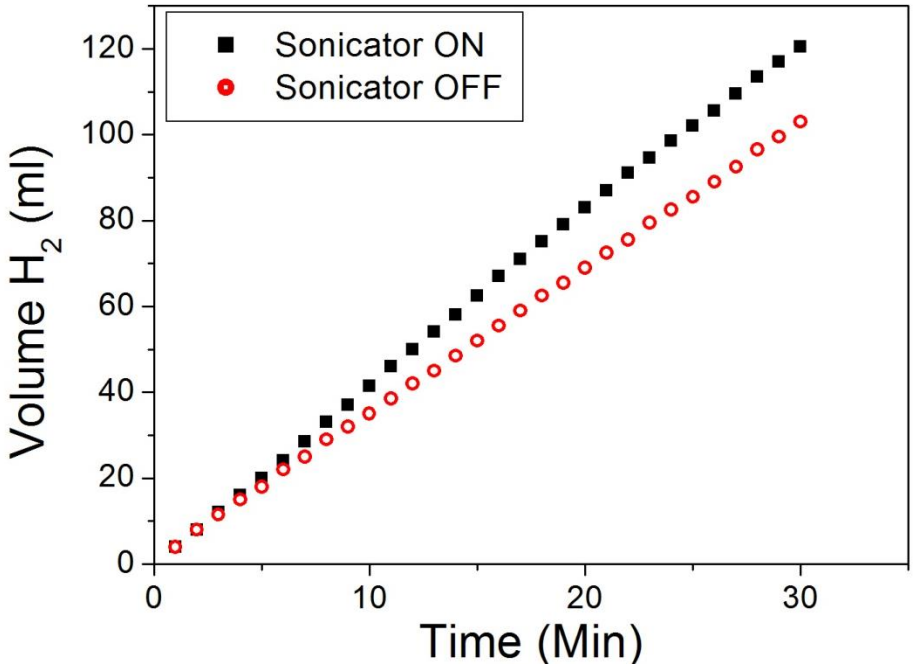

Figure 6.2: Volume of hydrogen generated using a Co-B catalyst from a $NaBH_4$ solution at 40 °C as a function of time with and without the use of a sonicator.

A comparison between the volumes of hydrogen generated as a function of time for identical conditions with and without the use of a sonicator is shown in Fig. 6.2. With the sonicator turned on, 120 ml of hydrogen is released from the solution in 30 minutes. This corresponds to a hydrogen generation rate of 4 ml min^{-1}. Without the use of a sonicator, an undisturbed solution releases 103 ml of hydrogen in 30 minutes. This is a hydrogen generation rate of 3.4 ml min^{-1}. By using the sonicator, the hydrogen generation rate is increased by a factor of approximately 1.2. As sonication increases the hydrogen generation rate, it was used for the remainder of the experiments as a method to enhance hydrogen release from the surface of the catalyst.

6.3 Catalyst Composition

Nanostructured catalysts are synthesised via the electroless deposition method discussed in Chapter 4. A polycarbonate membrane is used as a template structure during electroless deposition which results in the formation of a nanostructure comprising of end-open nanotubes connected at the top and base by a thin film. The

nanotubes have a length of 20 µm and an external pore diameter of 400 nm. A range of alloys have been deposited via this method to form nanostructures which can be used as catalysts for hydrogen generation.

We have carried out a study to determine which electrolessly deposited alloy has the largest catalytic activity for hydrogen release from $NaBH_4$. The alloys used were Co-B, Co-Ni-B, Co-Ni-Fe-B, Ni-Cu-B and Ni-B. The ratio of the metals was found using EDX spectroscopy. The EDX spectrum of a Co-Ni-Fe-B sample is shown in Fig. 6.3. The peaks represented in the spectrum are shown in Table. 6.1. Analysis of the spectrum determined a composition of $Co_{63}Ni_{20}Fe_{17}$. O and C peaks were also observed on the EDX spectrum, though these can be attributed to signals from the polycarbonate substrate, oxides forming on the alloy surface and contaminants from the deposition process. Other compositions determined via EDX analysis, were $Co_{75}Ni_7Fe_{18}$, $Co_{72}Ni_{28}$ and $Ni_{60}Cu_{40}$. All samples were deposited at a pH of 8 which from XPS analysis corresponds to a B content of approximately 40 at. %.

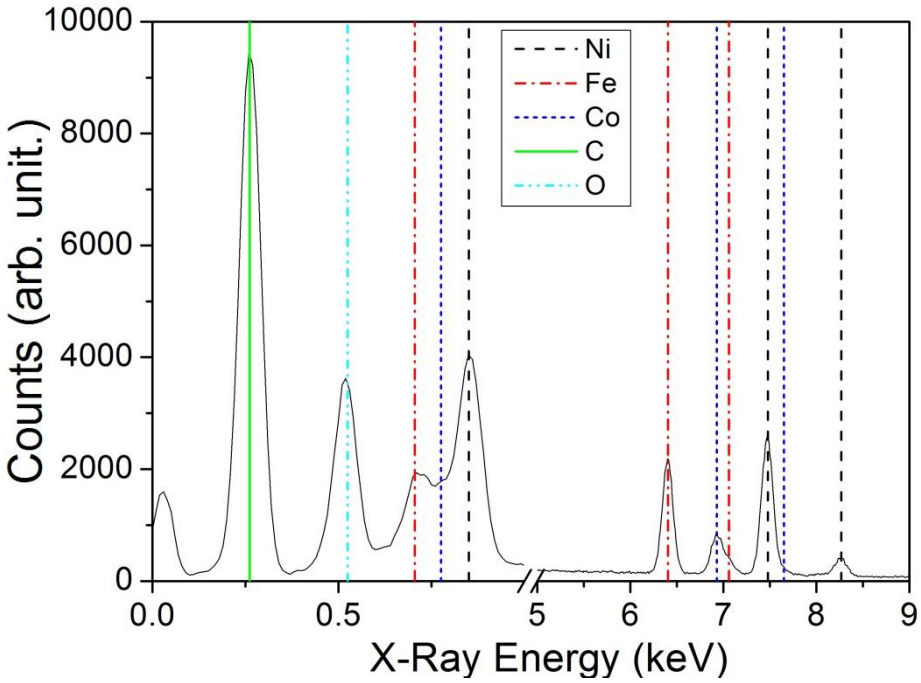

Figure 6.3: EDX Spectrum of CoNiFe nanostructure deposited on a polycarbonate membrane.

Energy (eV)	Element	X-Ray
277	C	K_α
525	O	K_α
705	Fe	L_α
776	Co	L_α
851	Ni	L_α
6404	Fe	K_α
6930	Co	K_α
7058	Fe	K_β
7478	Ni	K_α
7650	Co	K_β
8265	Ni	K_β

Table 6.1: Characteristic peaks recorded in the EDX spectrum of a Co-Ni-Fe nanostructure deposited on a polycarbonate membrane.

The volume of hydrogen generated as a function of time for each catalyst is shown in Fig. 6.4. The maximum volume of hydrogen produced was 93 ml in 30 minutes with a Co-B catalyst. When other metals, such as Ni and Fe, were alloyed with the Co-B catalyst, the volume of hydrogen generated was reduced. When Co was removed from the catalyst, the hydrogen generation rate decreased further with Ni-B and Ni-Cu-B showing very low activities with volumes of less than 10 ml released after 30 minutes. However, as there are slight variations in the mass of each catalyst due to the electroless deposition process, they must be normalised to hydrogen generation rate per unit mass.

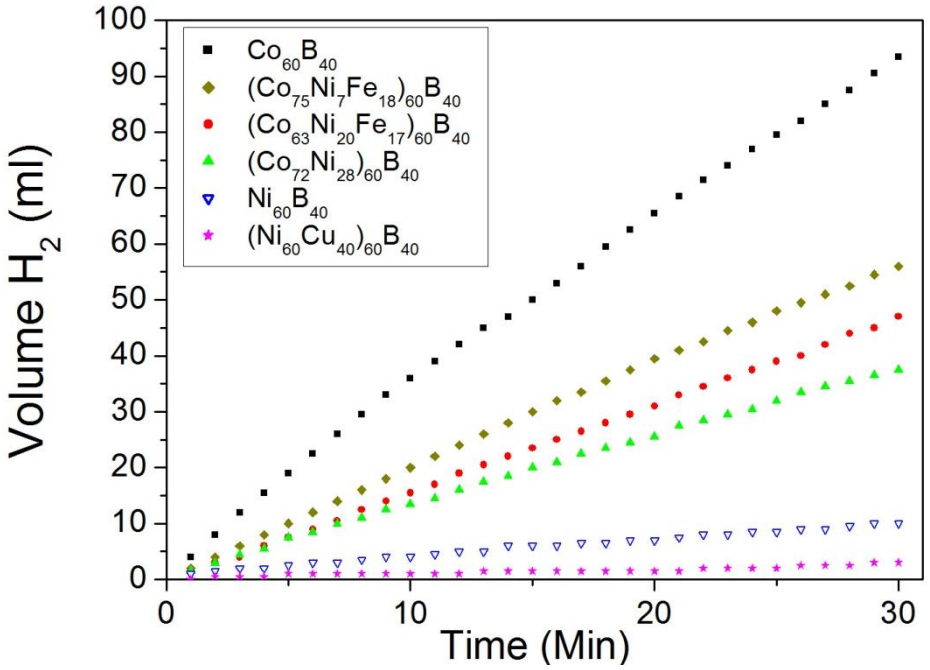

Figure 6.4: Volume of hydrogen generated as a function of time for nanostructured catalysts with a range of compositions, each with a similar catalytic mass at a temperature of 25 °C.

The hydrogen generation rates for each of the catalysts are shown in Table. 6.2. For the $Co_{60}B_{40}$ catalyst, 93 ml of hydrogen is released in 30 minutes which corresponds to a hydrogen generation rate of 3.1 ml min^{-1}. The mass of the catalyst is 1.15 mg which corresponds to a rate per unit mass of 2695 ml min^{-1} g^{-1}. As the Co content decreases, there is a corresponding decrease in the hydrogen generation rate. $(Co_{75}Ni_7Fe_{18})_{60}B_{40}$ releases 56 mg of H_2 in 30 minutes corresponding to a rate of 1.87 ml min^{-1}. The mass of the sample was 1.08 mg and thus the rate per unit mass was 1730 ml min^{-1} g^{-1}. The Ni content was increased and the Co content decreased to form a composition of $(Co_{63}Ni_{20}Fe_{17})_{60}B_{40}$. For this composition, the hydrogen generation rate decreased to 1120 ml min^{-1} g^{-1}, indicating that a large Co content results in a large hydrogen generation rate. However, the iron appears to also play a role in increasing the hydrogen generation as the removal of Fe from the Co-Ni-Fe-B catalyst results in a decrease in the hydrogen generation rate. For a composition of $(Co_{72}Ni_{28})_{60}$-B_{40}, a hydrogen generation rate of 700 ml min^{-1} g^{-1} was recorded.

Composition	H_2 Generation Rate (ml min^{-1} g^{-1})
$Co_{60}B_{40}$	2695
$(Co_{75}Ni_7Fe_{18})_{60}B_{40}$	1730
$(Co_{63}Ni_{20}Fe_{17})_{60}B_{40}$	1120
$(Co_{72}Ni_{28})_{60}B_{40}$	700
$Ni_{60}B_{40}$	300
$(Ni_{60}Cu_{40})_{60}B_{40}$	90

Table 6.2: Hydrogen generation rates of catalysts of a range of compositions in a solution with a $NaBH_4$ concentration of 10 wt. % and a temperature of 25 ºC.

With the complete removal of the Co from the catalyst, a further decrease in the hydrogen generation rate was recorded. For a $Ni_{60}B_{40}$ catalyst only 10.5 ml of hydrogen was generated in 30 minutes. This corresponds to a rate of 0.35 ml min^{-1}. The mass of the catalyst was 1.16 mg, giving a hydrogen generation rate of 300 ml min^{-1} g^{-1}. With Cu added to this catalyst, the rate decreased even further to 90 ml min^{-1} g^{-1}. From these results, it can be concluded that, of all the alloys that were deposited during these experiments, catalysts containing Co give the largest hydrogen generation rates. Therefore, in the remainder of this chapter, we will focus on the hydrogen generation properties of nanostructured Co-B catalysts deposited via electroless deposition.

6.4 Co-B Composition

An XPS spectrum of the Co-B catalyst is shown in Fig. 6.5. The elements observed were B, C, Co and O. Table. 6.3 shows the origin of each peak observed in the spectrum. The observed oxygen may be due to the formation of an oxide on the surface of the catalyst or the presence of precipitated chemicals from the deposition bath such as lactic acid, diammonium citrate or sodium hydroxide, all of which

contain oxygen. Pure boron should have a peak at 187.7 eV. However, the boron peak was observed at a binding energy of to 192.2 eV. This represents its oxidised form, B_2O_3. Due to the electroless deposition process in an alkaline solution, B will oxidise on the alloy surface to form B_2O_3. Similar results have been observed previously for Co-B catalysts and the catalytic activity of the catalyst is not affected [13]. The presence of C is attributed to contaminants from the organic lactic acid used during the deposition process. Analysis of the XPS data shown in Fig. 6.5 gives a composition of $Co_{60}B_{40}$.

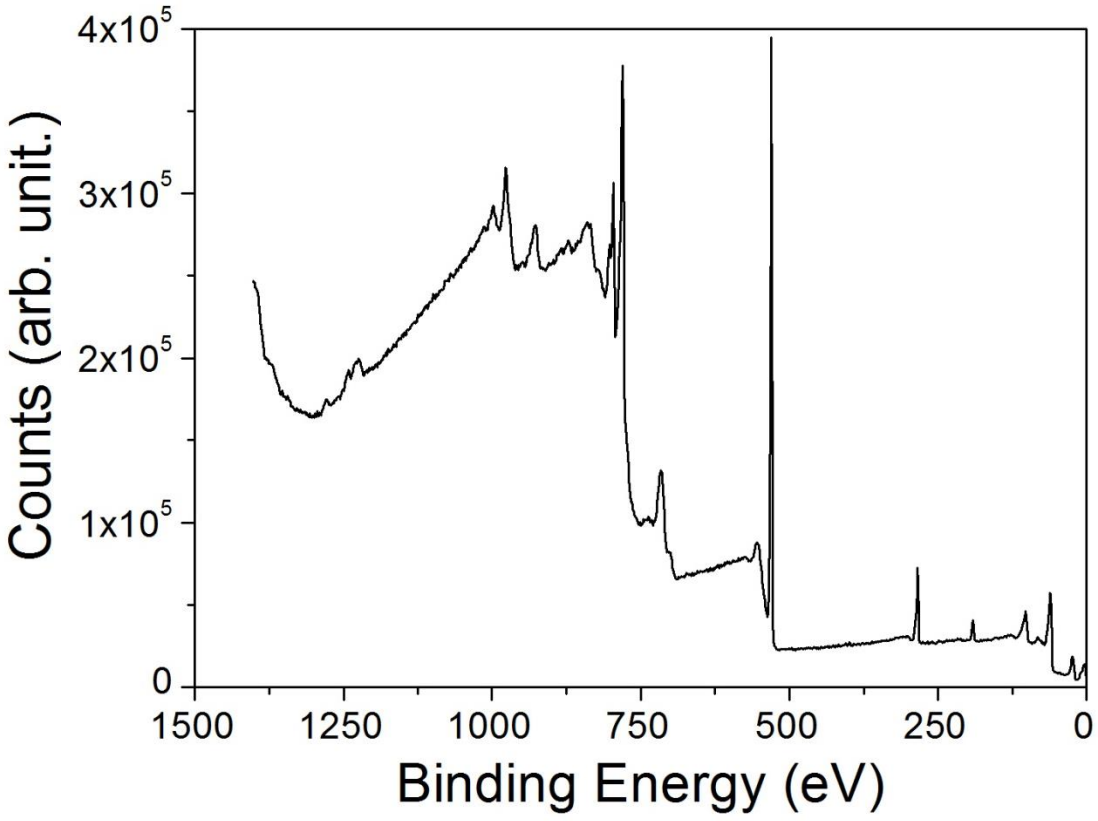

Figure 6.5: XPS spectrum of Co-B nanotubes deposited from the deposition bath described in Table 3.8.

Binding Energy (eV)	Electron Origin
4	O 2p
41	O 2s
59	Co 3p
101	Co 3s
192	B 1s
284	C 1s

532	O 1s
555	Background
715	Co Auger
780	Co 2p
800	Co 2p
840	Background
925	Co 2s
975	O Auger
998	O Auger
1230	C Auger
1281	B Auger

Table 6.3: Table of the origin of each of the peaks observed in the XPS spectrum in Fig. 6.5 for a nanostructured Co-B catalyst.

An XRD spectrum of a Co-B catalyst is shown in Fig. 6.6. As was observed previously in section 5.3.2 for electrolessly deposited alloys, no peaks are observed for a Co-B alloy. These results indicate the presence of an amorphous structure. This is expected due to the presence of boron within the structure, which prevents the formation of a crystalline Ni FCC structure. Variation in the pH of the electroless deposition bath results in alloys with varying B contents. However, this has no effect on the crystallinity of the sample.

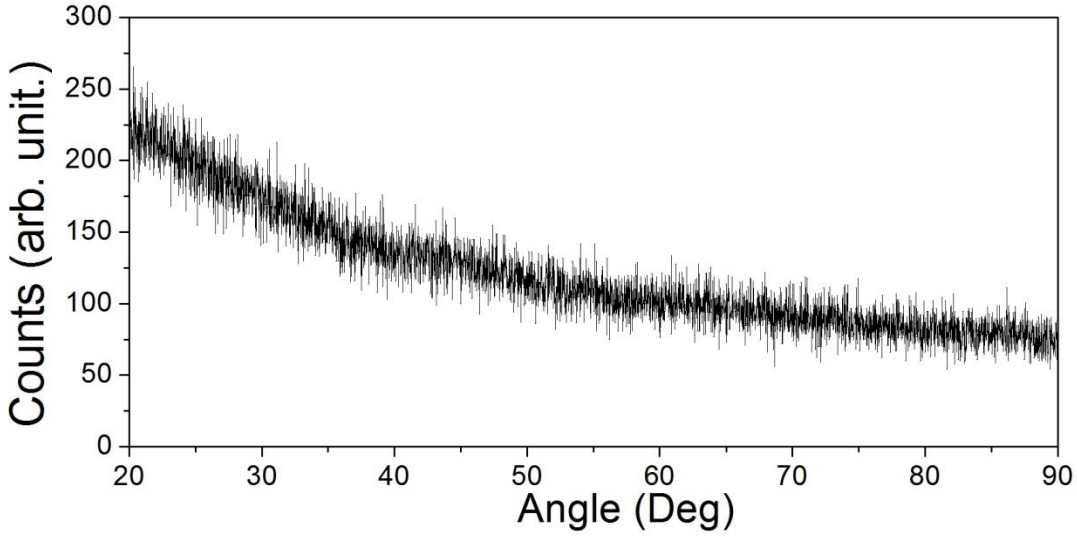

Figure 6.6: XRD spctrum of as deposited Co-B nanotubes deposited from the bath described previosly in Table 3.8.

As the pH of the electroless deposition bath increases, there is a corresponding decrease in the B content. At a pH of 7, the deposit composition is $Co_{54}B_{46}$. As the pH of the deposition bath increases, the B content increases with a composition of $Co_{82}B_{18}$ recorded for an electroless deposition bath at pH 10. The effect of B content of the Co-B alloy on the hydrogen generation rate was investigated. Fig. 6.7 shows the volume of hydrogen generation as a function of time for Co-B catalysts deposited from the electroless deposition bath described in Table 3.8 at a pH of 7, 8, 9 and 10.

For pH values of 7, 8 and 9, the volume of hydrogen generated in 20 minutes were all similar, 70 ml for $Co_{54}B_{46}$ (pH 7), 75 ml for $Co_{60}B_{40}$ (pH 8) and 77 ml for $Co_{71}B_{29}$ (pH 9). However, for a B content of 18 at. %, a decrease in the volume of hydrogen released was observed with 48 ml of hydrogen generated for a catalyst composition of $Co_{82}B_{18}$ (pH 10). This indicates that B plays an important role in the hydrogen generation reaction and is required to ensure a large hydrogen generation rate.

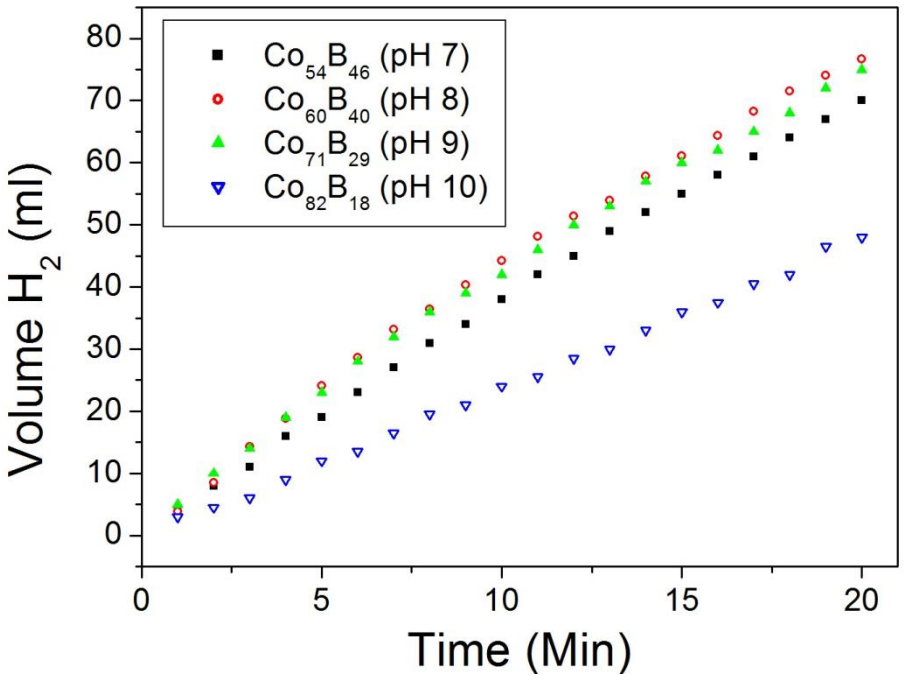

Figure 6.7: Volume of H_2 released as a function of time for Co-B catalysts deposited at a variety of pH values.

When Co and B are co-deposited via electroless deposition, B interacts with Co by transferring an electron to a vacant d-orbital of the metallic Co [14]. This makes the B electron deficient and the Co electron enriched. During the hydrogen generation reaction, discussed previously in section 3.12.2, electron transfer occurs between the $NaBH_4^-$ molecule and a hydrogen atom through the catalyst. The electron enriched Co catalyst facilitates this process providing a pathway for the hydrogen generation reaction. Therefore, the B atoms within the catalyst play a critical role in the hydrogen generation process. Here, we have found that Co-B catalyst with a B content between 29 at. % and 46 at. % has a large hydrogen generation rate compared to catalysts with lower B contents. Therefore, in this study, nanostructured Co-B catalysts with a composition of $Co_{60}B_{40}$ were used for hydrogen generation.

6.5 Reaction Kinetics

We studied the reaction kinetics of hydrogen generation from a $NaBH_4$ solution with a nanostructured $Co_{60}B_{40}$ catalyst. Fig. 6.8 shows a typical hydrogen evolution curve that we recorded. Initially, the rate of hydrogen evolution is constant and the amount of hydrogen generated varies linearly with time, indicating the presence of a zeroth order reaction. However, as the $NaBH_4$ concentration decreases, there is a change from zeroth order kinetics to first order kinetics. This causes the deviation from the linear response observed in Fig. 6.8.

The concentration of $NaBH_4$ can be calculated as a function of the total volume of hydrogen generated using Eqn. 6.3,

$$C_V = C_0\left(1 - \frac{V_{H2}}{V_{MAX}}\right) \tag{6.3}$$

where C_V = $NaBH_4$ concentration after a volume, V_{H2}, of hydrogen has been released, C_0 = initial $NaBH_4$ concentration and V_{MAX} = maximum amount of hydrogen released.

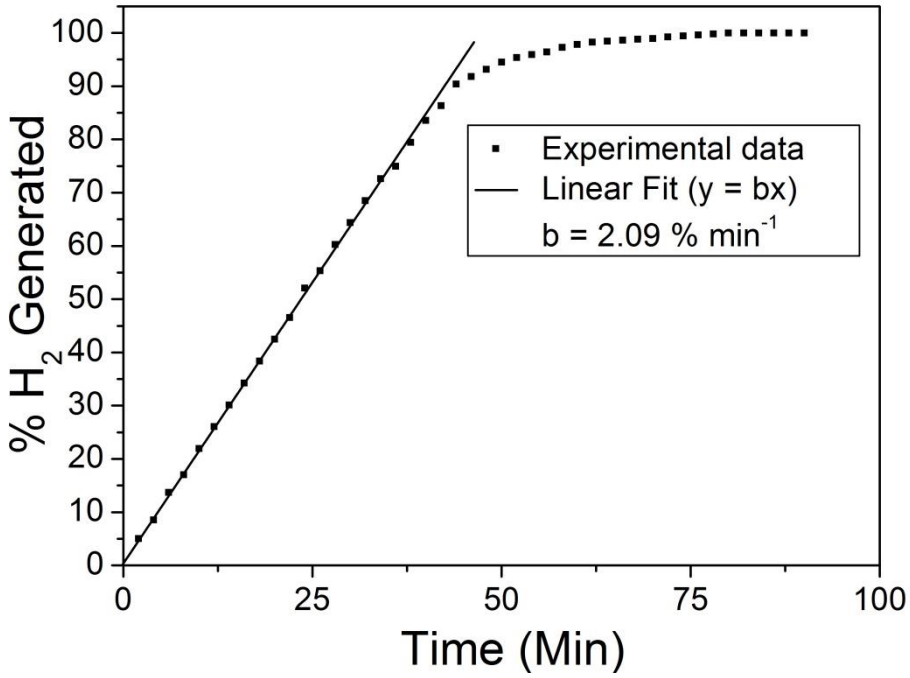

Figure 6.8: Percentage hydrogen generation as a function of time for a Co-B nanostructured catalyst from a 1 wt. % $NaBH_4$ solution at 40 ºC.

6.5.1 Zeroth Order Kinetics

A zeroth order reaction can be described by Eqn. 6.4, in which the rate of change reactant concentration with respect to time is equal to a constant, *k*. Integrating this leads to Eqn. 6.6, in which a linear relationship between reactant concentration and time is recorded.

$$-\frac{\mathrm{d}C_A}{\mathrm{d}t} = k \tag{6.4}$$

$$-\int_{C_0}^{C_A} \frac{\mathrm{d}C_A}{\mathrm{d}t}\,\mathrm{d}t = \int_0^t k\mathrm{d}t \tag{6.5}$$

$$C_0 - C_A = kt \tag{6.6}$$

Fig. 6.9 is a plot of the recorded experimental data fitted to Eqn. 6.6 over the linear region. The test was carried out in a $NaBH_4$ solution of 1 wt. %, which corresponds to an initial $NaBH_4$ concentration of 0.264 mol L^{-1}. A clear linear relationship between

$NaBH_4$ concentration and reaction time is observed in the initial region, indicating that the hydrogen generation reaction is a zeroth order reaction. As the $NaBH_4$ concentration drops to below approximately 0.03 M, a zeroth order reaction is no longer present and a change in the reaction kinetics is observed.

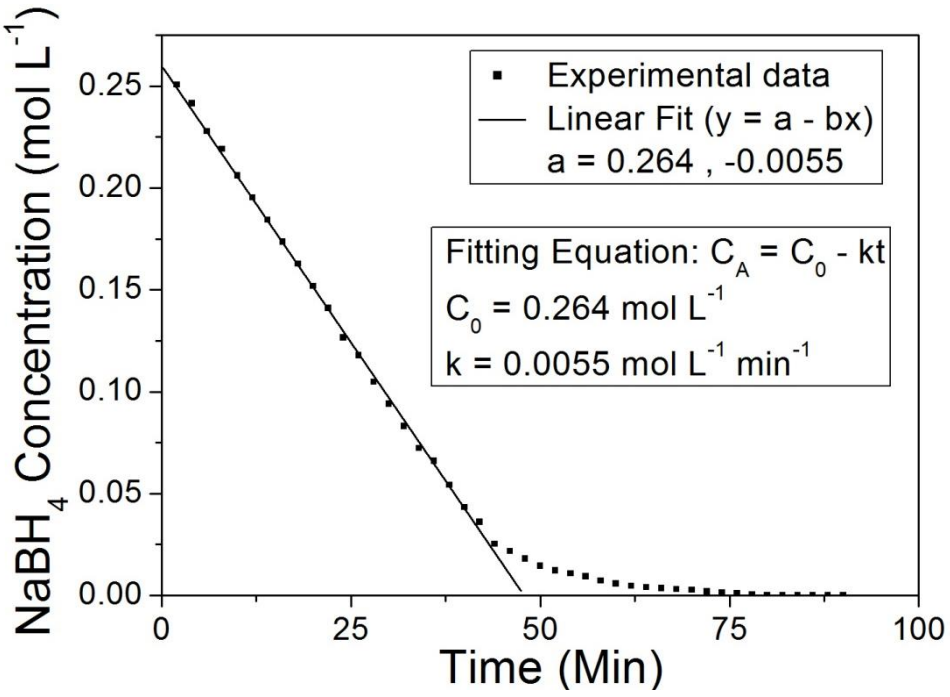

Figure 6.9: Rate of change of $NaBH_4$ concentration as a function of time for a Co-B nanostructured catalyst from a 1 wt. % $NaBH_4$ solution at 40 ºC. The linear fit shown corresponds to Eqn. 6.6 for a zeroth order reaction.

The presence of a zeroth order reaction can be attributed to the saturation of all sites on the surface of the Co-B catalyst at which electron transfer can occur. However, when the $NaBH_4$ concentration decreases, not all available sites will interact with a BH_4^- ion and thus a decrease in the deposition rate will be observed. The rate of change of concentration with respect to time for initial molarities of 0.066 M, 0.132 M, 0.198 M and 0.264 M is shown in Fig. 6.10. The molarity at which the reaction kinetics change from a zeroth order reaction to a first order reaction is constant, irrespective of the initial $NaBH_4$ concentration. All curves deviate from a linear relationship at a $NaBH_4$ molarity of approximately 0.03 M irrespective of the initial $NaBH_4$ concentration. Therefore, from this we conclude that 0.03 M is the

limiting molarity at which a zeroth order reaction can occur on our nanostructured Co-B catalysts.

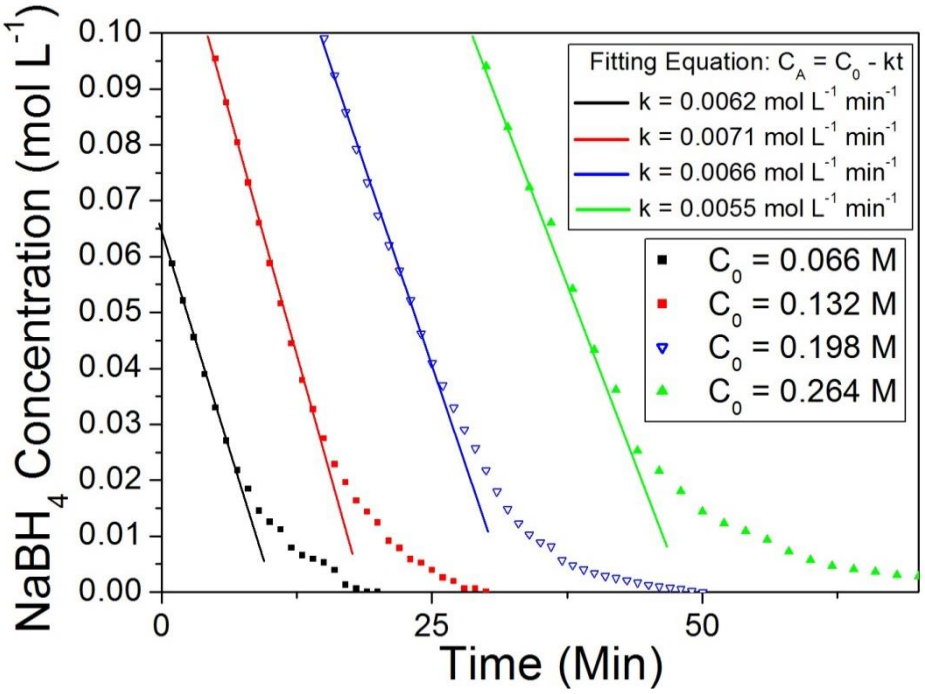

Figure 6.10: : Rate of change of $NaBH_4$ concentration as a function of time for a Co-B nanostructured catalyst at 40 ºC for a range of initial $NaBH_4$ concentrations. The linear fits shown correspond to Eqn. 6.6 for a zeroth order reaction.

6.5.2 First Order Kinetics

As the $NaBH_4$ concentration within the deposition bath decreases, the reaction kinetics change from a zeroth order reaction to a first order reaction. A first order reaction is defined by Eqn. 6.7, in which the rate of change of concentration is directly proportional to the concentration of the reactant.

$$-\frac{\mathrm{d}C_A}{\mathrm{d}t} = kC_A \tag{6.7}$$

Rearranging and integrating leads to Eqn. 6.9,

$$-\int_{C_0}^{C_A} \frac{\partial C_A}{C_A} = \int_0^t k\,\mathrm{d}t \tag{6.8}$$

$$\ln\left(\frac{C_0}{C_A}\right) = kt \tag{6.9}$$

Therefore, a plot of $\ln(C_A/C_0)$ with respect to time will provide a straight line for a first order reaction. This plot is shown in Fig. 6.11, using the data from Fig. 6.9, for molarities of less than 0.03 mol L^{-1} after the curve has deviated from a zeroth order reaction.

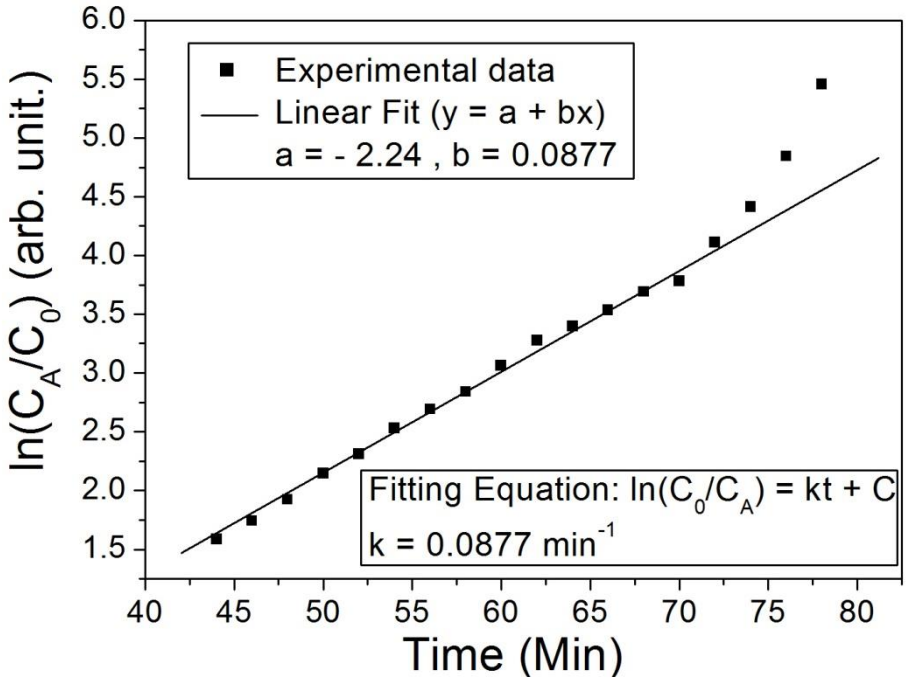

Figure 6.11: A plot of $\ln(C_A/C_0)$ as a function of time for a Co-B nanostructured catalyst at 40 ºC for a range of initial $NaBH_4$ concentrations. The linear fit shown corresponds to Eqn. 6.9 for a first order reaction.

The linear relationship observed indicates that a first order reaction is obtained when the $NaBH_4$ concentration is below a value of 0.03 M. These results are similar to those of Amendola et al. [4] who observed a zeroth order reaction at a $NaBH_4$ concentration of 0.1 wt. %, or 0.0264 M. The large deviation from a linear relationship, for values obtained at times of 75 minutes and greater, is due to experimental error because of the small volume of hydrogen released at very low $NaBH_4$ concentrations. These volumes of less than 0.2 ml min^{-1} cannot be recorded accurately via our experimental method.

6.5.3 Summary

The experimental results show that at a $NaBH_4$ concentration of 0.03 M, the hydrogen generation kinetics change from a zeroth order reaction to a first order reaction. The hydrogen generation rate remains constant during a zeroth order reaction. However, for a first order reaction, the hydrogen generation rate decreases with respect to time. Therefore, all hydrogen generation rates in this study refer to the rate during the initial zeroth order regime.

6.6 Nanotube Structure

6.6.1 Introduction

The $Co_{60}B_{40}$ catalysts that are used in this study are electrolessly deposited on porous polycarbonate membranes to form a nanostructure which consists of end-open nanotubes connected at both ends by a film as discussed previously in Chapter 4. These nanostructures have a much larger surface area than a thin film. A large percentage of the catalytic surface area is contained along walls of the nanotube. Therefore, it is likely that the nanotube structure will lead to a larger hydrogen generation rate than would be achieved with a thin film. To determine the nanostructured effect on the hydrogen generation rate, we investigated electrolessly deposited catalytic $Co_{60}B_{40}$ nanostructures with a range of deposition times and wall thicknesses.

6.6.2 Pore Diameter

The pore diameter as a function of deposition time for the Co-B nanostructures deposited at a temperature of 60 °C is shown in Fig. 6.12. Analogous to the Ni-B deposition study in Chapter 3, there is an approximate linear dependence of the pore

diameter with respect to the total deposition time. SEM images of the pore diameters at a variety of deposition times are shown in Fig. 6.13. Initially for very low deposition times of 10 and 20 seconds, the pore diameters of the nanotubes are approximately 350 nm, Fig. 6.13(a), and 300 nm respectively. The initial large decrease in the pore diameter is attributed to the catalytic deposition process that is occurring at the Pd atoms on the polycarbonate membrane. After this the change in pore diameter with respect to deposition time becomes almost linear with pore diameters of 280 nm, 180 nm and 110 nm recorded for deposition times of 30, 120 and 300 seconds shown in Fig. 6.13 (b), (c) and (d) respectively.

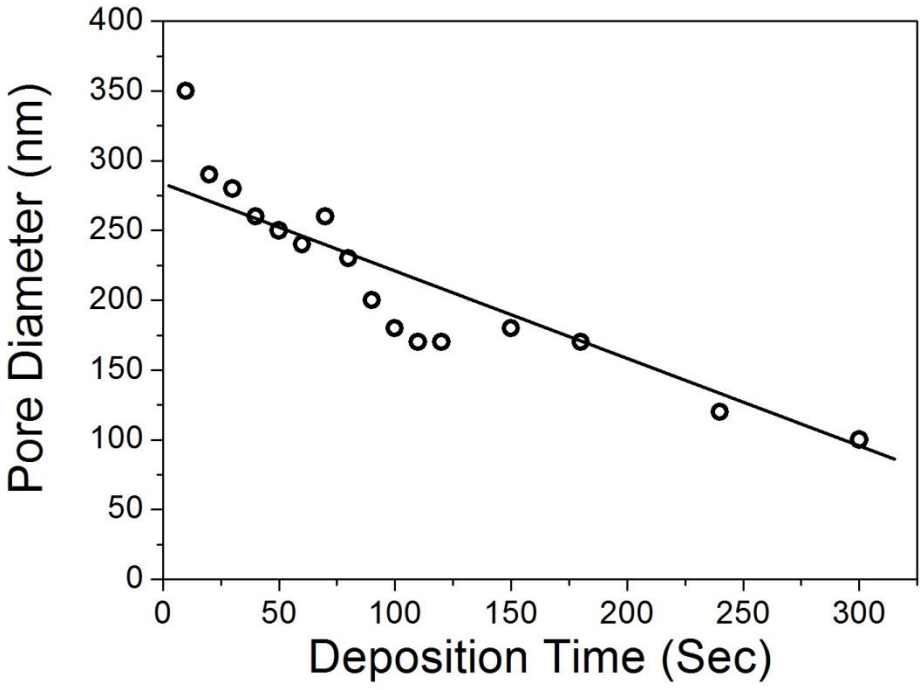

Figure 6.12: Pore diameter of $Co_{60}B_{40}$ nanotubes deposited from the deposition bath described previously in Table 3.8 at pH 8 as a function of deposition time. The linear fit acts a guide to the eye.

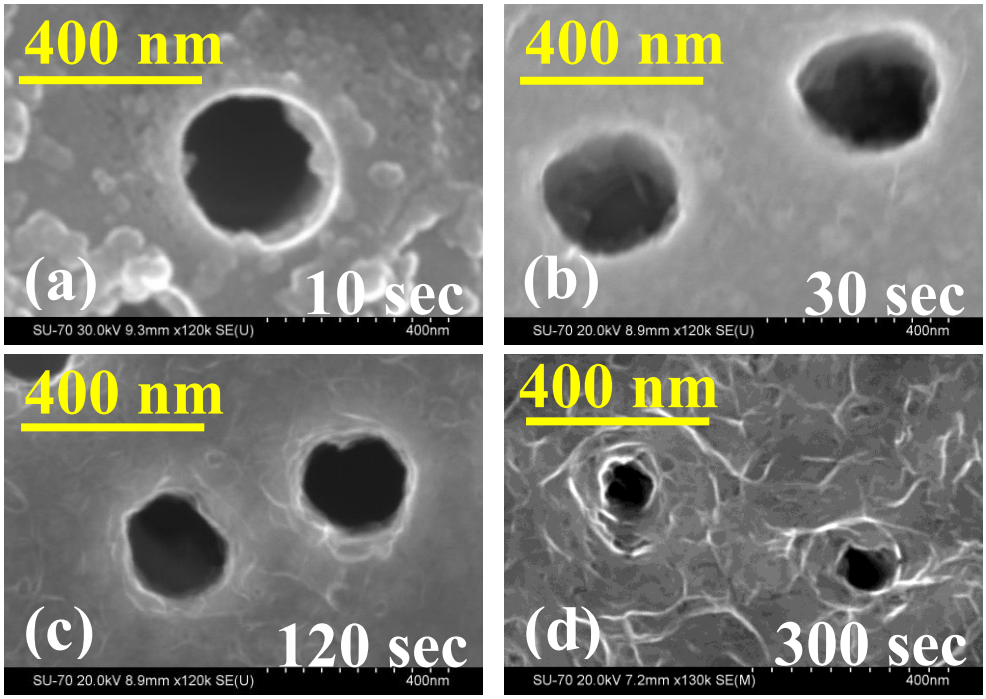

Figure 6.13: SEM images of Co-B nanotube pore diameters for nanotubes deposited from the bath described in Table 3.8 at PH 8 for deposition times of **(a)** 10 seconds **(b)** 30 seconds **(c)** 120 seconds and **(d)** 300 seconds.

6.6.3 Mass

The mass of the $Co_{60}B_{40}$ deposits with respect to deposition time are shown in Fig. 6.14. Initially there is a large deposition rate, known as the acceleration region of the deposition process. This corresponds to a large change in the Co-B mass with respect to time. As deposition continues, the rate decreases and a more constant change in deposition rate with respect to time is observed. The deposition process is almost identical to that of Ni-B discussed previously in Chapter 4, thus confirming the results recorded for the Ni-B deposition process. For a deposition time of 10 seconds, only 0.14 mg of Co-B is deposited throughout the polycarbonate membrane. This corresponds to the formation of Co-B islands and a continuous deposit is not formed. As deposition time increases, the mass of the deposit increases with masses of 1 mg recorded after 50 seconds and 1.6 mg recorded after 110 seconds of deposition. For a deposition time of 300 seconds a total mass of 2.5 mg has been deposited.

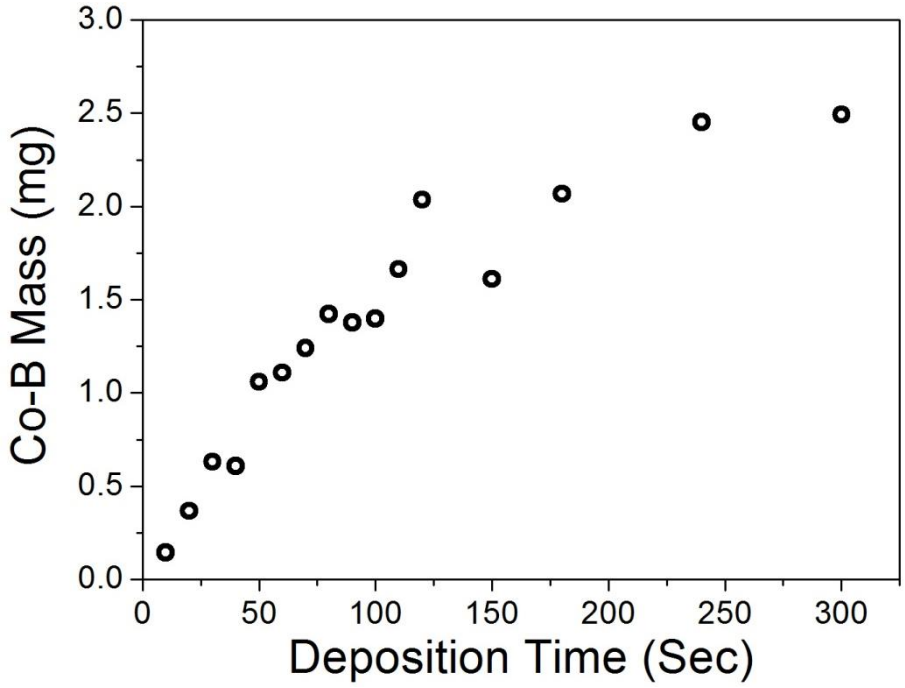

Figure 6.14: Mass of $Co_{60}B_{40}$ nanostructures deposited from the deposition bath described previously in Table 3.8 at pH 8 as a function of deposition time.

6.7 Hydrogen Generation

The volumes of hydrogen released as a function of time for each of the nanostructured catalysts for a range of deposition times are shown in Fig. 6.15, for a $NaBH_4$ solution temperature of 40 °C and a $NaBH_4$ concentration of 1 wt. %. The lowest volumes of hydrogen generated are recorded for Co-B catalysts at low deposition times of 10 – 40 seconds. For a Co-B catalyst deposited for 10 seconds, 38 ml of hydrogen is released in 30 minutes. This corresponds to a hydrogen generation rate of 1.27 ml min^{-1}. For a 20 second deposition, the volume of H_2 after 30 minutes is over three times larger with 119 ml released. The largest volume of H_2 released in 30 minutes was 260 ml for an 80 second deposition. The catalytic activity of the nanostructures can be determined by recording the hydrogen generation rate either as a function of membrane area or as a function of $Co_{60}B_{40}$ mass. Although mass is a commonly used standard, we will also investigate area because the hydrogen

generation rates as a function of both mass and area are dependent on the nanostructure of the catalyst.

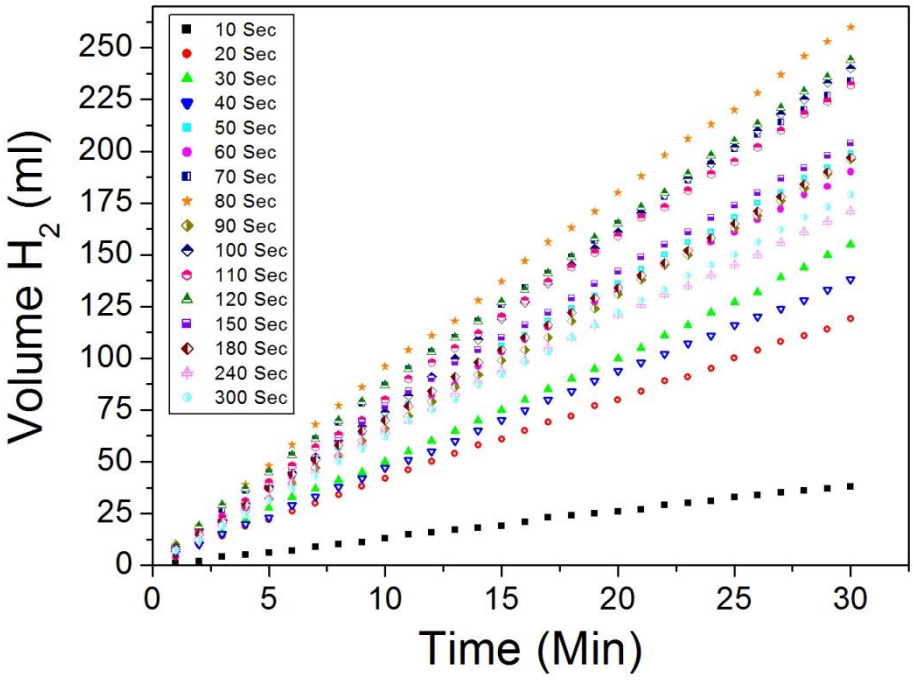

Figure 6.15: Volume of hydrogen generated as a function of time for a range of Co-B nanostructures of varying deposition time.

6.7.1 Hydrogen Generation Rate Per Unit Area

Each polycarbonate membrane has a surface area of 0.00049 m^2. As a full membrane is used in each test, the surface areas of the catalysts used for the graph in Fig. 6.15 are identical. Therefore, by dividing the rate of H_2 generation per minute by the surface area, the hydrogen generation rate per unit area can be found. The hydrogen generation rates per unit area with respect to Co-B deposition time are shown in Fig. 6.16.

The experimental error associated with the data in Fig. 6.16 is small as the hydrogen generation rates are obtained from the results shown in Fig. 6.15. We are satisfied that the error in the hydrogen generation rates obtained from Fig. 6.15 is below 0.1 ml min^{-1}, which corresponds to an error of 200 ml min^{-1} m^{-2} in Fig. 6.16. This error cannot explain the random distribution of the data shown. The deviation in the

results is instead explained by random defects present within the template structures, which affects both the shape and size of the deposited nanostructures.

After 10 seconds of deposition the hydrogen generation rate is 2600 ml min^{-1} m^{-2}. This is the lowest rate recorded for all the Co-B catalysts. As the deposition time increases, a continuous deposit forms and the hydrogen rate increases. A maximum hydrogen generation rate of 17,650 ml min^{-1} m^{-2} is obtained for a deposition time of 80 seconds. For deposition times greater than 80 seconds the hydrogen generation rate starts to decrease with values of 11,600 ml min^{-1} m^{-2} and 12,100 ml min^{-1} m^{-2} recorded for deposition times of 240 seconds and 300 seconds respectively.

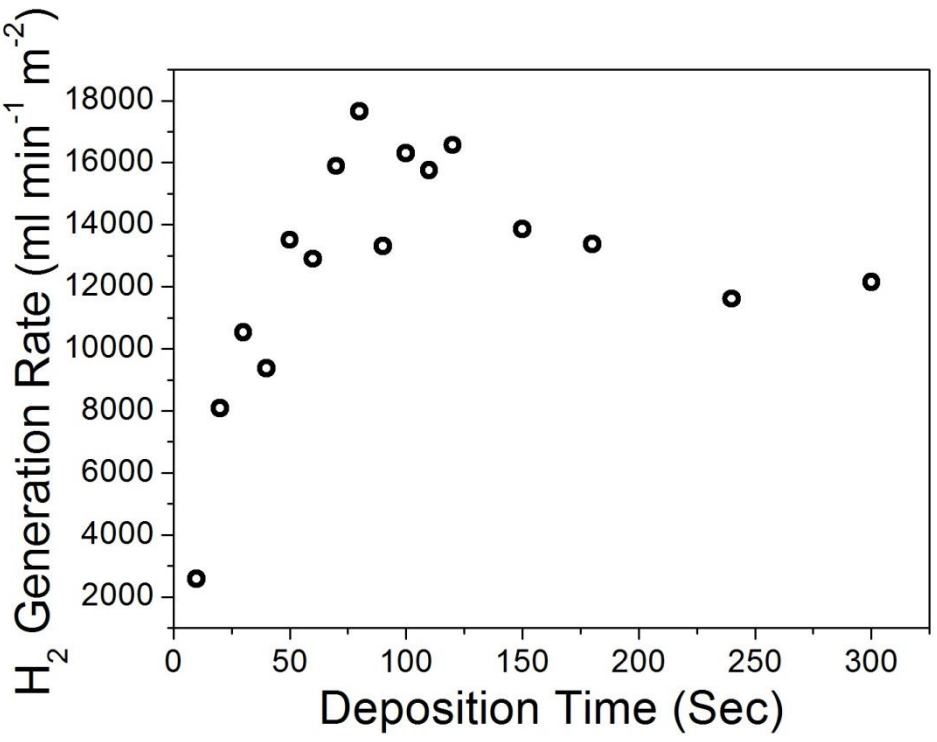

Figure 6.16: Hydrogen generation rate per unit area as a function of $Co_{60}B_{40}$ nanostructured catalyst deposition time.

To explain these results, the electroless deposition process described in Chapter 4 must be understood. Initial Co-B deposition occurs at Pd nucleation sites to form Co-B islands. Therefore, after 10 seconds of deposition, Co-B islands are present throughout the polycarbonate membrane. This minimises the catalytic surface area

and thus a low hydrogen generation rate is recorded. As the deposition time increases, a complete film is formed, thus resulting in an increased deposition rate. However, a continuous film forms on the surface of the polycarbonate membrane before continuous nanotubes are formed within the nanotube pores. A deposition time of 80 seconds corresponds to the time at which continuous nanotubes are formed, thus resulting in a maximised catalytic surface area and a maximised hydrogen generation rate. For a deposition time of 80 seconds, the pore diameter of the nanotube is 230 nm. As the deposition time increases, the pore diameter of the nanotubes decreases. As the pores close, diffusion of the $NaBH_4$ solution through the nanotube pores is limited and hydrogen bubbles can become trapped within the nanotube. This results in a decreasing hydrogen generation rate for deposition times of greater than 80 seconds.

From Fig. 6.16, it is clear that the hydrogen generation rate is levelling off at a value of approximately 12,000 ml min^{-1} m^{-2} for deposition times of 240 and 300 seconds. As these values are for small pore diameters, 120 nm and 100 nm respectively, the amount of catalysed hydrogen released within the tubes is negligible and thus the levelling off of the hydrogen generation rate is observed. Therefore, the hydrogen generation rate of 12,000 ml min^{-1} m^{-2} is attributed to the membrane surface and not the nanotube structure. For the maximum hydrogen generation rate of 18,000 ml min^{-1} m^{-2}, 12,000 ml min^{-1} m^{-2} is attributed to the membrane surface and 6,000 ml min^{-1} m^{-2} is attributed to the nanotube structure. Therefore, a 50 % increase in the hydrogen generation rate is achieved for a nanostructure within a polycarbonate membrane than for a thin film. From this, we can conclude that nanostructured catalysts offer an increased catalytic activity.

However, although the nanostructure contributes to the hydrogen generation process, the amount of catalysed hydrogen released from within the nanotube structure is small compared to the total catalytic surface area of the tubes. The nanotubes have a total internal surface area approximately 20 times larger than that of the membrane surface. However, twice as much hydrogen is catalysed on the membrane surface than within the nanotube pores. This indicates that there is a severe underutilization of the catalytic material within the nanostructure. As hydrogen is released within the nanotubes pores, hydrogen bubbles must escape from within the nanotube structure. This reduces the diffusion of $NaBH_4$ within the pores and thus the hydrogen generation rate remains relatively low.

6.7.2 Hydrogen Generation Rate Per Unit Mass

The more common method of calculating the hydrogen generation rate is to express it as a function of the total mass of the catalyst. Using this approach, a completely different trend for the hydrogen generation rate as a function of catalyst deposition time is achieved as shown in Fig. 6.17. There is a constant decrease in the hydrogen generation rate per unit mass as a function of Co-B deposition time. The largest hydrogen generation rates are achieved at low deposition times while the lowest hydrogen generation rates correspond to large deposition times. For a Co-B catalyst at a deposition time of 20 seconds, a hydrogen generation rate of 10,800 ml min^{-1} g^{-1} is recorded. However, for slightly larger deposition times the generation rate decreases sharply. Rates of 8,200 ml min^{-1} g^{-1} and 7,500 ml min^{-1} g^{-1} are recorded for deposition times of 30 and 40 seconds respectively. For a deposition time of 240 seconds, this value has decreased to 2,300 ml min^{-1} g^{-1}.

Again, these values can be explained by relating them to the electroless deposition process. At low deposition times, Co-B islands are present throughout the polycarbonate membrane at Pd nucleation sites. At times of 10 and 20 seconds, the total Co-B masses deposited throughout the membranes are 0.15 mg and 0.37 mg respectively. Therefore, there is an incomplete film present and a large amount of the deposited Co-B present catalyses the reaction.

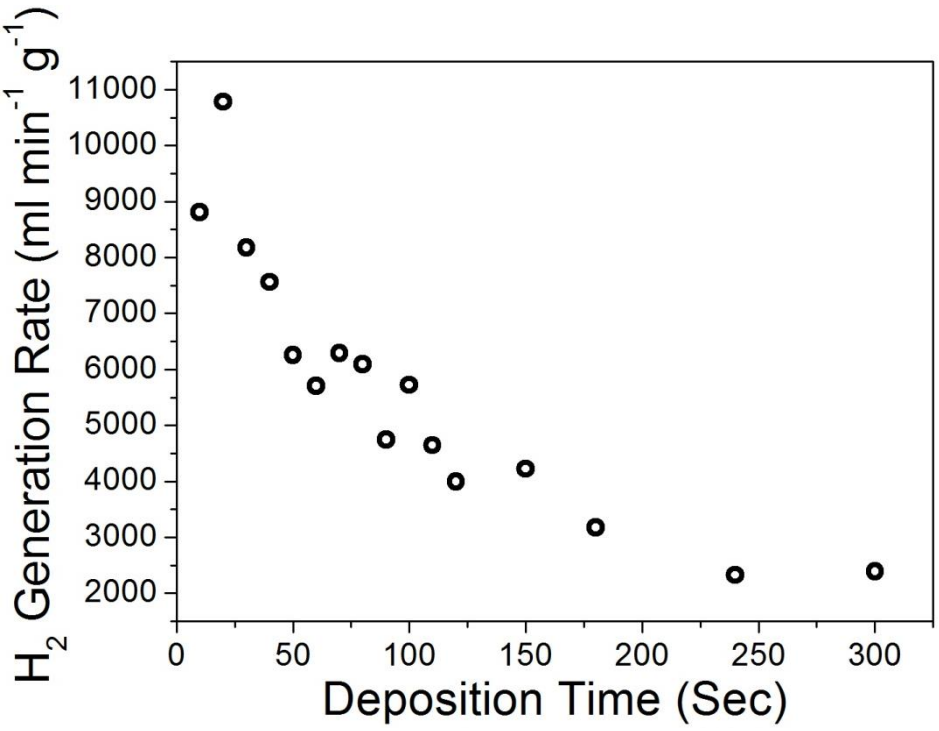

Figure 6.17: Hydrogen generation rate per unit mass as a function of $Co_{60}B_{40}$ nanostructured catalyst deposition time.

As deposition continues, the islands grow radially outward from each nucleation site. As this occurs, the catalytic surface area increases, resulting in an increased deposition rate per unit area as shown in Fig. 6.16. If the radius of the Co-B island doubles, the surface area increases by a factor of 4, increasing the deposition rate per unit area. However, the volume will increase by a factor of 8 and thus the deposition rate as a function of mass will decrease by a factor of 2. Once a complete film is formed, only the surface of the film catalyses the reaction. As the thickness of the film

increases the hydrogen generation rate per unit area remains constant, while the hydrogen generation rate per unit mass decreases. Therefore, a constant decrease in the generation rate per unit mass is recorded as Co-B deposition time increases.

The highest values reported previously for Co-B catalysts have been 26,000 ml min^{-1} g^{-1} [12] and 24,000 ml min^{-1} g^{-1} [11]. After this the next best values reported previously have been 11,000 ml min^{-1} g^{-1} [9], 8,500 ml min^{-1} g^{-1} [15] and 7,200 ml min^{-1} g^{-1} [16]. All of these values are for either Co-B nanoparticles or Co-B deposited on Ni-foam. A value of 5,100 ml min^{-1} g^{-1} [17] was reported previously for Co-B deposited on the walls of CNTS.

The maximum hydrogen generation rate of 11,000 ml min^{-1} g^{-1} recorded in this study compare well with the previously reported values within the literature. However, due to the low catalytic mass, the hydrogen generation rate per unit area is extremely low, thus making it impractical for use in future technologies. However, the Co-B catalyst deposited for 80 seconds has a large hydrogen generation rate per unit area and has a hydrogen generation rate per unit mass of 6,100 ml min^{-1} g^{-1}. Again this value is comparable with those obtained previously, though further increases in the hydrogen generation rate are still required.

6.8 Kinetically Controlled Nanostructure

By depositing nanotubes using the enhanced deposition process as described in Chapter 4, we proposed that the hydrogen generation rate would be increased. Instead of depositing the nanostructures in a deposition bath at a temperature of 65 ºC, the temperature was reduced to 30 ºC. This resulted in the formation of continuous uniform nanotubes with a uniform wall thickness. Our hypothesis was that using this deposition method would result in complete nanotubes with a larger pore diameter.

We expected that this would increase the diffusion of $NaBH_4$ solution throughout the nanotubes allowing for an increased hydrogen generation rate within the nanotube structure. The hydrogen generation rates of Co-B catalysts deposited via both methods are compared for samples of equal mass.

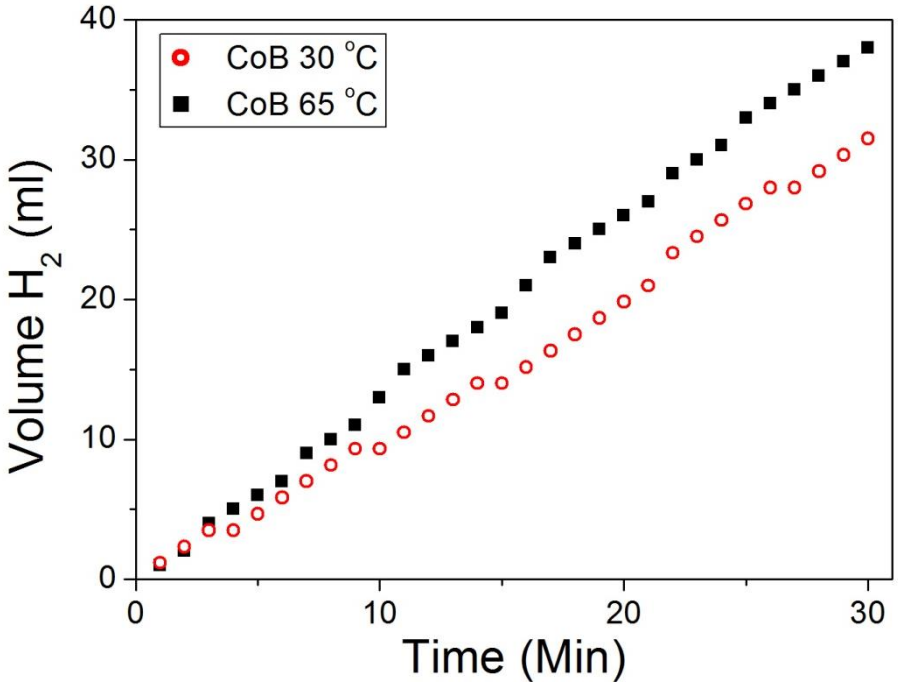

Figure 6.18: Volume of hydrogen generated as a function of deposition time for a 0.14 mg $Co_{60}B_{40}$ nanostructured catalyst deposited at 65ºC and a 0.12 mg catalyst deposited at 35 ºC. Hydrogen generation is done in a 1 wt. % $NaBH_4$ solution at a temperature of 40 ºC.

Fig. 6.18 shows the volume of hydrogen produced as a function of time for two Co-B catalysts with a low mass deposited at two different temperatures. The Co-B catalyst deposited at a temperature of 65 ºC has a mass of 0.14 mg after 10 seconds of deposition and the Co-B catalyst deposited at a temperature of 30 ºC has a mass of 0.12 mg after 150 seconds of deposition. For the 0.14 mg Co-B nanostructure deposited at 65 ºC, 38 ml of hydrogen are generated in 30 minutes of deposition. This corresponds to a hydrogen generation rate of 9050 ml min^{-1} g^{-1}. For the 0.12 mg catalyst deposited at 30 ºC, 32 ml of H_2 was released after 30 minutes giving a hydrogen generation rate of 8,800 ml min^{-1} g^{-1}. There is almost no difference in the hydrogen generation rates at 30 ºC and 65 ºC for a low catalyst mass. In both cases,

the Co-B deposit exists in the form of Co-B islands. Therefore, the hydrogen generation rates are almost identical and are independent of the deposition temperature.

For larger masses of 0.5 mg, 1 mg and 1.5 mg, there is still very little difference in the hydrogen generation rates for Co-B catalysts deposited at 65 ºC and 30 ºC. The total volume of hydrogen produced for Co-B catalysts with a mass of approximately 1.5 mg is shown in Fig. 6.19. 260 ml of H_2 was generated in 30 minutes for a Co-B catalyst with a mass of 1.42 mg deposited at a temperature of 65 ºC for 80 seconds. 254 mg of H_2 was generated for a catalyst with a mass of 1.45 mg deposited at 30 ºC for 10 minutes. These correspond to hydrogen generation rates of 6,100 mg min^{-1} g^{-1} for the catalyst deposited at 65 ºC and 5,850 ml min^{-1} g^{-1} for the catalyst deposited at 30 ºC indicating that there is no appreciable difference in the deposition rates.

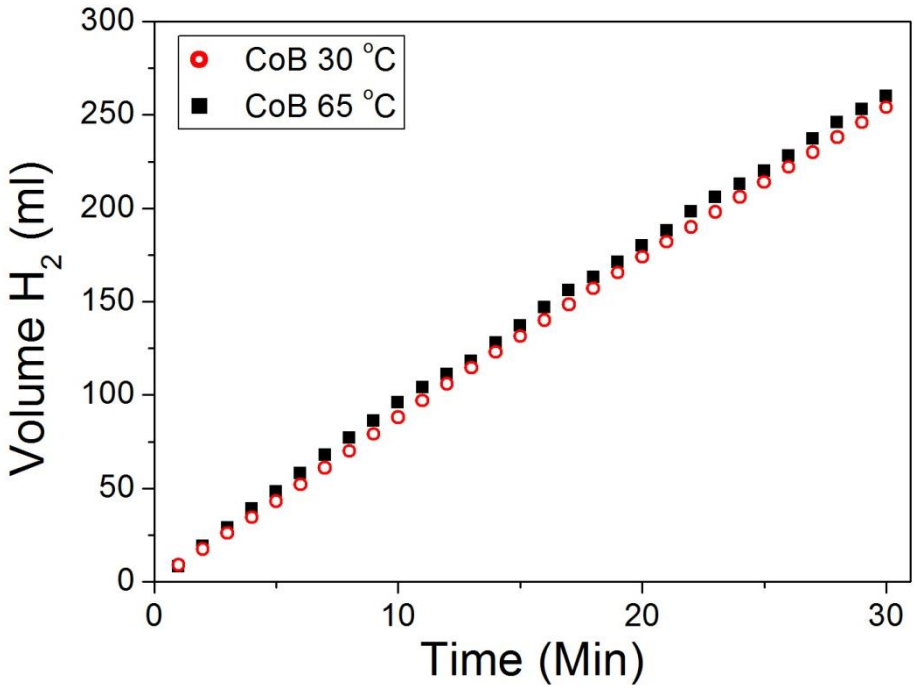

Figure 6.19: Volume of hydrogen generated as a function of deposition time for a 1.5 mg $Co_{60}B_{40}$ nanostructured catalyst deposited at 35 ºC and 65 ºC. Hydrogen generation is done in a 10 wt. % NaBH4 solution at a temperature of 40 ºC.

The 80 second catalyst deposited at 65 ºC corresponded to the deposition time at which the largest hydrogen generation rate per unit area was recorded. The Co-B had a pore diameter of 230 nm. By reducing the deposition temperature, the pore diameter increased to 280 nm. However, as can be seen from the hydrogen rates, this has no appreciable effect on the hydrogen generation rate. This indicates that the pore diameter is not the limiting factor in the hydrogen generation rate. Hydrogen bubbles that are created within the nanotubes cause a severe decrease in diffusion of electrolyte. A small increase in the pore diameter of 20 % has no appreciable effect on the diffusion of hydrogen gas out of the nanotubes and thus no change in the deposition rate is observed.

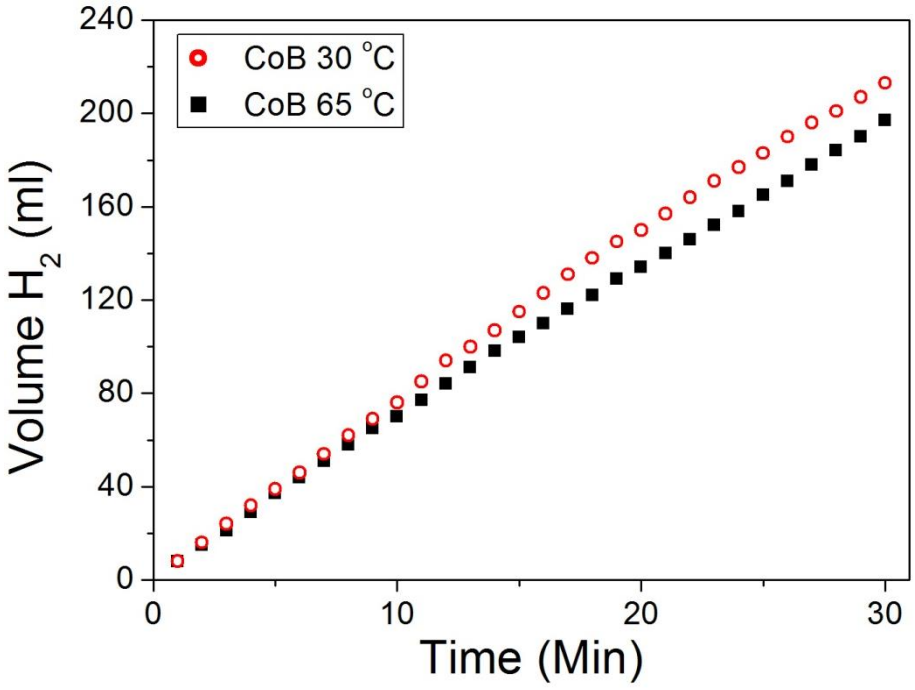

Figure 6.20: Volume of hydrogen generated as a function of deposition time for a 2 mg $Co_{60}B_{40}$ nanostructured catalyst deposited at 35 ºC and 65 ºC. Hydrogen generation is done in a 10 wt. % $NaBH_4$ solution at a temperature of 40 ºC.

However, a slight difference in the hydrogen generation rates for a total deposited mass of approximately 2 mg has been observed. Fig. 6.20 shows the hydrogen generation rates for Co-B catalysts with a mass of 2.06 mg deposited at a temperature of 35 ºC and a mass of 2.07 mg deposited at 65 ºC. 213 ml of H_2 are generated in

30 minutes for a 2.06 mg Co-B catalyst deposited at 35 ºC, corresponding to a hydrogen generation rate of 3,450 ml min^{-1} g^{-1}. 197 ml of H_2 are generated for a 2.07 mg catalyst deposited at 65 ºC, corresponding to a hydrogen generation rate of 3150 ml min^{-1} g^{-1}.

The difference in deposition rates is small, only 10 %, though may be significant. For the 30 ºC sample the pore diameter is 240 nm, while the pore diameter has decreased to 170 nm for the 65 ºC sample. Therefore, it is possible that there is a small amount of extra catalysed hydrogen released within the nanotube of the 35 ºC due to a slightly larger pore diameter, although the amount is minor. Even if the 2 mg sample does display a slightly larger hydrogen generation rate when deposited at 35 ºC, the hydrogen generation rate of 3,450 ml min^{-1} g^{-1} is already quite low.

From this investigation we can conclude that our hypothesis was incorrect because the deposition of nanostructures at lower temperatures has little effect on the hydrogen generation rate. This is due to the vast amount of catalytic activity occurring on the surface of the polycarbonate membrane and not within the nanotube pores. As the hydrogen generation within the nanotube structure is diffusion limited, small changes in pore diameter do not significantly enhance the hydrogen generation rate as was previously claimed in the initial hypothesis.

6.9 Temperature

The dependence of the hydrogen generation rate on the temperature of the $NaBH_4$ solution was investigated to calculate the activation energy of the $Co_{60}B_{40}$ catalyst. Fig. 6.21 shows the volume of hydrogen generated with respect to time for a $Co_{60}B_{40}$ catalyst with a deposition time of 60 seconds deposited at 65 ºC. As the temperature of the solution increases, there is a corresponding increase in the volume of hydrogen

released. For hydrogen generation at 25 ºC, 117 ml of hydrogen is released in 30 minutes. At a temperature of 40 ºC, this has increased to 320 ml. At 45 ºC and 50 ºC, 320 ml of hydrogen has been released after 25 and 20 minutes respectively and a first order regime is present at 30 minutes. A total $NaBH_4$ mass of 0.15 g was placed in a 15 ml solution, which corresponds to a solution composition of 1 wt. % $NaBH_4$ and a molarity of 0.265 M. The maximum volume of hydrogen that can be achieved is 355.5 ml. Once the $NaBH_4$ concentration reaches approximately 0.1 wt. % (0.03 M), the hydrogen generation process follows a first order reaction. The hydrogen generation rates are calculated for the zeroth order reaction observed for the first 15 minutes of the reaction.

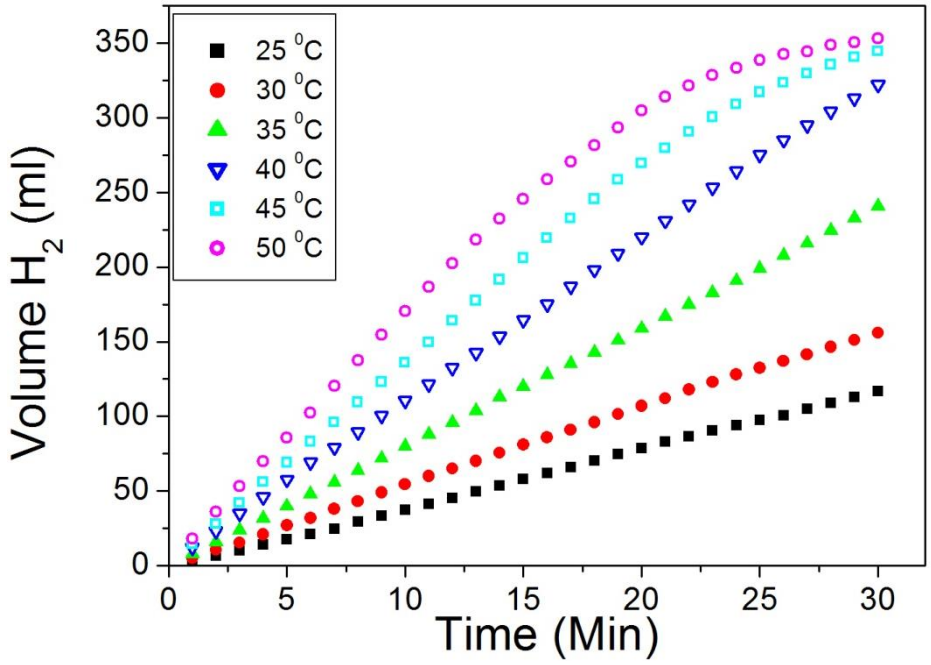

Figure 6.21: Hydrogen generation rate as a function of hydrogen generation solution temperature for a nanostructured Co-B catalyst deposited for 60 seconds at 65 ºC on a polycarbonate membrane from the deposition bath described in Table 3.8 at pH 8.

As shown in Fig. 6.22, the observed increase in hydrogen generation rate with respect to temperature is not linear. Instead an exponential growth with respect to temperature is observed. A hydrogen generation rate of 104 ml min^{-1} mol^{-1} (2,350 ml min^{-1} g^{-1}) was recorded at 298 K (25 ºC). At 313 K (40 ºC) the hydrogen generation rate had

increased to 287 ml min^{-1} mol^{-1} (6,500 ml min^{-1} g^{-1}). A 10 K increase in temperature to 323 K (50 ºC) resulted in an almost doubling of the hydrogen generation to 521 ml min^{-1} mol^{-1} (11,650 ml min^{-1} g^{-1}). This hydrogen generation rate is larger than the maximum rate of 10,800 ml min^{-1} g^{-1} at 40 ºC recorded in section 6.7.2, for a catalyst deposited for 20 seconds. The hydrogen generation rate per unit area at 50 ºC is increased to 22,850 ml min^{-1} g^{-1}. Again, this value is larger than any value that was recorded previously in section 6.7.1. A small change in temperature, from 40 ºC to 50 ºC, resulted in almost a doubling of the hydrogen rates and plays an important role in increasing the hydrogen generation rate. However, in the literature, hydrogen generation rates are commonly quoted at temperatures of between 25 ºC and 40 ºC.

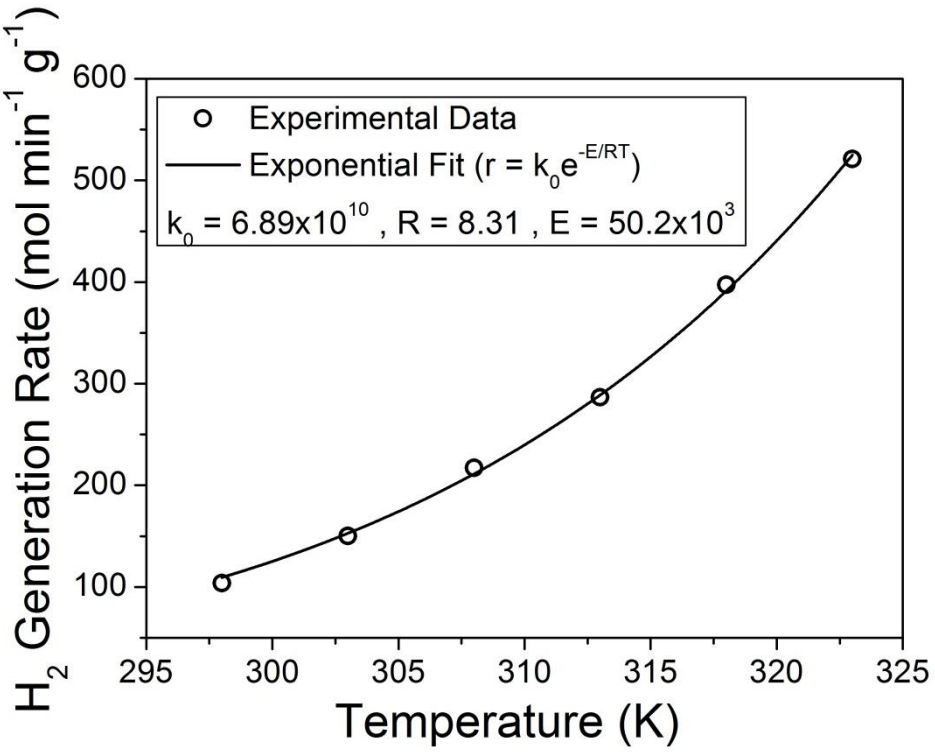

Figure 6.22: Rate of the number of moles of hydrogen generated per unit mass as a function of temperature for a nanostructured $Co_{60}B_{40}$ catalyst deposited for 60 seconds on a polycarbonate membrane from the deposition bath described in Table 3.8 at pH 8. The exponential fit corresponds to Eqn. 6.10. From the fitting we obtain k_0 = 6.89 x 10^{10} mol min^{-1} g^{-1}, E = 50.2 kJ mol^{-1} where R = ideal gas constant 8.31 J K^{-1} mol^{-1}.

The relationship between the hydrogen generation rate and the temperature is given by Eqn. 6.10,

$$r = k_0 e^{-\frac{E}{RT}} \tag{6.10}$$

where r = hydrogen generation rate, k_0 = reaction rate constant, E = activation energy, R = ideal gas constant (8.31 J K^{-1} mol^{-1}) and T = temperature. An exponential fit to the experimental data using Eqn. 6.10 is shown in Fig. 6.22.

The Arrhenius equation, shown in Eqn. 6.11, can be obtained by taking the natural logarithim of Eqn. 6.10,

$$\ln(r) = \ln(k_0) - \frac{E}{RT} \tag{6.11}$$

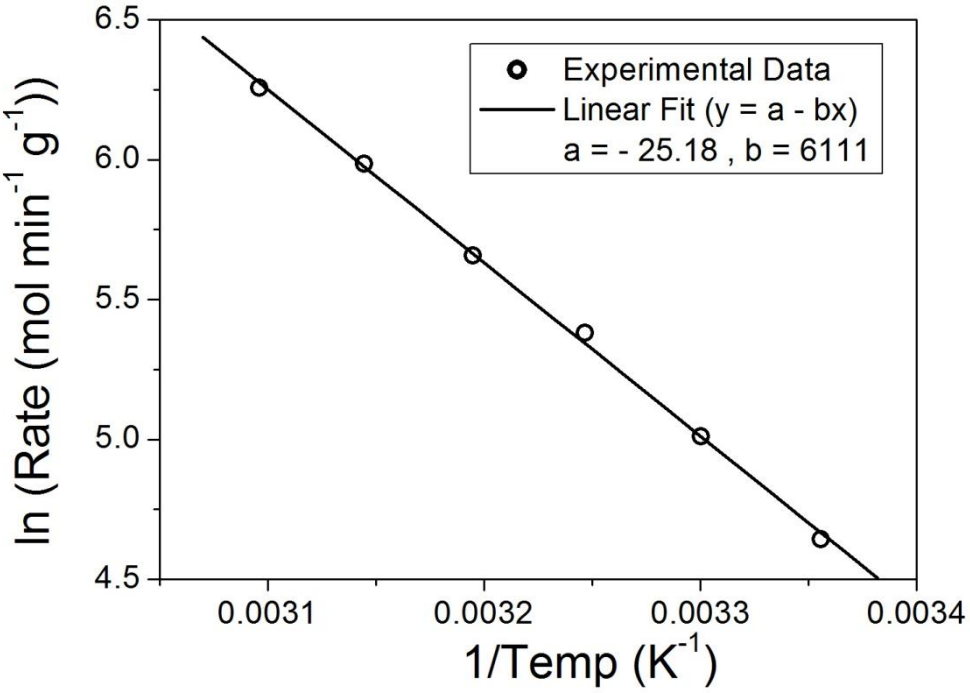

Figure 6.23: Arrhenius plot for a nanostructured $Co_{60}B_{40}$ catalyst deposited for 60 seconds on a polycarbonate membrane from the deposition bath described in Table 3.8 at pH 8. The linear fit corresponds to the Arrhenius equation shown in Eqn. 6.11 where a = -25.18 and b = 6111 K.

An Arrhenius plot can be used to determine the activation energy of a catalyst and is obtained by graphing the ln(*r*) vs. 1/*T* as shown in Fig. 6.23. The slope of the graph obtained is equal to *-E/R* and the *y*-intercept is equal to ln(k_0). The activation energy can be found by multiplying the slope of the graph by the real gas constant *R*. A least square regression fit to the Arrhenius plot in Fig. 6.23 gives a slope of -6111 K and a

y-intercept of 25.18. From these values, the activation energy and a reaction constant are calculated as 50.7 kJ mol^{-1} and 8.62 x 10^{10} mol min^{-1} g^{-1} respectively. The error in the slope of the line determined from the fitting is ± 115 K, which gives an activation energy of 50.7 kJ mol^{-1} ± 0.9 kJ mol^{-1}. The error in the calculation of the activation energy is less than 2 % because the slope of the line determines the activation energy. However, because of the exponential relationship between the rate constant and *y*-intercept, small changes in the *y*-intercept, result in large changes of the rate constant. The error in the y-intercept determined from the linear fit is ± 0.37. From this, the reaction constant is 8.62 x 10^{10} mol min^{-1} g^{-1} ± 4.11 x 10^{10} mol min^{-1} g^{-1}. Therefore, there is a significant error associated with the calculated value of the rate constant with an error of 48 % obtained.

Activation energies were calculated for Co-B catalysts with deposition times of 40, 60 and 80 seconds. Arrhenius plots for each of these deposition times are shown in Fig. 6.24. Deposition times around 60 seconds were investigated as they have the largest hydrogen generation rates per unit area. The activation energies recorded were 43.4 kJ mol^{-1}, 50.2 kJ mol^{-1} and 41.8 kJ mol^{-1} for deposition times of 40, 60 and 80 seconds respectively. These values are comparable to the activation energies found previously for nanostructured catalysts such as Co-B deposited on Ni foam of 44 kJ mol^{-1} [15] and 33 kJ mol^{-1} [9], Co-B Nanoparticles of 43 kJ mol^{-1} [18] and Co-B deposited on carbon nanotubes of 40 kJ mol^{-1} [17]. These results are expected as the activation energy is dependent on the composition of the catalyst and not the catalytic surface area.

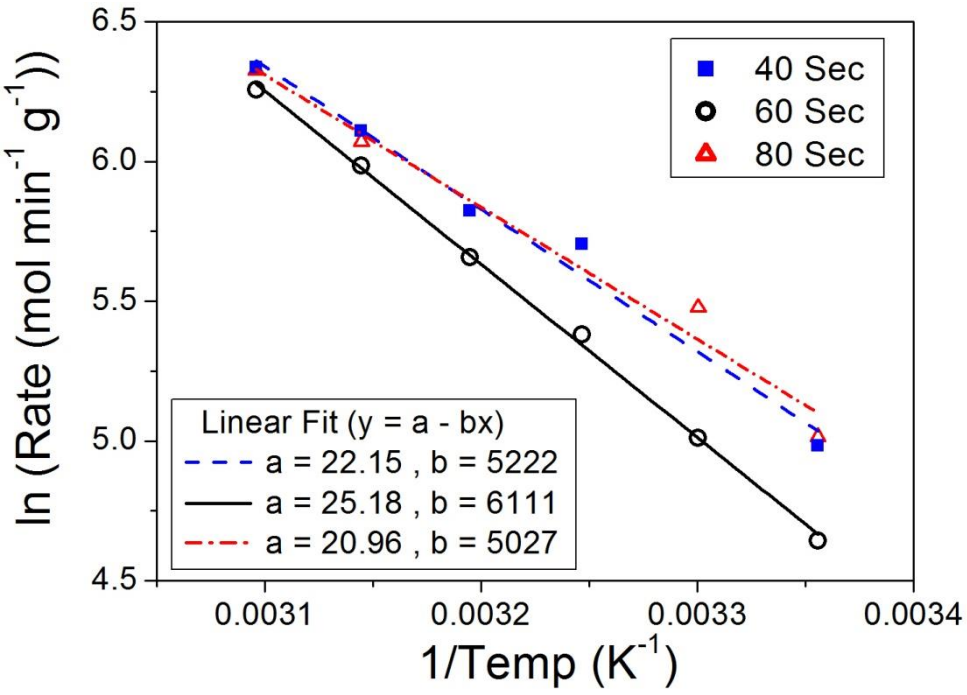

Figure 6.24: Arrhenius plot for $Co_{60}B_{40}$ nanostructures with deposition times of 40 seconds, 60 seconds and 80 seconds. The linear fits correspond to the Arrhenius equation shown in Eqn. 6.11.

The maximum hydrogen generation rate per unit mass that we recorded at a high temperature was for a deposition time of 40 seconds at 50 °C with a value of 12,600 ml min^{-1} g^{-1}. This compares relatively well to other hydrogen production rates that have been achieved by other groups previously for Co-B catalysts [2,14]. For a deposition time of 80 seconds, the hydrogen generation rate per unit mass at 50 ºC was 11,500 ml min^{-1} g^{-1}. This corresponds to a hydrogen generation rate of almost 23,800 ml min^{-1} m^{-2}, which was the largest hydrogen generation rate per unit area that was achieved.

6.10 Effect of pH

The dependence of the hydrogen generation rate on the pH of the hydrogen generation solution was investigated as it has been reported previously that solution pH has a slight effect on the hydrogen generation rate [8]. It was expected that variations in the pH of the solution would result in a change in the hydrogen generation rate. However,

as shown in Fig. 6.25, there was very little change in the hydrogen generation rate as a function of pH. $Co_{60}B_{40}$ catalysts deposited for 60 seconds were used as the catalysts for this investigation. The solution temperature was held at 40 ºC and a $NaBH_4$ concentration of 1 wt. % was used.

At a pH of 10 a hydrogen generation of 6,550 ml min^{-1} g^{-1} was recorded. At a pH of 11 the hydrogen generation rate was 5,900 ml min^{-1} g^{-1}, while rates of 6,200 ml min^{-1} g^{-1} and 6,150 ml min^{-1} g^{-1} were recorded at pH values of 12 and 13 respectively. The variation between the largest and smallest hydrogen generation rates was less than 10 %. These small variations in rate are attributed to the differences in the Co-B catalysts used as each had slightly different masses and thus slightly different structures. Therefore, we conclude that variations in the pH values above pH 10 do not affect the hydrogen generation rate.

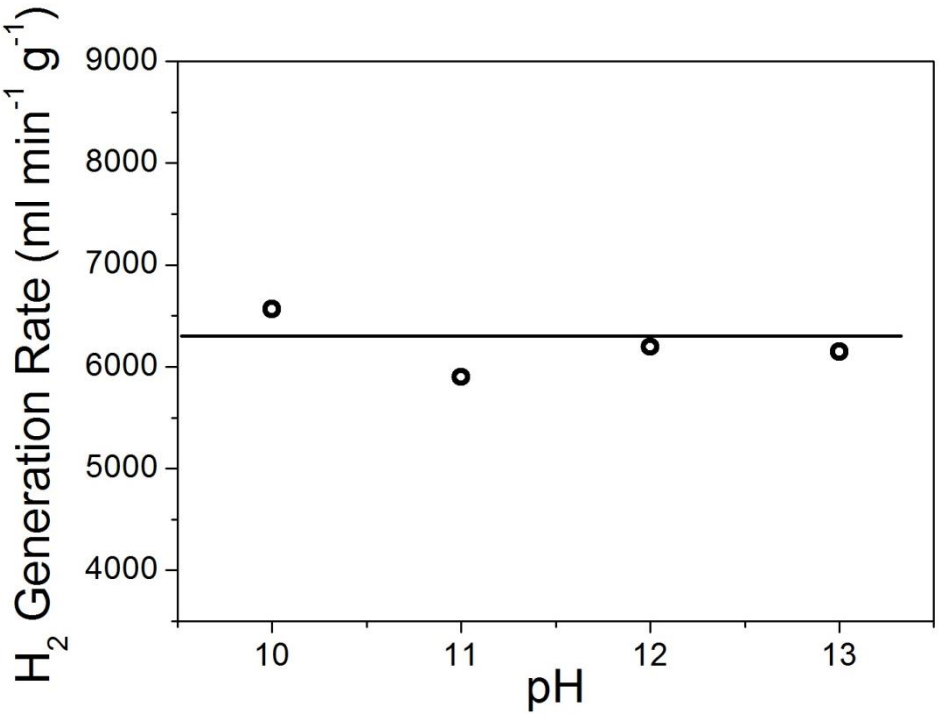

Figure 6.25: Hydrogen generation rate as a function of pH for a nanostructured $Co_{60}B_{40}$ catalyst at a temperature of 40 ºC.

6.11 $NaBH_4$ Concentration

For future technologies, large hydrogen storage densities are required for a viable technology. The DOE target is a storage density of 7.5 wt. % H_2. In pure form, $NaBH_4$ exceeds this target with a H_2 storage density of 10.5 wt. %. However, when added to water this storage density decreases, with a 7.5 wt. % H_2 density corresponding to a $NaBH_4$ concentration of 6.87 M (26 wt. % $NaBH_4$). Therefore, ideally hydrogen generation would be carried out in solutions with a large $NaBH_4$ concentration.

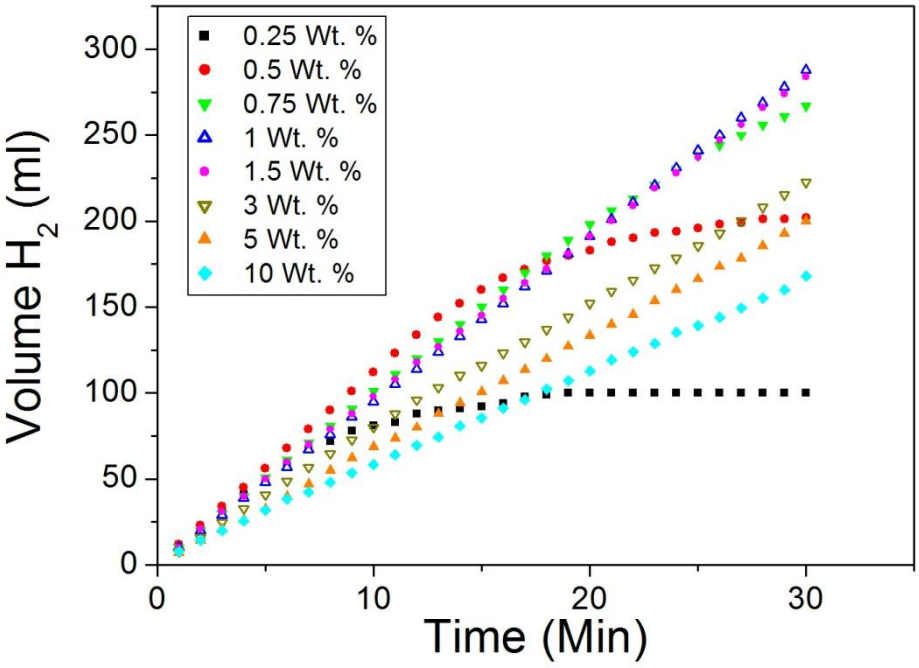

Figure 6.26: Volume of hydrogen generation as a function of time for a range of $NaBH_4$ concentrations for a nanostructured $Co_{60}B_{40}$ catalyst at a temperature of 40 ºC.

In this study, we have investigated $NaBH_4$ concentrations between 0.25 wt. % and 10 wt. %. The volume of hydrogen generated with respect to time, for a range of $NaBH_4$ concentrations is shown in Fig. 6.26. The experiments were carried out in a 20 ml solution at a temperature of 40 ºC and a pH of 10. For $NaBH_4$ concentrations of 0.25 wt. % and 0.5 wt. %, all of the available hydrogen is released within 30 minutes. For a concentration of 0.75 wt. %, the hydrogen generation process has become a first

order reaction at 30 minutes. For these $NaBH_4$ concentrations, the hydrogen generation rates were calculated from the zeroth order reaction regime only.

After a deposition time of 15 minutes, approximately 150 ml of H_2 have been released from $NaBH_4$ solutions with concentrations ranging from 0.5 to 1.5 wt. %. However, the exact hydrogen generation rates must be calculated from the mass of the samples. $NaBH_4$ concentrations of 3, 5 and 10 wt. % release the lowest amount of hydrogen as a function of deposition time. This indicates that as the $NaBH_4$ solution concentration increases, the hydrogen generation rate decreases.

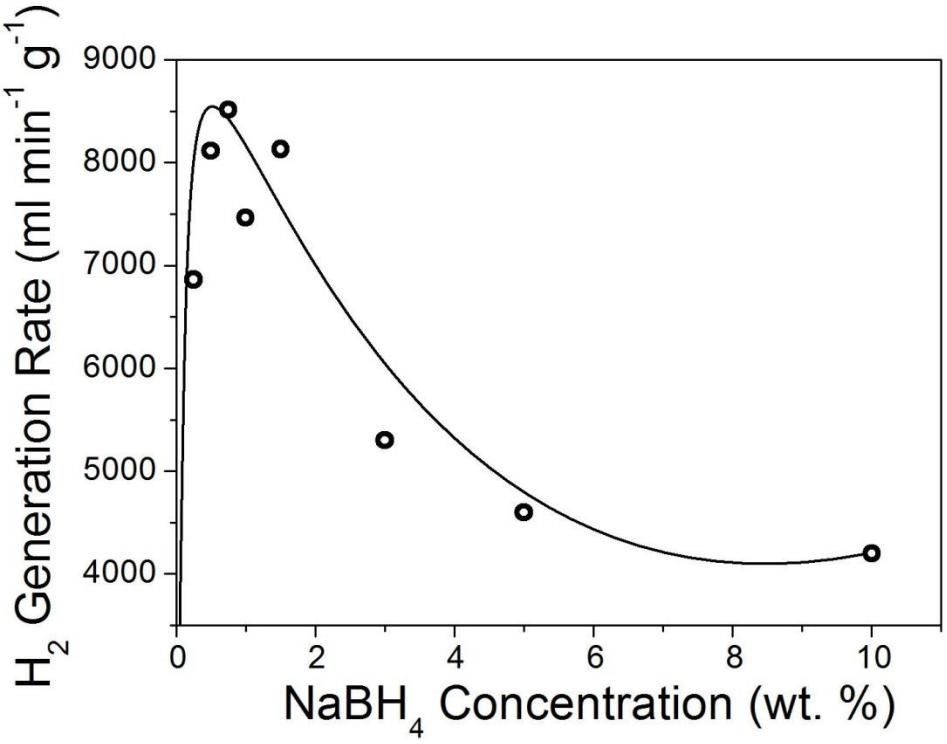

Figure 6.27: Hydrogen generation rate as a function of $NaBH_4$ concentration for a nanostructured $Co_{60}B_{40}$ catalyst at a temperature of 40 ºC. The line shown is a guide for the eye.

A plot of the hydrogen generation rates as a function of $NaBH_4$ concentration is shown in Fig. 6.27. The line shown is a guide for the eye and does not represent a fit of the data. At low $NaBH_4$ concentrations a large hydrogen generation rate is recorded with a maximum value of 8,550 ml min^{-1} g^{-1} recorded at a $NaBH_4$ concentration of 0.75 wt. %. Values of between 7,400 and 8,200 ml min^{-1} g^{-1} are recorded for $NaBH_4$

concentrations of 0.5, 1 and 1.5 wt. %. However, a large decrease in the hydrogen generation rate is observed above 1.5 wt. %. The rate has decreased to a value of 5,400 ml min^{-1} g^{-1} for a concentration of 3 wt. %, with a further decrease to less than half the maximum value of 4,200 ml min^{-1} g^{-1} for a 10 wt. % $NaBH_4$ solution. The observed trend can be explained by a model proposed by Wu et al. [19].

In this model they propose that hydrogen generation takes place in steps as shown in Eqn. 6.12-6.15.

$$BH_4^- + M \underset{\longrightarrow}{\overset{K_{BH4}}{\longleftarrow}} MBH_4 \tag{6.12}$$

$$OH^- + M \underset{\longrightarrow}{\overset{K_{BH4}}{\longleftarrow}} MOH \tag{6.13}$$

$$MBH_4 + MOH \underset{\longrightarrow}{\overset{k_1}{\longleftarrow}} MBH_3OH + MH \tag{6.14}$$

$$MH + H_20 \underset{\longrightarrow}{\overset{k_2}{\longleftarrow}} MOH + H_2 \tag{6.15}$$

Wu et al., propose that hydroxide ion activation on the metal surface (Eqn. 6.13) is the limiting step and thus the overall reaction turnover rate can be written as,

$$r = k_1[NaBH_4][NaOH] = \frac{k_1 K_{BH_4}[BH_4^-] K_{OH}[OH^-]}{\left(1 + K_{BH_4}[BH_4^-] + K_{OH}[OH^-]\right)^2} \tag{6.16}$$

where k_1, K_{BH4} and K_{OH} are the reaction constants. Therefore, when the sodium borohydride concentration is large the equation can be reduced to:

$$K_{BH_4}[BH_4^-] \gg 1 + K_{OH}[OH^-]$$

$$r = \frac{k_1 K_{OH}[OH^-]}{K_{BH_4}[BH_4^-]} \tag{6.17}$$

This indicates that for high $NaBH_4$ concentrations, the reaction rate is inversely proportional to the sodium borohydride concentration. However, for very low $NaBH_4$ concentrations the equation can be written as:

$$K_{BH_4}[BH_4^-] \ll 1 + K_{OH}[OH^-]$$

$$r = \frac{k_1 K_{BH_4}[BH_4^-]}{K_{OH}[OH^-]} \tag{6.18}$$

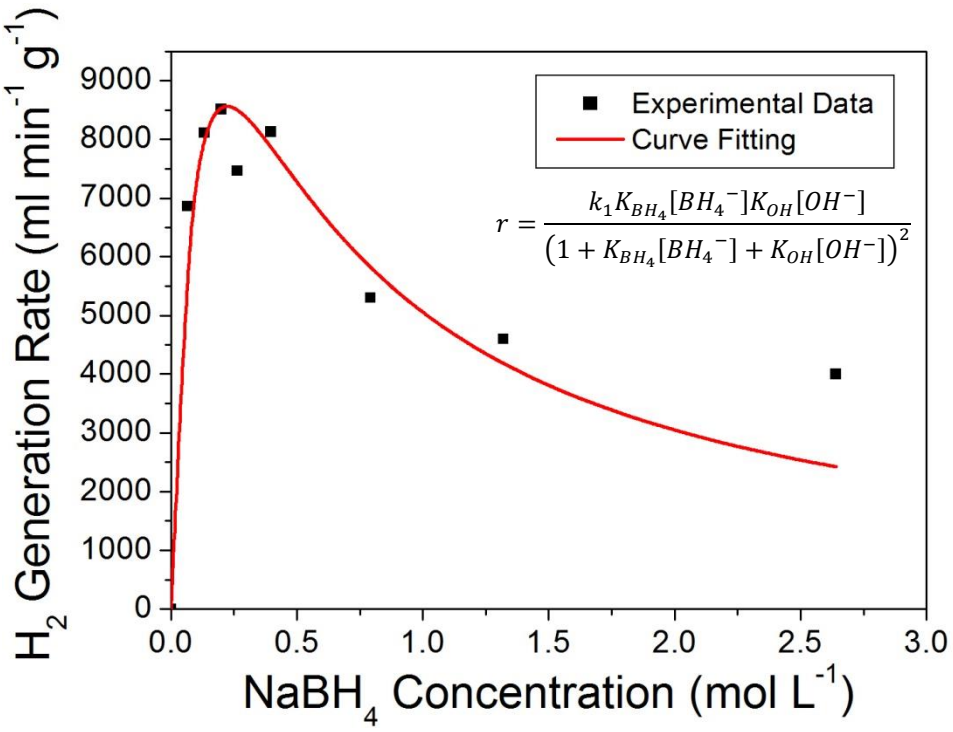

Figure 6.28: A fit of Eqn. 6.16 to our experimental data for a nanostructured $Co_{60}B_{40}$ catalyst at a temperature of 40 ºC where, r = H_2 generation rate, $[BH_4^-]$ = $NaBH_4$ concentration, k_1 = 3.44 x 10^4 ml min^{-1} g^{-1}, K_{BH4} = 3 x 10^6 ml min^{-1} g^{-1} and $K_{OH}[OH^-]$ = 6.5 x 10^5 mol min^{-1} g^{-1}.

Therefore, at low concentrations, an increase in the reaction rate with respect to $NaBH_4$ concentration is observed. Our results agree directly with those observed by Wu et al. [19], where they achieved a maximum hydrogen production rate at a $NaBH_4$ concentration of 0.25 M, which corresponds to a 1 wt. % solution. A curve for Eqn. 6.16 can be fitted to our experimental data as shown in Fig. 6.28, plotting the $NaBH_4$ concentration as molarity instead of percentage weight. This data proves that

our results follow the model proposed by Wu et al. [19] and a maximum hydrogen generation rate is recorded at $NaBH_4$ concentrations of approximately 1 wt. %.

Similar behaviours with large hydrogen generation rates at low $NaBH_4$ concentrations have been observed previously with Co-B catalysts [13, 16]. However, other studies have indicated that $NaBH_4$ concentrations of 10 wt. % [28] or 15 wt. % [29] have the largest hydrogen generation rates for Co-B catalysts. For future applications, large $NaBH_4$ concentrations would be required to make the technology feasible. We recorded a maximum hydrogen generation rate at a $NaBH_4$ concentration of 0.75 wt. %. This corresponds to a hydrogen storage capacity of less 0.2 wt. % H_2. This is far below the target set by the DOE. However, even though a 10 wt. % $NaBH_4$ solution has a low hydrogen generation rate, hydrogen is still produced at an appreciable rate. However, this would only correspond to a hydrogen storage capacity of 2 wt. %.

6.12 Recyclability

Another important factor in the potential use of Co-B catalysts for future technologies is their recyclability. As the Co-B nanostructures in this study are deposited within a polycarbonate membrane, removal from the $NaBH_4$ solution after hydrolyses can easily be achieved. During this study, the catalysts were rinsed with de-ionised water after removal from the hydrogen generation solution. They were then re-used as catalysts for hydrogen generation from an identical solution. The volume of hydrogen produced with respect to time is shown in Fig. 6.29 for a recycled nanostructured $Co_{60}B_{40}$ catalyst. In total 9 cycles were done at 40 ºC in a $NaBH_4$ solution. It is clear that as the number of cycles increases, the deposition rate decreases. Initially, when the catalyst is placed in solution 100 % of the available hydrogen is released within

the first hour. By the ninth cycle it takes over 3 hours for all the available hydrogen to be released. This indicates that the nanostructured Co-B catalyst lacks recyclability.

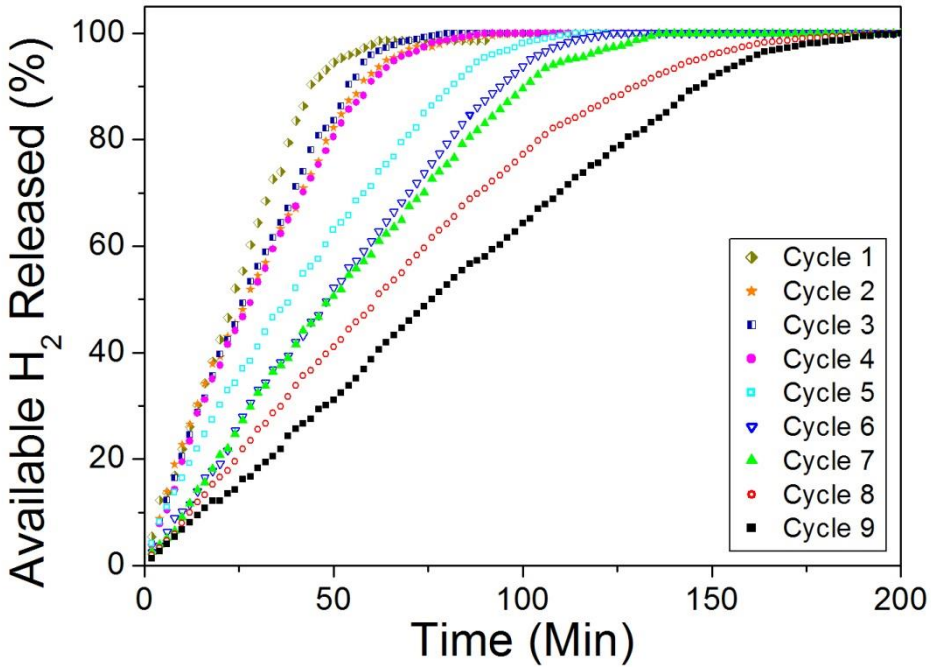

Figure 6.29: Percentage of hydrogen generated as a function of deposition time for a recycled $Co_{60}B_{40}$ nanostructured catalyst.

The hydrogen generation rate as a function of cycle number is shown in Fig. 6.30. Initially for the first cycle, a hydrogen generation rate of 7,850 ml min^{-1} g^{-1} is recorded. This has decreased to less than 5,000 ml min^{-1} g^{-1} by the 5^{th} cycle. On the 9^{th} cycle, the rate has decreased to 2,250 ml min^{-1} g^{-1}, less than 30 % of the initial value. These results are similar to those of Rakap et al. [20] and Liang et al. [10] who observed a 50 % drop in catalytic activity for Co based catalysts after 6 cycles. After 6 cycles we achieved a rate of 3,700 ml min^{-1} g^{-1}, approximately 50 % of the initial rate.

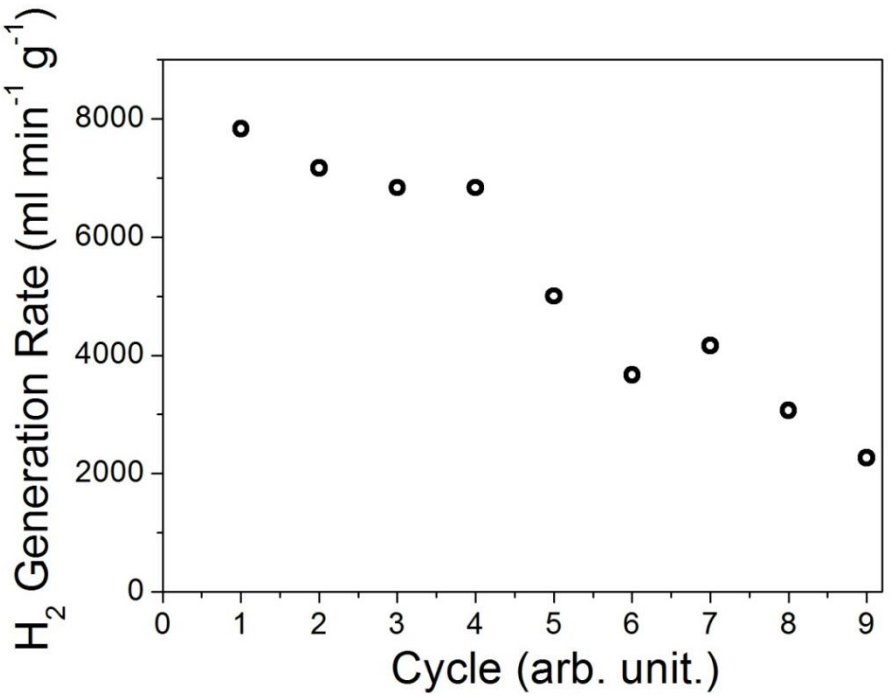

Figure 6.30: Hydrogen generation rate of a nanostructured recycled $Co_{60}B_{40}$ catalyst as a function of cycle number.

The time taken for 100 % of the available hydrogen to be released as a function of cycle number is shown in Fig. 6.31. An exponential curve can be fitted to the data with a formula of $t = 37.8 + 24.1e^{0.215C}$, where t = time and C = cycle number.

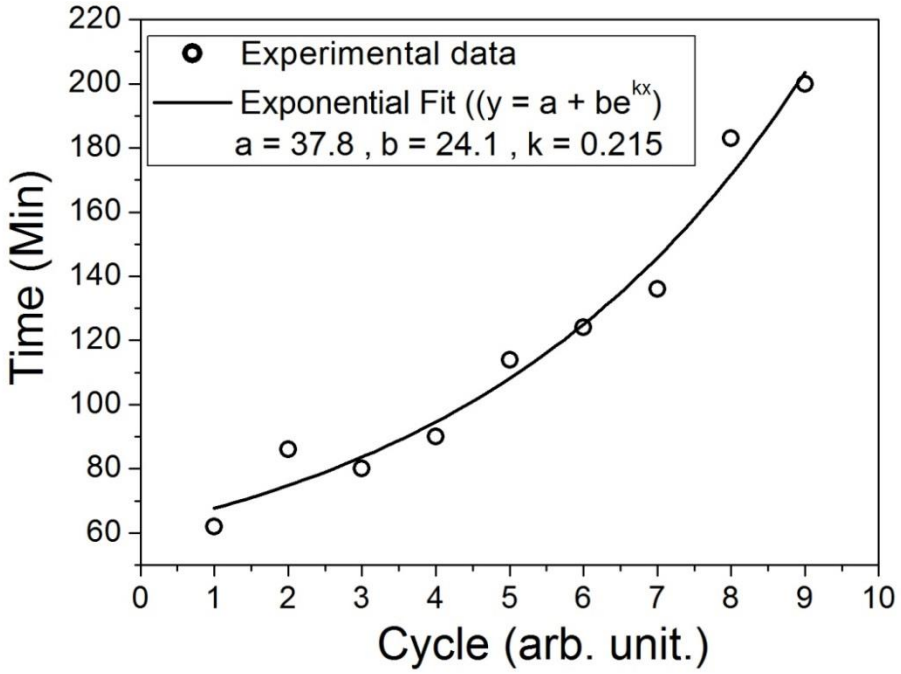

Figure 6.31: Time taken for 100 % H_2 release from $NaBH_4$ as a function of cycle for a recycled $Co_{60}B_{40}$ catalyst. Fitting represents an exponential fit of $y = a + be^{kx}$, where a = 37.8 min, b = 24.1 min and k = 0.215.

Previously, it has been suggested that the decrease in activity as the catalyst is recycled is due to precipitation of hydrolysis by-products such as $NaBO_2$, $Na_2B_4O_7$ and B_2O_3 on the catalyst surface [13]. To investigate this suggestion for our catalysts, XPS analysis was carried out on samples prior to H_2 generation and after 6 cycles of hydrogen generation. The complete XPS spectra recorded for both samples are shown in Fig. 6.32. Both spectra appear the same and no clear differences in the peaks can be observed.

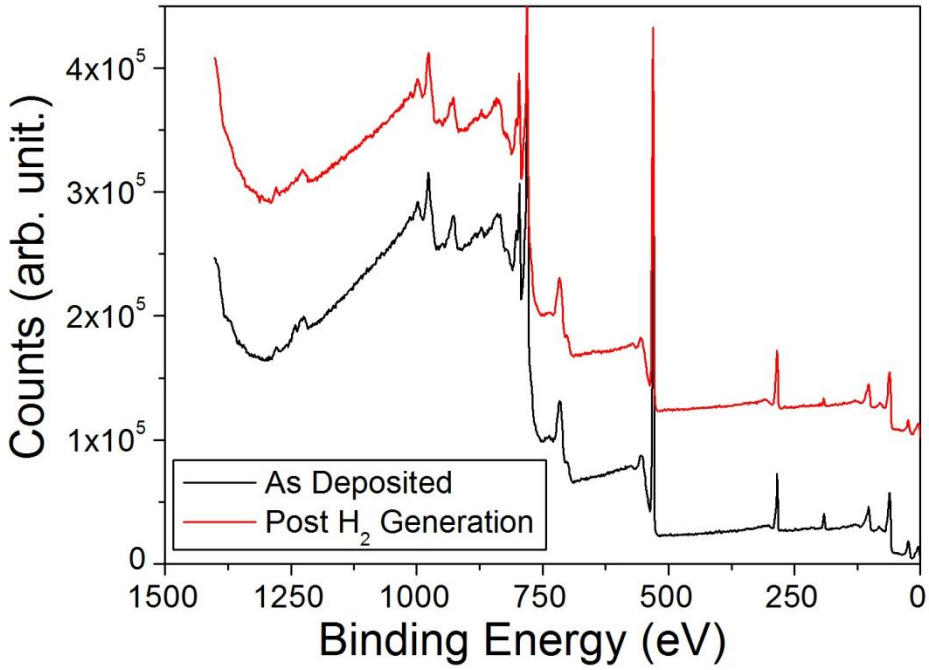

Figure 6.32: Comparison of the XPS spectra of catalytic $Co_{60}B_{40}$ nanostructures pre and post H_2 generation.

To carry out a detailed investigation of the Co-B bonding structure before and after hydrogen generation, high resolution XPS spectra were taken around 800 eV for Co and 190 eV for B. The high resolution spectrum for Co is shown in Fig. 6.33. There are 6 different peaks recorded in the Co spectrum before and after deposition. The bonds that correspond to each peak are shown in Table 6.4. The two major peaks at binding energies of 781.3 eV and 797.2 eV correspond to the energy level doublet within the 2p orbital. For the p orbital, the principle quantum number n = 2. The

angular momentum quantum number $l = n - 1$, so for the p orbital $l = 1$. The total angular momentum quantum number $j = l + s$, where s = spin angular momentum number and can have values of ± 1/2. Therefore, for the p orbital, j can have values of 1/2 or 3/2, each have which have different binding energies. The peak at 781.3 eV corresponds to j = 3/2, while 797.2 eV corresponds to j = 1/2. The area below the 781.3 eV is double that of j = 1/2 as 4 electrons in the 2p orbital have a total angular momentum quantum number = 3/2, while only 2 electrons have a value of 1/2. The two smaller peaks, recorded after the principle peak, are called satellite peaks. They are caused by emitted electrons losing energy to valence electrons giving the appearance of having higher binding energies due to their lower kinetic energy.

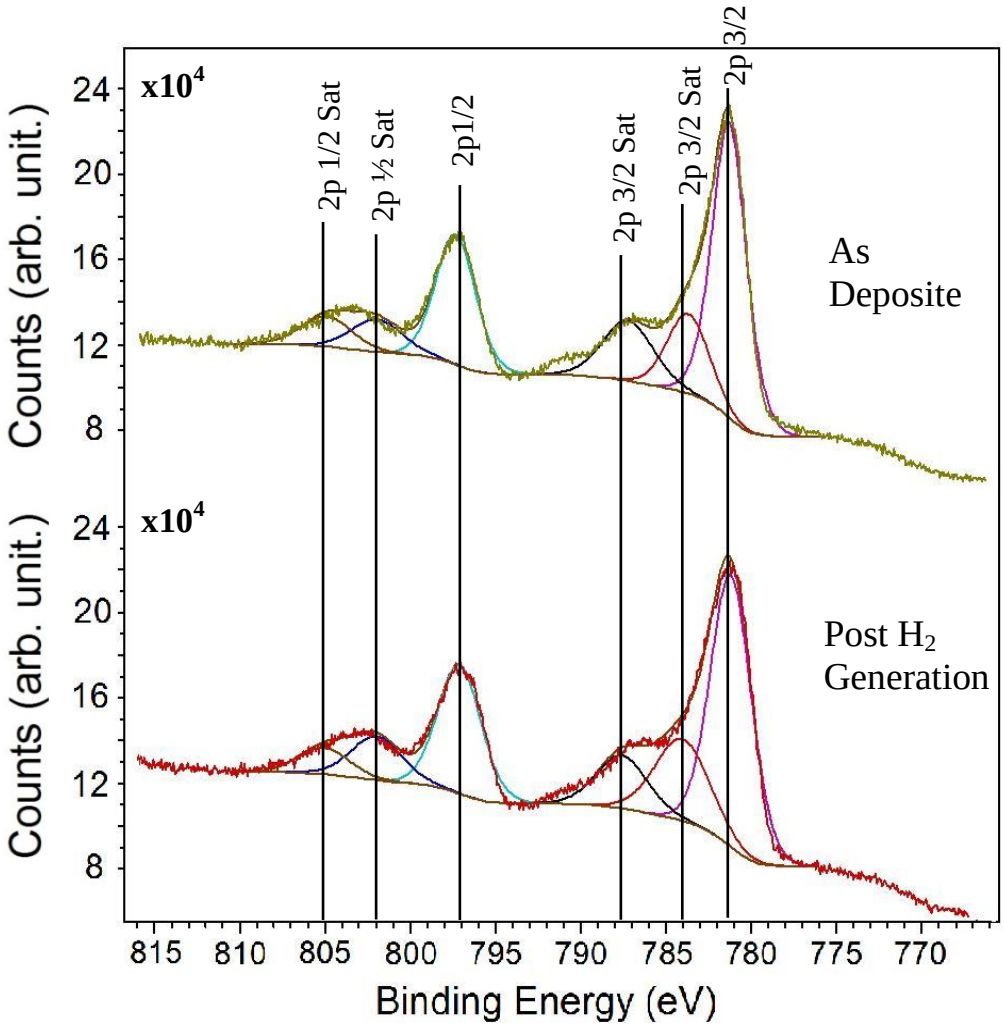

Figure 6.33: XPS analysis of Co 2p spectra of $Co_{60}B_{40}$ nanostructures pre and post hydrogen generation.

Name	Structure	Binding Energy (eV)
Co 2p_1	2p3/2 $Co(OH)_2$	781.3
Co 2p_2	2p3/2:Satellite	784.2
Co 2p_3	2p3/2:Satellite	787.7
Co 2p	2p1/2	797.2
Co 2p_3	2p1/2:Satellite	802.1
Co 2p	2p1/2:Satellite	805.2

Table 6.4: Binding energies associated with the peaks observed in the high resolution Co 2p XPS spectrum.

If oxidation of the Co metal occurred during hydrogen catalysis, a shift in the spectra would be expected. However, after H_2 generation, there is no change in the peaks recorded for the Co spectrum indicating that there is no change in the structure of the Co metal during the hydrogen generation process.

As the expected precipitates do not contain any Co metal, no change in the Co spectrum would be expected. Each of the proposed precipitates contain B, so shifts in the B spectra may be seen. However, as shown in Fig. 6.34, no change is observed in the B spectrum. The peak at 192.2 eV represents oxidised B^{+3}. However, this peak is also present in the as deposited Co-B sample in the form of B_2O_3 on the surface of the catalsyst. Therefore, it is difficult to say for certain whether or not precipitates containing boron, such as $NaBO_2$, $Na_2B_4O_7$, $NaBH_4$ or B_2O_3, are deposited on the surface as they all contain B^{+3}. However, Na peaks are not observed in the spectrum post hydrogen generation, indicating that neither $NaBO_2$ nor $Na_2B_4O_7$ nor $NaBH_4$ are precipitated onto the surface of the catalyst during hydrogen generation.

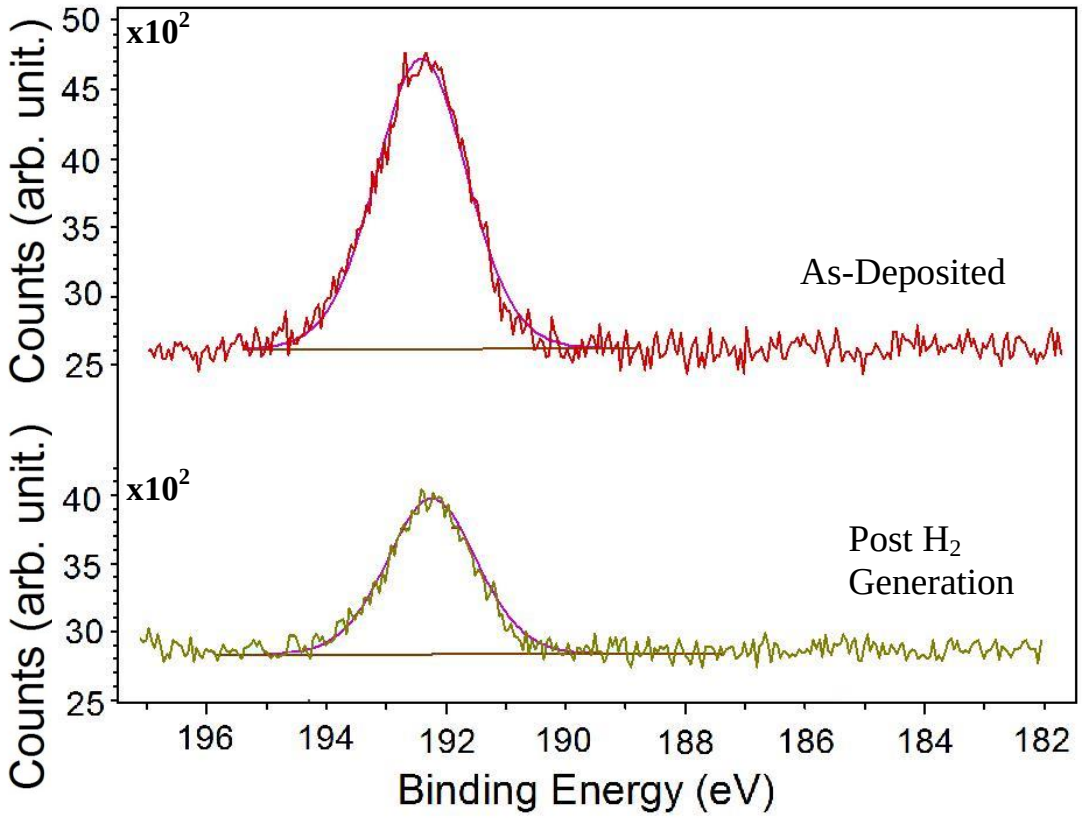

Figure 6.34: XPS analysis of B 1s spectra of $Co_{60}B_{40}$ nanostructures pre and post hydrogen generation.

6.13 Potential

In this chapter, we have investigated the hydrogen generation rates of nanostructured Co-B catalysts. The potential viability of the system for future technologies depends on three main factors, the hydrogen storage density, the recyclability potential of the catalysts and the hydrogen generation rates. In this study, we have shown that the maximum hydrogen generation rates of the electrolessly deposited Co-B catalysts occur at very low storage densities. The maximum rate is achieved for a $NaBH_4$ solution concentration of 0.75 wt. %. This corresponds to a hydrogen storage density of less than 0.2 % H_2. In terms of recyclability, the catalysts have a poor lifetime. There is a large degrading of the catalytic activity as the samples are recycled. After only 6 cycles, the catalytic activity has reduced to less than 50 % of the original value.

For this technology to become viable, the storage density and recyclability capability will have to be increased.

To investigate the potential of the Co-B catalysts that we have developed, a theoretical study used by Muir et al. can be used. A hydrogen generation rate of 1 mole of H_2 per minute has the potential to generate a current of 3.2 kA. Taking a fuel cell with an output voltage of 0.7 V, 1 mole of H_2 gas has the potential to produce a power output of 2.24 kW, enough to power an electric heater.

The largest hydrogen generation rate we achieved at 40 ºC was 10,800 ml min^{-1} g^{-1} for a Co-B catalyst deposited for 20 seconds. This corresponds to 0.48 moles of H_2 per minute. To produce a power output of 2.24 kW just over 2 g of the catalyst would be required. However, the hydrogen generation rate per unit area for this catalyst was only, 8,050 ml min^{-1} m^{-2}. Therefore, almost 3 m^2 of catalyst would be required to provide 2.24 kW of power. Therefore, an improved areal density is required.

For the Co-B catalyst with a deposition time of 80 seconds, the hydrogen generation rates per unit mass and area were 6,100 ml min^{-1} g^{-1} and 17,650 ml min^{-1} m^{-2} respectively. Therefore, almost 4 g of catalyst would be required to produce a power output of 2.24 kW, though this would only require a catalytic surface area of 1.5 m^2. If the generation temperature was increased to 50 ºC, the hydrogen generation rates increase to 11,500 ml min^{-1} g^{-1} and 23,800 ml min^{-1} m^{-2}. Now 2g of catalyst would be required corresponding with a total area of just less than 1 m^2. If this was to be considered for larger fuel cells, such as an electric vehicle, the power output required would be around 100 kW. Therefore 90 g of catalyst on a total surface area of 45 m^2 would be required to power the vehicle. In light of this data, our hydrogen generation system is not currently a viable alternative for future technologies.

6.14 Conclusions

In this study, the hydrogen generation rate of nanostructured catalysts deposited via electroless deposition have been maximised. Through the use of a Co-B alloy, large hydrogen generation rates were achieved. Agitation of the catalyst within the solution was required to ensure that hydrogen nucleation on the catalyst surface was prevented, allowing for a large hydrogen generation rate. We have shown that a nanostructured catalyst achieves a 50 % increase in the hydrogen generation rate per unit area over the generation rate for a thin film. The activation energies of the Co-B catalysts were found to lie in the range of 40 – 50 kJ mol^{-1}. However, the largest hydrogen generation rates occur at very low hydrogen storage densities of only 0.2 wt. % H_2, far below the targeted 7.5 wt. % H_2. The recyclability of the Co-B catalysts is also poor with a 50 % decrease in the catalytic activity after only 6 cycles.

Although the nanostructured Co-B catalysts investigated in this study display large hydrogen generation rates, comparable with other catalysts in the literature, the total mass and catalytic area required to produce enough hydrogen to power a fuel cell are impractical. Larger hydrogen generation rates are required for this system to be considered as an alternative source of power. In this study, the nanostructure is not removed from the template. Therefore, only the internal walls of the nanotubes can catalyse the reaction. If the polycarbonate membrane could be removed, without the loss of the nanostructure shape, then it is possible that a larger hydrogen generation rate could be achieved. However, in this case, the Co-B catalyst will be suspended in solution and a method for its removal would be required to allow for recyclability.

In essence, there are many challenges remaining to make this a viable technology. From this study, we can conclude that the nanostructured catalyst provides an

enhanced hydrogen generation rate over a thin film catalyst. Therefore, if an alternative catalytic material or an alternative hydrogen storage system is developed, a nanostructured catalyst such as the one presented in this study could be used to provide an enhanced hydrogen generation rate.

6.15 References

[1] L. Schlapbach and A. Züttel, *Nature*, **414**, 353 (2001).
[2] S. S. Muir and X. Yao, *International Journal of Hydrogen Energy*, **36**, 5983 (2011).
[3] H. C. Brown and C. A. Brown, *Journal of the American Chemical Society*, **84**, 1494 (1962).
[4] S. C. Amendola, S. L. Sharp-Goldman, M. Saleem Janjua, M. T. Kelly, P. J. Petillo and M. Binder, *Journal of Power Sources*, **85**, 186 (2000).
[5] V. I. Simagina, P. A. Storozhenko, O. V. Netskina, O. V. Komova, G. V. Odegova, T. Y. Samoilenko and A. G. Gentsler, *Kinet Catal*, **48**, 168 (2007).
[6] A. A. Vernekar, S. T. Bugde and S. Tilve, *International Journal of Hydrogen Energy*, **37**, 327 (2012).
[7] K. S. Eom, K. W. Cho and H. S. Kwon, *Journal of Power Sources*, **180**, 484 (2008).
[8] J. C. Ingersoll, N. Mani, J. C. Thenmozhiyal and A. Muthaiah, *Journal of Power Sources*, **173**, 450 (2007).
[9] H. B. Dai, Y. Liang, P. Wang and H. M. Cheng, *Journal of Power Sources*, **177**, 17 (2008).
[10] Y. Liang, P. Wang and H. B. Dai, *Journal of Alloys and Compounds*, **491**, 359 (2010).
[11] S. S. Muir, Z. Chen, B. J. Wood, L. Wang, G. Q. Lu and X. Yao, *International Journal of Hydrogen Energy*, **39**, 414 (2014).
[12] B. H. Liu and Q. Li, *International Journal of Hydrogen Energy*, **33**, 7385 (2008).
[13] J. H. Kim, K. T. Kim, Y. M. Kang, H. S. Kim, M. S. Song, Y. J. Lee, P. S. Lee and J. Y. Lee, *Journal of Alloys and Compounds*, **379**, 222 (2004).
[14] N. Patel, R. Fernandes and A. Miotello, *Journal of Power Sources*, **188**, 411 (2009).
[15] P. Krishnan, S. G. Advani and A. K. Prasad, *Applied Catalysis B*, **86**, 137 (2009).
[16] J. Lee, K. Y. Kong, C. R. Jung, E. Cho, S. P. Yoon, J. Han, T. G. Lee and S. W. Nam, *Catalysis Today*, **120**, 305 (2007).
[17] Y. Huang, Y. Wang, R. Zhao, P. K. Shen and Z. Wei, *International Journal of Hydrogen Energy*, **33**, 7110 (2008).
[18] Z. Wu and S. Ge, *Catalysis Communications*, **13**, 40 (2011).
[19] Z. Wu, X. Mao, Q. Zi, R. Zhang, T. Dou and A. C. K. Yip, *Journal of Power Sources*, **268**, 596 (2014).
[20] M. Rakap and S. Özkar, *Applied Catalysis B*, **91**, 21 (2009).

Chapter 7 - Conclusions and Future Work

7.1 Introduction

This thesis presents an investigation into the electroless deposition process and associated properties of metallic nanotubes. There were 3 main research objectives associated with this work.

1. Understand and develop an electroless deposition method with which continuous nanotubes with a uniform wall thickness could be formed.
2. Characterise the magnetic properties of the nanotubes as a function of composition, crystal structure and size so that the associated magnetic properties could be controlled.
3. Characterise the catalytic activity of electrolessly deposited nanotubes and investigate their potential as catalysts in future hydrogen storage technologies for hydrogen generation from $NaBH_4$.

In this chapter, the conclusions of each of these research objectives are discussed along with future work that is required to build upon our findings.

7.2 Contribution 1: Electroless Nanotube Deposition

7.2.1 Stages of Deposition

We carried out the electroless deposition process using a polycarbonate membrane as a template structure. As deposition occurs both within the membrane pores to form nanotubes and on the membrane surface to form a thin film, the resultant nanostructure comprises continuous nanotubes connected at both ends by a thin film.

As deposition continues, the nanotubes become end-closed and a continuous film forms on the membrane surface. We have found that incomplete nanotubes with non-uniform wall thicknesses are formed due to a difference in deposition rates on the membrane surface and within the membrane pores. We conclude that this is due to a diffusion limited reaction within the membrane pores and to achieve continuous uniform nanotubes, a kinetically controlled deposition process is required.

Using the electroless Ni-B deposition process as an exemplar, we investigated the effect of the deposition bath parameters on the deposition rate. We have found that, the deposition rate is dependent on citrate concentration, pH and bath temperature. Diammonium citrate inhibits deposition while increasing temperatures and pH values promote deposition. Therefore, to achieve a kinetically controlled deposition process, we conclude that, low temperatures, low pH values and large citrate concentrations are required.

7.2.2 Kinetically Controlled Model

By investigating the external pore diameter of the nanotubes as a function of total deposited mass, we have developed a model which provides evidence of the occurrence of a kinetically controlled reaction. For a kinetically controlled reaction, deposition occurs at an equal rate throughout the membrane pores and on the membrane surface. We have shown that for deposition temperatures below 30 ºC, at pH 10 and citrate concentration of 0.118 M, three distinct regimes of deposition can be observed. Initially a catalytic reaction occurs during which deposition occurs at a large rate and deposition within the nanotubes is diffusion limited. After the initial catalytic process, deposition becomes kinetically controlled and continuous uniform nanotubes are formed. However, we have found that once the inner diameter becomes

too small, deposition becomes diffusion limited and the nanotubes become end-closed. We conclude that the critical pore diameter is dependent on the deposition rate and can be maximised with a reduced deposition rate.

7.2.3 Uniform Nanotubes

Using a template structure with a 400 nm pore diameter, the maximum wall thickness that we achieved for a kinetically controlled reaction was approximately 110 nm for a deposition temperature of 20 ºC. At 30 ºC, a kinetically controlled deposition process could only be achieved up to a maximum wall thickness of 80 nm. From this work, we conclude that a kinetically controlled deposition process is required to achieve the formation of uniform nanotubes. Through the investigation of the electroless deposition process, we have achieved our first research objective and have successfully synthesised nanotubes with a uniform wall thickness.

7.3 Contribution 2: Magnetic Properties

7.3.1 Specific magnetisation

From our investigations of the magnetic properties of Ni-B, we conclude that B plays a vital role in the determination of the specific magnetisation of the electrolessly deposited alloy. When B and Ni are co-deposited, B interacts with Ni by transferring electrons to a vacant d-orbital of the metallic Ni. This results in a decrease in the specific magnetisation of the electrolessly deposited alloy. We have found that the B content of the electrolessly deposited alloy is dependent on the pH of the electrolyte, with a large pH corresponding to a low B content. Deposition below pH 8.5 results in the formation of a Ni-B alloy with a negligible magnetisation. Therefore, we conclude that a large pH > 8.5 is required to deposit an alloy with an appreciable specific magnetisation. The largest specific magnetisation that we achieved for the as-

deposited Ni-B nanostructures was 33.7 J^{-1} T^{-1} kg^{-1} for a $Ni_{88}B_{12}$ nanostructure deposited at pH 12. This is 60 % of the maximum possible value of 55.4 J^{-1} T^{-1} kg^{-1} for pure Ni.

We have shown that annealing up to a maximum of 500 ºC increases the specific magnetisation of the Ni-B nanotubes. During annealing B diffuses out of the bulk structure which leads to an increased magnetic moment from the electrolessly deposited magnetic alloy. Annealing of Ni-B nanotubes for 1 hour at 500 °C leads to a maximum magnetisation of 48.6 J^{-1} T^{-1} kg^{-1}, 88 % of the maximum possible value. We have found that the specific magnetisation achieved at 500ºC is independent of the B content. Therefore, we conclude that nanotubes can be deposited at low pH values to ensure the formation of continuous nanotubes with a uniform wall thickness and then annealed to increase the specific magnetisation.

The addition of ferromagnetic elements such as Fe also increases the specific magnetisation of the deposited Ni-B alloy. We recorded a maximum specific magnetisation of 84.3 J T^{-1} kg^{-1} for a Ni-Fe-B alloy with a composition of $(Ni_{62}Fe_{38})_{60}B_{40}$. Here, we have shown that through variations of B content, crystal structure and addition of alloys such as Fe, we can control the specific magnetisation of the electrolessly deposited nanostructures.

7.3.2 Coercivity

The coercivity of the nanotubes is dependent on the boron content, crystal structure and composition of the nanotubes. We have found that as the B content of the nanostructures decreases, larger coercivities are recorded. This is due to an increase in the size of the Ni grain structure as the B content decreases. Annealing also results in grain formation and growth within the Ni-B alloy. Therefore, a corresponding

increase in the coercivities of the magnetic nanotubes is obtained. From these results, we conclude that the magnetic properties of the electrolessly deposited nanotubes can be altered by controlling the B content within the deposited alloy and by annealing at different temperatures.

Through the addition of Fe to the Ni-B nanotubes, decreases in squareness and coercivity are observed for increased Fe contents. By altering the Fe content of the nanotubes, we can control magnetic properties such as specific magnetisation, coercivity and squareness. The addition of Cu to the Ni-B nanotubes also affects the magnetic properties of the nanotubes. These results indicate that we have achieved our second research objective and we can control the magnetic properties of the nanotubes through alterations of the nanotube composition. Therefore, it may be possible to tailor the magnetic properties of the nanotubes to suit a range of potential applications.

7.3.3 Magnetic Anisotropy

There is a large anisotropy associated with the as-deposited nanostructures. This anisotropy is due to the presence of the thin film on the membrane surface because in-plane orientations of magnetic moments are favoured within a magnetic film. However, once the film is removed, the electrolessly deposited nanotubes display a very small associated anisotropy. For continuous Ni-B and Ni-Fe-B nanotubes deposited at low temepratures, a vortex reversal mechanism was recorded, for which a minimum coercivity was observed parallel to the nanotube axis. However, for Co-B a transverse reversal mechanism was observed with a minimum coercivity recorded perpendicular to the nanotube axis due to the large nucleation field associated with the vortex reversal mode for Co-B nanotubes. From these results, we conclude that the

reversal mechanism of the nanotubes is dependent on the tube structure and can be used to control the magnetic anisotropy of the tubes.

7.4 Contribution 3: Catalytic Activity

7.4.1 Composition

Through the study of a range of alloyed nanostructured catalysts, we have found that Co-B alloy has the largest hydrogen generation rate. We have found that a B content between 29 at. % and 46 at. % is required to maximise the hydrogen generation rate, because B provides the electrons required for electron transfer between the BH_4^- ions and the aqueous H^+ ions. The activation energies of the Co-B catalysts were found to lie in the range of 40 – 50 kJ mol^{-1}.

7.4.2 Structure

We have found that the catalytic activities of the deposited Co-B nanostructures depend on the deposited nanostructure. We recorded a maximum hydrogen generation rate per unit mass of 10,800 ml min^{-1} g^{-1} at 40 ºC for a Co-B catalyst with a deposition time of only 20 seconds. At this deposition time, Co-B islands are present and thus the majority of deposited Co catalyses hydrogen release from $NaBH_4$. However, the largest hydrogen generation rate per unit area that we recorded was 18,000 ml min^{-1} m^{-2} for a deposition time of 80 seconds. This corresponds to the deposition time for which a maximum catalytic surface area is present due to the formation of continuous nanotubes. As the deposition time increases, the nanotubes become end-closed and a decrease in the hydrogen generation rate was observed. For the maximum hydrogen generation rate of 18,000 ml min^{-1} m^{-2}, we attributed 12,000 ml min^{-1} m^{-2} to a catalysed reaction on the membrane surface, while 6,000 ml min^{-1} m^{-2} was attributed to a catalysed reaction within the nanotube

structure. From these results, we conclude that a nanostructured catalyst results in a 50 % increase in the hydrogen generation rate per unit area.

7.4.3 Potential

Our hydrogen generation rates are similar to those achieved previously, though larger hydrogen generation rates have been achieved for Co-B nanoparticles and Co-B deposited on Ni foam. We achieved a maximum hydrogen generation rate for a $NaBH_4$ solution that contained 1 wt. % $NaBH_4$. For potential use in future applications, a much larger storage capacity is required with the DOE target of 7.5 wt. % H_2. This corresponds to a $NaBH_4$ concentration of 6.87 M (26 wt. % $NaBH_4$). The recyclability of the nanostructured Co-B catalysts is also important for their potential use in future technologies. We found that after 6 cycles, the activity of the catalysts decreased by 50 %. From these results, we conclude that the electrolessly deposited nanostructured Co-B catalysts are not feasible for future technologies. However, due to their nanostructure, an increase in the catalytic activity is observed and so may have potential in different systems.

7.5 Summary

Through a range of experimentation, we have achieved the three research objectives that were associated with this work. Firstly, using an electroless deposition process, continuous nanotubes with a uniform wall thickness have been deposited. The nanotubes had an outer diameter of 400 nm and a maximum wall thickness of approximately 100 nm. Using the deposition process and deposition model that we have described, researchers can now distinguish between the presence of a kinetically controlled deposition process and a diffusion limited process. Further research in the

area should lead to the formation of nanotubes with a larger wall thickness or smaller external diameter.

We have achieved our second research objective by controlling the magnetic properties of the electrolessly deposited nanotubes through variations of the composition, crystal structure and nanostructure. We have achieved control over the specific magnetisation of the nanotubes, while also controlling the coercivity, remanence and saturation field. We have found that nanotubes with a large Fe content display the largest specific magnetisation and lowest coercivities and hence have many applications in future technological areas such as power technologies, electronic devices, sensor applications and bio-technology. This should enable the tailoring of the magnetic properties of the nanotubes to suit each unique application.

Our third research objective was achieved by investigating the catalytic activities of Co-B nanostructures for use in future hydrogen generation technologies. We found that the electrolessly deposited nanostructure displays a 50 % increase in the associated catalytic activity when compared to a film. However, due to recyclability issues and an overall low hydrogen storage capacity the electrolessly deposited nanostructures have limited potential for future hydrogen technology applications. However, due to the increased activity, the nanostructures may be suitable for other catalytic applications.

From this research, we have gained an increased understanding of the electroless deposition process, the magnetic properties and the catalytic properties of electrolessly deposited nanotubes. The results that we achieved have the potential to form the basis for a large range of future research, from which enhanced nanostructures with enhanced magnetic and catalytic properties can be formed.

7.6 Future Work

7.6.1 Deposition Process

Although we have achieved a kinetically controlled deposition process for nanotubes with an external diameter of 400 nm, many challenges remain in the area. We achieved a maximum wall thickness of approximately 110 nm which corresponds to an internal diameter of 180 nm. Ideally, nanotubes with larger aspect ratios and smaller external diameters such as 200 nm, 100 nm and 50 nm would be synthesised via electroless deposition. However, further research must be undertaken to achieve a kinetically controlled deposition process at these small diameters.

To achieve smaller diameters, the initial catalytic process that causes a sharp initial closure of the pores must be minimised to allow for a more controlled reaction. One possible solution to this challenge is reducing the number of deposited Pd nuclei, though this could result in a more uneven surface. Other methods of catalysis could also be attempted, which may not display the same large initial deposition rate. Through further research, the challenges preventing the electroless deposition of nanotubes with a small external diameter can be overcome and the fabrication of these nanotubes should be possible.

7.6.2 Magnetic Properties

We have found that the electrolessly deposited nanotubes are soft magnetic materials. Soft magnetic nanotubes have potential applications in future power technologies for use in components such as integrated inductors and transformers in future electronic devices. Other potential applications include use in sensor application and bio-technology in areas such as targeted drug delivery. Future work on the magnetic

properties of the nanotubes should focus on achieving nanotubes with lower coercivities and squareness values to decrease the energy losses involved.

As we have shown in this work, this can be done by altering a range of parameters including the shape and size of the nanotubes, such as external diameters, wall thicknesses and lengths, the composition of the nanotubes and the structure of the nanotubes. We have shown that the addition of other non-magnetic materials such as Cu can subtly alter certain magnetic properties while maintaining others constant. Therefore, more work should be done on alloying magnetic nanotubes with a range of non-magnetic elements. A systematic study of Ni, Fe and Co nanotubes alloyed with other elements such as P, Cu, Pt and O should be undertaken to achieve a range of magnetic properties. By continuing this work, it should be possible to tailor the magnetic properties of the electrolessly deposited nanotubes to suit a range of potential applications.

7.6.3 Catalytic Properties

Although the hydrogen generation rates of the Co-B nanostructures are probably too low for future hydrogen technologies, there is a vast amount of future work which can still be carried out. The external diameter of the nanotubes is 400 nm and appears to result in a diffusion limited catalytic reaction within the nanotube pores. Therefore, nanotubes with larger external diameters should be considered. We have investigated the catalytic activity of the as-deposited nanostructures within the polycarbonate template. Therefore, only the internal walls of the nanotubes catalyse hydrogen generation. By removing the nanotubes from the template structure, the external walls would be exposed to the solution. This should result in a larger hydrogen generation rate because the reaction would not be diffusion limited, like it is within the nanotube

pores. However, a method to remove the polycarbonate membrane and recover the nanotubes has proved difficult. Although annealing is one possible method, it will result in the segregation of B and Co, which will reduce the catalytic activity of the structure. Therefore, this challenge has yet to be overcome.

However, if a new catalytic material with a large activity, or a new storage material with a large hydrogen storage capacity is discovered, then a nanostructured type catalyst similar to the one presented here may be considered. Because the nanostructured catalyst has an increased catalytic activity, future research should not be limited to hydrogen technologies. There may also be potential use for the nanostructured catalyst in other chemical applications, which require increased catalytic activities.